

Мнистарство просвете науке и технолошког развоја  
Матични научни одбор за физику  
Датум: 05.07.2022. године  
Београд

**Институт за физику у Београду**  
**Др Дејан Ђокић, научни сарадник**

Прегревица 118  
11080 Београд

Поштовани др Ђокићу,

Матични научни одбор за физику је на својој седници од 24. јуна 2022. године разматрао Ваш захтев за признавање и категорисање публикације "Transport properties of nanoscopic solids as probed by spectroscopic techniques" аутори Дејан М. Ђокић, Новица Пауновић, Бојан Стојадиновић, Димитрије Степаненко, Саша Лазовић, Зорана Д. Дохчевић-Митровић из 2021. године у монографији „Fundamentals and Properties of Multifunctional Nanomaterials“, издавач Elsevier.

Одбор је једногласно донео одлуку да се наведена публикација категорише као истакнута монографија међународног значаја, а Ваш допринос као монографска студија у оквиру ове монографије, која се на основу Прилога 1 Правилника о стицању истраживачких и научних звања категорише као публикација категорије М13.

С поштовањем,

Председник Матичног научног одбора за физику



др Антун Балаж, научни саветник

Мнистарство просвете науке и технолошког развоја  
Матични научни одбор за физику  
Датум: 05.07.2022. године  
Београд

**Институт за физику у Београду**  
**Др Зорана Дохчевић Митровић, научни саветник**

Прегревица 118  
11080 Београд

Поштована др Дохчевић Митровић,

Матични научни одбор за физику је на својој седници од 24. јуна 2022. године разматрао Ваш захтев за признавање и категорисање публикације „Temperature-dependent Raman spectroscopy for nanostructured materials characterization“ аутори Зорана Д. Дохчевић-Митровић, Соња Ашкрабић, Бојан С. Стојадиновић, Дејан М. Ђокић, из 2022. године у монографији „Design, Fabrication, and characterization of multifunctional nanomaterials“, издавач Elsevier.

Одбор је једногласно донео одлуку да се наведена публикација категорише као истакнута монографија међународног значаја, а Ваш допринос као монографска студија у оквиру ове монографије, која се на основу Прилога 1 Правилника о стицању истраживачких и научних звања категорише као публикација категорије М13.

С поштовањем,

Председник Матичног научног одбора за физику



др Антун Балаж, научни саветник

# *Temperature-dependent Raman spectroscopy for nanostructured materials characterization*

Zorana D. Dohčević-Mitrović, Sonja Aškračić, Bojan S. Stojadinović,  
Dejan M. Djokić

*Nanostructured Matter Laboratory, Institute of Physics Belgrade, University of Belgrade,  
Belgrade, Serbia*

## Chapter Outline

- 1. Introduction 11
- 2. Anharmonicity in nanostructured materials 13
  - 2.1 Basic theory of phonon-phonon interactions 13
  - 2.2 Phonon-phonon interactions in nanomaterials 16
- 3. Size/microstrain effects and phase separation 19
- 4. Raman thermometry 23
- 5. Temperature behavior of acoustic vibrations in nanocrystalline materials studied by low-frequency Raman spectroscopy 26
- 6. Electron-phonon interaction 29
- 7. Electromagnons in cycloidal multiferroic nanostructures 33
- 8. Spin-phonon interaction 35
- 9. Summary 39
- Acknowledgment 40
- References 40

## 1. Introduction

Raman spectroscopy (RS) is one of the most important nondestructive and noncontact vibrational spectroscopy method providing primarily an information on the vibrational and electronic properties in confined systems [1]. The beauty and the power of RS (conventional and micro-Raman) can be summarized as follows: no sample preparation or damage; high spatial resolution (submicron resolution when combined with a microscopic tool), sensitivity, and easy use. It is powerful and handy analytical tool for the

characterization of great variety of nanomaterials such as quantum dots, quantum wells, nanowires, nanopowders, nanocomposites and advanced ceramics, thin films, and biomaterials [1].

In nanostructured confined materials, due to the violation of the  $q \approx 0$  selection rule, phonons over the entire Brillouin-zone contribute to the Raman line shape causing a shift and asymmetrical broadening of Raman optical or acoustic modes [2,3]. Proper analysis of temperature dependent changes of the phonon mode line shape in nanostructures is of fundamental importance to understand the changes in phonon dynamics. Significant information regarding the phonon-phonon interactions in nanomaterials, i.e., anharmonicity in the lattice potential energy can be obtained. Decay dynamics of the optical/acoustic phonon modes can be complex and dependent not only on anharmonic phonon-phonon decay mechanisms, but on other parameters like particle size and shape, size distribution, type and magnitude of the strain (compressed or tensile) and lattice disorder, structural anisotropy, or surface states. From the temperature dependence of Raman spectra it is possible to deduce about their influence on other nanomaterials properties like thermal expansion, specific heat, or thermal conductivity.

RS, as a complementary technique to X-ray diffraction, has proved to be a useful tool to identify structural stability of nanomaterials. Raman scattering is sensitive to the changes in crystal structure and can be applied for detecting new phases and/or phase transitions in investigated nanomaterials at elevated temperatures.

RS has been extensively employed for investigation the interplay between charge, spin, and lattice degrees of freedom in nanocrystalline materials. Understanding of electron-phonon interaction is of great importance, as this interaction plays a significant role in thermal conduction, charge carrier mobility, and recently discovered superconductivity in nanoparticles [4,5]. Information about the electron-phonon interaction can be obtained from the phonon shift and linewidth of Raman modes, or through the appearance of new modes in heterostructures of 2D materials [6]. The temperature-dependent variation of charge coupled Raman modes enables to deduce about the strength of electron-phonon coupling.

In magnetic nanomaterials, magnetic ordering has a well pronounced effect on the phonon frequencies near magnetic ordering temperature because the exchange coupling between magnetic ions influences Raman mode position, linewidth and integrated intensity. The subtle interplay between the spin and lattice degrees of freedom may be pivotal mechanism for understanding the superconductivity in nanocomposite structures known as nanosuperconductors [7] or can mediate magnetoelectric coupling in type-II multiferroic materials. In composite multiferroic nanostructures spin and phonons can be strongly coupled to the lattice strain as well, and this type of coupling is important aspect in manipulating the magnetic or ferroelectric properties of these materials [8]. An intense spin-phonon interaction manifests as hardening or softening of the phonon frequency or as

nontrivial behavior of optical phonon linewidth and integrated intensity near the magnetic ordering temperature. Due to the complexity of magnetic interactions in nanomaterials, the coupling between the lattice and spin degrees of freedom (spin-phonon coupling) can be different for different phonon modes, and the coupling strength may vary even in the case of the same spin-spin interaction. Electron-phonon and spin-phonon coupling strength in low-dimensional materials are size-dependent [9–11], and temperature-dependent RS offers a unique opportunity of probing the temperature evolution of electron-phonon and/or spin-phonon coupling in low-dimensional materials. Since electron-phonon and spin-phonon interactions in nanoscaled materials can be notably modified with respect to bulk materials, it is of great importance to get much better insight into these phenomena having a large impact on the electronic device engineering based on novel nanosized materials [5,6,8].

In this chapter we give a brief overview of the state-of-the-art applications of temperature-dependent RS for analyzing diverse fundamental physical processes in low-dimensional materials. Understanding of these processes enables to predict many novel thermophysical, optical, electric, magnetic, and superconducting nanomaterials features.

## 2. Anharmonicity in nanostructured materials

Anharmonic effects at elevated temperatures ( $T$ ) and pressures ( $p$ ), strongly affect a number of processes in nanostructured materials including thermal and electronic transport properties, structural phase transformation or optical properties. Although theory predicts that heat transport is performed mainly by lower frequency acoustic phonons, the anharmonic decay of optical phonons into acoustic phonons can also contribute to the thermal conductivity [12,13]. Information on phonon scattering processes is therefore important for further improvement of functionality of the nanointegrated devices. RS provides a great deal of information about the phonon vibrations and lattice anharmonicity and the following section will be dedicated to the research of anharmonic interactions in nanomaterials by using temperature-dependent RS.

### 2.1 Basic theory of phonon-phonon interactions

Anharmonicity in the interatomic potentials (vibrational potential energy), induced by temperature variations, causes the changes of the Raman normal modes frequency ( $\omega$ ), linewidth ( $\Gamma$ ), and mode intensity. Because of the anharmonicity of the lattice forces, an optical mode can interchange energy with other lattice modes and decays into phonons of lower energies or is scattered by thermal phonons into modes of different higher energies. The phonon-phonon interactions are characterized by the complex quantity, *phonon self-energy* [14].

$$\Delta(\omega) - i\Gamma(\omega) \quad (2.1)$$

For a phonon of frequency  $\omega$  and wave vector  $q$  in the  $j$ th branch, the real part  $\Delta_j(\omega, q)$  represents the frequency shift due to anharmonicity, whereas the imaginary part  $\Gamma_j(\omega, q)$  corresponds to reciprocal of the phonon lifetime  $\tau$  ( $\tau^{-1} = 2\Gamma$ ,  $2\Gamma$  is the full width at half maximum [FWHM] of the Raman peak) [14].

In nonmagnetic, insulating, or semiconductor nanomaterials, the variation of the frequency of the  $j$ th normal mode with temperature at constant pressure arises from two contributions: frequency-independent pure-volume contribution ( $\Delta_j^E(q)$ ), emerging from thermal expansion of the crystal and frequency-dependent, pure-temperature contribution ( $\Delta_j^A(\omega, q)$ ), which results from cubic ( $\Delta_{j3}(\omega, q)$ ), and quartic ( $\Delta_{j4}(\omega, q)$ ) anharmonic terms in the vibrational potential energy. The real part of phonon self-energy  $\Delta(\omega)$  can be presented as a sum of these two contributions [15].

$$\Delta_j(\omega, q) = \Delta_j^E(q) + \Delta_j^A(\omega, q) = \Delta_j^E(q) + \Delta_{j3}(\omega, q) + \Delta_{j4}(\omega, q) \quad (2.2)$$

Both  $\Delta_j^E(q)$  and  $\Delta_j^A(\omega, q)$  give rise to temperature-dependent frequency shift from the harmonic mode frequency  $\omega_0$ . The Raman mode frequency  $\omega_j$ , as a function of temperature, can be expressed as

$$\omega_j(T) = \omega_0 + \Delta_j^E(q) + \Delta_{j3}(\omega, q) + \Delta_{j4}(\omega, q) \quad (2.3)$$

In most solids  $\Delta_j^E(q) < 0$ , i.e., lattice dilation results in phonon mode softening. Frequency shift due to thermal expansion can be evaluated from the following equation [16]:

$$\Delta^E = \omega_0 \left( e^{-3\gamma_i \int_0^T \alpha(T') dT'} - 1 \right) \quad (2.4)$$

where  $\alpha(T)$  is the coefficient of linear thermal expansion and  $\gamma_i$  is the mode-Gruneisen parameter. The multiphonon processes associated with the cubic terms represent the three-phonon decay (scattering) processes. The low-order perturbation calculations show that frequency shift and broadening of the  $j$ th Raman mode due to these processes should be linearly dependent on  $T$  [17–19].

$$\begin{aligned} \Delta_{j3}(\vec{0}, j; \omega) &= -\frac{18}{\hbar^2} \sum_{\vec{q}_1, j_1} \sum_{\vec{q}_2, j_2} \left| V(\vec{0}, j; \vec{q}_1, j_1; \vec{q}_2, j_2) \right|^2 \\ &\times \mathcal{P} \left[ \frac{n_1 + n_2 + 1}{\omega + \omega_1 + \omega_2} - \frac{n_1 + n_2 + 1}{\omega - \omega_1 - \omega_2} + \frac{n_1 - n_2}{\omega - \omega_1 + \omega_2} - \frac{n_1 - n_2}{\omega + \omega_1 - \omega_2} \right] \\ \Gamma_{j3}(\vec{0}, j; \omega) &= \frac{18\pi}{\hbar^2} \sum_{\vec{q}_1, j_1} \sum_{\vec{q}_2, j_2} \left| V(\vec{0}, j; \vec{q}_1, j_1; \vec{q}_2, j_2) \right|^2 \times \{(n_1 + n_2 + 1) \\ &\times [\delta(\omega - \omega_1 - \omega_2) - \delta(\omega + \omega_1 + \omega_2)] + (n_1 - n_2)[\delta(\omega + \omega_1 - \omega_2) - \delta(\omega - \omega_1 + \omega_2)]\} \end{aligned} \quad (2.5)$$

(2.6)

The first two terms in  $\Delta_{j3}$  and  $\Gamma_{j3}$  present the contribution from phonon decay into two phonons of lower energy (*down-conversion* three-phonon processes). The last two terms describe the processes in which a nonequilibrium phonon is destroyed by a thermal phonon and a phonon of higher energy is created (*up-conversion* three-phonon processes). Up-conversion processes contribute at higher temperatures and vanish as  $T$  approaches zero, whereas the down-conversion processes always have a finite contribution even at  $T = 0$  K [20]. From Eq. (2.5) is obvious that cubic contribution is negative ( $\Delta_{j3} < 0$ ), giving rise to a negative frequency shift. The quartic terms correspond to four-phonon processes and vary linearly, but also quadratically with  $T$  [19].

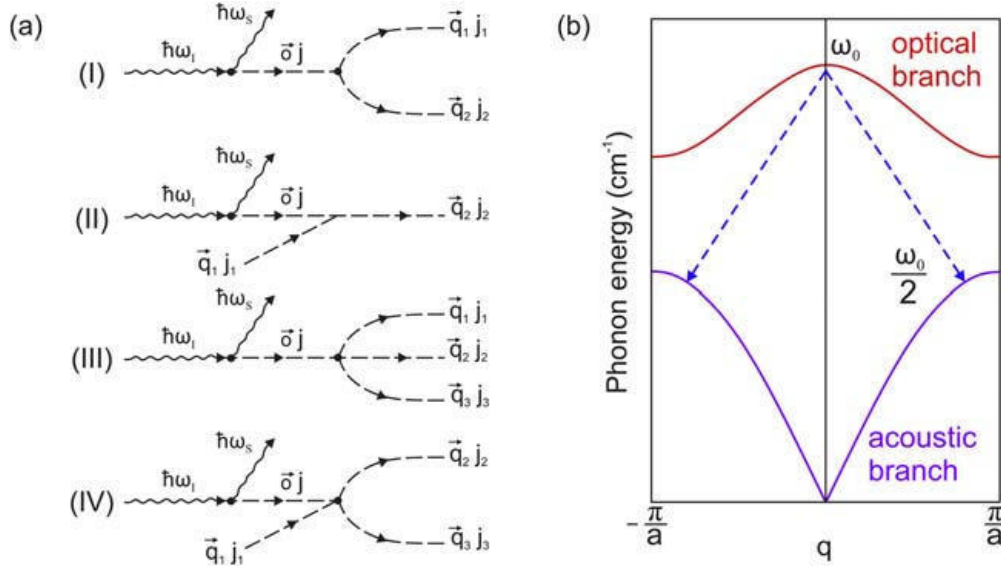
$$\Delta_{j4a}(\vec{0}, j; \omega) = \frac{24}{\hbar} \sum_{\vec{q}_1, j_1} V(\vec{0}, j; \vec{0}, j; \vec{q}_1, j_1; -\vec{q}_1, j_1) \left(n_1 + \frac{1}{2}\right) \quad (2.7)$$

$$\begin{aligned} \Delta_{j4b}(\vec{0}, j; \omega) &= -\frac{96}{\hbar^2} \sum_{\vec{q}_1, j_1} \sum_{\vec{q}_2, j_2} \sum_{\vec{q}_3, j_3} \left| V(\vec{0}, j; \vec{q}_1, j_1; \vec{q}_2, j_2; \vec{q}_3, j_3) \right|^2 \\ &\times \mathcal{P} \left\{ [(n_1 + 1)(n_2 + 1)(n_3 + 1) - n_1 n_2 n_3] \times \left[ \frac{1}{\omega + \omega_1 + \omega_2 + \omega_3} - \frac{1}{\omega - \omega_1 - \omega_2 - \omega_3} \right] \right. \\ &\left. + 3[n_1(n_2 + 1)(n_3 + 1) - (n_1 + 1)n_2 n_3] \times \left[ \frac{1}{\omega - \omega_1 + \omega_2 + \omega_3} - \frac{1}{\omega + \omega_1 - \omega_2 - \omega_3} \right] \right\} \end{aligned} \quad (2.8)$$

$$\begin{aligned} \Delta_{j4c}(\vec{0}, j; \omega) &= -\frac{576}{\hbar^2} \sum_{\vec{q}_1, j_1} \sum_{j_2} \sum_{\vec{q}_3, j_3} V(\vec{0}, j; \vec{0}, j_1; -\vec{q}_1, j_1; \vec{q}_1, j_2) V(\vec{q}_1, j_1; -\vec{q}_1, j_2; \vec{q}_3, j_3; -\vec{q}_3, j_3) \\ &\times \mathcal{P} \left[ \frac{n_1 + n_2 + 1}{\omega_1 + \omega_2} - \frac{n_1 - n_2}{\omega_1 - \omega_2} \right] \left(n_3 + \frac{1}{2}\right) \end{aligned} \quad (2.9)$$

$$\begin{aligned} \Gamma^{(4)}(\vec{0}, j; \omega) &= \frac{96\pi}{\hbar^2} \sum_{\vec{q}_1, j_1} \sum_{\vec{q}_2, j_2} \sum_{\vec{q}_3, j_3} \left| V(\vec{0}, j; \vec{q}_1, j_1; \vec{q}_2, j_2; \vec{q}_3, j_3) \right|^2 \\ &\times \{ [(n_1 + 1)(n_2 + 1)(n_3 + 1) - n_1 n_2 n_3] [\delta(\omega - \omega_1 - \omega_2 - \omega_3) - \delta(\omega + \omega_1 + \omega_2 + \omega_3)] \\ &+ 3[n_1(n_2 + 1)(n_3 + 1) - (n_1 + 1)n_2 n_3] \times [\delta(\omega + \omega_1 - \omega_2 - \omega_3) - \delta(\omega - \omega_1 + \omega_2 + \omega_3)] \} \end{aligned} \quad (2.10)$$

In the aforementioned equations  $n_j(\omega_j) = \left[ \exp\left(\frac{\hbar\omega_j}{k_B T}\right) - 1 \right]^{-1}$  is the thermal (Bose-Einstein) population factor of the  $j$ th phonon mode with wave vector  $q$  and frequency  $\omega_j$ . The quartic terms (Eqs. 2.7–2.9) may be positive or negative. Accordingly, the resultant frequency shift due to phonon-phonon interaction may be either positive or negative depending on the relative magnitudes of the anharmonic terms in the interatomic potential. The *up* and *down-conversion* three (four)-phonon processes are shown diagrammatically in Fig. 2.1A.


**Figure 2.1**

Three and four-phonon anharmonic processes (A) (I), (III) down-conversion and (II), (IV) up-conversion processes. (B) three-phonon processes according to Klemens model. *Based on M. Balkanski, R.F. Wallis, E. Haro, Anharmonic effects in light scattering due to optical phonons in silicon. Phys. Rev. B 28 (1983) 1928–1934.*

Following the approach of Klemens, [21], if the optical phonon decays into two or three acoustical phonons of lower mutually equal energies and opposite momenta, the temperature variation of the Raman phonon frequency and linewidth can be simplified:

$$\omega_j(T) = \omega_0 + C \left[ 1 + \frac{2}{e^x - 1} \right] + D \left[ 1 + \frac{3}{e^y - 1} + \frac{3}{(e^y - 1)^2} \right] = \omega_0 + \Delta\omega(T) \quad (2.11)$$

$$\Gamma(T) = \Gamma_0 + A \left[ 1 + \frac{2}{e^x - 1} \right] + B \left[ 1 + \frac{3}{e^y - 1} + \frac{3}{(e^y - 1)^2} \right] = \Gamma_0 + \Delta\Gamma \quad (2.12)$$

where  $\omega_0$  is the harmonic frequency,  $x = \frac{\hbar\omega_0}{2k_B T}$ ,  $y = \frac{\hbar\omega_0}{3k_B T}$ ,  $A$ ,  $B$ ,  $C$ ,  $D$  are anharmonic constants and  $\Gamma_0$  is the intrinsic mode linewidth (temperature-independent broadening). In Fig. 2.1B is presented a three-phonon decay process according to Klemens model. This model, although too simplistic, is generally accepted especially after the work of Hart et al. on Si [22].

## 2.2 Phonon-phonon interactions in nanomaterials

For many crystalline semiconductor or insulator materials, due to increased temperature, the anharmonic frequency shift and broadening of the Raman modes follow down or up-conversion three-phonon processes, [14,20], but at higher temperatures ( $T > 300$  K) four-phonon processes begin to dominate [19]. In nanocrystalline materials, beside the anharmonic effects, temperature induced changes of the Raman line profile depend on several other factors like phonon confinement, strain, disorder/defects. Consequently,



anharmonic processes in nanomaterials can show quite distinct behavior from those of bulk counterparts. For more precise determination of influence of these factors on the Raman line profile, the temperature-dependent Raman spectra can be well modeled using phonon confinement model (PCM) [23,24] for spherical nanoparticles in which are incorporated size, inhomogenous strain and anharmonicity [25,26].

$$I(\omega, T) \propto \sum_{i=1}^n \int_0^{\infty} \rho(L) dL \int \frac{\exp\left(\frac{-q^2 L^2}{8\beta}\right) d^3 q}{BZ[\omega - (\omega_i(q) + \Delta\omega)]^2 + \left(\frac{\Gamma(T)}{2}\right)^2} \quad (2.13)$$

In the above equation, the frequency shift  $\Delta\omega = \Delta\omega_i(q, L) + \Delta\omega(T)$ , where the first term presents strain contribution and the second one originates from anharmonicity;  $\rho(L)$  is Gaussian distribution of particle size,  $q$ -wave vector expressed in units of  $2\pi/a$  ( $a$ -lattice cell parameter),  $L$ -particle diameter,  $\beta$ -confinement strength and  $\Gamma(T)$  is a phonon linewidth, which encompasses broadening due to confinement, strain, and anharmonicity [25]. The integration is performed along all optical dispersion branches within first Brillouin-zone characteristic for certain material. As an example, in Fig. 2.2A are shown

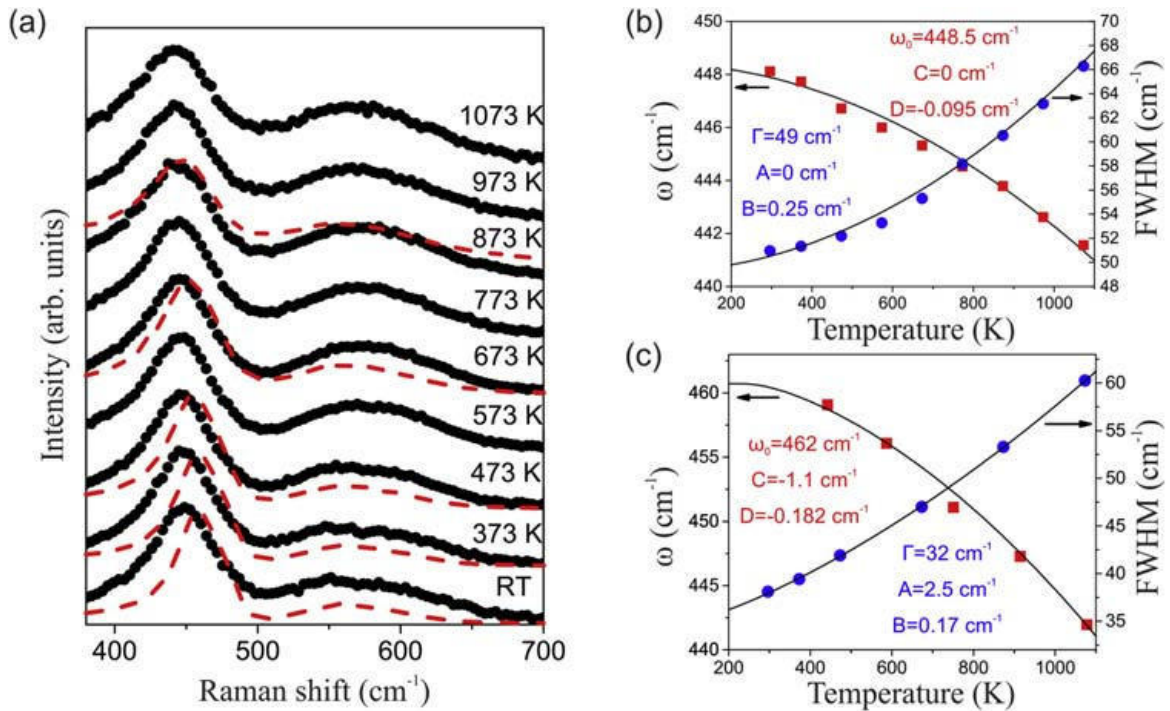


**Figure 2.2**

(A) Raman spectra of  $\text{Ce}_{0.75}\text{Nd}_{0.25}\text{O}_{2-\delta}$  sample upon heating (circles) and cooling (dashed lines). The variation of frequency and linewidth of  $F_{2g}$  mode during (B) heating and (C) cooling. Full lines present calculated values for the peak position and linewidth using the PCM model with Klemens anzats. The best fit anharmonic parameters are given as well. Reprinted from Z.D.

Dohčević-Mitrović, M. Radović, M. Šćepanović, M. Grujić-Brojčin, Z.V. Popović, B. Matović, S. Bošković, Temperature-dependent Raman study of  $\text{Ce}_{0.75}\text{Nd}_{0.25}\text{O}_{2-\delta}$  nanocrystals, *Appl. Phys. Lett.* 91 (2007) 203118, with the permission of AIP Publishing.

Raman spectra of cerium dioxide nanocrystals doped with 25% of Nd ( $\text{Ce}_{0.75}\text{Nd}_{0.25}\text{O}_{2-\delta}$ ) upon heating over the temperature range of 293–1073 K (circles) and gradual cooling down to room temperature (dashed lines) [25]. During the heating, the most intense  $F_{2g}$  Raman mode, positioned at  $\sim 450\text{ cm}^{-1}$  at room temperature (RT), shifts to lower frequencies, whereas its linewidth increases as presented in Fig. 2.2B. These spectra are fitted using the PCM model (Eq. 2.13) with Klemens anzats (Eqs. 2.11 and 2.12). The best fits of the peak position and linewidth of  $F_{2g}$  mode (full lines in Fig. 2.2B) upon heating were obtained including only four-phonon anharmonic processes ( $D, B > 0, A = C = 0$ ), contrary to the bulk materials for which three-phonon anharmonic processes are dominant. Such a behavior implies that phonon decay channels are different in nanocrystalline particles. During the cooling process that followed annealing to 1073 K (Fig. 2.2C), anharmonic interactions in  $\text{Ce}_{0.75}\text{Nd}_{0.25}\text{O}_{2-\delta}$  nanocrystals are similar to the ones in polycrystalline  $\text{CeO}_2$  [25]. Namely, three-phonon anharmonic processes dominated over the four-phonon processes (constants  $A$  and  $C$  are much higher than  $B$  and  $D$ ), designating that after the heat treatment the particle size increased enough, so that the anharmonic interactions are more similar to bulk materials.

Phonon-phonon interactions were investigated in  $\text{Ce}_{0.85}\text{Gd}_{0.15}\text{O}_{2-\delta}$  nanocrystals [27] by following the changes of the  $F_{2g}$  Raman mode at elevated temperatures (293–1073 K). High-temperature Raman spectra were analyzed by PCM model (Eq. 2.13) in which are incorporated size, strain and anharmonic phonon decay processes which dominated over the thermal expansion [27]. The temperature variation of  $F_{2g}$  Raman mode position and linewidth is presented in Fig. 2.3A and B.

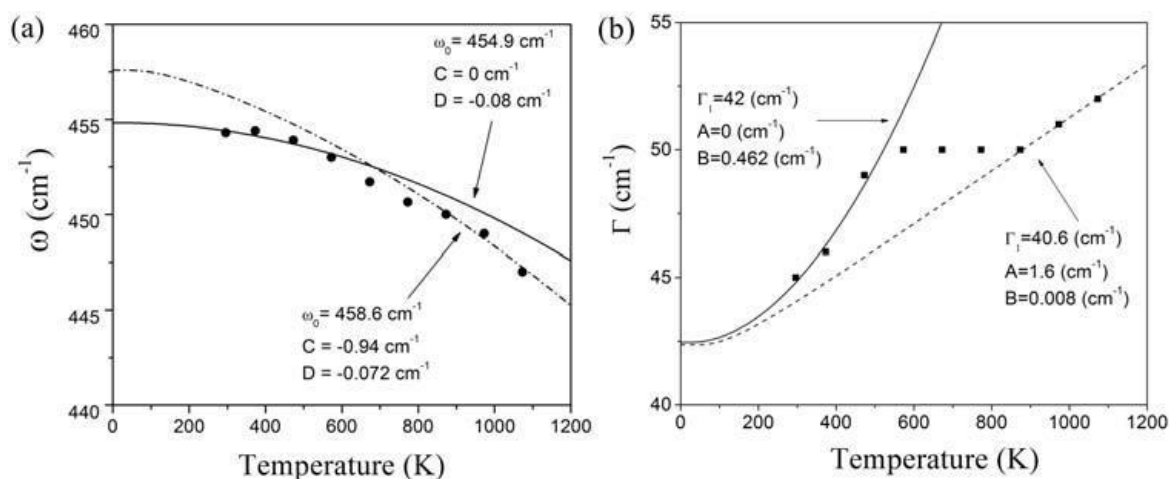


**Figure 2.3**

Temperature dependence of (A) frequency and (B) linewidth of the  $F_{2g}$  Raman mode in  $\text{Ce}_{0.85}\text{Gd}_{0.15}\text{O}_{2-\delta}$  nanopowders. The anharmonic parameters of the best fits are also presented.

Reprinted from S. Askračić, Z.D. Dohcević-Mitrović, M. Radović, M. Šćepanović, Z.V. Popović, Phonon-phonon interactions in  $\text{Ce}_{0.85}\text{Gd}_{0.15}\text{O}_{2-\delta}$  nanocrystals studied by Raman spectroscopy, *J. Raman Spectrosc.* 40 (2009) 650–655 with the permission of John Wiley & Sons.

As can be seen from Fig. 2.3A,  $F_{2g}$  Raman mode position over the whole temperature range was not possible to fit with a single curve based on three or four-phonon anharmonic processes. The best fit of the experimental values in the 293–573 K temperature range was obtained using only four-phonon anharmonic processes (full line), whereas in the 873–1073 K temperature range three-phonon coupling prevailed (dotted line). It was concluded that anharmonic processes were different in two temperature ranges. The  $F_{2g}$  mode linewidth dependency on temperature showed even more distinct behavior, as illustrated in Fig. 2.3B. The  $\Gamma(T)$  firstly increased with annealing, then experienced a plateau-like behavior between 573 and 873 K and after that increased again. Such a behavior was ascribed to the effect of increased average particle size which was estimated from the PCM. As the particle size increased with annealing, nanoparticles started to take on the bulk properties and the three-phonon processes became dominant, which was confirmed from the experiment on cooling down the  $\text{Ce}_{0.85}\text{Gd}_{0.15}\text{O}_{2-\delta}$  nanocrystals to RT [27]. This study obviously points to subtle interplay between size and anharmonic effects in nanostructured materials, which have to be taken into account.

In the temperature-dependent Raman spectra of ZnO nanopowders [28] it was found that  $E_2$  (low) phonon mode linewidth exhibited anomalous behavior with temperature. In Fig. 2.4A and B are presented frequency (circles) and linewidth (squares) dependence on temperature for two Raman modes,  $E_2$  (high) and  $E_2$  (low) modes. As can be seen from Fig. 2.4A and B, the nonpolar optical phonon ( $E_2$  (high)) has shown expected frequency redshift and increased broadening with increasing temperature (Fig. 2.4A) which is in good accordance with cubic and quartic anharmonicity. On the contrary, the  $E_2$  (low) mode experienced an anomalous linewidth decrease with increasing temperature. This anomaly was ascribed to the increased interference of acoustic and surface modes with  $E_2$  (low) optical phonon mode [28].

Optical phonon modes in most nanostructures experience frequency redshift (softening) with increasing temperature due to the cumulative effect of thermal expansion contribution and three-phonon processes (Eqs. 2.4 and 2.5), which give rise to a negative frequency shift. Contrary to this, the most intense  $E_g$  mode (positioned at  $\sim 144 \text{ cm}^{-1}$  under ambient conditions) of nanophase anatase  $\text{TiO}_2$  shifts to higher frequency (blueshift) with temperature rise, whereas the other anatase modes exhibit expected softening [29–32]. Although the blueshift and broadening of this mode with regard to bulk counterpart can be ascribed to the phonon confinement, oxygen nonstoichiometry and surface defects, [29,31], the main contribution originates from the anharmonic interactions that generate positive frequency shift, i.e., four-phonon anharmonic processes (Eq. 2.7) [32].

### 3. Size/microstrain effects and phase separation

Changes of the wavenumber and the linewidth of the Raman modes at elevated temperatures carry important information about the particle size and shape or about

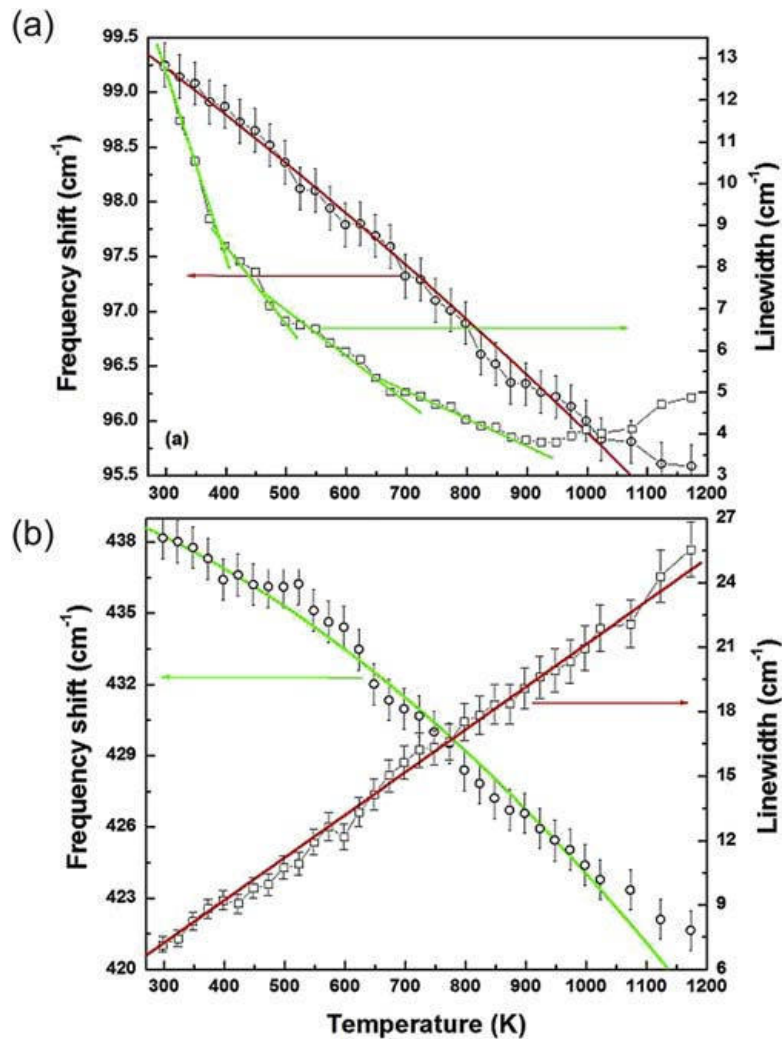


**Figure 2.4**

Frequency and linewidth dependence on temperature for (A)  $E_2$  (low) and (B)  $E_2$  (high) Raman modes of ZnO nanopowders. The *solid lines* (excluding the linewidth of  $E_2$  (low) mode) are the best theoretical fits using Klemens model. *Reprinted from H.K. Yadav, R.S. Katiyar, V. Gupta, Temperature-dependent dynamics of ZnO nanoparticles probed by Raman scattering: A big divergence in the functional areas of nanoparticles and bulk material. Appl. Phys. Lett. 100 (2012) 051906 with the permission of AIP Publishing.*

structural phase transition which manifests itself through the appearance of new Raman modes. The PCM, described in [Section 1.2](#), is often used to model a Raman mode intensity distribution in nanostructured materials where the size and strain effects lead to significant phonon shift and asymmetric broadening [2,3,23,24]. Using the PCM, effects of particle size, size distribution and microstrain can be disentangled. For example, in related study, oxygen deficient  $\text{CeO}_{2-\delta}$  nanopowders were annealed in the air in the temperature range (200–500 °C) in order to study structural and vibrational properties of nanophase  $\text{CeO}_{2-\delta}$  at elevated temperatures [33]. Raman spectra of the annealed samples (S2–S5) are presented in [Fig. 2.5A](#) together with as-synthesized  $\text{CeO}_{2-\delta}$ . The most intense  $F_{2g}$  mode

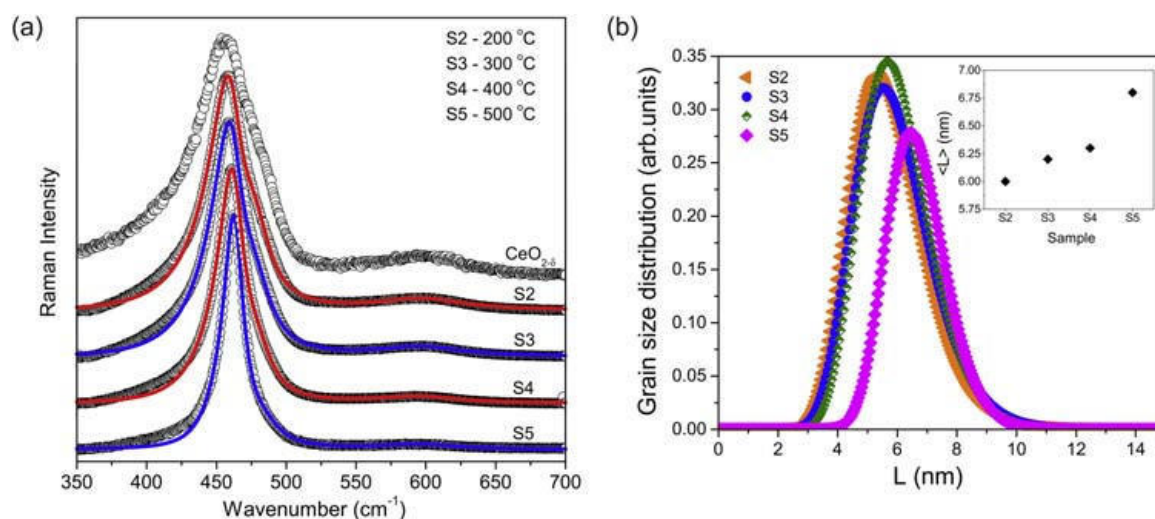


**Figure 2.5**

(A) Raman spectra of  $F_{2g}$  mode for the  $\text{CeO}_{2-\delta}$  nanopowders at RT and annealed at different temperatures (circles), fitted by PCM (full lines). (B) Nanocrystalline particle size distribution deduced from the PCM. Samples S2–S5 represent powders annealed at different temperatures 200–500 °C. The inset presents the average particle size increase with annealing, obtained from PCM. Reprinted from S. Aškrić, Z. Dohčević-Mitrović, A. Kremenović, N. Lazarević, V. Kahlenberg, Z.V. Popović, Oxygen vacancy-induced microstructural changes of annealed  $\text{CeO}_{2-x}$  nanocrystals, *J. Raman Spectrosc.* 43 (2012) 76–81 with the permission of John Wiley & Sons.

( $\sim 458 \text{ cm}^{-1}$ ) was shifted to higher wavenumbers and became more symmetric for the samples annealed at higher temperatures ( $>300 \text{ °C}$ ). Another mode which was ascribed to the intrinsic oxygen vacancies defect mode (around  $600 \text{ cm}^{-1}$ ) became less intensive in the samples annealed above  $300 \text{ °C}$ . This implies that with annealing the concentration of oxygen vacancies decreased. PCM was employed [25,33] to model the changes of  $F_{2g}$  mode from Fig. 2.5A. The average lattice parameters were determined by Rietveld analysis of X-ray diffraction spectra [33] and the empirical relation between lattice parameter and particle size,  $a = a_0 + k_1 \cdot \exp(-k_2/L)$ , was used in PCM, where  $k_1$  and  $k_2$  are fitting parameters. Combined XRD and Raman analysis showed that during the thermal treatment average particle size distribution (Fig. 2.5B) and particle size (inset of Fig. 2.5B) haven't changed much, but the average microstrain was significantly reduced, almost three times in samples annealed at  $400 \text{ °C}$  and  $500 \text{ °C}$ . As content of oxygen vacancies decreased too, it was deduced that relaxation of microstrain due to the improved stoichiometry dominantly contributed to the changes seen in the Raman spectra [33].

Another temperature-dependent study of  $\text{MoO}_3$  nanoribbons [34] by Raman spectroscopy have shown anomalies in wavenumber and linewidth behavior in the  $150\text{--}400 \text{ °C}$  temperature range. As shown in Fig. 2.6A and B, in  $\omega(T)$  and  $\Gamma(T)$  dependences (black circles and squares) of  $155 \text{ cm}^{-1}$  Raman mode, a plateau was observed. The  $\omega(T)$  and  $\Gamma(T)$  dependences departed from the anharmonic decay model in bulk  $\text{MoO}_3$ , for which the Raman mode frequency/linewidth monotonously decreased/increased with the

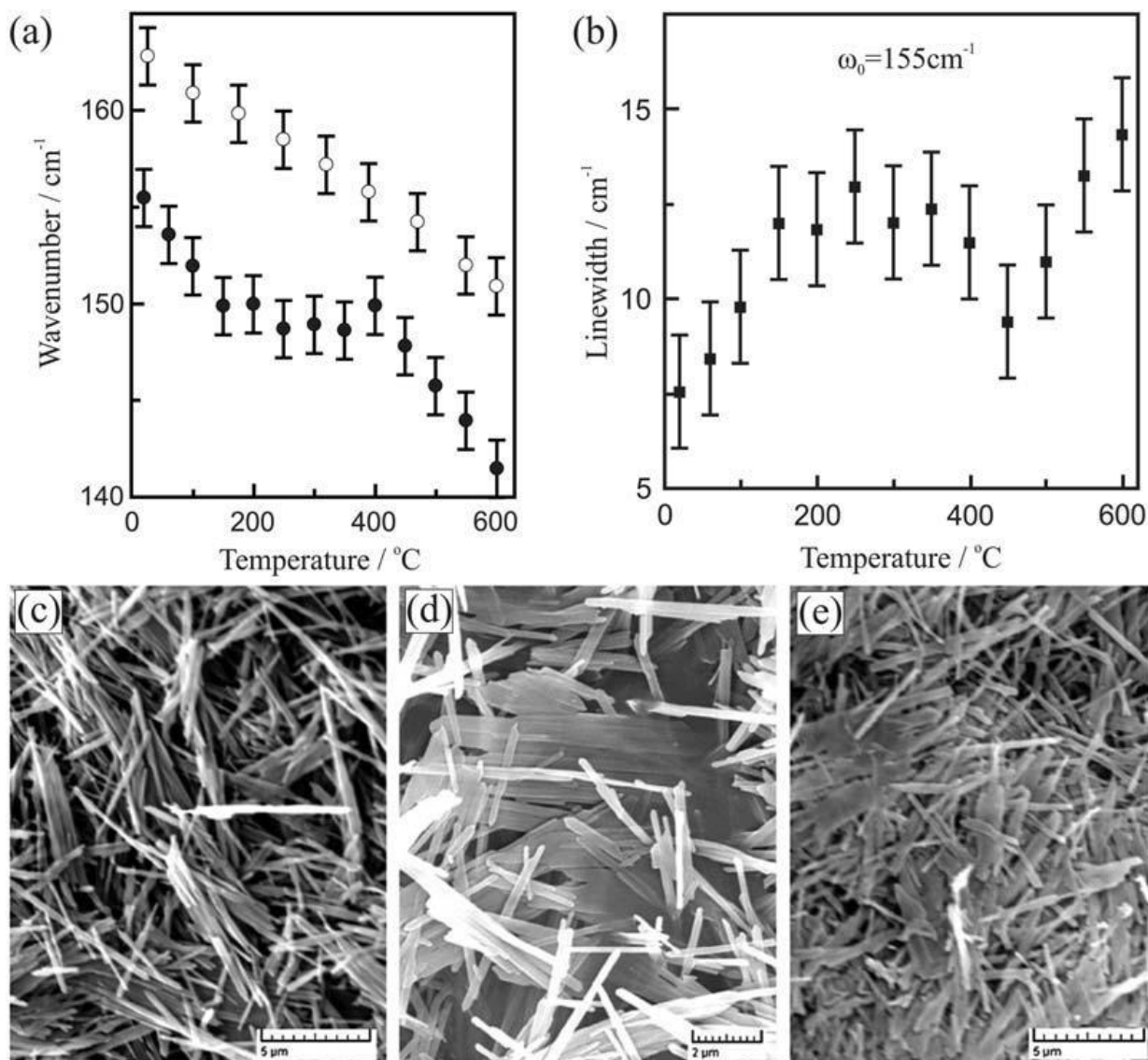


**Figure 2.6**

Temperature dependence of (A) frequency (*black circles*) and (B) linewidth of 155 cm<sup>-1</sup> Raman mode of MoO<sub>3</sub> nanoribbons. Open circles present frequency versus temperature plot for bulk counterpart. SEM images at different temperatures: (C) T = 25 °C, (D) T = 150 °C and (E) T = 350 °C. Reprinted from J.V. Silveira, L.L. Vieira, J.M. Filho, A.J.C. Sampaio, O.L. Alves, A.G. Souza Filho, *Temperature-dependent Raman spectroscopy study in MoO<sub>3</sub> nanoribbons*, *J. Raman Spectrosc.* 43 (2012) 1407–1412 with the permission of John Wiley & Sons.

temperature rise. Such a behavior could not be ascribed to a structural phase transition, as MoO<sub>3</sub> nanoribbons are structurally stable up to 650 °C, but can be a consequence of size-induced effects. During the thermal treatment, the crystallite size of MoO<sub>3</sub> nanoribbons increased. In the 150–400 °C temperature range, the anharmonic interactions and the coalescence process are competing processes that lead to the departure from the optical phonon anharmonic decay model and appearance of a plateau [34]. Above 400 °C nanoribbons adopted bulk properties. SEM images of MoO<sub>3</sub> nanoribbons treated at

different temperatures (Fig. 2.6C–E) confirmed morphological changes. Namely, in the temperature regime between 150 °C and 400 °C, besides the isolated nanoribbons, large slab structures have been formed due to the coalescence of nanoribbons. At temperatures above 400 °C the nanoribbons were almost totally converted into large slabs behaving more like the bulk counterpart.

A similar appearance of a plateau-like behavior in the  $F_{2g}$  mode linewidth dependence on temperature was observed in the case of  $\text{Ce}_{0.85}\text{Gd}_{0.15}\text{O}_{2-\delta}$  nanopowders from Fig. 2.3B [27]. From the PCM model it was deduced that anomalous behavior of the  $F_{2g}$  mode linewidth in the temperature range 573–873 K can be ascribed to the particle size increase and change of the particle size distribution with annealing when nanomaterials begin to resemble the bulk crystals [27].

RS has a potential to detect the presence of other phases through the appearance of the peaks characteristic for a certain crystalline structure, present even in small concentrations, and particularly in the case when two phases are very similar and cannot be resolved through X-ray diffraction spectra [35,36]. An illustration of phase separation can be found in the Raman spectra of  $\text{Ce}_{0.85}\text{Gd}_{0.15}\text{O}_{2-\delta}$  nanopowders which are gradually cooled down from 1073 K to RT [27]. During the cooling process, in the Raman spectra at 473 K a new mode appeared at  $\sim 483\text{ cm}^{-1}$ . This new mode presented one of the strongest Raman modes of  $\text{Gd}_2\text{O}_3$  phase, confirming that phase separation took place [27]. Another example concerns  $\text{BaTiO}_3$  which has the property of forming four structural phases depending on the temperature [37]. At low temperatures, it has rhombohedral (*R*) structure and the phase transition to orthorhombic (*O*), tetragonal (*T*), and cubic (*C*) phase occurs approximately at 180, 275 and 400 K [37]. Temperature-dependent Raman spectra of  $\text{BaTiO}_3$  nanoparticles, with a 300 nm average particle size, are a good example how to follow the structural phase transitions in this ferroelectric material [37]. In Fig. 2.7A and B are shown Raman spectra of 300 nm  $\text{BaTiO}_3$  nanoparticles recorded at two different temperatures (83 and 503 K).

The changes in the polar  $A_1$  (TO) mode position with increasing temperatures were found to be a very good indicator of the onset of each of four phases for 300 nm nanoparticles, as presented in Fig. 2.7C. Namely, the redshift of this mode with temperature signifies the presence of one phase, whereas the temperature at which this mode starts to shift to higher wavenumbers (blueshift) points to the onset of a phase transition. In Fig. 2.7C are also indicated the temperatures of the structural phase transitions of the corresponding phases (*R*, *O*, *T*, *C*).

#### 4. Raman thermometry

Less known application of RS concerns its use in thermometry. RS as a noncontact method of high spatial resolution can be used to measure the local temperature of the

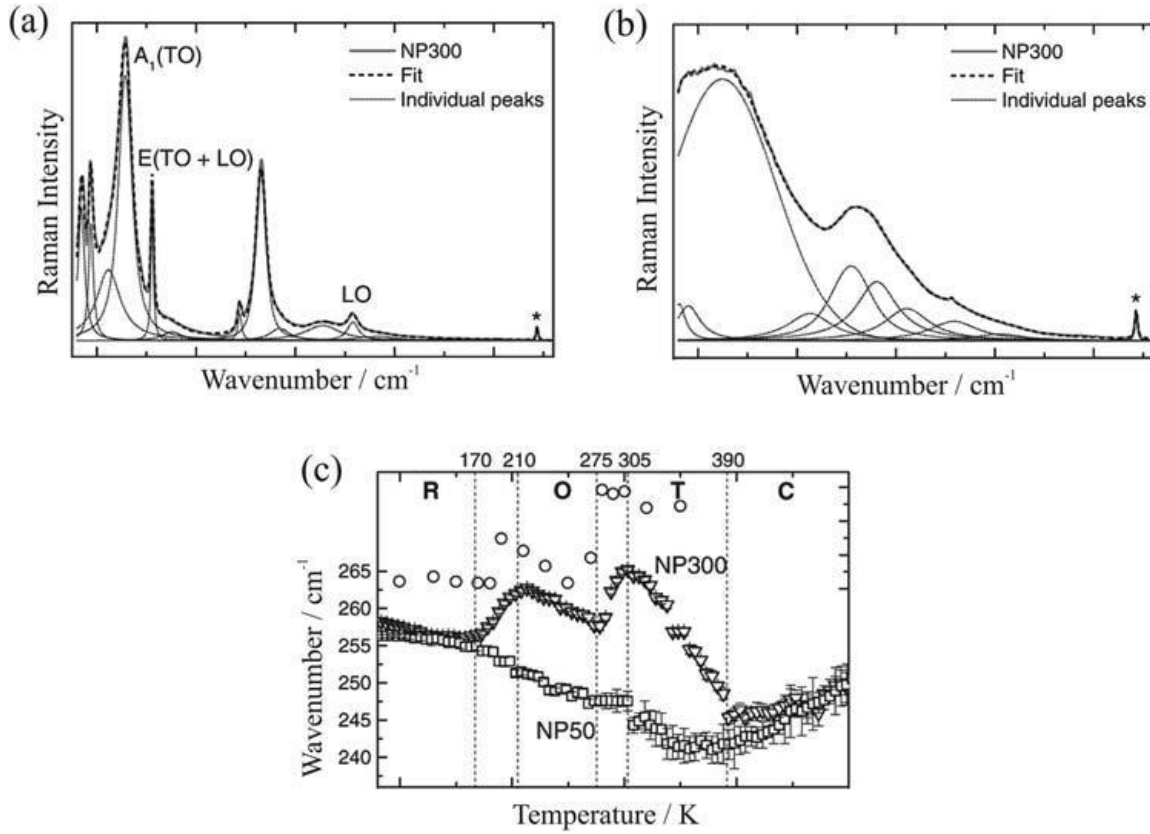


**Figure 2.7**

Raman spectra of  $\text{BaTiO}_3$  nanoparticles at (A) 83 K and (B) 503 K; (C) wavenumber shift of the  $A_1(TO)$  mode versus temperature for nanoparticles of 300 and 50 nm average sizes. *Adapted from M. Sendova, B.D. Hosterman, R. Raud, T. Hartmann, D. Koury, Temperature-dependent, micro-Raman spectroscopic study of barium titanate nanoparticles, J. Raman Spectrosc. 46 (2015) 25–31 with the permission of John Wiley & Sons.*

material. It is known that Raman mode position will shift with temperature increase/decrease due to the change of the bond length and anharmonic effects. From the peak shift dependence on temperature a calibration curve can be formed and used for material's temperature estimation, but caution should be taken to accurately control the reference material's temperature. It is of great importance to use extremely low excitation powers in order to prevent additional heating due to the excitation power absorption by the sample. Another way to determine the temperature is to measure intensities of a Raman band at the Stokes ( $I_S$ ) and anti-Stokes ( $I_{AS}$ ) positions and calculate the temperature from the formula based on the Placzek's approximation

$$\frac{I_{AS}}{I_S} = \frac{(\omega_I + \omega_S)^4}{(\omega_I - \omega_S)^4} e^{-\frac{h\omega_S}{k_B T}} \quad (2.14)$$

where  $\omega_I$  and  $\omega_S$  are wavenumbers of laser excitation line and a Stokes line, respectively. RS is nowadays readily used to determine the temperature or temperature sensitivity of various nanocrystalline materials.



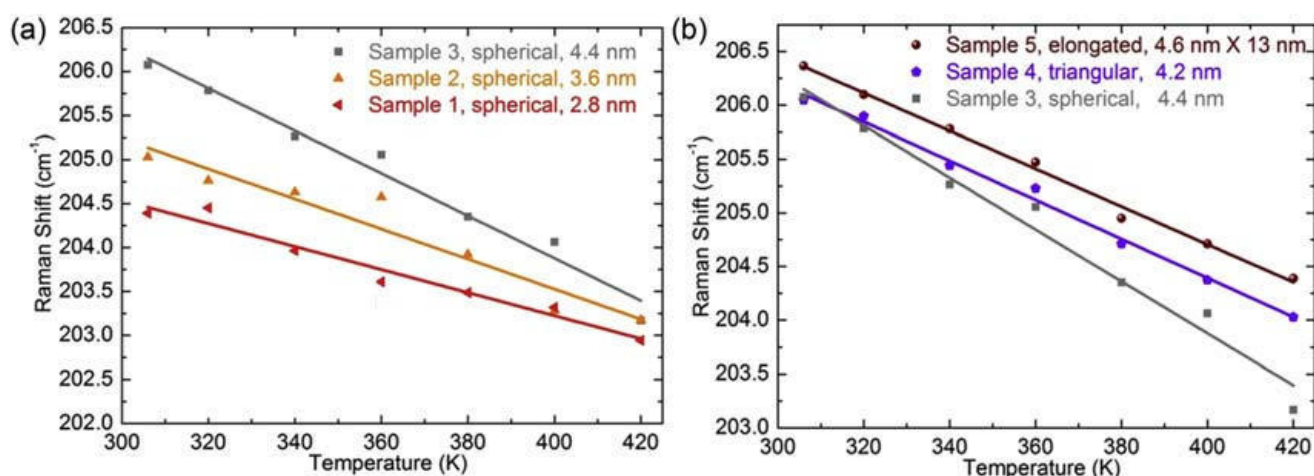


**Figure 2.8**

$A_1(\text{LO})$  frequency shift as a function of temperature for (A) spherical CdSe NCs of different size, and (B) various shaped CdSe NCs of similar size. Reprinted from L. Chen, K. Rickey, Q. Zhao, C. Robinson, X. Ruan, *Effects of nanocrystal shape and size on the temperature sensitivity in Raman thermometry*, *Appl. Phys. Lett.* 103 (2013) 083107 with the permission of AIP Publishing.

A study by Chen and coworkers [38] dealt with the effects of different size and shape of CdSe nanocrystals (NCs) on the temperature sensitivity of the  $A_1(\text{LO})$  Raman mode shift. This study was performed in the temperature range 300–420 K. In Fig. 2.8 is shown the  $A_1(\text{LO})$  mode position dependency on temperature for CdSe NCs of different sizes and shapes.

In the case of CdSe spherical NCs of different size (Fig. 2.8A), it was shown that temperature sensitivity is higher for larger nanocrystals. From the fitting of frequency shift (full lines) based on a model which incorporates thermal expansion and anharmonic effects, it was deduced that in larger nanocrystals anharmonic phonon processes dominate over the decreasing thermal expansion coefficient. In nanocrystals of different shape (triangular and elongated from Fig. 2.8B), the temperature sensitivity decreased because the effect of reduced thermal expansion coefficient overwhelms the anharmonic processes [38]. Since the temperature sensitivity is dependent on crystal size and morphology, this study points to the necessity of finding a balance between nanometric size and morphology for the application of nanomaterials in noncontact thermometry.

Raman thermometry can be also employed for thermal conductivity measurements [39,40]. This is relatively simple method with an advantage of avoiding the influence of thermal contact resistance on the intrinsic thermal conductivity. Applying the Raman shift method, heat is generated by a laser spot and the detected Raman mode shift carries an information on the induced average temperature change. The measured dependence of the peak position on the power dissipated in the material ( $\partial\omega/\partial P$ ) can be later used to estimate thermal conductivity using the premise of radial or plane wave heat propagation away from the laser spot position on the sample [39,40].

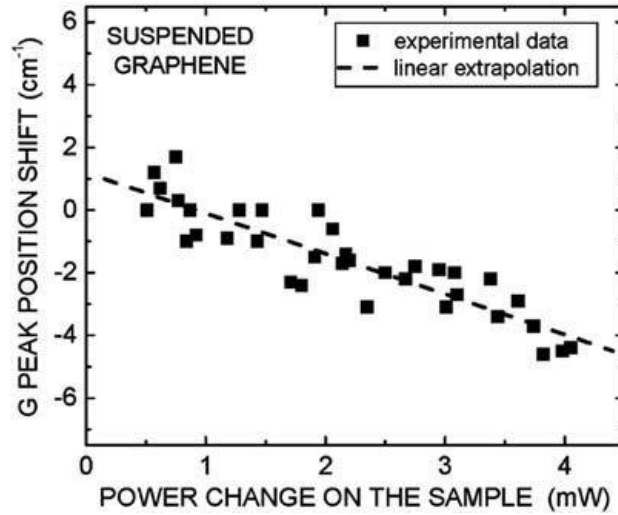


Figure 2.9

G mode position shift as a function of total dissipated power for single-layer graphene. The spectra are collected at RT using 488 nm laser excitation line. Reprinted with permission from A.A. Balandin, S. Ghosh, W.Z. Bao, I. Calizo, D. Teweldebrhan, F. Miao, C.N. Lau, *Superior thermal conductivity of single-layer graphene*, *Nano Lett.* 8 (2008) 902–907. Copyright (2008) American Chemical Society.

In the case of a graphene flakes placed over a trench made in Si/SiO<sub>2</sub> substrate, [39], and supposing that the G mode position linearly depends on the sample temperature ( $\omega = \omega_0 + \chi_G T$ ), thermal conductivity can be expressed as [39,41].

$$K = \frac{L}{2aW} \chi \left( \frac{\partial \omega}{\partial P} \right)^{-1} \quad (2.15)$$

where  $L$  is the lateral dimension of the sample along which the wave propagates,  $W$  is the sample width,  $a$ , the sample thickness and  $\partial \omega$  is a shift of G peak position due to the variation in the heating power  $\partial P$  on the sample surface. Fig. 2.9 shows the G mode position shift dependence on the total dissipated power change, from which the slope value,  $\partial \omega / \partial P$ , can be extracted. The temperature coefficient  $\chi_G$  can be obtained by explicit Raman measurements of the G mode shift dependency on temperature change in a separate experiment when temperature is changed in a controlled way, i.e., heating of the entire sample in a heating stage.

Using Raman thermometry, thermal conductivity of a single-layer graphene flake was deduced to be  $\sim 5300$  W/(mK) [39]. This value is much larger compared to other carbon materials which is of significance for this material application. In a similar way, thermal conductivities of individual single-wall and multiwall carbon nanotubes were estimated to be 2400 W/(mK) and 1400 W/(mK) [40].

## 5. Temperature behavior of acoustic vibrations in nanocrystalline materials studied by low-frequency Raman spectroscopy

Low-frequency Raman acoustic modes have been observed in nanocrystalline materials of various morphologies (spheres, ellipsoids, rods, etc.) and of crystallite size less than tens

of nanometers [42–45]. The appearance of these modes in the spectra of nanocrystals results from the geometrical confinement and coupling of longitudinal and transversal acoustic modes within a nanocrystalline particle [46,47]. According to the theory of Lamb, [48], the frequencies of acoustic vibrations are inversely proportional to the particle diameter:  $\omega_{ln} = \beta_{ln}/D$ , where  $\omega_{ln}$  is the mode frequency,  $D$  is particle diameter and  $\beta_{ln}$  nondimensional eigensolutions of the Navier equation for homogenous elastic sphere. According to the selection rules, only the spheroidal modes with angular quantum numbers  $l = 0$  and  $l = 2$  are Raman active [46]. The strongest modes in the low-frequency region of the Raman spectra can be used to determine the particle diameter. Intensity of the Raman modes enables the determination of the nanocrystalline size distribution and can be described by the relation [45,49].

$$I(\omega) = \frac{n(\omega) + 1}{\omega} C(\omega)g(\omega) \quad (2.16)$$

where  $n(\omega)$  is Bose-Einstein factor,  $C(\omega)$  is the mode-radiation coupling factor,  $g(\omega)$  is the density of vibrational states. The  $l = 0$  and  $l = 2$  modes are usually of the highest intensity from which the size distribution can be estimated. Taking the relation between mode frequency and particle diameter into account, in off-resonant conditions,  $C(\omega) \sim D \sim 1/\omega$  and the density of states  $g(\omega)$  reflects the particle size distribution  $N(D) \sim g(\omega_{ln} = \beta_{ln}/D)$ . The simple relation can then be used to determine the particle size distribution  $N(D)$  [45]:

$$N(D) \sim g(\omega) = \frac{I(\omega)\omega^2}{n(\omega) + 1} \quad (2.17)$$

Therefore, temperature dependent study of low-frequency acoustic modes in nanomaterials can potentially contribute to the pool of noncontact methods for the estimation of nanocrystalline size and/or size distribution change with temperature variation.

Although there is a huge number of papers in the literature dedicated to the temperature-dependent behavior of optical phonons in various nanostructures, little is known about the acoustic phonons dynamics as a function of temperature, despite their relevance in nonradiative relaxation processes or exciton decoherence and dephasing in nanocrystalline solids [50]. Temperature-dependent acoustic mode dynamics can be complex and dependent not only on anharmonicity, but on other parameters like particle size, structural anisotropy, morphology, surface states, or interactions with the charge carriers and therefore deserves more profound investigation.

One of rare studies on temperature dependence of breathing-mode acoustic vibrations in CdSe nanocrystals was presented in the work of Mork et al. [50] The temperature evolution of low-frequency Raman modes of CdSe NCs of several sizes is presented in Fig. 2.10A. All low-frequency Raman modes have shown the expected phonon

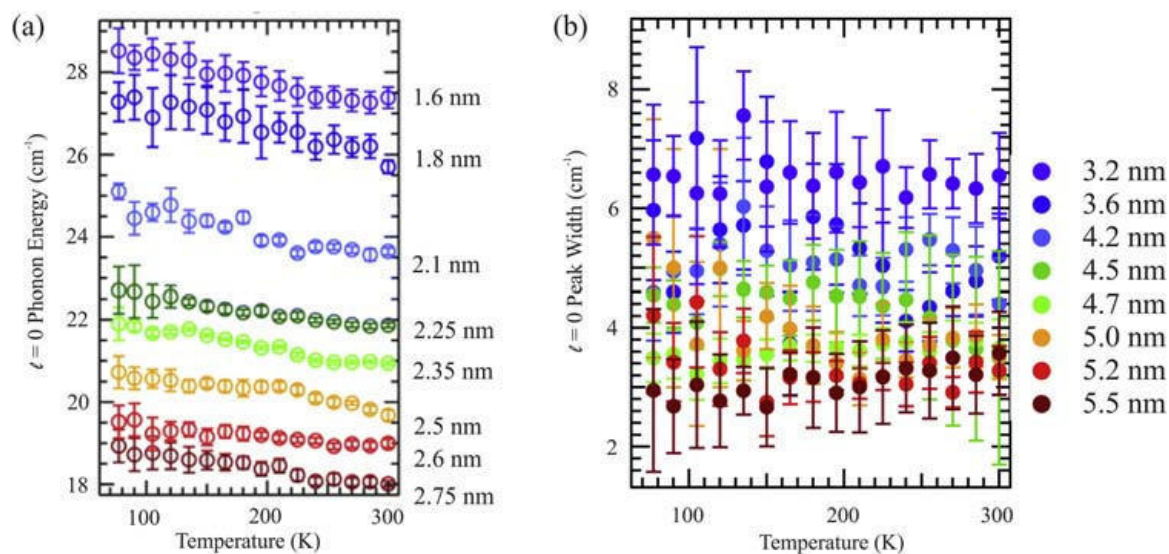


**Figure 2.10**

Temperature dependence of (A) acoustic phonon energy and (B) linewidth for CdSe NCs of different diameters. Adapted from A.J. Mork, E.M.Y. Lee, W.A. Tisdale, *Temperature dependence of acoustic vibrations of CdSe and CdSe–CdS core-shell nanocrystals measured by low-frequency Raman spectroscopy*, *Phys. Chem. Chem. Phys.* 18 (2016) 28797–28801. Published by the PCCP Owner Societies.

softening, regardless the particle size, but the magnitude of observed phonon softening could not be explained by Lamb's model only. Since, the acoustic vibrations are dependent not only on size, but also on bulk modulus, density, and transverse and longitudinal sound velocities, their change with temperature has to be taken into account. In the case of CdSe NCs, it was shown that the bulk modulus and density changes in the investigated temperature range were less than 5%, which was insufficient to explain the observed frequency change. It was concluded that organic ligands on the nanoparticle surface, with different elastic modulus, can significantly contribute to the acoustic phonon shift [50]. The linewidth (Fig. 2.10B) has shown no expected change with temperature. Such a temperature-independent behavior of linewidth was ascribed to the strong environmental damping and inhomogeneous contribution of different nanocrystalline sizes to the linewidth [50].

A complex temperature-dependent behavior of acoustic phonons was observed in ZnO nanoparticles too [51]. Fig. 2.11 shows the low-frequency Raman spectra of ZnO nanoparticles recorded at elevated temperatures (300–600 K). The prominent mode (around 22/cm) at 300 K, ascribed to spheroidal acoustic mode, shifted toward lower wavenumbers with temperature increase and after 600 K disappeared under the Rayleigh wing. Analyzing the temperature induced shift of the acoustic mode from Fig. 2.11B (open circles), it was deduced that at lower temperatures under 500 K, anharmonic decay processes and bond strength weakening were responsible for mode softening. At higher temperatures (>500 K), fast exponential decrease of peak frequency was attributed to the

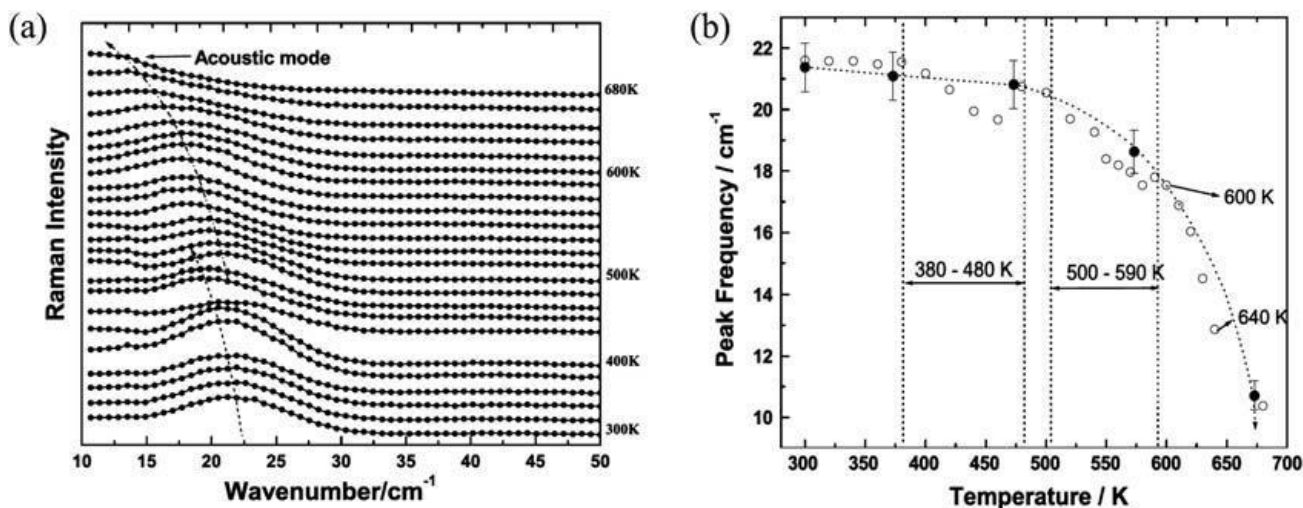


**Figure 2.11**

Temperature-dependent (A) low-frequency Raman spectra of ZnO nanoparticles and (B) acoustic mode frequency (*open circles*) obtained from the fitting of the acoustic mode [51]. *Black circles* are the calculated values of the peak frequency [51] and dotted line presents expected frequency behavior including anharmonic and size effects. Reprinted from H.K. Yadav, K. Sreenivas, R.S. Katiyar, V. Gupta, *Softening behavior of acoustic phonon mode in ZnO nanoparticles: the effect of impurities and particle size variation with temperature*, *J. Raman Spectrosc.* 42 (2011) 1620–1625 with the permission of John Wiley & Sons.

increased particle growth and coalescence process. Evident anomalous softening in the temperature ranges 380–480 K and 500–580 K originated from the impurities and reaction byproducts present on the surface of ZnO nanoparticles, the presence of which was proved by thermogravimetric analysis and differential scanning calorimetry measurements [51].

## 6. Electron-phonon interaction

Investigation of the interaction between electrons and lattice vibrations in nanocrystalline materials is an important topic because it has substantial influence on electronic and thermal transport, optical properties, or superconductivity. RS is convenient method for studying the electron-phonon (*e-ph*) interaction and enables to quantitatively determine the electron-phonon coupling constant. In metallic and polar or heavily doped semiconductor nanomaterials, the interaction of phonons with the conduction electrons or electron-hole pairs reflects in the Raman spectra as the asymmetric mode shift and broadening. Asymmetric line shapes of the Raman phonon spectra originate from a Fano-type interference effect between the discrete one-phonon states and a continuum of electronic transitions and can be well described with the Fano line shape [52,53].

$$I(\omega) = \sum_i I_{0i} \frac{(\varepsilon_i + q_i)^2}{1 + \varepsilon_i^2} \quad (2.18)$$

where  $\varepsilon_i = 2(\omega - \omega_i)/\Gamma_i$ ,  $I_{0i}$ ,  $\omega_i$  and  $\Gamma_i$  are the intensity, bare phonon frequency and linewidth of the  $i$ th phonon mode and  $q_i$  is the Fano asymmetric parameter for the  $i$ th mode. The parameter  $q$  controls the asymmetry of the Raman mode with respect to a standard Lorentzian profile, whereas the value  $1/q$  serves as a measure of electron-phonon coupling strength. The increase of  $1/q$  value indicates stronger coupling and in the limit  $|1/q| \rightarrow 0$  the Fano profile reduces to the Lorentzian line shape [53].

The electron-phonon coupling strength can also be estimated from the Allen formula [54] which connects the linewidth  $\gamma_i$  of the  $i$ th phonon mode with electron-phonon coupling constant  $\lambda_i$  [54,55]

$$\lambda_i = \frac{2g_i\gamma_i}{\pi N_{\varepsilon_f} \omega_{bi}^2} \quad (2.19)$$

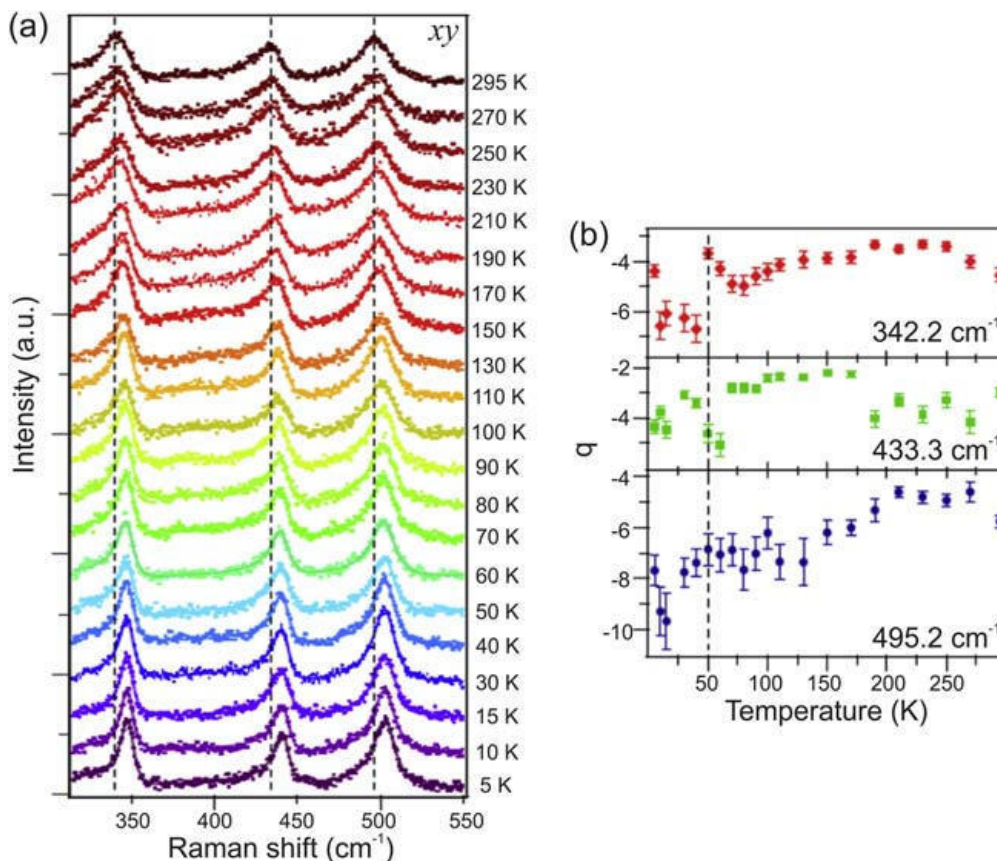
where  $N_{\varepsilon_f}$  is the electronic density of states at the Fermi surface per spin per unit cell,  $g_i$  is the mode degeneracy, and  $\omega_{bi}$  is the bare phonon frequency in the absence of electron-phonon interaction. In the framework of Allen's theory, the electronic density of states  $N_{\varepsilon_f}$  can be estimated from the relation [55,56].

$$\gamma_i = -\frac{\pi}{2} N_{\varepsilon_f} \omega_{bi} \Delta\omega \quad (2.20)$$

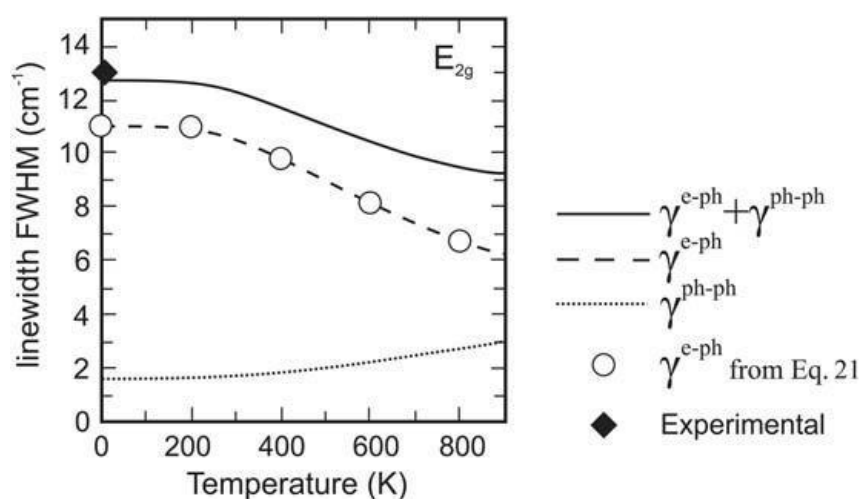
where  $\Delta\omega$  presents the difference between the bare phonon frequency and the observed frequency.

A good example of  $e$ -ph coupling in nanophase materials presents the Raman temperature study on  $\text{LiTi}_2\text{O}_4$  superconducting thin films [57]. In Fig. 2.12A are presented temperature-dependent Raman spectra of three  $T_{2g}$  modes ( $342.2 \text{ cm}^{-1}$ ,  $433.3 \text{ cm}^{-1}$ , and  $495.2 \text{ cm}^{-1}$ ) of  $\text{LiTi}_2\text{O}_4$ . All  $T_{2g}$  modes had asymmetric Fano line shape in the whole temperature range 5–300 K and were well fitted with the Fano function (full lines on Fig. 2.12A). The parameters  $q$ , obtained from the fitting of  $T_{2g}$  modes from Fig. 2.12A, are displayed in Fig. 2.12B. There is an obvious anomaly in the asymmetry parameters around the temperature of 50 K, where the negative to positive magnetoresistance transition takes place [57]. This anomaly was ascribed to the onset of other competing order like orbital-related state, which can suppress the  $e$ -ph coupling by modifying the electron density of states [57].

Electron-phonon interactions can be responsible for some anomalous behavior of phonon linewidths and intensities as a function of temperature. As an example, calculations from first principles [58] have proven that the anomalous decrease of  $E_{2g}$  ( $G$  band) phonon linewidth in graphene is dominated by  $e$ -ph interactions. In Fig. 2.13 is shown the total


**Figure 2.12**

Temperature-dependent (A) Raman spectra of three  $T_{2g}$  modes of  $\text{LiTi}_2\text{O}_4$  thin films and (B) Fano asymmetry factor  $q$  of the  $T_{2g}$  modes. Reprinted figure with permission from D. Chen, Y.-L. Jia, T.-T. Zhang, Z. Fang, K. Jin, P. Richard, H. Ding, Raman study of electron-phonon coupling in thin films of the spinel oxide superconductor  $\text{LiTi}_2\text{O}_4$ , *Phys. Rev. B* 96 (2017) 094501. Copyright (2017) by the American Physical Society.


**Figure 2.13**

Calculated temperature dependence of the total  $E_{2g}$  mode linewidth of graphene (full line), e-ph (dashed line), and ph-ph (dotted line) contributions, from first principles together with experimental results and the results (open circles) based on Eq. (2.21). Reprinted figure with permission from N. Bonini, M. Lazzeri, N. Marzari, F. Mauri, Phonon anharmonicities in graphite and graphene, *Phys. Rev. B* 99 (2007) 176802. Copyright (2007) by the American Physical Society.

linewidth of  $E_{2g}$  mode (full line) computed from first principles, whereas dashed and dotted lines present  $e$ -ph and ph-ph contributions. These calculations are in very good agreement with respect to measurements [58] and have shown that the  $e$ -ph coupling has dominant role in the temperature dependence of  $E_{2g}$  mode linewidth. Furthermore, these calculations are compared with the results (open circles in Fig. 2.13) obtained from the simplified model for temperature dependence of  $E_{2g}$  phonon linewidth due to  $e$ -ph coupling [58,59].

$$\gamma^{e-ph}(T) = \gamma^{e-ph}(0) \left[ f\left(-\frac{\hbar\omega_0}{2k_B T}\right) - f\left(\frac{\hbar\omega_0}{2k_B T}\right) \right] \quad (2.21)$$

where  $f(x) = [\exp(x) + 1]^{-1}$ ,  $k_B$  is the Boltzmann constant and  $\hbar\omega_0$  is the  $E_{2g}$  phonon energy. As can be seen from Fig. 2.13, the simplified model very well reproduces the calculations for the linewidth behavior of  $E_{2g}$  phonon with temperature confirming the dominant role of  $e$ -ph coupling.

Another temperature-dependent Raman study on nanostructured cuprous oxide ( $\text{Cu}_2\text{O}$ ) film (Fig. 2.14), revealed the anomalous temperature behavior of the LO components of

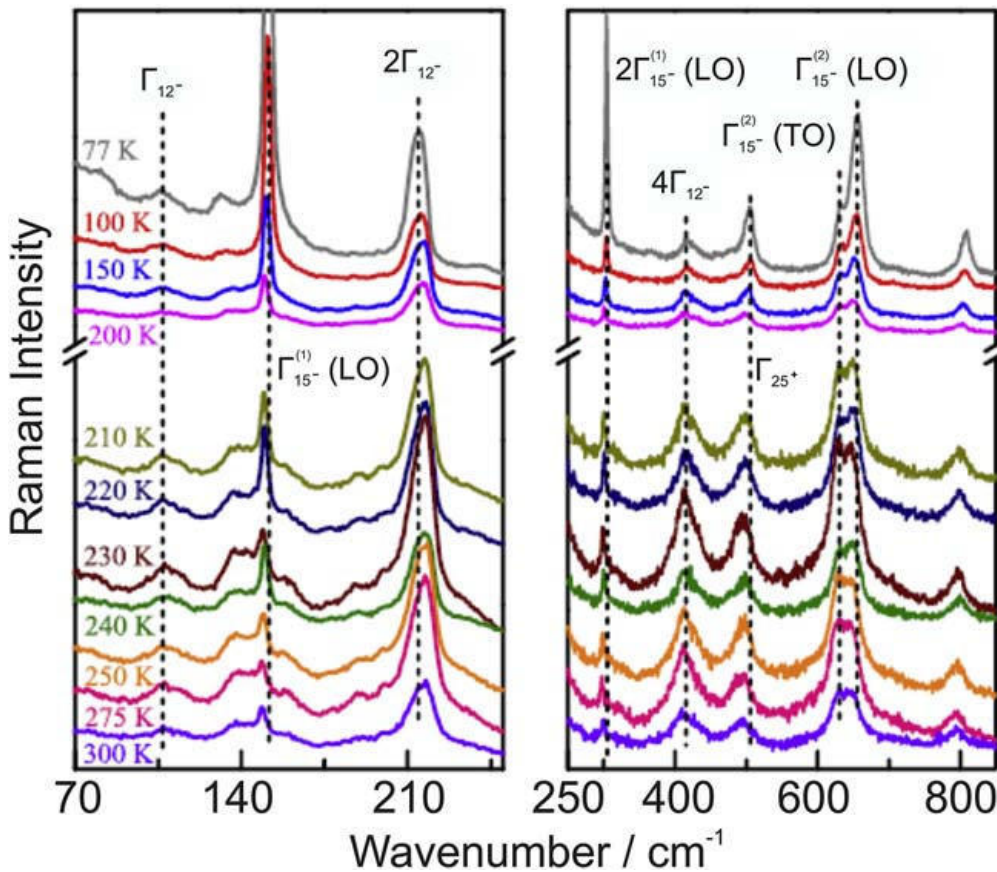


Figure 2.14

Temperature-dependent Raman spectra of  $\text{Cu}_2\text{O}$  film. Dashed lines present the guides to the eye of the Raman modes shift with temperature. Reprinted from W. Yu, M. Han, K. Jiang, Z. Duan, Y. Li, Z. Hu, J. Chu, Enhanced Fröhlich interaction of semiconductor cuprous oxide films determined by temperature-dependent Raman scattering and spectral transmittance, *J. Raman Spectrosc.* 44 (2013) 142–146 with the permission of John Wiley & Sons.



the infrared-active polar  $\Gamma_{15-}^{(1)}$  and  $\Gamma_{15-}^{(2)}$  modes [60]. Namely, an appearance of  $\Gamma_{15-}^{(1)}$  and  $\Gamma_{15-}^{(2)}$  modes at 151 and 655  $\text{cm}^{-1}$  in the Raman spectra from Fig. 2.14 indicated the presence of strong  $e$ -ph coupling mediated by Fröhlich interaction. At lowest temperature of 77 K, these modes were sharp and of high intensity. With temperature increase, their intensity decreased and after 200 K intensities of both modes were significantly reduced. This study pointed to much stronger Fröhlich interaction at temperatures lower than 200 K. The larger TO-LO splitting of  $\Gamma_{15-}^{(2)}$  mode at temperatures below 200 K imply that Fröhlich interaction is very sensitive to temperature [60].

It is worth to mention that Raman studies on nanocrystalline materials [9,61] suggest that the strength of  $e$ -ph interaction is dependent on nanocrystalline size. Therefore, analyzing the temperature-dependent Raman spectra of nanostructured materials it is important to correctly estimate the contributions from size effects, anharmonicity and  $e$ -ph coupling on the Raman line profile.

## 7. Electromagnons in cycloidal multiferroic nanostructures

Raman scattering is an efficient tool for studying the mutual and complex coupling between the magnetic (magnons) and lattice (phonons) excitations. One such example are the single-magnon spin waves with an electric dipole activity, called electromagnons, which can be excited by the electric component of electromagnetic waves and are consequently much stronger coupled to the light than ordinary magnons which interact through magnetic dipole excitations. Up to date, electromagnons were registered in a variety of crystalline antiferromagnets like  $\text{CuFe}_{1-x}\text{Ga}_x\text{O}_2$ , [62], garnets, [63], multiferroics like  $\text{RMn}_2\text{O}_5$  ( $R = \text{Y}, \text{Tb}, \text{Eu}$ ), [64],  $\text{Ba}_2\text{CoGe}_2\text{O}_7$ , [65], manganites [66].

The presence of electromagnons was first discovered in the low-temperature Raman spectra of cycloidal multiferroic  $\text{BiFeO}_3$  single crystals [67,68] and recently in  $\text{BiFeO}_3$  thin films [69]. In Fig. 2.15A is presented the electromagnon Raman spectra of  $\text{BiFeO}_3$  crystal measured at 7 K in parallel and crossed polarizations in (010) plane.

Two types of electromagnon excitations were registered in the Raman spectra of  $\text{BiFeO}_3$  crystal, which lie in (cyclon modes,  $\varphi$ ) and out (extra-cyclon modes,  $\psi$ ) of (-12-1) cycloidal plane [67]. The cycloidal plane is formed by the vector of spontaneous polarization  $P$  along [111] direction and cycloid propagation defined by the wavevector  $q$  along [10-1] direction, as sketched in Fig. 2.15B. These low-energy Raman modes show sudden increase of intensity at temperatures close to the spin reorientation phase transition (140 K) which is additional confirmation of their magnetic nature [67].

In the framework of simple Landau-Ginzburg model for cycloidal multiferroics, Sousa and Moore [70] have shown that the modes which propagate along the cycloidal plane

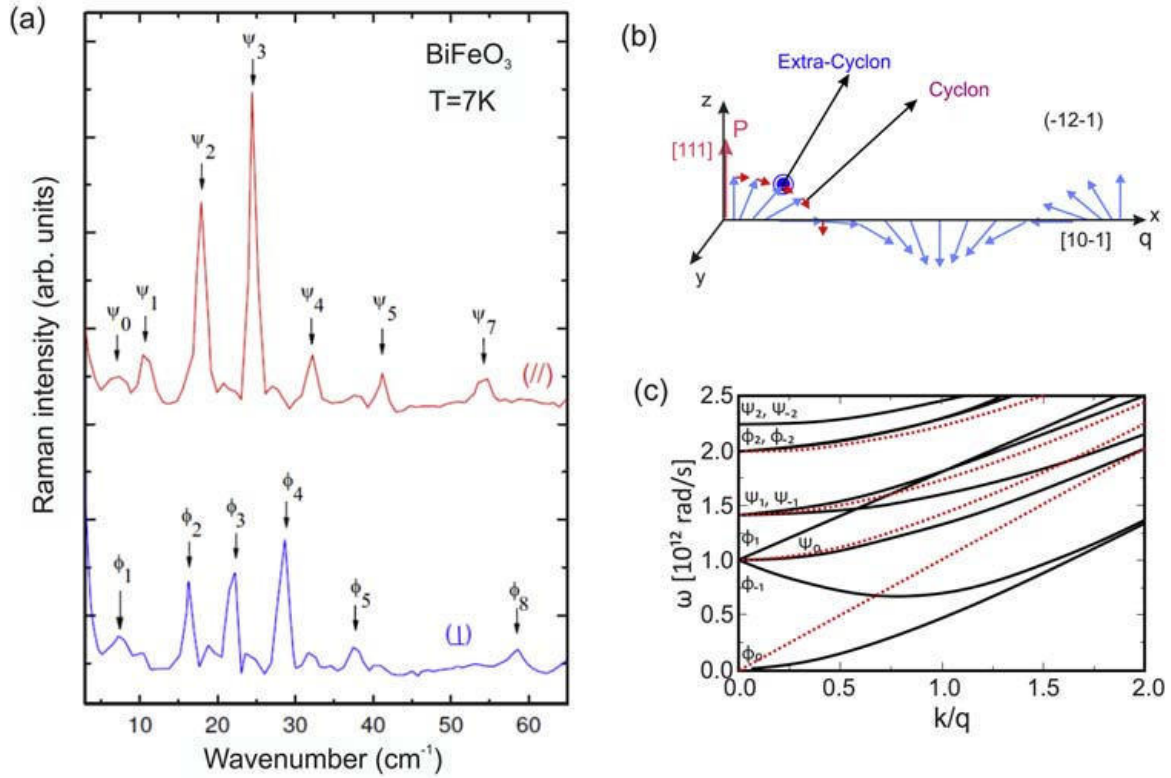


**Figure 2.15**

(A) Electromagnon Raman spectra of BiFeO<sub>3</sub> single crystal obtained using parallel (//) and crossed (⊥) polarizations in the (010) plane; (B) schematic representation of cycloidal magnetic order in BiFeO<sub>3</sub> and (C) dispersion curves of cyclon ( $\varphi$ ) and extra-cyclon ( $\psi$ ) modes in the direction perpendicular to (-12-1) cycloidal plane (*full lines*), and along [111] direction (*dashed lines*).

Reprinted figure with permission from M. Cazayous, Y. Gallais, A. Sacuto, R. de Sousa, D. Lebeugle, D. Colson, Possible observation of cycloidal electromagnons in BiFeO<sub>3</sub>, *Phys. Rev. Lett.* 101 (2008) 037601. Copyright (2008) by the American Physical Society, R. De Sousa, J.E. Moore, Optical coupling to spin waves in the cycloidal multiferroic BiFeO<sub>3</sub>, *Phys. Rev. B* 77 (2008) 012406. Copyright (2008) by the American Physical Society.

( $k_y = 0$ ), are simple plane waves with different dispersions depending on their coupling to electrical polarization

$$\omega'^2 = c\tilde{k}^2 (\varphi \text{ modes}) \quad (2.22)$$

$$\omega'^2 = c\left(\tilde{k}^2 + q^2\right) (\Psi \text{ modes}) \quad (2.23)$$

with  $\tilde{k} = (k_x + nq)^2 + k_y^2 + k_z^2$  and  $n$  as integer. The propagation along the  $k_y$  direction leads to the appearance of small gaps in the propagation frequency due to the pinning of the cycloidal plane by the electrical polarization. The numerical solutions of spin waves propagation [70] in the direction perpendicular to (-12-1) cycloidal plane (full lines) and along [111] direction (dashed lines) are shown in Fig. 2.15C.

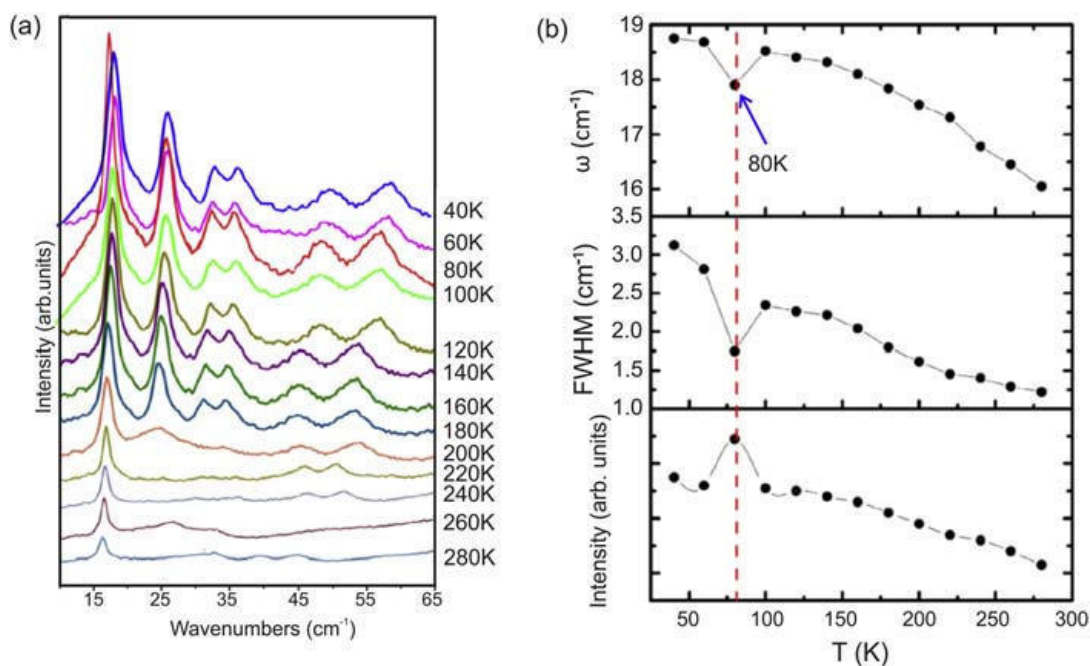


**Figure 2.16**

Temperature dependence of (A) electromagnon spectra of BiFeO<sub>3</sub> thin films in normal configuration (B) wavenumber, linewidth (FWHM), and intensity of electromagnon mode at 18.75 cm<sup>-1</sup>. Reprinted from W. Azeem, S. Riaz, A. Bukhtiar, S.S. Hussain, Y. Xu, S. Naseem, *Ferromagnetic ordering and electromagnons in microwave synthesized BiFeO<sub>3</sub> thin films*, *J. Magnet. Magnet. Mater.* 475 (2019) 60–69, Copyright (2019) with permission from Elsevier.

Recently, electromagnons have been found in the low-frequency Raman spectra of BiFeO<sub>3</sub> thin films [69]. The temperature-dependent electromagnon spectra is shown in Fig. 2.16A. Two intense modes (at 18.75 cm<sup>-1</sup> and 25.8 cm<sup>-1</sup>) together with four other modes of lower intensity were observed at 40 K. These two low-energy electromagnon modes are strongly affected by temperature. In Fig. 2.16B is presented the temperature variation of the wavenumber, linewidth and intensity of 18.75 cm<sup>-1</sup> electromagnon mode. As can be seen, neither frequency, linewidth nor intensity exhibit monotonic behavior. Instead, there is an anomaly at around 80 K. Such a behavior can be correlated with changes in the cycloid spin arrangements at low temperatures like spin reorientation transition in BiFeO<sub>3</sub> single crystal [68] or in orthoferrites like TmFeO<sub>3</sub> [71].

From these studies, it can be concluded that RS is a suitable optical method not only for detection of electromagnons, but for revealing more about the anharmonicity in magnetic order of cycloidal multiferroic nanostructures.

## 8. Spin-phonon interaction

RS is a useful tool to elucidate spin-phonon (*s-ph*) coupling mechanism, because the Raman modes in magnetic materials can be sensitive to the magnetic ordering.

Spin-phonon interaction manifests as nontypical temperature dependence of optical phonon frequency, linewidth and integrated intensity, since all these phonon features can be influenced by the exchange coupling between magnetic ions at and below the temperatures of magnetic phase transitions. It is expected that the coupling between the lattice and spin degrees of freedom (spin-phonon coupling) is different for different phonon modes because the magnetic interactions can be complex and the spin-phonon coupling constant may vary even in the case of the same spin-spin interaction [72].

In magnetic materials, the change of a  $j$ th phonon mode frequency with temperature can be expressed as:

$$\omega_j(T) - \omega_j(T_0) = \Delta\omega_j(T) = \Delta\omega_{\text{latt}} + \Delta\omega_{\text{anh}} + \Delta\omega_{e\text{-ph}} + \Delta\omega_{s\text{-ph}} \quad (2.24)$$

The first three terms present the change of the phonon frequency due to the lattice expansion/contraction, intrinsic anharmonicity and electron-phonon coupling, whereas the fourth term accounts for the effect of the  $s$ -ph contribution. The frequency shift due to  $s$ -ph coupling can be expressed as [73,74].

$$\Delta\omega_{s\text{-ph}} = \omega - \omega_0 = -\lambda_{s\text{-ph}} \langle S_i S_j \rangle \quad (2.25)$$

where  $\omega_0$  is the eigenfrequency in the absence of  $s$ -ph coupling;  $S_i S_j$  denotes the spin-spin correlation function for adjacent spins localized at the  $i$ th and  $j$ th sites and  $\lambda_{s\text{-ph}}$  is the  $s$ -ph coupling constant which is different for each phonon and may have positive or negative sign [73]. From the mean field theory and considering nearest neighbor interaction it follows that

$$\langle S_i S_j \rangle = S^2 \phi(T) \quad (2.26)$$

where  $\phi(T)$  is the normalized short-range order parameter which is estimated from the mean field theory [73] and defined as  $\phi(T) = |S_i S_j| / S^2$ . According to the mean field theory,  $\phi(T)$  decreases with temperature from 1 at  $T = 0$  K and falling to 0 at temperature of magnetic phase transition (either  $T_N$  or  $T_C$ ). The  $\Delta\omega_{s\text{-ph}}$  can be now expressed as

$$\Delta\omega_{s\text{-ph}} = -\lambda_{s\text{-ph}} S^2 \phi(T) \quad (2.27)$$

On the other hand, according to the mean field approximation the  $S_i S_j \propto \left(\frac{M(T)}{M_S}\right)^2$ , where  $M(T)$  is the temperature-dependent average magnetization per magnetic ion and  $M_S$  is the saturation magnetization [75–77]. Therefore, the shift of the Raman mode due to  $s$ -ph coupling is  $\omega_{s\text{-ph}} \propto \left(\frac{M(T)}{M_S}\right)^2$ . In antiferromagnetic (AF) and ferromagnetic (FM) materials spin correlation function  $S_i S_{i+1}$  approaches zero for  $T > T_N, T_C$  and the spin-phonon coupling usually terminates in the paramagnetic phase.

Raman spectroscopy has been utilized to study spin-phonon coupling in various magnetic nanomaterials [11,78–80] through the temperature-dependent variation of the one-phonon or two-phonon Raman spectra. CuO nanowires are a good example to study spin-phonon interaction and the effect of size decrease on the spin-phonon coupling constant [11]. In Fig. 2.17A are presented Raman spectra of in-plane CuO nanowires, with the mean diameter of 120 nm, at different temperatures across the Néel temperature,  $T_N$  ( $\sim 143$  K).

Two well-defined modes at around 300 and 348  $\text{cm}^{-1}$  of  $A_g$  and  $B_g^1$  symmetries were registered at 193 K. With temperature decrease an additional mode at  $\sim 231$   $\text{cm}^{-1}$

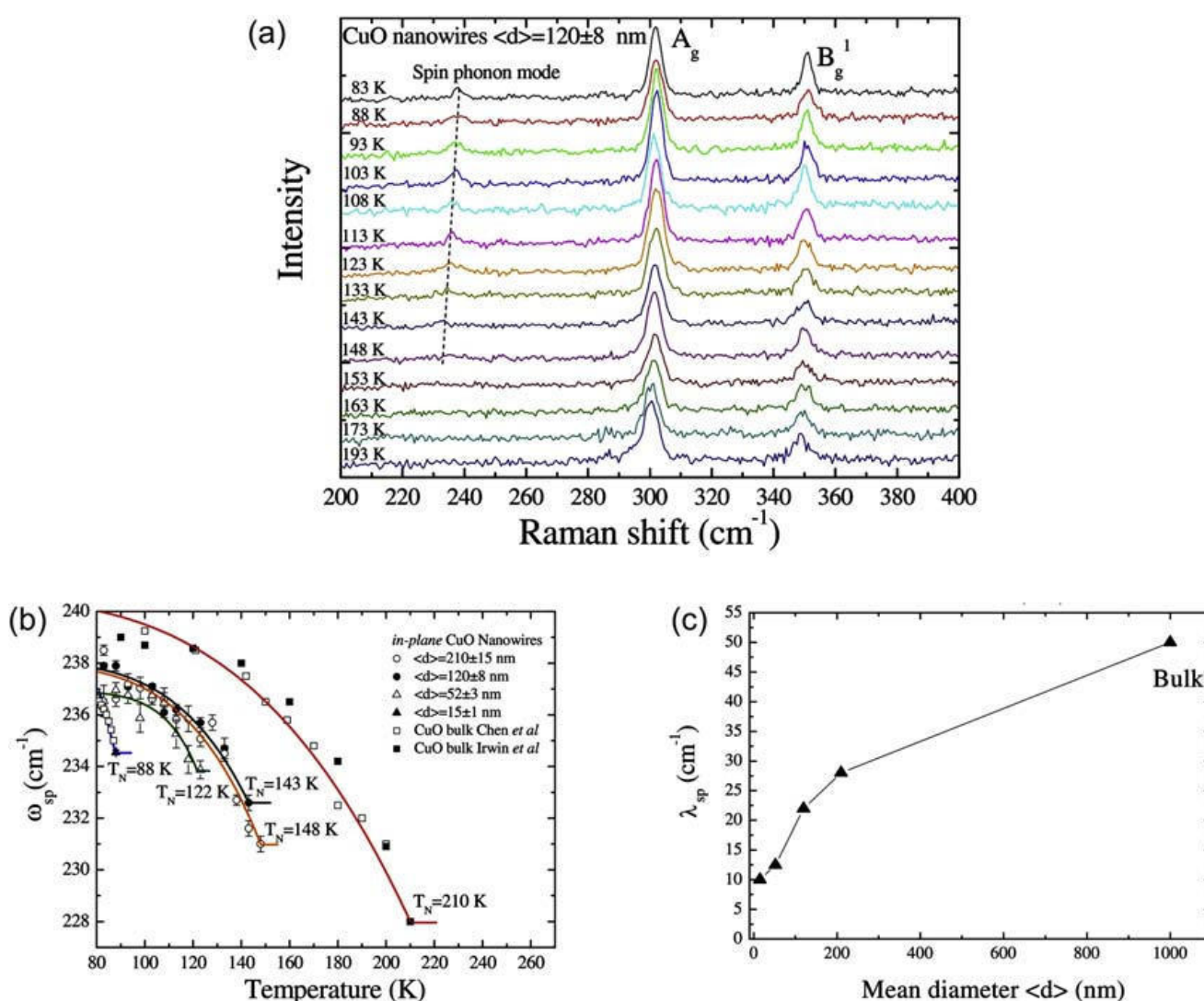
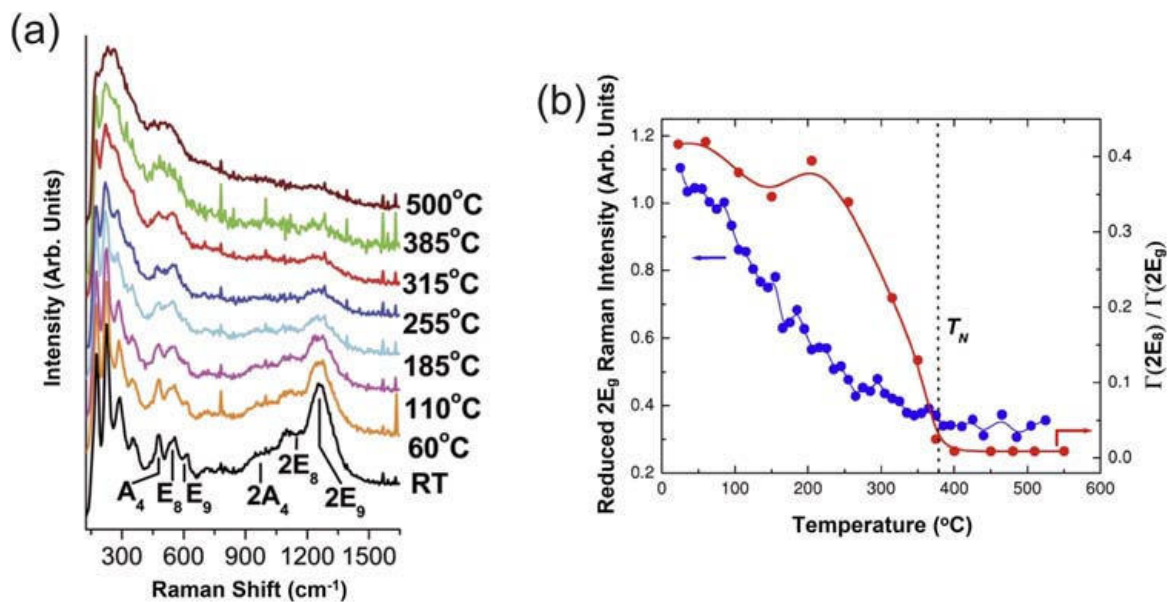


Figure 2.17

(A) Raman spectra of CuO nanowires with mean diameter  $\langle d \rangle = 120 \pm 8$  nm at various temperatures across the  $T_N$ ; (B) temperature variation of spin-phonon mode frequency and (C) change of spin-phonon coupling constant on nanowires mean diameter. Reprinted from P.-H. Shih, C.-L. Cheng, S.Y. Wu, *Short-range spin-phonon coupling in in-plane CuO nanowires: a low-temperature Raman investigation*, *Nanoscale Res. Lett.* 8 (398) (2013) 1–6 with the permission of SpringerNature.

appeared. This mode is ascribed to the zone-folded LA phonon from the  $Z'$  point of the Brillouin-zone boundary, which can appear in the Raman spectra below  $T_N$  as a consequence of the onset of long-range AF magnetic order and phonon modulation of the exchange constant [72]. This mode exhibits unusual variation both in intensity and frequency with decreasing temperature below  $T_N$ . Namely, intensity of this mode abruptly increases, whereas the frequency significantly hardens below  $T_N$ . This anomalous behavior results from a strong spin-phonon interaction [72]. The temperature variation of spin-phonon mode frequency for CuO nanowires of different mean diameter and bulk counterpart is shown Fig. 2.17B. The spin-phonon mode temperature variation can be well described by Eq. (2.27) (solid lines) for  $S^2 \sim 1/4^{73}$  using empirical formula for  $\phi(T) = 1 - (T/T_N)^\gamma$  (solid lines) [79]. In such a way  $T_N$  and spin-phonon coupling constant  $\lambda_{s-ph}$  can be estimated. As can be seen from Fig. 2.17B and C, with decreasing diameter,  $T_N$  and  $\lambda_{s-ph}$  tend to decrease. This implies that the size effect weakens the strong spin-phonon interaction, favorizing the short-range AF ordering [11].

Another example of strong spin-phonon interaction was reported in multiferroic BiFeO<sub>3</sub> thin films [80] evidenced through the temperature behavior of the two-phonon Raman modes,  $2A_4$ ,  $2E_8$  and  $2E_9$ . These modes are positioned at around 968, 1110, and 1265 cm<sup>-1</sup> at RT. Upon heating, as shown in Fig. 2.18A, all Raman modes slightly shift to



**Figure 2.18**

(A) Temperature dependence of unpolarized Raman spectra of BiFeO<sub>3</sub> film and (B) reduced integrated intensity of 1260 cm<sup>-1</sup> two-phonon Raman mode (*blue dots*). Temperature dependence of the integrated intensity ratio between 2E8 and 2E9 two-phonon modes is presented with *red circles*. The *solid lines* are guide to the eye. Reprinted from M.O. Ramirez, M. Krishnamurthi, S. Denev, A. Kumar, S.-Y. Yang, Y.-H. Chu, E. Saiz, J. Seidel, A.P. Pyatakov, A. Bush, D. Viehland, J. Orenstein, R. Ramesh, V. Gopalan, Two-phonon coupling to the antiferromagnetic phase transition in multiferroic BiFeO<sub>3</sub>, *Appl. Phys. Lett.* 92 (2008) 022511 with the permission of AIP Publishing.

lower frequency and broaden due to anharmonicity, but the integrated intensity of two-phonon modes drastically decrease, particularly of two-phonon mode  $2E_9$ . Above the Néel temperature, this mode almost disappeared. Eliminating the contribution from Bose-Einstein population, the reduced intensity of  $2E_9$  mode is presented in Fig. 2.18B (blue circles) and compared to the reduced intensity of  $2E_8$  mode (red circles). As can be seen, a remarkable decrease of the integrated intensity of  $2E_9$  mode is seen when approaching  $T_N$ , and above the temperature of magnetic phase transition it is almost constant. The integrated intensity ratio,  $\Gamma(2E_8)/\Gamma(2E_9)$ , is almost constant up to 200 °C and abruptly decreases in the vicinity of Néel temperature, indicating strong spin-two-phonon coupling in BiFeO<sub>3</sub> [80].

## 9. Summary

This chapter presents a brief review how temperature-dependent RS comes to be of significant importance for investigating various phenomena in nanostructured materials. Raman spectra of diverse nanomaterials in the form of metal-oxide nanopowders, quantum dots, nanowires, nanoribbons, carbon-based, and multiferroic nanostructures were analyzed as examples.

It was shown that the application of RS at elevated temperatures is a very convenient method to study the anharmonic interactions through the evolution of optical phonon modes in nanophase materials. The temperature evolution of the Raman modes can be successfully modeled by PCM which incorporates size, strain, and anharmonic effects and enables to estimate the contribution of each of these effects. It was shown that the size, morphology, and size distribution largely determine which of the anharmonic processes (three or four-phonon anharmonic interaction) will be dominant, pointing out that phonon-phonon interactions can be different in nanomaterials compared to their bulk counterpart. Low-frequency RS provided the information about the acoustic phonons dynamics as a function of temperature in nanocrystalline solids as well. It was demonstrated that the decay dynamics of the acoustic phonons was complex and dependent not only on different size and size distribution, i.e., coalescence process at higher temperatures, but also on organic ligands with different elastic modulus and impurities bound to the nanoparticle surface.

Temperature-dependent Raman scattering has a potential to detect the formation of other structural phases, present even in small concentrations, through the appearance of new peaks characteristic for a certain crystalline structure. As a noncontact method of high spatial resolution, RS can be used in thermometry for the measurements of the local temperature or thermal conductivity of nanomaterials.

RS is a suitable optical method for probing lattice and charge excitations, as well as interplay between them. In the Raman spectra of low-dimensional materials electron-phonon interaction manifests itself by an asymmetric Fano line shape of the phonon modes. The electron-phonon coupling strength can be estimated directly from the fitting of the Raman spectra at different temperatures with the Fano function or from the linewidth of the phonon modes using Allen's formula. Besides, in nanophase materials, the electron-phonon interaction is sensitive to temperature and nanocrystallite size.

Special class of nanomaterials present magnetic and multiferroic nanomaterials. In these materials, it was shown that phonon frequency, linewidth, and integrated intensity may all be influenced by the exchange coupling between magnetic ions and from their temperature dependence it is possible to investigate both spin-ordering and spin-reorientation transitions, revealing more about the complexity of magnetic interactions in nanophase materials.

In summary, from the temperature induced changes of the Raman features (peak position, intensity, or linewidth) it is possible to predict many new thermophysical, electric, and magnetic nanomaterials properties.

## ***Acknowledgment***

The authors acknowledge funding by the Institute of Physics Belgrade, through the grant by the Serbian Ministry of Education, Science and Technological Development.

## ***References***

- [1] C.S.S.R. Kumar, *Raman Spectroscopy for Nanomaterials Characterization*, Springer-Verlag Berlin Heidelberg, 2012.
- [2] H. Richter, Z.P. Wang, L. Ley, The one phonon Raman spectrum in microcrystalline silicon, *Solid State Commun.* 39 (1981) 625–629.
- [3] I.H. Campbell, P.M. Fauchet, The effects of microcrystal size and shape on the one phonon Raman spectra of crystalline semiconductors, *Solid State Commun.* 58 (1986) 739–741.
- [4] L. Donetti, F. Gámiz, N. Rodriguez, F. Jimenez, C. Sampedro, Influence of acoustic phonon confinement on electron mobility in ultrathin silicon on insulator layers, *Appl. Phys. Lett.* 88 (2006) 122108.
- [5] A.C. Gandhi, S.S. Gaikwad, J.-C. Peng, C.-W. Wang, T.S. Chan, S.Y. Wu, Strong electron-phonon coupling in superconducting bismuth nanoparticles, *APL Mater.* 7 (2019) 031111.
- [6] G.S.N. Eliel, M.V.O. Moutinho, A.C. Gadelha, A. Righi, L.C. Campos, H.B. Ribeiro, P.-W. Chiu, K. Watanabe, T. Taniguchi, P. Puech, M. Paillet, T. Michel, P. Venezuela, M.A. Pimenta, Intralayer and interlayer electron–phonon interactions in twisted graphene heterostructures, *Nat. Commun.* 9 (2018) 1221.
- [7] H. Rijckaert, P. Cayado, R. Nast, J.D. Sierra, M. Erbe, P.L. Dominguez, J. Hänisch, K. De Buysser, B. Holzapfel, I. Van Driessche, Superconducting  $\text{HfO}_2\text{-YBa}_2\text{Cu}_3\text{O}_{7-\delta}$  nanocomposite films deposited using ink-jet printing of colloidal solutions, *Coatings* 10 (2020) 17.
- [8] C.Y. Tsai, H.M. Cheng, H.R. Chen, K.F. Huang, L.N. Tsai, Y.H. Chu, C.H. Lai, W.F. Hsieh, Spin and phonon anomalies in epitaxial self-assembled  $\text{CoFe}_2\text{O}_4\text{-BaTiO}_3$  multiferroic nanostructures, *Appl. Phys. Lett.* 104 (2014) 252905.



- [9] D.M. Sagar, J.M. Atkin, P.K.B. Palomaki, N.R. Neale, J.L. Blackburn, J.C. Johnson, A.J. Nozik, M.B. Raschke, M.C. Beard, Quantum confined electron-phonon interaction in silicon nanocrystals, *Nano Lett.* 15 (2015) 1511–1516.
- [10] D. Paramanik, S. Varma, Raman scattering characterization and electron phonon coupling strength for MeV implanted InP (111), *J. Appl. Phys.* 101 (2007) 023528.
- [11] P.-H. Shih, C.-L. Cheng, S.Y. Wu, Short-range spin-phonon coupling in in-plane CuO nanowires: a low-temperature Raman investigation, *Nanoscale Res. Lett.* 8 (2013) 398.
- [12] G.S. Doerk, C. Carraro, R. Maboudian, Temperature dependence of Raman spectra for individual silicon nanowires, *Phys. Rev. B* 80 (2009) 073306.
- [13] M. Kazan, S. Pereira, M.R. Correia, P. Masri, Contribution of the decay of optical phonons into acoustic phonons to the thermal conductivity of AlN, *Phys. Rev. B* 77 (2008) 180302.
- [14] J. Kulda, A. Debernardi, M. Cardona, F. de Geuser, E.E. Haller, Self-energy of zone-boundary phonons in germanium: ab initio calculations versus neutron spin-echo measurements, *Phys. Rev. B* 69 (2004) 045209.
- [15] Z. Dohčević-Mitrović, Z.V. Popović, M. Šćepanović, Anharmonicity effects in nanocrystals studied by Raman scattering spectroscopy, *Acta Phys. Pol. A* 116 (2009) 36–41.
- [16] G. Lucazeau, Effect of pressure and temperature on Raman spectra of solids: anharmonicity, *J. Raman Spectrosc.* 34 (2003) 478–496.
- [17] A.A. Maradudin, A.E. Fein, Scattering of neutrons by an anharmonic crystal, *Phys. Rev. B* 128 (1962) 2589–2608.
- [18] R.P. Lowndes, Anharmonic self-energy of a soft mode, *Phys. Rev. Lett.* 27 (1971) 1134–1136.
- [19] M. Balkanski, R.F. Wallis, E. Haro, Anharmonic effects in light scattering due to optical phonons in silicon, *Phys. Rev. B* 28 (1983) 1928–1934.
- [20] G. Morell, W. Pérez, E. Ching-Prado, R.S. Katiyar, Anharmonic interactions in beryllium oxide, *Phys. Rev. B* 53 (1996) 5388–5395.
- [21] P.G. Klemens, Anharmonic decay of optical phonons, *Phys. Rev.* 148 (1966) 845–848.
- [22] T.R. Hart, R.L. Aggarwal, B. Lax, Temperature dependence of Raman scattering in silicon, *Phys. Rev. B* 1 (1970) 638–642.
- [23] Z. Dohčević-Mitrović, M. Grujić-Brojčin, M. Šćepanović, Z.V. Popović, S. Bošković, B. Matović, M. Zinkevich, F. Aldinger, The size and strain effects on the Raman spectra of  $\text{Ce}_{1-x}\text{Nd}_x\text{O}_{2-\delta}$  ( $0 \leq x \leq 0.25$ ) nanopowders, *Solid State Commun.* 137 (2006) 387–390.
- [24] Z. Dohčević-Mitrović, M. Grujić-Brojčin, M. Šćepanović, Z.V. Popović, S. Bošković, B. Matović, M. Zinkevich, F. Aldinger,  $\text{Ce}_{1-x}\text{Y}(\text{Nd})_x\text{O}_{2-\delta}$  nanopowders: potential materials for intermediate temperature solid oxide fuel cells, *J. Phys. Condens. Matter* 18 (2006) S2061–S2068.
- [25] Z.D. Dohčević-Mitrović, M. Radović, M. Šćepanović, M. Grujić-Brojčin, Z.V. Popović, B. Matović, S. Bošković, Temperature-dependent Raman study of  $\text{Ce}_{0.75}\text{Nd}_{0.25}\text{O}_{2-\delta}$  nanocrystals, *Appl. Phys. Lett.* 91 (2007) 203118.
- [26] J. Spanier, R. Robinson, F. Zhang, S.-W. Chan, I. Herman, Size-dependent properties of  $\text{CeO}_{2-y}$  nanoparticles as studied by Raman scattering, *Phys. Rev. B* 64 (2001) 245407.
- [27] S. Askračić, Z.D. Dohčević-Mitrović, M. Radović, M. Šćepanović, Z.V. Popović, Phonon-phonon interactions in  $\text{Ce}_{0.85}\text{Gd}_{0.15}\text{O}_{2-\delta}$  nanocrystals studied by Raman spectroscopy, *J. Raman Spectrosc.* 40 (2009) 650–655.
- [28] H.K. Yadav, R.S. Katiyar, V. Gupta, Temperature dependent dynamics of ZnO nanoparticles probed by Raman scattering: a big divergence in the functional areas of nanoparticles and bulk material, *Appl. Phys. Lett.* 100 (2012) 051906.
- [29] Y.L. Du, Y. Deng, M.S. Zhang, Variable-temperature Raman scattering study on anatase titanium dioxide nanocrystals, *J. Phys. Chem. Solid.* 67 (2006) 2405–2408.
- [30] K. Gao, Strong anharmonicity and phonon confinement on the lowest-frequency Raman mode of nanocrystalline anatase  $\text{TiO}_2$ , *Phys. Status Solidi* 244 (2007) 2597–2604.

- [31] M.J. Šćepanović, M. Grujić-Brojčin, Z.D. Dohčević-Mitrović, Z.V. Popović, Temperature dependence of the lowest frequency  $E_g$  Raman mode in laser-synthesized anatase  $TiO_2$  nanopowder, *Appl. Phys. A* 86 (2007) 365–371.
- [32] G.R. Hearne, J. Zhao, A.M. Dawe, V. Pischedda, M. Maaza, M.K. Nieuwoudt, P. Kibasomba, O. Nemraoui, J.D. Comins, M.J. Witcomb, Effect of grain size on structural transitions in anatase  $TiO_2$ : a Raman spectroscopy study at high pressure, *Phys. Rev. B* 70 (2004) 134102.
- [33] S. Aškračić, Z. Dohčević-Mitrović, A. Kremenović, N. Lazarević, V. Kahlenberg, Z.V. Popović, Oxygen vacancy-induced microstructural changes of annealed  $CeO_{2-x}$  nanocrystals, *J. Raman Spectrosc.* 43 (2012) 76–81.
- [34] J.V. Silveira, L.L. Vieira, J.M. Filho, A.J.C. Sampaio, O.L. Alvares, A.G. Souza Filho, Temperature-dependent Raman spectroscopy study in  $MoO_3$  nanoribbons, *J. Raman Spectrosc.* 43 (2012) 1407–1412.
- [35] J.M. Todorović, Z.D. Dohčević-Mitrović, D.M. Đokić, D. Mihailović, Z.V. Popović, Investigation of thermostability and phonon-phonon interactions in  $Mo_6S_3I_6$  nanowires by Raman scattering spectroscopy, *J. Raman Spectrosc.* 41 (2010) 978–982.
- [36] M. Testa-Anta, M.A. Ramos-Docampo, M. Comesaña-Hermo, B. Rivas-Murias, V. Salgueiriño, Raman spectroscopy to unravel the magnetic properties of iron oxide nanocrystals for bio-related applications, *Nanoscale Adv.* 1 (2019) 2086–2103.
- [37] M. Sendova, B.D. Hosterman, R. Raud, T. Hartmann, D. Koury, Temperature-dependent, micro-Raman spectroscopic study of barium titanate nanoparticles, *J. Raman Spectrosc.* 46 (2015) 25–31.
- [38] L. Chen, K. Rickey, Q. Zhao, C. Robinson, X. Ruan, Effects of nanocrystal shape and size on the temperature sensitivity in Raman thermometry, *Appl. Phys. Lett.* 103 (2013) 083107.
- [39] A.A. Balandin, S. Ghosh, W.Z. Bao, I. Calizo, D. Teweldebrhan, F. Miao, C.N. Lau, Superior thermal conductivity of single-layer graphene, *Nano Lett.* 8 (2008) 902–907.
- [40] Q. Li, C. Liu, X. Wang, S. Fan, Measuring the thermal conductivity of individual carbon nanotubes by the Raman shift method, *Nanotechnology* 20 (2009) 145702.
- [41] S. Ghosh, I. Calizo, D. Teweldebrhan, E.P. Pokatilov, D.L. Nika, A.A. Balandin, W. Bao, F. Miao, C.N. Lau, Extremely high thermal conductivity of graphene: prospects for thermal management applications in nanoelectronic circuits, *Appl. Phys. Lett.* 92 (2008) 151911.
- [42] M. Fujii, T. Nagareda, S. Hayashi, K. Yamamoto, Low-frequency Raman scattering from small silver particles embedded in  $SiO_2$  thin films, *Phys. Rev. B* 44 (1991) 6243–6248.
- [43] L. Saviot, B. Champagnon, E. Duval, A.I. Ekimov, I.A. Kudriavtsev, Size dependence of acoustic and optical vibrational modes of CdSe nanocrystals in glasses, *J. Non-Cryst. Solids* 197 (1996) 238–246.
- [44] A. Diéguez, A. Romano-Rodríguez, Nondestructive assessment of the grain size distribution of SnO nanoparticles by low-frequency Raman spectroscopy, *Appl. Phys. Lett.* 71 (1997) 1957–1959.
- [45] M. Ivanda, K. Furić, S. Musić, M. Ristić, M. Gotić, D. Ristić, A.M. Tonejc, I. Djerdj, M. Mattarelli, M. Montagna, F. Rossi, M. Ferrari, A. Chiasera, Y. Jestin, G.C. Righini, W. Kiefer, R.R. Gonçalves, Low wavenumber Raman scattering of nanoparticles and nanocomposite materials, *J. Raman Spectrosc.* 38 (2007) 647–659.
- [46] E. Duval, Far-infrared and Raman vibrational transitions of a solid sphere: selection rules, *Phys. Rev. B* 46 (1992) 5795–5797.
- [47] M. Montagna, R. Dusi, Raman scattering from small spherical particles, *Phys. Rev. B* 52 (1995) 10080–10089.
- [48] H. Lamb, On the vibrations of an elastic sphere, *Proc. Lond. Math. Soc.* 13 (1882) 189–212.
- [49] R. Shuker, W. Gammon, Raman-scattering selection-rule breaking and the density of states in amorphous materials, *Phys. Rev. Lett.* 25 (1970) 222–225.
- [50] A.J. Mork, E.M.Y. Lee, W.A. Tisdale, Temperature dependence of acoustic vibrations of CdSe and CdSe-CdS core-shell nanocrystals measured by low-frequency Raman spectroscopy, *Phys. Chem. Chem. Phys.* 18 (2016) 28797–28801.

- [51] H.K. Yadav, K. Sreenivas, R.S. Katiyar, V. Gupta, Softening behavior of acoustic phonon mode in ZnO nanoparticles: the effect of impurities and particle size variation with temperature, *J. Raman Spectrosc.* 42 (2011) 1620–1625.
- [52] U. Fano, Effects of configuration interaction on intensities and phase shifts, *Phys. Rev.* 124 (1961) 1866–1878.
- [53] W.-L. Zhang, H. Li, D. Xia, H.W. Liu, Y.-G. Shi, J.L. Luo, J. Hu, P. Richard, H. Ding, Observation of a Raman-active phonon with Fano line shape in the quasi-one-dimensional superconductor  $K_2Cr_3As_3$ , *Phys. Rev. B* 92 (2015) 060502.
- [54] P.B. Allen, Neutron spectroscopy of superconductors, *Phys. Rev. B* 6 (1972) 2577–2579.
- [55] J. Winter, H. Kuzmany, Landau damping and lifting of vibrational degeneracy in metallic potassium fulleride, *Phys. Rev. B* 53 (1996) 655–661.
- [56] Z.V. Popović, Z.D. Dohčević-Mitrović, N. Paunović, M. Radović, Evidence of charge delocalization in  $Ce_{1-x}Fe_x^{2+(3+)}O_{2-y}$  nanocrystals ( $x=0, 0.06, 0.12$ ), *Phys. Rev. B* 85 (2012) 014302.
- [57] D. Chen, Y.-L. Jia, T.-T. Zhang, Z. Fang, K. Jin, P. Richard, H. Ding, Raman study of electron-phonon coupling in thin films of the spinel oxide superconductor  $LiTi_2O_4$ , *Phys. Rev. B* 96 (2017) 094501.
- [58] N. Bonini, M. Lazzeri, N. Marzari, F. Mauri, Phonon Anharmonicities in graphite and graphene, *Phys. Rev. B* 99 (2007) 176802.
- [59] M. Lazzeri, S. Piscanec, F. Mauri, A.C. Ferrari, J. Robertson, Phonon linewidths and electron-phonon coupling in graphite and nanotubes, *Phys. Rev. Lett.* 73 (2006) 155426.
- [60] W. Yu, M. Han, K. Jiang, Z. Duan, Y. Li, Z. Hu, J. Chu, Enhanced Fröhlich interaction of semiconductor cuprous oxide films determined by temperature-dependent Raman scattering and spectral transmittance, *J. Raman Spectrosc.* 44 (2013) 142–146.
- [61] H.-M. Cheng, K.-F. Lin, H.-C. Hsu, C.-J. Lin, L.-J. Lin, W.-F. Hsieh, Enhanced resonant Raman scattering and electron-phonon coupling from self-assembled secondary ZnO nanoparticles, *J. Phys. Chem. B* 109 (2005) 18385–18390.
- [62] S. Seki, N. Kida, S. Kumakura, R. Shimano, Y. Tokura, Electromagnons in the spin collinear state of a triangular lattice antiferromagnet, *Phys. Rev. Lett.* 105 (2010) 097207.
- [63] D. Rogers, Y.J. Choi, E.C. Standard, T.D. Kang, K.H. Ahn, A. Dubroka, P. Marsik, C. Wang, C. Bernhard, S. Park, S.-W. Cheong, M. Kotelyanskii, A.A. Sirenko, Adjusted oscillator strength matching for hybrid magnetic and electric excitations in  $Dy_3Fe_5O_{12}$  garnet, *Phys. Rev. B* 83 (2011) 174407.
- [64] A.B. Sushkov, R. Valdés Aguilar, S. Park, S.-W. Cheong, H.D. Drew, Electromagnons in multiferroic  $YMn_2O_5$  and  $TbMn_2O_5$ , *Phys. Rev. Lett.* 98 (2007) 027202.
- [65] I. Kézsmárki, N. Kida, H. Murakawa, S. Bordács, Y. Onose, Y. Tokura, Enhanced directional dichroism of terahertz light in resonance with magnetic excitations of the multiferroic  $Ba_2CoGe_2O_7$  oxide compound, *Phys. Rev. Lett.* 106 (2011) 057403.
- [66] A. Pimenov, A.A. Mukhin, V.Y. Ivanov, V.D. Travkin, A.M. Balbashov, A. Loidl, Possible evidence for electromagnons in multiferroic manganites, *Nat. Phys.* 2 (2006) 97–100.
- [67] M. Cazayous, Y. Gallais, A. Sacuto, R. de Sousa, D. Lebeugle, D. Colson, Possible observation of cycloidal electromagnons in  $BiFeO_3$ , *Phys. Rev. Lett.* 101 (2008) 037601.
- [68] M.K. Singh, R.S. Katiyar, J.F. Scott, New magnetic phase transitions in  $BiFeO_3$ , *J. Phys. Condens. Matter* 20 (2008) 252203.
- [69] W. Azeem, S. Riaz, A. Bukhtiar, S.S. Hussain, Y. Xu, S. Naseem, Ferromagnetic ordering and electromagnons in microwave synthesized  $BiFeO_3$  thin films, *J. Magn. Magn Mater.* 475 (2019) 60–69.
- [70] R. De Sousa, J.E. Moore, Optical coupling to spin waves in the cycloidal multiferroic  $BiFeO_3$ , *Phys. Rev. B* 77 (2008) 012406.
- [71] S. Venugopalan, M. Dutta, A.K. Ramdas, J.P. Remeika, Magnetic and vibrational excitations in rare-earth orthoferrites: a Raman scattering study, *Phys. Rev. B* 31 (1985) 1490–1497.
- [72] X.K. Chen, J.C. Irwin, J.P. Franck, Evidence for a strong spin-phonon interaction in cupric oxide, *Phys. Rev. B* 52 (1995) R13130–R13133.

- [73] D.J. Lockwood, Spin-phonon interaction and mode softening in  $\text{NiF}_2$ , *Low Temp. Phys.* 28 (2002) 505–509.
- [74] X.-B. Chen, N.T.M. Hien, K. Han, J.C. Sur, N.H. Sung, B.K. Cho, I.-S. Yang, Raman studies of spin-phonon coupling in hexagonal  $\text{BaFe}_{12}\text{O}_{19}$ , *J. Appl. Phys.* 114 (2013) 013912.
- [75] E. Granado, A. García, J.A. Sanjurjo, C. Rettori, I. Torriani, F. Prado, R.D. Sánchez, A. Caneiro, S.B. Oseroff, Magnetic ordering effects in the Raman spectra of  $\text{La}_{1-x}\text{Mn}_{1-x}\text{O}_3$ , *Phys. Rev. B* 60 (1999) 11879–11882.
- [76] J. Laverdière, S. Jandl, A.A. Mukhin, I.V. Yu, V.G. Ivanov, M.N. Iliev, Spin-phonon coupling in orthorhombic  $\text{RMnO}_3$  (R=Pr, Nd, Sm, Eu, Gd, Tb, Dy, Ho, Y): a Raman Study, *Phys. Rev. B* 73 (2006) 214301.
- [77] R. Katoch, C.D. Sekhar, V. Adyam, J.F. Scott, R. Gupta, A. Garg, Spin phonon interactions and magnetodielectric effects in multiferroic  $\text{BiFeO}_3\text{--PbTiO}_3$ , *J. Phys. Condens. Matter* 28 (2016) 075901.
- [78] A. Jaiswal, R. Das, T. Maity, K. Vivekanand, S. Adyanthaya, P. Poddar, Temperature-dependent Raman and dielectric spectroscopy of  $\text{BiFeO}_3$  nanoparticles: signatures of spin-phonon and magnetoelectric coupling, *J. Phys. Chem. C* 114 (2010) 12432–12439.
- [79] C.-H. Hung, P.-H. Shih, F.-Y. Wu, W.-H. Li, S.Y. Wu, T.S. Chan, H.-S. Sheu, Spin-phonon coupling effects in antiferromagnetic  $\text{Cr}_2\text{O}_3$  nanoparticles, *J. Nanosci. Nanotechnol.* 10 (2010) 4596–4601.
- [80] M.O. Ramirez, M. Krishnamurthi, S. Denev, A. Kumar, S.-Y. Yang, Y.-H. Chu, E. Saiz, J. Seidel, A.P. Pyatakov, A. Bush, D. Viehland, J. Orenstein, R. Ramesh, V. Gopalan, Two-phonon coupling to the antiferromagnetic phase transition in multiferroic  $\text{BiFeO}_3$ , *Appl. Phys. Lett.* 92 (2008) 022511.

# *Transport properties of nanoscopic solids as probed by spectroscopic techniques*

Dejan M. Djokić<sup>1</sup>, Novica Paunović<sup>1</sup>, Bojan Stojadinović<sup>1</sup>,  
Dimitrije Stepanenko<sup>1</sup>, Saša Lazović<sup>2</sup>, Zorana Dohčević-Mitrović<sup>1</sup>

<sup>1</sup>Nanostructured Matter Laboratory, Institute of Physics Belgrade, University of Belgrade, Belgrade, Serbia; <sup>2</sup>Biomimetics Laboratory, Institute of Physics Belgrade, University of Belgrade, Belgrade, Serbia

## Chapter Outline

- 1. Introduction 9
- 2. Raman scattering 10
  - 2.1 Short introduction to Raman scattering technique 10
  - 2.2 Multiferroic BiFeO<sub>3</sub> nanoparticles 13
- 3. Infrared reflection 21
  - 3.1 Short introduction to infrared reflection technique 21
  - 3.2 Doped nanocrystalline CeO<sub>2</sub> 24
- 4. Electron spin resonance 26
  - 4.1 Short introduction to electron spin resonance technique 26
  - 4.2 Carbon nanotubes 30
- 5. Concluding remarks 32
- Acknowledgments 33
- References 34

## 1. Introduction

Nanoscale world is at the border between the quantum realm at the smaller dimensions and the classical one at larger. At the quantum side of this divide, systems under consideration consist of few particles and the properties of the sample often do not average into well-behaved quantities with deviations from the mean value much smaller than the mean value itself. So standard assumptions of both the classical physics and the standard statistics can break down within the nanoscale domain. This occurrence impacts the methods for probing the transport at the nanoscale.

Noncontact measurements of transport can offer distinct advantages. Macroscopic contacts necessary for the standard transport measurements often disturb the system since they are immensely larger than it. The structure of the contacts needs to impact the system as little as possible, requiring cooling to very low temperatures. Thermal noise introduced by contacts is hard to distinguish from the quantum noise that is an interesting property of the probed system.

Experiment is always performed on an object composed of nonidentical units and averaging of the properties does not automatically occur within the measurement apparatus. Moreover, the most interesting properties are often encoded into distribution of the results of measurements, and not exclusively in their mean values. Quantum side of the breakdown is somewhat different. The quantum transport theory deals with universality of the transport. In the quantum limit, as most transparently seen in the Landauer formula for conductivity, the whole variety of the transport behavior boils down to the number and transmitivities of transport channels. The variety of quantum behavior in transport appears due to macroscopic quantum phenomena or lies hidden in the variability of nominally identical nanoscale systems.

To probe the rich variety of transport phenomena at the nanoscale, it is preferable to look at the properties of conducting quasiparticles than to look at the integral characteristics of a collection of them. Quasiparticles are most easily accessed through spectroscopic techniques, like Raman spectroscopy, electron spin resonance (ESR), and infrared reflection (IRR) spectroscopy. Resonant nature of excitations and response detection in spectroscopy offer us a way to discriminate between constituents of the nanoscale system and look exclusively at the processes that are in resonance with the appropriate driving. Therefore the noncontact spectroscopic measurements give us an opportunity to see the nanoscale world in more detail.

This chapter is partitioned in three sections which are organized as follows. In the first section, we provide a short introduction to the Raman scattering technique followed with a review on an indirect finding of the two different variable range hopping (VRH) transport mechanisms based on the analysis of the temperature dependent electronic Raman background of nanocrystalline  $\text{BiFeO}_3$  [1]. The subsequent section tackles a summary on how both particle size decreased and Nd doping influence the Plasmon–phonon interaction and optical conductivity in  $\text{CeO}_{2-y}$  nanocrystals investigated by IRR spectroscopy [2]. Finally, in the third section, the main aspects of conduction ESR have been briefly introduced in which terms the temperature evolution and character of transport properties of single-walled carbon nanotubes have been elaborated [3].

## ***2. Raman scattering***

### ***2.1 Short introduction to Raman scattering technique***

In solid state spectroscopy, the inelastic scattering of photons by lattice vibrations (LVs) is known as Raman effect. The photon energy can be lost or gained in such processes, which

is accomplished by the phonon creation or annihilation, and termed in literature as Stokes or anti-Stokes Raman excitation, respectively. Brillouin Raman scattering (RS), however, stands for a particular case of RS that concerns the scattering by acoustic phonons of very low frequencies, unlike common Raman which involves optical phonons. The theory of Raman spectroscopy can be found elsewhere. Nevertheless, for a rather comprehensive elaboration the reader is further referred to seminal Mitra's work [4], some of which fragments we will rely on in what follows.

Following the first principles of electromagnetism, the incident electromagnetic field of the photons is coupled with the phonons via dipole moments that are induced by the phonon field. The electronic  $3 \times 3$  polarizability tensor  $\alpha_{mn}$  is modulated by the variation of the lattice due to the normal vibration of frequency  $\omega_p$  and can be expanded in terms of the time dependent atomic displacement components  $u_p = u_p(0)e^{i\omega_p t}$  as

$$\alpha_{mn} = \alpha_{mn}^{(0)} + \sum_p \alpha_{mn,p}^{(1)} u_p + \frac{1}{2} \sum_p \sum_q \alpha_{mn,pq}^{(2)} u_p u_q + \dots \quad (2.1)$$

where

$$\alpha_{mn,p}^{(1)} = \left( \frac{\partial \alpha_{mn}}{\partial u_p} \right)_{u_p=0}, \quad \alpha_{mn,pq}^{(2)} = \left( \frac{\partial^2 \alpha_{mn}}{\partial u_p \partial u_q} \right)_{u_p=0, u_q=0} \dots \quad (2.2)$$

If  $\vec{E}$  denotes the electric field of incident electromagnetic radiation with frequency  $\omega$ ,

$$\vec{E} = \vec{E}(0)e^{i\omega t}, \quad (2.3)$$

then the induced dipole moment can be written as

$$\vec{M} = \hat{\alpha} \vec{E}, \quad (2.4)$$

which ultimately yields induced dipole moment along  $p$  mode

$$\vec{M}_p = \hat{\alpha}^{(0)} \vec{E}_0 e^{i\omega t} + \hat{\alpha}^{(1)} \vec{E}_0 e^{i(\omega \pm \omega_p)t} u_p(0) + \hat{\alpha}^{(2)} \vec{E}_0 e^{i(\omega \pm 2\omega_p)t} u_p^2(0) + \dots \quad (2.5)$$

First term in Eq. (2.5) represents nothing but elastic Rayleigh scattering process. The energy of the electromagnetic radiation remains unchanged in this case. The derivative of the electronic polarizability in the second term in Eq. (2.5) gives rise to the first-order RS processes when incident photon  $(\hbar \vec{k}_1, \hbar\omega_1)$  is absorbed or created to create or destroy a phonon  $(\hbar \vec{k}, \hbar\omega)$ . The final photon, with both different wave vector and frequency  $(\hbar \vec{k}_2, \hbar\omega_2)$  from the incident one, gets emitted in such a way that the energy and the momentum are totally conserved. Reduced Planck's constant is denoted as  $\hbar$ .

In doped semiconductors and disordered metals, spectral recoil of light in RS consistently comprises a number of distinctive peaks generated by optically active phonons, as well as, an extended frequency continuum which is in direct relationship with electronic response [6]. This continuous spectral background originates from low-energy electronic excitations, which reflects the charge carrier scattering rate, and is familiarly known in literature as the Raman electronic background [1,7–11]. Falkovsky [7] was first to provide a theoretical foundation for the spectral profiles of Raman electronic background in “dirty” metals. The effects of electronic excitations in Raman are usually observed at low-energy scales and are attributed to scattering by phonons or impurities involving finite momentum transfers ( $k \neq 0$ ) as a result of the finite penetration depth of light in materials. Later on, Zawadowski and Cardona [8] proposed a Feynman diagrammatic approach to estimating the Kubo spectral response function within the scope of ladder approximation [12] at  $q \approx 0$ . Most importantly, these authors were first to recognize an intimately related link between the nonresonant electronic excitations seen in Raman with the carrier transport.

As with nonresonant RS electronic response, the related Feynman diagrams (see Fig. 2.1) are composed of wavy lines denoting photon propagators. Their initial and final (momentum, energy) are respectively  $(\hbar \vec{k}_1, \hbar \omega_1)$  and  $(\hbar \vec{k}_2, \hbar \omega_2)$ . An electron-hole pair of (momentum:  $\vec{k} = \vec{k}_1 - \vec{k}_2$ , energy:  $\omega = \omega_1 - \omega_2$ ), scattered by phonons and/or impurities, become generated by the incoming photon propagator. Phonon propagator, given in dashed line (Fig. 2.1), can be excited by the electron/hole inside a pair and is further captured by its counterpart (hole/electron), as is enforced by the ladder approximation. At last, upon summing up all the dominating ladder-like diagrams, Raman differential cross section due to the purely electronic response [9,11], reads as

$$\frac{d^2\sigma}{d\omega d\Omega} \propto \frac{1}{1 - \exp(-\hbar\omega/k_B T)} \times \frac{\omega\tau}{1 + (\omega\tau)^2}. \quad (2.6)$$

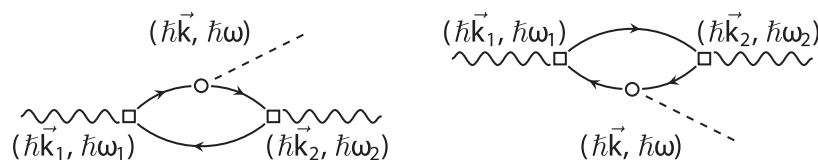


**Figure 2.1**

Raman scattering of light (*wavy lines*) due to phonons (*dashed lines*). Electron-hole formations (*solid lines*) represented via loops in the Feynman diagrams of third order (first order Raman scattering). Processes involving electron and hole contributions are given in left and right diagrams, respectively. Vertex  $\square$  represents electron-photon interaction, while vertex  $\circ$  represents electron-phonon interaction as is given in Ref. [5]. *The drawing is adapted from D.M. Djokić, B.*

*Stojadinović, D. Stepanenko, Z. Dohčević-Mitrović, Probing charge carrier transport regimes in BiFeO<sub>3</sub> nanoparticles by Raman spectroscopy, Scr. Mater. 181 (2020) 6–9. <https://doi.org/10.1016/j.scriptamat.2020.02.008>.*



At a particular value of the effective scattering rate,  $1/\tau$ , the proportionality factor in Eq. (2.6) is a function of different variables depending on the type of the experimental setup [10]. The temperature-dependent Bose-Einstein factor and expression resembling Drude function are respectively given as the second and third term in the product of Eq. (2.6), while  $1/\tau$  involves two terms in the sum as follows

$$1/\tau = 1/\tau_0 + Dq^2. \quad (2.7)$$

$1/\tau_0$  stands for the charge carrier scattering rate due to phonons/impurities in  $q \rightarrow 0$  limit, which is concerned with nothing but bulk channels. The second term ( $Dq^2$ ), however, gives rise to the effects of processes nonconserving momenta, very often pronounced in nanocrystals [1]. It is safe to neglect the bulk term ( $1/\tau_0$ ) if there is no experimental evidence for the electronic Raman background in the case of bulk materials.  $D$  is the diffusion constant which is, based on the Einstein relation, related to electric conductivity  $\sigma$  in the following manner

$$D = \sigma / (g(\epsilon_F) e^2), \quad (2.8)$$

where  $e = 1.6 \times 10^{-19}$  C. The average value of the electronic density states close to the Fermi level [9] is denoted with  $g(\epsilon_F)$ .

## 2.2 Multiferroic BiFeO<sub>3</sub> nanoparticles

Crystalline bismuth ferrite stands for a multiferroic material increasingly attracting the attention among the researchers and is also one of few materials to provide both ferroelectric ( $T_C \approx 1100$  K) and antiferromagnetic ( $T_N \approx 643$  K) properties at room temperature [13] and even higher. It is important to know that BiFeO<sub>3</sub> has proven undemanding to obtain in ambient conditions. BiFeO<sub>3</sub> is classed as rhombohedrally distorted ABO<sub>3</sub> perovskite structure (space group  $R3c$ ) with lattice parameter  $a_{\text{rh}} = 3.965$  Å, a rhombohedral angle  $\alpha_{\text{rh}}$  of 89.30–89.48°, and ferroelectric polarization along  $[111]_{\text{pseudocubic}}$  direction at room temperature [14]. Primitive unit cell consists of two unit formulas and contains 10 atoms. This structure can be represented as two distorted perovskite unit cells, connected along the main pseudocubic diagonal  $[111]$  to form a rhombohedral unit cell, as is given in Fig. 2.2A. Bi<sup>3+</sup> ions are situated at A lattice sites and are surrounded by 12 oxygen atoms. On the other hand side, Fe<sup>3+</sup> ions are located at B lattice sites, and they are surrounded by six oxygen atoms with which it forms a FeO<sub>6</sub> octahedron. In this configuration, Bi<sup>3+</sup> and Fe<sup>3+</sup> ions are shifted along  $[111]$  direction, and two oxygen octahedrons are rotated around  $[111]$  direction in the opposite directions by 14° that can be seen from the position of the green octahedrons in Fig. 2.2B. This means that the Fe-O-Fe angle deviates from 180° to amount nearly 154–156° [16,17]. The unit cell can also be described in a hexagonal frame of reference, where the hexagonal

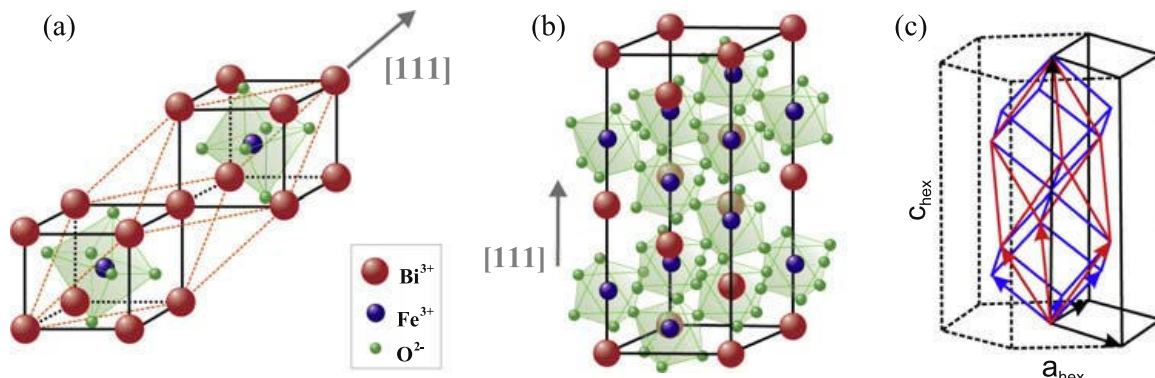


**Figure 2.2**

Schematic representation of (A) rhombohedral structure framed by orange dashed lines, (B) hexagonal perovskite structure of  $\text{BiFeO}_3$  with  $[111]$  ferroelectric polarization direction given in gray arrow, and (C) hexagonal cell (black), rhombohedral (red), and pseudocubic (blue) unit cell with corresponding unit vectors drawn in arrows. The figure is to a rather large extent reworked from J.-G. Park, M.D. Le, J. Jeong, S. Lee, *Structure and spin dynamics of multiferroic  $\text{BiFeO}_3$* , *J. Phys. Condens. Mat.* 26 (2014) 433202. <https://doi.org/10.1088/0953-8984/26/43/433202>.

$c$ -axis is aligned parallel to the diagonals of the perovskite cube. In other terms,  $[001]_{\text{hexagonal}} \parallel [111]_{\text{pseudocubic}}$ . The corresponding hexagonal lattice parameters (Fig. 2.2C) are  $a_{\text{hex}} = 5.579 \text{ \AA}$  and  $c_{\text{hex}} = 13.869 \text{ \AA}$  [14,18].

Bulk  $\text{BiFeO}_3$  is a semiconductor with literature values of the bandgap determined by optical measurements at room temperature in the range from 2.1 to 2.8 eV. Several authors claim that  $\text{BiFeO}_3$  has a direct bandgap transition at about 2.1–2.8 eV [19–22]. There are, however, published studies in which it has been shown that  $\text{BiFeO}_3$  has an indirect bandgap transition of about 0.4–1.0 eV, quite smaller as compared to the values obtained for the direct transition [23]. Density functional theory calculations [24,25] have corroborated an indirect energy transition of about 2.1 eV, while in the room temperature absorption spectra recorded on  $\text{BiFeO}_3$  thin film, the transition at approximately 2.17 eV has been observed [26].

Finally, according to Catalan and some of the references therein [16], based on two-probe DC resistivity measurements carried out on high-quality bulk samples of  $\text{BiFeO}_3$ , the log resistivity value undergoes two slopes in Arrhenius law with increasing temperature. Actually, it has been found that the activation energy of the charge carriers decreases from nearly 1.3 down to nearly 0.6 eV as the material is heated above  $T_N$  with the anomaly around it. However, one does not expect such type of conducting behavior when the scale of the crystal moves down to several nanometers. Indeed, in the case of defective nanoparticles with a core/shell structure [1], the nanoparticle shell may have metallic and/or semiconducting features, while the nanoparticle core prominently features insulating properties. This casts a shadow over models that are commonly applied in pristine bulk materials to fit the resistivity data in systems with disorder and/or decreased dimensions.

At a scale ranging down to nanometers, BiFeO<sub>3</sub> has proven very prospective for a potential use in satellite communications, electrically accessed magnetic memory, commercial applications for photovoltaics and alternative sensors [16]. Most essentially, the electric resistance of BiFeO<sub>3</sub> is found to be a key parameter that should comply with the prime industrial requirements. Accomplishing high-electric conductivity value in this nanoscopic compound from its powders is one of the major assets and is perceived as a very promising in development of the novelty. Moreover, it proves quite demanding to identify the charge carrier transport, as well as, to distill electric conductivity value using the contact probes themselves invasively [27,28]. On the other hand, RS tool is widely known as a local and highly informative experimental probe capable of assessing the origin and dynamics of charge carriers in conducting materials. This makes Raman technique a reliable, yet noninvasive, means for investigating the transport properties of materials that are treated with utmost delicacy.

Fairly recent temperature-dependent RS study, carried out on the multiferroic BiFeO<sub>3</sub> nanoparticles of high purity and relied on the temperature evolution electronic Raman background [1], has explored an exciting prospect of extracting the relevant piece of information about the electric transport in this nanoscopic compound.  $\mu$ -RS measurements were recorded over the temperature range of 80–723 K, while the related spectra were gathered at the backscattering arrangement with solid state 532 nm Nd:YAG laser as excitation at sub-mW laser powers on the sample itself. There were more than 13 optical phonon modes (symmetry:  $A_1$  and  $E$ ) detected in the experiment, while the spectra were decomposed with Lorentzian lineshape profiles, as is presented in Fig. 2.3 at four different temperatures. The entire number, together with frequency positions, of the optically active phonon modes of BiFeO<sub>3</sub> nanoparticles detected with Raman were found exactly the same with those observed in temperature-dependent RS spectra undertaken for bulk crystalline BiFeO<sub>3</sub> [29]. However, the authors [1] properly commented on the emerged splittings of a number of few polar LO+TO phonon modes, which naturally appear in the case of BiFeO<sub>3</sub> nanoparticles [30,31]. As with bulk, the prediction based on the factor group analysis turns out to be in accordance with the experiment implying 13 ( $4A_1 + 9E$ ) optically active modes in phonon Raman spectra [32].

In contrast to Raman spectra recorded for on bulk BiFeO<sub>3</sub>, Raman active optical modes pertinent to BiFeO<sub>3</sub> nanoparticles were evidenced to seat on quite a broad spectroscopic profile (Fig. 2.3 shaded in light gray). Such a spectroscopic feature has a pronounced temperature dependence and is familiarly known as Raman electronic background. In literature, indeed there are spectroscopic backgrounds akin to one studied in Ref. [1] such as nonresonant Raman continuous profile observed in metal-oxide thin films [33]. However, the related profile is quite shapeless, moreover with strong intensity, and is ascribed to entirely electronic RS recoil independent of bands due to the phonons. This Raman electronic background emerges as a result of the surface roughness at atomic scale.

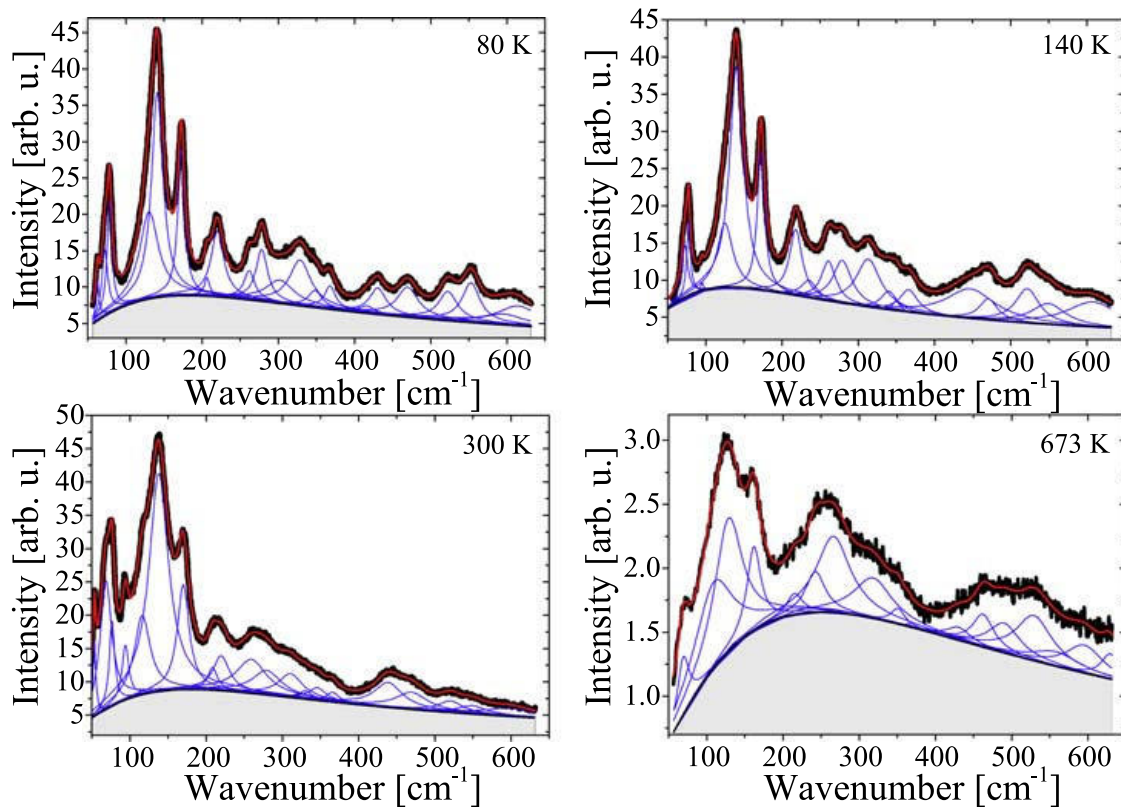


**Figure 2.3**

Raman scattering spectra given for four representative temperatures (data points presented in black). The spectra are composed of a continuous electronic background (shaded in light gray) and Lorentzian phonon peaks (lines in blue). The overall fitting line is drawn with red line. The figure is adopted from the published work D.M. Djokić, B. Stojadinović, D. Stepanenko, Z. Dohčević-Mitrović, *Probing charge carrier transport regimes in BiFeO<sub>3</sub> nanoparticles by Raman spectroscopy*, *Scr. Mater.* 181 (2020) 6–9. <https://doi.org/10.1016/j.scriptamat.2020.02.008>.

In addition, it has been reported that, in extremely small metallic particles [34] and metallic thin film islands with adsorbents [35], RS due to the particle-hole pair excitations brings about the emergence of the phononless continuous electronic background. This can be explained in terms of the momentum conservation violation generated in the presence of the electronic states at surface. Furthermore, even in the bulk hole-doped manganese perovskites, the broad electronic Raman response associated with the scattering by conduction electrons has been determined to cause a drastic change at the phase transition, as shown by Liu et al. [36]. The evolution of the effects of electron correlations in this compound could be assessed computably with temperature.

The authors of Ref. [1] have fittingly cast the surface states situated at particle boundaries in the role of localization centers via which the conduction can run efficiently. In terms of energy, these states are located near the vicinity of the Fermi level and they are, in general, unequally distributed to evolve with both spatial and energy gap between them. Therefore, the charge carrier conduction mechanism in which the hopping energy varies

with the hopping range can be safely modeled for description of the transport over an extended temperature range in disordered semiconductors and/or amorphous solids, such as nanoscaled materials. Commonly, exceptionally high-electric resistivity values are observed in such systems. As such, these values serve as a definite fingerprint to rule out any conventional metallic/semiconducting type of conductivity mechanism intrinsic to (semi)conductors. VRH mechanism, nonetheless [37], stands for a rather viable transport mechanism in nanoparticles with no other alternative acceptable, as was reported in Ref. [1] for BiFeO<sub>3</sub> nanoparticles. Two different types of VRH charge carrier transport mechanisms in 3D have been probed in a contactless way using temperature-dependent Raman spectroscopy, and it has been evidenced that these two are affected by different degrees of the electron correlation strengths on the opposite sides of the antiferromagnetic phase transition. Below the transition temperature, the transport undergoes the mechanism explained by Efros and Shklovskii [38], whereas at high temperatures, the charge carrier transport adheres to the traditional Mott VRH theory [37].

Here we provide a brief account of the Mott and Efros–Shklovskii laws based on a concise analysis from a seminal paper by Arginskaya and Kozub [39]. The central focus of this study was on a considerable diversity of theoretical results emerging from calculations for the exponential prefactors in various VRH expressions, as well as, the crossover from VRH conductivity of Mott type in which the density of electronic states at Fermi level is  $g(\varepsilon \approx \varepsilon_F) = \text{const}$  toward VRH conductivity running via states separated by a Coulomb gap when  $g(\varepsilon \approx \varepsilon_F) \propto \varepsilon^2$ . Aharony et al. [40] have made an attempt to obtain the universal analytic expression for the temperature dependence of conductivity,  $\sigma(T)$ , in the crossover region from Mott to Efros–Shklovskii law. In general terms, temperature dependence of the VRH conductivity  $\sigma(T)$  can be written down as

$$\sigma(T) = \sigma_n \exp\left(-\frac{T_n}{T}\right)^n, \quad (2.9)$$

where  $n$  might take on 1/4 or 1/2 in 3D with respect to the law chosen, Mott's or Efros–Shklovskii's. Constant factors  $\sigma_n$  and  $T_n$  depend on the preferred of the two models. However, the common feature of most of the relevant studies in the field of VRH boils down to simplistic approaches in estimating the exponential prefactor  $\sigma_n$ . As a traditional rule,  $\sigma_n$  is generally assumed to have no temperature dependence.

Factors  $\sigma_n$  and  $T_n$ , which are given in Eq. (2.9), can be computed straightforwardly by optimizing the correlation linking the energy and spatial separation between the lattice sites. Once an electric field is applied, hopping in the direction of the field is rather preferred at different probabilities with respect to both distance and energy separation. As with the 3D free electron case, in original Mott paper [37], it was in a simplified way presented that the hopping energy is inversely proportional to the cube of the hopping distance, while the hopping frequency  $\nu$  for a given temperature  $T$  was found to depend on

two following parameters:  $r$  as the spatial distance between the sites in units of localization length  $\xi$  and  $W$  as their typical hopping energy separation. Namely,

$$\nu = \nu_0 \exp\left(-\frac{2r}{\xi} - \frac{W}{k_B T}\right), \quad (2.10)$$

where  $\nu \equiv \nu_0$  for both  $r = 0$  and  $W = 0$ , whereas  $k_B = 1.38 \times 10^{-23}$  J/K stands for Boltzmann constant. The hopping frequency characterizes the relative number of directed charge carrier hops due to the electric field. Indeed, in noncrystalline systems, the variables  $r$  and  $W$  are not randomly independent so that one can be combined into a single parameter by minimizing the total exponent in (Eq. 2.10). In the actual fact, the hopping from one site to another with a lower energy/distance occurs at high rate. However, reaching both low energy/distance sites at the same time remains utterly impossible. The same reasoning applies for the large energy/distance sites that altogether justifies the application of variation method and thence the term ‘‘variable’’ in VRH.

Variable hopping processes translate a charge carrier by a range  $r$  within a time  $\sim 1/\nu$ , but at a preferred  $W$  value that maximizes the electric current via hopping. This proportionality squarely leads to the VRH expression for conductivity which is given in (Eq. 2.9). Yet, to relate  $r$  with  $W$  or vice versa, one has to further assume that most of the mobile carriers come from a narrow energy window near the Fermi level of width  $\sim k_B T$ . In such a way, the carrier density  $n_c$  of spin  $S = 1/2$  which as the other factor prominently figures in the expression for the conductivity and can be computed by integration as

$$n_c = 2 \int_{\epsilon_F}^{\epsilon_F + k_B T} g(\epsilon) d\epsilon, \quad (2.11)$$

where  $g(\epsilon)$  measures the total number of states ( $dN$ ) per both energy ( $dE$ ) and volume unit ( $V$ ), each of which is double degenerated ( $2S + 1 = 2$ ).

One must emphasize that the wise choice of  $g(\epsilon)$  leads to the correct expression for the exponent  $T_n$ , which differs by switching from 3D Mott ( $n = 1/4$ ) to Efros–Shklovskii regime ( $n = 1/2$ ). Experimental measurements in disordered systems do reveal that the electron density of states (DOSs) may strongly vary in the vicinity of Fermi level, and it seems reasonable to suggest that the theoretical concept of uniform DOSs near the Fermi level is certainly insufficient to describe conduction mechanisms which account for the Coulomb gap, as there is a jump in the electron DOSs due to Coulomb interactions between localized states. In general, one can write down

$$k_B T_n = \begin{cases} c_p / (g(\epsilon_F) \xi^3), & \text{for } n = 1/4 \\ e^2 / (4\pi\epsilon_0 \epsilon_r \xi), & \text{for } n = 1/2 \end{cases} \quad (2.12)$$

where  $k_B = 1.38 \times 10^{-23}$  J/K and  $\epsilon_0 = 8.85 \times 10^{-12}$  F/m, while  $\xi$  stands for the localization length of electron wave function of the surface states.  $c_p$  represents the percolation constant varying from 5 to 20.  $\epsilon_r$  corresponds to the relative permittivity constant. Nevertheless, even when the DOSs is not constant, the 3D Mott VRH conductivity pattern is fully recovered if presented like Eq. (2.9), but is rather referred to as the 3D Efros–Shklovskii VRH [38] when  $n$  is, in particular, equal to 1/2. In Ref. [41], a few temperature dependencies of the hopping conductivity, which come under exponent 1/4 or 1/2, are presented and the reader is further redirected to this reference to properly infer the validity of use of VRH at high temperatures in disordered materials.

Nanoscaled BiFeO<sub>3</sub> puts itself forward as a suitable candidate for exploring the crossover from 1/2 to 1/4 exponent VRH conductivity as demonstrated in Ref. [1] based on the Raman spectra. More interesting is the fact that crystalline BiFeO<sub>3</sub> nanoparticles do not only undergo a crossover but even a pronounced phase transition at  $\sim 640$  K below which Coulomb correlations take place to form the antiferromagnetic ordering. Above the transition temperature, however, these correlations become overwhelmed by the temperature fluctuations through the concrete manifestation of the metallic-like paramagnetic state.

There is a presence of localized surface states occupying the energies near the Fermi level in the BiFeO<sub>3</sub> nanomaterial. These states through a mediation back the VRH transport even over a broad range of temperature. Temperature variations of  $\ln(1/\tau)$ , which is proportional to  $\ln(\sigma)$  based on the Einstein relation from Eq. (2.8) are linearized against  $T^{-n}$  in Fig. 2.4A with  $n = 1/2$  and Fig. 2.4B with  $n = 1/4$ , in the strongly correlated ( $T < T_N$ ) and paramagnetic phase ( $T > T_N$ ), respectively. Relying on the calculation for  $\epsilon_r \approx 28$  from the impedance dielectric spectroscopy of BiFeO<sub>3</sub> nanoparticles [42] and following (12) one can find that  $\xi \approx 7$  nm, while the DOSs  $g(\epsilon_F)$  in the high-temperature phase nearly amounts  $2.1 \times 10^{18}$  localized states per (eV  $\times$  cm<sup>3</sup>). The result  $\xi \approx 7$  nm is physically meaningful since  $\xi < \langle \ell \rangle$ , where the average particle size  $\langle \ell \rangle \approx 66$  nm has been computed from the Gaussian particle size distribution recorded by Scanning Electron Microscopy at room temperature on BiFeO<sub>3</sub> (Fig. 2.4C and D). Finally,  $\rho = 1/\sigma \approx 4\pi^2\tau/(\langle \ell \rangle^2 e^2 g(\epsilon_F)) \approx 350$  mΩcm, which stands for an extraordinarily high value that is not commonly encountered in conventional metals. This value goes beyond the maximum resistivity value ( $\sim 1$  mΩcm) limited by the Mott-Ioffe-Regel criterion [43,44], which categorizes crystalline BiFeO<sub>3</sub> nanoparticles into a family of bad conductors and ultimately suggests that the conduction bands are vanishing. This eliminates any possibility for the fixed thermally activated transport generic to intrinsic semiconductors to dominate over 3D VRH.

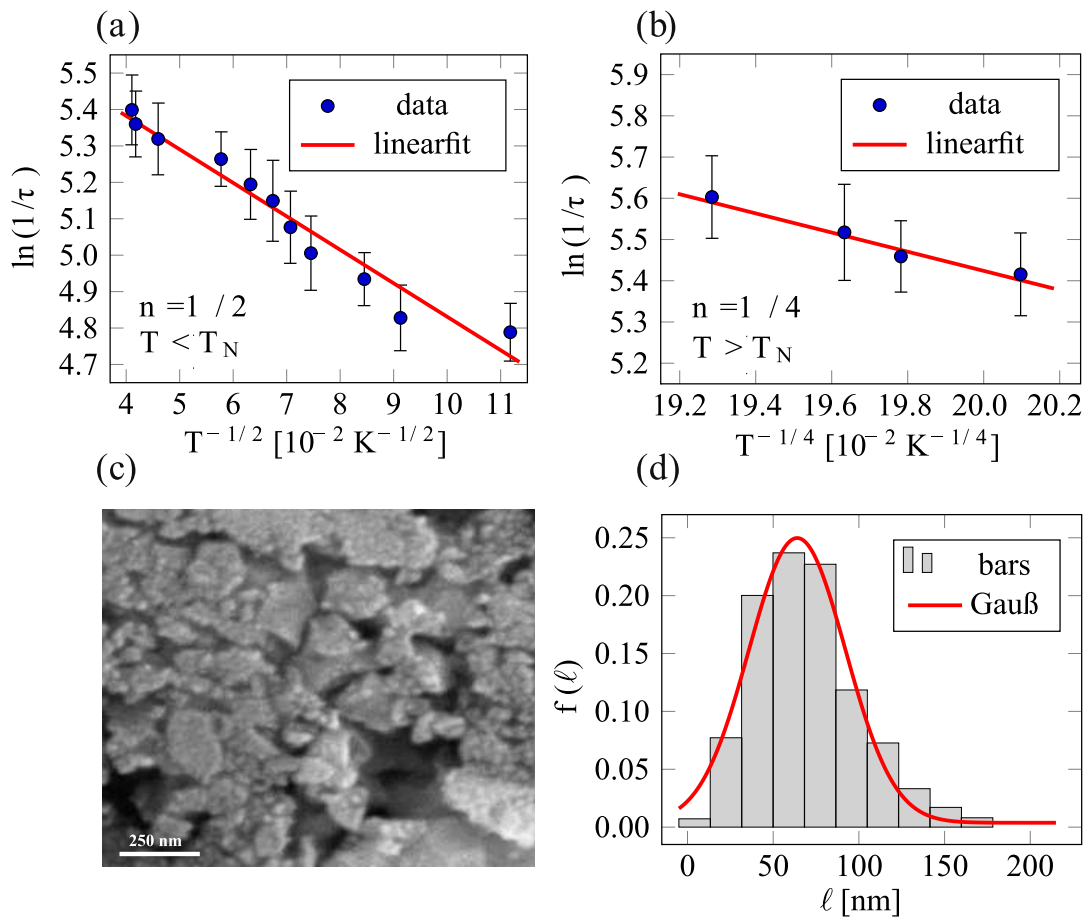


**Figure 2.4**

The dependence ( $T^{-n}$ ) versus ( $\ln(1/\tau)$ ) in both paramagnetic phase (subfigure (A),  $n = 1/2$ ) and antiferromagnetic phase (subfigure (B),  $n = 1/4$ ) with the linear fitting curves given in red.

The surface morphology of the nanocrystalline  $\text{BiFeO}_3$  particles made with TESCAN SM-300 (subfigure (C)) and the corresponding histogram of the distribution of the particle size given in gray, fitted by the Gauß distribution (red line), where  $(64 \pm 2)$  nm is mean value and  $(28 \pm 2)$  nm is standard deviation (subfigure (D)). The frequency of occurrence is labeled as  $f(\ell)$ . *The entire figure is taken from D.M. Djokić, B. Stojadinović, D. Stepanenko, Z. Dohčević-Mitrović, Probing charge carrier transport regimes in  $\text{BiFeO}_3$  nanoparticles by Raman spectroscopy, Scr. Mater. 181 (2020) 6–9.*

<https://doi.org/10.1016/j.scriptamat.2020.02.008>.

In certain disordered semiconductors, Ioffe and Regel [45], as well as Mott [46], have altogether realized that conduction states pertinent to such systems fail to survive due to the indefinite reduction in free mean path of carriers that scatters by. The key argument is that it can never become shorter than the typical interatomic spacing. In this case, the concept of carrier velocity cannot be properly formulated, and the entire coherent quasiparticle motion is lost. The notion of a minimum metallic conductivity is actually in accordance with a minimum mean free path.



Generally, the choice of 3D VRH ought to be provisionally accepted as an assumption. In the case of BiFeO<sub>3</sub> nanoparticles, the existence of the Mott VRH mechanism has already been deduced from the DC/AC measurements. These results are presented in Ref. [27]. Furthermore, the assumption about the validity of VRH is substantiated by the fact that the estimated resistivity value ultimately exceeds the Mott-Ioffe-Regel maximum ( $350 \text{ m}\Omega\text{cm} \gg 1 \text{ m}\Omega\text{cm}$ ). This implies that the conduction band energy sector tends to fade away leaving no room for the fixed thermally activated transport to prevail, which typically requires a markedly high density of conduction band states. Therefore, the BiFeO<sub>3</sub> nanoparticles are safe to be termed as bad conductors that retain metallic behavior, through qualitative features such as temperature evolution. Quantitatively, however, the bad conductors very much resemble the electric insulators as was observed in Ref. [1]. Specifically, the BiFeO<sub>3</sub> nanoparticle shell exhibits metallic behavior whereas the core insulator one, which is a case in defective nanoparticles with a core/shell structure.

### **3. Infrared reflection**

#### **3.1 Short introduction to infrared reflection technique**

Infrared solid state spectroscopy stands for one of the most powerful and versatile techniques meant for optically probing a diverse family of materials in a contactless manner. The IRR response can assume either a purely electronic or a purely LV character. The two cases have distinctly different approaches to the quantitative treatment of the interaction processes between the radiation field and matter. The latter has conclusively proven powerful for analyzing propagating vibrations with which crystal structures can be revealed in ionic crystals and polar semiconductors. This analytical probe is highly useful even for systems poor in the degree of crystallinity, which is oftentimes encountered in nanoscopic matter.

In the long-wave limit ( $q \approx 0$ ), optically active vibrations of an ionic bipartite lattice encapsulate the motion of one type of atoms relative to that of the other sublattice, yet both in spatial phase. The natural concomitants of such motions comprise strong electric dipoles of the material that can, accordingly, be directly coupled with the external electric field at a given polarization angle of the incident electromagnetic radiation. The theory of the IRR response originating from the interaction between the radiation field and the matter is purely phenomenological and can be found elsewhere [4,47,48], based on Maxwell's and the macroscopic equations describing the vibrations in a polar material. The reflective IRR spectroscopic recoil begins with a singularity in the dielectric function observed at the transverse optical (TO) frequency of the polar phonon mode. The singularity occurs as the radiation field of the incident electromagnetic wave couples with the TO phonon mode. Coulombic force effects in the polar crystal shift the LO mode to higher energies in contrast to the TO mode. The TO mode has a complex pole of the

complex dielectric response function  $\tilde{\varepsilon}(\omega)$ , whereas the LO mode is associated with a complex zero of  $\tilde{\varepsilon}(\omega)$ . Consequently, the incident infrared electromagnetic waves at frequencies over the so-called *reststrahlen* TO-LO window are dispersed in such a way that they fail to propagate through the condensed medium, but undergo reflection. In an ideal polar crystal with undamped oscillators, the frequency selective reflectivity amounts exactly 100%, but the reality is rather followed with the oscillator damping. Formally, the reflectivity is given by the Fresnel formula

$$R(\omega) = \left| \frac{\tilde{n}(\omega) - 1}{\tilde{n}(\omega) + 1} \right|^2 = \frac{(n(\omega) - 1)^2 + \kappa^2(\omega)}{(n(\omega) + 1)^2 + \kappa^2(\omega)}, \quad (2.13)$$

where  $R(\omega)$  is the frequency-dependent fraction of light intensity reflected. Complex frequency dependent index of refraction,  $\tilde{n}(\omega)$ , is related to the complex dielectric response as

$$\tilde{n}(\omega) = n(\omega) - i\kappa(\omega) = \sqrt{\tilde{\varepsilon}(\omega)}. \quad (2.14)$$

The frequency dependent real part,  $n(\omega)$ , and imaginary part,  $\kappa(\omega)$  as the extinction coefficient, of the complex refractive index  $\tilde{n}(\omega)$  satisfy the following relationships

$$\varepsilon_1(\omega) = n(\omega)^2 - \kappa(\omega)^2 \quad \text{and} \quad \varepsilon_2(\omega) = 2n(\omega)\kappa(\omega), \quad (2.15)$$

where finally

$$\tilde{\varepsilon}(\omega) \equiv \varepsilon_1(\omega) + i\varepsilon_2(\omega). \quad (2.16)$$

For this reason, it is of uppermost importance to model, as well as, parametrize  $\tilde{n}\varepsilon(\omega)$  that properly describe the system probed by the IRR technique.

IRR signal of poorly conductive ionic crystals with large splitting between TO and LO frequencies is commonly fitted with a complex dielectric function given by the following expression

$$\tilde{\varepsilon}(\omega) = \varepsilon_\infty \prod_j \frac{\omega_{\text{LO}j}^2 - \omega^2 + i\omega\gamma_{\text{LO}j}}{\omega_{\text{TO}j}^2 - \omega^2 + i\omega\gamma_{\text{TO}j}}, \quad (2.17)$$

where  $\omega_{\text{LO}j}$  and  $\omega_{\text{TO}j}$  are longitudinal and transverse frequencies of the  $j$ -th oscillator, respectively, while  $\gamma_{\text{TO}j}$  and  $\gamma_{\text{LO}j}$  are their energy dampings, and  $\varepsilon_\infty$  corresponds to the high-frequency dielectric constant ( $\omega \rightarrow \infty$ ). This model presents four tunable parameters for each TO/LO mode and is employed for description of purely phononic spectra. The model is familiarly known as the LV model, or habitually, four-parameter factorized form of the dielectric function. Its major disadvantage consists in the fact that it considers no contribution from the itinerant electronic excitations, neither single particle nor collective [49].

However, a great deal of semiconductors has a sizable portion of itinerant charge carriers. Accordingly, the full description of the infrared optical reflectivity data of such materials has to allow for both phonon and electronically collective (plasmon) excitations. The cohabitation between the phonons and plasmons brings inexorably about a somewhat pronounced interaction between the plasmons and LO phonons. This effect becomes the most striking if the plasma frequency  $\omega_P$  lies situated close to the LO phonon energy. In this case, the complex dielectric function [50] can be factorized to read as follows

$$\tilde{\varepsilon}(\omega) = \varepsilon_\infty \frac{\prod_{j=1}^{m+n} (\omega^2 + i\omega\gamma_{LOj} - \omega_{LOj}^2)}{\omega^m \prod_{j=1}^m (\omega + i\gamma_{Pj}) \prod_{j=1}^n (\omega^2 + i\omega\gamma_{TOj} - \omega_{TOj}^2)}, \quad (2.18)$$

where  $\omega_{TOj}$  and  $\gamma_{TOj}$  are frequencies and damping of the TO modes, respectively.  $\gamma_P$  represents the plasma damping rate. The equation directly expresses the coupled plasmon-LO phonon frequencies  $\omega_{LOj}$  and damping rates  $\gamma_{LOj}$ . This model is in literature termed as the coupled plasmon-phonon (CPP) model.

In conducting oxides [48], on the other hand side, the Drude model can be employed with no coupling for fitting the infrared reflectivity spectra. The plasmon contribution to the complex dielectric function is expressed through the Drude term so that  $\tilde{\varepsilon}(\omega)$  is composed of two additive terms in the following manner

$$\tilde{\varepsilon}(\omega) = \varepsilon_\infty \left( \prod_j \frac{\omega_{LOj}^2 - \omega^2 + i\omega\gamma_{LOj}}{\omega_{TOj}^2 - \omega^2 + i\omega\gamma_{TOj}} - \frac{\omega_P^2}{\omega(\omega - i\gamma_P)} \right). \quad (2.19)$$

The first product term is concerned with the pure phonon contribution, while the second term represents the contributions originating from the collective electronic excitations—plasmons. The  $\omega_{(TO/LO)j}$  and  $\gamma_{(TO/LO)j}$  are (TO/LO) frequencies and the related damping rates of the decoupled phonon modes. The  $\omega_P$  and  $\gamma_P$  are the plasma frequency and its damping rate. This model brings us a material advantage in decoupling the phonon from the plasmon contributions, and is called the decoupled plasmon-phonon (DPP) model. Besides the aforementioned “classical” Drude term, sometimes the so-called Double-damped Drude term is used, as is given in

$$\tilde{\varepsilon}(\omega) = \varepsilon_\infty \left( \prod_j \frac{\omega_{LOj}^2 - \omega^2 + i\omega\gamma_{LOj}}{\omega_{TOj}^2 - \omega^2 + i\omega\gamma_{TOj}} - \frac{\omega_P^2 + i(\gamma_P - \gamma_0)\omega}{\omega(\omega - i\gamma_0)} \right). \quad (2.20)$$

The difference between the dynamic damping ( $\gamma_P$ ) at plasma frequency and the static damping ( $\gamma_0$ ) at zero frequency represents particular distinctiveness of this model.

The second term in the additive form of  $\tilde{\varepsilon}(\omega)$  turns into the classical Drude term once

$\gamma_P = \gamma_0$ . The use of this model, which is also called DPP, provides more flexibility. In fact, a rather precise description of the parametrized complex dielectric function is offered by the model in numerical fittings based on it.

As with nanomaterials, the related IRR spectra can be properly analyzed using the Bruggeman effective medium approximation [51]. The basic Bruggeman model includes the influence of porosity as

$$\left( \frac{\tilde{\epsilon}(\omega) - \tilde{\epsilon}_{\text{eff}}(\omega)}{\tilde{\epsilon}(\omega) + 2\tilde{\epsilon}_{\text{eff}}(\omega)} \right) \tilde{f} + \left( \frac{1 - \tilde{\epsilon}_{\text{eff}}(\omega)}{1 + 2\tilde{\epsilon}_{\text{eff}}(\omega)} \right) (1 - \tilde{f}) = 0. \quad (2.21)$$

A decrease of the powder volume fraction as compared to the ambient air leads to a decrease in the reflectivity values, and thence the IRR features may become significantly broadened if there is a greater air fraction in the powder. For the binary material with a great degree of inhomogeneity, constituted of the material  $\tilde{\epsilon}(\omega)$  and air ( $\epsilon_{\text{air}} = 1$ ) with the volume fractions  $\tilde{f}$  and  $1 - \tilde{f}$ , respectively, the empirical relation for the complex effective dielectric function  $\tilde{\epsilon}_{\text{eff}}(\omega)$  must obey the above-written equation.

### 3.2 Doped nanocrystalline CeO<sub>2</sub>

As one of the most stable oxide of cerium, cerium dioxide CeO<sub>2</sub> is considered to be highly important functional material with outstanding applications in many various fields. It crystallizes into a fluorite face centered cubic structure with space group  $F_{m3m}$  (No. 225) to form a simple cubic oxygen suba lattice where the cerium ions occupy alternate cube centers (see Fig. 2.5A) [52]. In terms of Wyckoff positions, Ce atoms are located at the centers of the tetrahedrons (4a) (0,0,0) of which corners are populated with

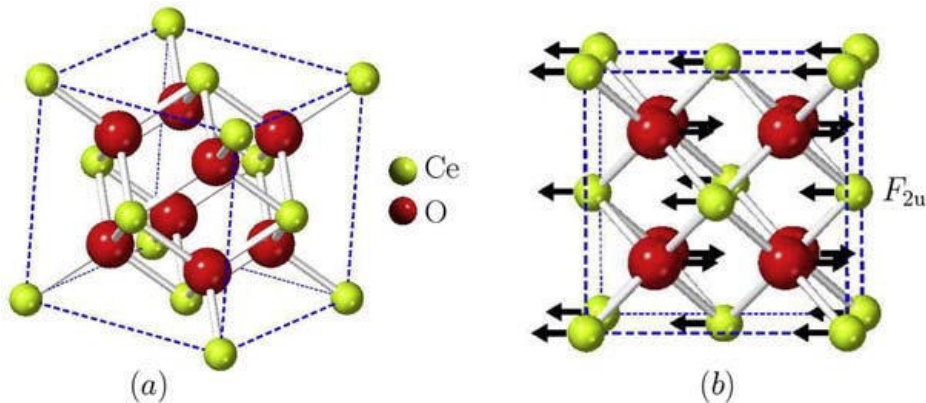


**Figure 2.5**

The fluorite face centered cubic crystal structure of CeO<sub>2</sub> (A) and its normal mode of the infrared active lattice vibrations of (B). Ce ions are denoted in green, while O ions are denoted in red.

oxygen ions ( $8c$ ) ( $1/4, 1/4, 1/4$ ). Observing the existence of the center of inversion, the structure has exactly one IRR ( $F_{2u}$ ) and one Raman ( $F_{2g}$ ) active mode [32], both of which are triple degenerated. As is shown in Fig. 2.5B, the normal mode of the infrared optically active vibrations consist of motions of both Ce and O atoms, but in the opposite directions.

Nanocrystalline  $\text{CeO}_2$  is distinguished by its enhanced electric conductivity, size lattice relaxation, as well as, many other advantages to bulk  $\text{CeO}_2$ . As to what has been reviewed in Ref. [53], decreasing particle size of crystalline  $\text{CeO}_2$  particles down to nanoceria dioxide crystals results in the formation of oxygen vacancies which can be further employed as descriptors for determining the valence state of Ce in the nanoparticles. Actually, the large surface to volume ratio, then the inclination toward the oxygen consumption, and basically, freeing Ce because of the reversible transition between  $\text{Ce}^{3+}$  and  $\text{Ce}^{4+}$  ions altogether lead to enormous catalytic capacity of this material. Nanoscaled  $\text{CeO}_2$  is furthermore found applicable to the active area of research for renewable energy, solid oxide fuel cells, water and air purification, optical glass polishing and decolorizing, UV ray filters, and many others [53].

Doped nanocrystalline  $\text{CeO}_2$ , however, deserves a special attention as the optimal doping with Cu or Nd has proven efficient in inducing the semiconductor-to-metallic state crossover [2,52] in nanoceria dioxide. Moreover, electrons localized at the vacancies may behave like free charge carriers to contribute drastically to the electrical conductivity [54]. This originates from the presence of free charge carriers, which are numbered in the nanoceria lattice, as the number of oxygen vacancies becomes increased by Nd content [55].

Following Ref. [2], the IRR spectroscopy has been applied to nondestructively investigate the mechanism of the influence of the plasmon due to the enhanced conductivity upon the phonon spectra with increasing Nd content in nanocrystalline  $\text{CeO}_2$ . This material is a polar semiconductor so that both phonon and plasmon excitations can be registered in the IRR spectra, whereby the plasmon-phonon coupling mechanism can be explored, while the extent to which the system acquires metallicity can be assessed. Radović et al. [2] have recorded the infrared reflectivity spectra on pure and Nd-doped  $\text{CeO}_{2-y}$  nanopowders at ambient temperature in far-infrared region from 100 up to  $700 \text{ cm}^{-1}$ .

Fig. 2.6 shows the IRR spectra of undoped and Nd-doped  $\text{CeO}_{2-y}$  nanopowders fitted with the two models: coupled plasmon-phonon and decoupled plasmon-phonon with double-damped Drude term. The concentration of the dopant is increased from 0% to 25%. The IRR spectra markedly differ from those done on bulk  $\text{CeO}_2$ , as the bulk reststrahlen region is split into two extended TO-LO modes over  $200\text{--}550 \text{ cm}^{-1}$  range with decreasing crystallite size. The splitting is more pronounced in samples with rather small crystallite sizes and is accompanied with the redshift of the two LO modes, as well. Also, one can

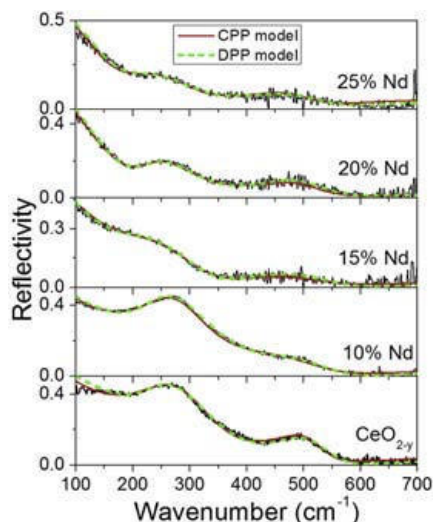


**Figure 2.6**

Infrared reflectivity spectra of undoped and Nd-doped  $\text{CeO}_{2-y}$  nanopowders involving the two theoretical fits based on coupled plasmon-phonon and decoupled plasmon-phonon model. *The credits for the figure are given to M. Radović, Z. Dohčević-Mitrović, N. Paunović, S. Bošković, N. Tomić, N. Tadić, I. Belča, Infrared study of plasmon-phonon coupling in pure and Nd-doped  $\text{CeO}_{2-y}$  nanocrystals, J. Phys. D Appl. Phys. 48 (2015) 065301–065306. <https://doi.org/10.1088/0022-3727/48/6/065301>.*

notice that with the raise of the dopant concentration, the low energy Drude tail and the screening of the phonon modes became more and more prominent, due to the strong presence of the free charge carriers. In the actual fact, increasing Nd content in the nanoceria dioxide lattice can generate a huge number of oxygen vacancies [2], while the plasmon-phonon interaction in the Nd-doped samples gets stronger.

Following the fits based upon both models applied (Fig. 2.6), all the plasmon modes registered in all nanoceria dioxide samples exhibit a frequency decrease with Nd doping, as can be seen from Fig. 2.7. The shift in the plasma frequency toward lower energies with increasing Nd concentration occurs owing to the weighted effective charge carrier mass, as there is no dopant impact on the free carrier concentration [2]. In fact, the plasma frequency is inversely proportional to the effective electron mass. This feature, together with the enhanced plasmon-phonon coupling with Nd doping, affords us a better insight into the transport properties of crystalline nanoceria based on the infrared-derived optical conductivity [48].

## 4. Electron spin resonance

### 4.1 Short introduction to electron spin resonance technique

ESR exemplifies a very sensitive and informative experimental technique, based on the use of magnetic field, which continues to find countless applications not only in solid state and

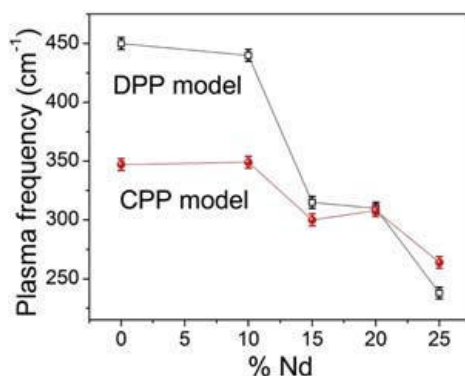


**Figure 2.7**

Evolution of the plasma frequency with the increased Nd dopant concentration as inferred from the two models: coupled plasmon-phonon and decoupled plasmon-phonon. *The credits for the figure are given to M. Radović, Z. Dohčević-Mitrović, N. Paunović, S. Bošković, N. Tomić, N. Tadić, I. Belča, Infrared study of plasmon-phonon coupling in pure and Nd-doped CeO<sub>2-y</sub> nanocrystals, J. Phys. D Appl. Phys. 48 (2015) 065301–065306. <https://doi.org/10.1088/0022-3727/48/6/065301>.*

nano, but also in biomedical and environmental sciences. By means of ESR spectroscopy, one is able to directly probe electron spin response at resonance that certainly makes ESR as one of the most powerful probe to investigate magnetic properties in various compounds. More interestingly, ESR stands for both noninvasive and contactless tool with ability to analyze accurately the nature and dynamics of charge carriers in conductive systems no matter how their geometry welcomes electrical leads and contacts in an electrical circuit.

Familiarly known as CESR in abbreviated term, conduction electron spin resonance has captivated much scientific attention for its capacity to measure the electrical conductivity of systems from bulk over micro-sized down to nanoscopic conducting materials. In the actual fact, in the conducting systems, the free electron motion exerting eddy current leaves an impact upon the recorded signal at resonance through asymmetry as the definite signature. This was originally recognized by Feher and Kip [56], Dyson [57] who put forward that asymmetric CESR lineshapes originate as linear combinations due to the two facts: (1) the attenuation of the AC field through the skin depth and (2) the capability of itinerant electrons to diffuse backward and forward through the skin depth region in many instances between consecutive spin flips that is only critical to transmission-based CESR techniques. In the case of transmissive CESR, magnetization can penetrate far deeply into metals unlike the AC magnetic field. This gives an extra contribution to enhancing the asymmetry of the signals at resonance [58,59].

Dating back to the 1950's, Freeman John Dyson is the first in the field to be credited with fully deriving the asymmetric CESR profiles. For the obvious reasons, such CESR lines are referred in literature to as Dysonians of which asymmetry extent is oftentimes quantified using  $A/B$  ratio (see the inset in Fig. 2.8), as common signature of metallicity in CESR experiments.

As with CESR operating in the reflection mode, Chapman et al. [61] developed an approach based on Dyson's theory to grasp both on- and off-resonance signal for the various crystal shapes, such as flat plates, long cylinders, and spheres. This allows the prediction of the asymmetric nature of CESR absorption profiles depending on geometry of the conducting samples with different size. Furthermore, Platzman and Wolf [62] examined spin waves excitations at resonance in paramagnetic metals that are described within the frame of Fermi-liquid theory. Their extended theory boils down to Dyson's in the limit of short momentum relaxation times. Dyson's theory was additionally generalized to involve various shapes of conducting crystals at desirable resonant magnetic field directions [63–65]. Later on, Kaplan pointed out that there is a substantial discrepancy between Dyson's theory and experimental results recorded in CESR based on the reflection mode [66]. Actually, CESR becomes recoiled rather with electric than magnetic component of the frequency-dependent electromagnetic field. The component of electric field is known to get easily coupled with the free electron momentum across the surface via relativistic spin-orbit interaction. This fact finds its application in the quantum mechanical density matrix method, which ultimately brings about the rather general form of CESR signal as [67]:

$$\chi''(\omega)\cos\phi + \chi'(\omega)\sin\phi. \quad (2.22)$$

Terms  $\chi''$  and  $\chi'$  represent the absorptive and dispersive parts of the CESR signal. The magnitudes of their contributions are measured with  $\cos\phi$  and  $\sin\phi$ , respectively, both of which disappear in the limit of highly conductive samples, where  $\phi$  is the signal phase. Eq. (2.22) does represent a particular manifestation of Dysonian, which falls into the range of the so-called “NMR limit” [68,69]. In that case, the electron diffusion rate is considerably slower as compared to the spin relaxation rate, and there is no need to consider other limits so as to reasonably infer CESR spectra of usual metallic samples. Spin dynamics itself as regards this case can lead to nothing but Lorentzian-profiled absorptions ( $\chi''$ ), unlike the situations with reduced dimensionality or motionally narrowed signals [70,71].

In a recent CESR study [60], the authors have favored Kaplan's approach, made for analyzing the CESR lineshape, to impart a valuable piece of information on the conductivity of samples with different geometries. Key lengths and points of CESR lines, necessary for simplification of a fitting procedure of CESR lineshape, have been established in this account to analytically derive, as well as, grasp the geometry independent asymmetry ratio limit  $A/B \rightarrow (5 + 3\sqrt{3})/4$ , encountered in literature as universal 2.55 limit, when the CESR is carried out on extremely conducting samples.  $A/B$  ratio value markedly evolves once nano- or micro-sized metallic samples start to agglomerate into larger ones that makes the CESR technique especially helpful in



monitoring the extent to which the clustering takes place [72,73]. Moreover, in Ref. [60], the phase dependence of the asymmetry ratio  $A/B$  is given as

$$A/B = \frac{\left(1 + 2\cos\frac{2\phi}{3}\right)\left(3\cos\left(\frac{\pi}{6} - \frac{\phi}{3}\right) + \sin\phi\right)}{4\cos\left(\frac{\pi}{6} - \frac{\phi}{3}\right)\left(1 + \sin\left(\frac{\pi}{6} - \frac{2\phi}{3}\right)\right)^2}, \quad (2.23)$$

which can be further employed to relate  $A/B$  with the conductivity. Namely, Chapman et al. [61] introduced the parameter  $\eta \equiv d/\delta$ , where  $d$  represents the characteristic length of the sample (thickness or diameter), while  $\delta$  is the skin depth at given resonant frequency. It is exactly this quantity that is in correlation with the sample conductivity. The absorptive and dispersive parts of the CESR signal in Ref. [61] are respectively  $x(\eta)$  and  $y(\eta)$  so that  $y(\eta)/x(\eta)$  exactly corresponds to  $\tan\phi$  in Ref. [60]. According to Ref. [61],  $x(\eta)$  and  $y(\eta)$  for the three relevant geometries look like

$$\text{Plate} \Rightarrow \begin{cases} x(\eta) = \frac{\sinh(\eta) + \sin(\eta)}{2\eta(\cosh(\eta) + \cos(\eta))} + \frac{1 + \cosh(\eta)\cos(\eta)}{(\cosh(\eta) + \cos(\eta))^2}, \\ y(\eta) = \frac{\sinh(\eta) - \sin(\eta)}{2\eta(\cosh(\eta) + \cos(\eta))} + \frac{\sinh(\eta)\sin(\eta)}{(\cosh(\eta) + \cos(\eta))^2}. \end{cases} \quad (2.24)$$

$$\text{Cylinder} \Rightarrow \begin{cases} x(\eta) = 1 - \frac{2(\text{Ber}(\vartheta)\text{Ber}'(\vartheta) + \text{Bei}(\vartheta)\text{Bei}'(\vartheta))(\text{Ber}(\vartheta)\text{Bei}'(\vartheta) - \text{Ber}'(\vartheta)\text{Bei}(\vartheta))}{(\text{Ber}^2(\vartheta) + \text{Bei}^2(\vartheta))^2}, \\ y(\eta) = \frac{(\text{Ber}^2(\vartheta) - \text{Bei}^2(\vartheta))(\text{Bei}'^2(\vartheta) - \text{Ber}'^2(\vartheta)) - 4\text{Ber}(\vartheta)\text{Bei}(\vartheta)\text{Ber}'(\vartheta)\text{Bei}'(\vartheta)}{(\text{Ber}^2(\vartheta) + \text{Bei}^2(\vartheta))^2}, \\ \text{where } \vartheta \equiv \eta/\sqrt{2}. \end{cases} \quad (2.25)$$

$$\text{Sphere} \Rightarrow \begin{cases} \frac{4}{9}x(\eta) = \frac{8 + \eta^4}{\eta^4} - \\ \frac{8(\sinh(\eta) + \sin(\eta))}{\eta^3(\cosh(\eta) - \cos(\eta))} + \frac{8\sinh(\eta)\sin(\eta)}{\eta^2(\cosh(\eta) - \cos(\eta))^2} + \frac{\sinh(\eta) - \sin(\eta)}{\eta(\cosh(\eta) - \cos(\eta))} - \frac{\sinh^2(\eta) - \sin^2(\eta)}{(\cosh(\eta) - \cos(\eta))^2}, \\ \frac{4}{9}y(\eta) = \\ \frac{8(\sinh(\eta) - \sin(\eta))}{\eta^3(\cosh(\eta) - \cos(\eta))} - \frac{4(\sinh^2(\eta) - \sin^2(\eta))}{\eta^2(\cosh(\eta) - \cos(\eta))^2} + \frac{\sinh(\eta) + \sin(\eta)}{\eta(\cosh(\eta) - \cos(\eta))} - \frac{2\sinh(\eta)\sin(\eta)}{(\cosh(\eta) - \cos(\eta))^2}. \end{cases} \quad (2.26)$$

This set of the three dependencies allows us to compute  $A/B$  versus  $\log \eta$  as is presented in Fig. 2.8. Oftentimes,  $A/B$  can be expanded in the form of the linear approximation with respect to either  $\eta$  or is proportional to the conductivity of the probed spins. The latter approximation works well in the case of the carbon nanotubes [3] of which CESR-based charge carrier transport is going to be discussed in detail throughout the upcoming section.

## 4.2 Carbon nanotubes

As a building brick that takes fascinating variety of forms such as diamond, fossil fuels, and graphite, together with innumerable compounds derived from it, carbon stands for one of the most impressive elements in the periodic table. Increased focus of renewed scientific interest in carbon has stepped into the realm of novel carbon-based materials, specifically known as the carbon allotropes at nanoscopic level, such as carbon nanotubes. These were first discovered as multiwalled forms by Iijima in 1991 [74] initiating the golden era of the physics and chemistry of carbon nanostructures. Carbon nanotubes are distinguished by their outstanding electronic, mechanical, and transport properties revealing uncorrelated (semi)conducting nature of the tubes in relation to the curvature and chirality. They also prove suitable for various applications which span from the use as light and electron emitters [75] up to optical biosensors for life sciences and biomedicine [76].

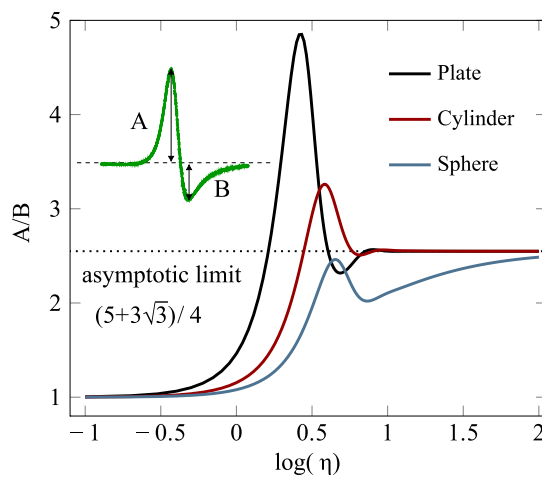


**Figure 2.8**

Asymmetry ratio  $A/B$  dependence on  $\log(\eta)$  regarding the three relevant geometries: infinite plate (black), long cylinder (dark red), and sphere (dark blue). All the three curves converge to the asymptotic  $A/B$  ratio of  $(5 + 3\sqrt{3})/4$  at  $\eta \rightarrow \infty$ . The inset represents graphically the  $A/B$  ratio in an arbitrarily selected CESR line. The figure is adopted from D.M. Djokić, D. Stepanenko, Z. Dohčević-Mitrović, *Extreme conduction electron spin resonance:  $A/B \rightarrow (5 + 3\sqrt{3})/4$ , the universal limit of lineshape asymmetry ratio*, *J. Magn. Magn. Mater.* 491 (2019) 165616. <https://doi.org/10.1016/j.jmmm.2019.165616>.

Even with the aid of nanoscaled technologies, making ideal electric contacts to adequately probe nanotube conductivity remains a perplexing puzzle. Electron backscattering, imbalanced injection of incident electron modes, and high-ohmic contact resistance are identified as the chief culprits at minuscule dimensions. However, nanotubes with large diameters have the added advantage of favoring low-ohmic contact resistance in a four-probe electric measurement [77]. This made them perfectly suited for the investigation of quantum interference caused by the Aharonov–Bohm effect specific by the pronounced magneto-resistance oscillations as a function of magnetic flux [78].

Despite their short diameters, transport electric properties of multiwalled nanotubes oftentimes remain consistent with theoretical models used to describe disordered conductors in  $2D$ . This might be explained by the fact that the electron wavelength is quite smaller than the nanotube diameter [79]. On the other hand side, one-dimensional essence of carbon nanotubes becomes already evident through specific heat and thermal lattice conductivity measurements since the phonon wavelength exceeds typical nanotube diameters [80], unlike the before-mentioned electron wavelength. Moreover, according to Ref. [81], it has been demonstrated that the electric transport in single walled carbon nanotubes exhibit a dependence in agreement with Luttinger liquid models.

Temperature and power-dependent CESR on an ensemble of metallic SWCNTs have been performed to infer their transport properties based on the insights into the spin dynamics [3]. The powder-form samples comprised acid-purified laser-oven SWCNTs which were prepared using the standardized annealing procedure, while the related CESR spectra were recorded as a function of temperature from 3.4 K to the ambient temperature at the X-band spectrometer. To yield a rather detailed insight into the transport mechanism, the authors of Ref. [3] studied the temperature evolution of the asymmetry Dysonian line shape parameter,  $\alpha \equiv A/B$ , which is to the first order approximation proportional to the conductance of the probed electron spins. These can relax by interaction with itinerant electrons that are present in metallic SWCNTs. In addition, the spin dephasing rate at resonance narrows with increasing temperature, which is a signature of the motional narrowing, a phenomenon that is particular to metallic systems.

Temperature dependence of the natural logarithm of conductivity,  $\ln(\sigma)$  which in this case boils down to  $\ln(\alpha)$ , is oftentimes plotted versus  $n$ -th root of inverse temperature [41]. Exponent  $n$  provides information on the charge carrier transport mechanism and when  $n$  approaches  $1/4$ , it leaves a hallmark of 3D Mott VRH transport mechanism [37].

As shown in Fig. 2.9, the Dysonian asymmetry parameter tends to follow a three-dimensional variable-range hopping behavior at low  $T$ . From the scaling relationships in Eq. (2.12), the localization length of the electronic wave function,  $\xi$ , is roughly estimated to be  $\sim 100$  nm, whereas the DOSs  $g(\epsilon_F)$  amounts  $\sim 10^{19}$  localized states per  $(\text{eV} \times \text{cm}^3)$

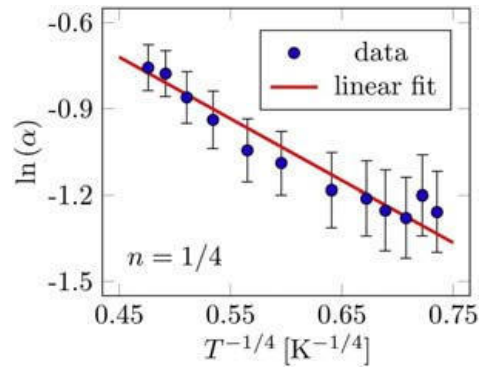


**Figure 2.9**

Natural logarithm of the asymmetry parameter,  $\alpha \equiv A/B$ , graphed versus the fourth root of inverse temperature. The logarithm is found to undergo the 3D VRH mechanism. *The data are taken from W.D. Rice, R.T. Weber, P. Nikolaev, S. Arepalli, V. Berka, A.L. Tsai, J. Kono, Spin relaxation times of single-wall carbon nanotubes, Phys. Rev. B 88 (2013) 041401–041405. <https://doi.org/10.1103/PhysRevB.88.041401>.*

around the Fermi energy. The traditional four-point probe transport measurements on the similarly prepared SWCNT samples [3] have, to some extent, corroborated the present picture of the CESR observed 3D VRH at low  $T$ .

As with nanoscopic systems such as SWCNTs, one can even venture to state that the VRH conduction mechanism, owing to the localized edge/surface states positioned around Fermi level, may extend even over a wide range of temperatures [1]. At high temperatures, the conduction mechanism in bulk systems commonly runs intrinsically via thermal activation through conduction bands. On the other hand side, there are, as a rule, defect states across the nanotube surface, effectively making its pristine length quite short and comparable to nanoscaled dimensions (Fig. 2.10). In this case, the overlaps between the orbitals decrease to cause the bands to become less dense. This leads to the band splittings to eventually open up wide gaps at rather high energies. Bands that are high in energy have, therefore, tendency to fade away so does the conduction band, as contrary to an ideally pristine SWCNT. It is thus reasonable to adopt that VRH mechanisms may apply up to somewhat higher temperatures in defected nanotubes. Certainly, the intrinsic thermally activated transport via conduction band can be ignored comparing to the VRH due to the evanescent DOSs, as is given in Fig. 2.10.

## 5. Concluding remarks

In summary, noncontact measurements of transport have been evidenced to offer various advantages to studying novel nanoscopic materials such as: multiferroic crystalline  $\text{BiFeO}_3$  nanoparticles, doped nanocrystalline  $\text{CeO}_2$  used for fuel cell applications, as well as,

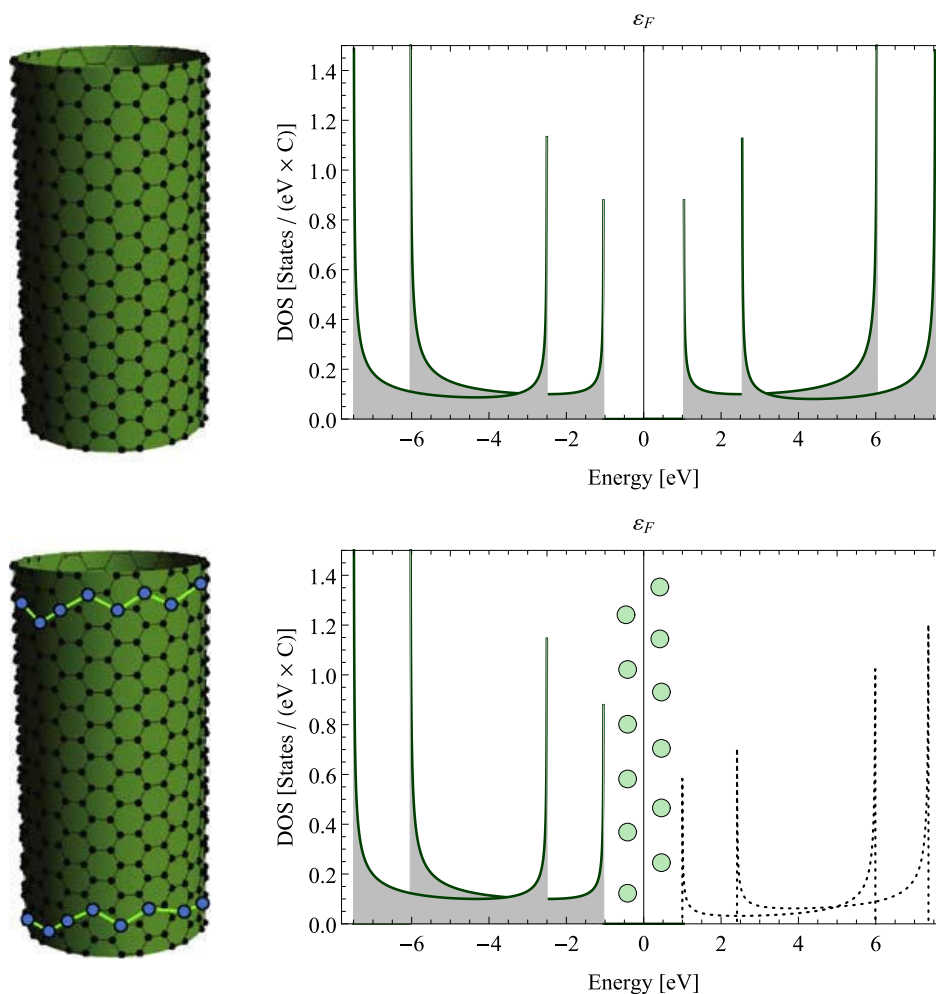


**Figure 2.10**

Plots of the electronic density of states versus energy for an ideally pristine (upper part) and a defected semiconducting SWCNT (lower part), computed using the tight-binding model. The electronic states of the defects forming the effective SWCNT edges are given in *green circles*. They are distributed around Fermi level at zero energy above which the DOS perishes gradually as the energy goes higher.

single walled carbon nanotubes exploited for molecular electronics and spintronics.

The transport properties of these novel multifunctional materials have been reviewed in this chapter in the light of noninvasive spectroscopic techniques which involve: RS, IRR, and ESR. Through brief introductions made at the beginning of each section, these three contactless spectroscopic tools have been described in detail.

## Acknowledgments

The authors greatly acknowledge funding provided by the Institute of Physics Belgrade, through the grant by the Ministry of Education, Science, and Technological Development of the Republic of Serbia.

## References

- [1] D.M. Djokić, B. Stojadinović, D. Stepanenko, Z. Dohčević-Mitrović, Probing charge carrier transport regimes in BiFeO<sub>3</sub> nanoparticles by Raman spectroscopy, *Scripta Mater.* 181 (2020) 6–9, <https://doi.org/10.1016/j.scriptamat.2020.02.008>.
- [2] M. Radović, Z. Dohčević-Mitrović, N. Paunović, S. Bošković, N. Tomić, N. Tadić, I. Belča, Infrared study of plasmon-phonon coupling in pure and Nd-doped CeO<sub>2-y</sub> nanocrystals, *J. Phys. D Appl. Phys.* 48 (2015) 065301–065306, <https://doi.org/10.1088/0022-3727/48/6/065301>.
- [3] W.D. Rice, R.T. Weber, P. Nikolaev, S. Arepalli, V. Berka, A.L. Tsai, J. Kono, Spin relaxation times of single-wall carbon nanotubes, *Phys. Rev. B* 88 (2013) 041401–041405, <https://doi.org/10.1103/PhysRevB.88.041401>.
- [4] S.S. Mitra, *Infrared and Raman Spectra Due to Lattice Vibrations*, Springer US, 1969, pp. 333–451, [https://doi.org/10.1007/978-1-4757-1123-3\\_14](https://doi.org/10.1007/978-1-4757-1123-3_14).
- [5] M. Cardona, *Light Scattering in Solids I - Introductory Concepts*, Springer-Verlag, Berlin, 1983.
- [6] L.A. Falkovsky, Investigation of semiconductors with defects using Raman scattering, *Phys. Usp.* 47 (2004) 249–272, <https://doi.org/10.1070/pu2004v047n03abeh001735>.
- [7] L.A. Falkovsky, Raman scattering of light by electrons in a metal with impurities, *Sov. Phys. JETP* 68 (1989) 661–663.
- [8] A. Zawadowski, M. Cardona, Theory of Raman scattering on normal metals with impurities, *Phys. Rev. B* 42 (1990) 10732–10734, <https://doi.org/10.1103/PhysRevB.42.10732>.
- [9] T.P. Devereaux, Theory for the effects of impurities on the Raman spectra of superconductors, *Phys. Rev. B* 45 (1992) 12965–12975, <https://doi.org/10.1103/PhysRevB.45.12965>.
- [10] E.Y. Sherman, O.V. Misochko, Raman scattering in metals with disorder: beyond the zero-momentum approximation, *J. Phys. Condens. Matter* 15 (2003) 3751–3758, <https://doi.org/10.1088/0953-8984/15/22/309>.
- [11] T.P. Devereaux, R. Hackl, Inelastic light scattering from correlated electrons, *Rev. Mod. Phys.* 79 (2007) 175–233, <https://doi.org/10.1103/RevModPhys.79.175>.
- [12] A.A. Abrikosov, L.P. Gorkov, I.E. Dzyaloshinsky, *Quantum Field Theoretical Methods in Statistical Physics*, Pergamon Press, Oxford, 1965.
- [13] H. Zhang, K. Kajiyoshi, Hydrothermal synthesis and size-dependent properties of multiferroic bismuth ferrite crystallites, *J. Am. Ceram. Soc.* 93 (2010) 3842, <https://doi.org/10.1111/j.1551-2916.2010.03953.x>.
- [14] F. Kubel, H. Schmid, Structure of a ferroelectric and ferroelastic monodomain crystal of the perovskite BiFeO<sub>3</sub>, *Acta Crystallogr. B* 46 (1990) 698, <https://doi.org/10.1107/S0108768190006887>.
- [15] J.-G. Park, M.D. Le, J. Jeong, S. Lee, Structure and spin dynamics of multiferroic BiFeO<sub>3</sub>, *J. Phys. Condens. Mat.* 26 (2014) 433202, <https://doi.org/10.1088/0953-8984/26/43/433202>.
- [16] G. Catalan, J.F. Scott, Physics and applications of bismuth ferrite, *Adv. Mater.* 21 (2009) 2463–2485, <https://doi.org/10.1002/adma.200802849>.
- [17] C.-H. Yang, D. Kan, I. Takeuchi, V. Nagarajan, J. Seidel, Doping BiFeO<sub>3</sub>: approaches and enhanced functionality, *Phys. Chem. Chem. Phys.* 14 (2012) 15953, <https://doi.org/10.1039/C2CP43082G>.
- [18] J.D. Bucci, B.K. Robertson, W.J. James, The precision determination of the lattice parameters and the coefficients of thermal expansion of BiFeO<sub>3</sub>, *J. Appl. Cryst.* 5 (1972) 187–191, <https://doi.org/10.1107/S0021889872009173>.
- [19] J.F. Ihlefeld, N.J. Podraza, Z.K. Liu, R.C. Rai, X. Xu, T. Heeg, Y.B. Chen, J. Li, R.W. Collins, J.L. Musfeldt, X.Q. Pan, J. Schubert, R. Ramesh, D.G. Schlom, Optical band gap of BiFeO<sub>3</sub> grown by molecular-beam epitaxy, *Appl. Phys. Lett.* 92 (2008) 142908, <https://doi.org/10.1063/1.2901160>.
- [20] Y. Xu, M. Shen, Structure and optical properties of nanocrystalline BiFeO<sub>3</sub> films prepared by chemical solution deposition, *Mater. Lett.* 62 (2008) 3600, <https://doi.org/10.1016/j.matlet.2008.04.006>.

- [21] A. Kumar, R.C. Rai, N.J. Podraza, S. Denev, M. Ramirez, Y.-H. Chu, L.W. Martin, J. Ihlefeld, T. Heeg, J. Schubert, D.G. Schlom, J. Orenstein, R. Ramesh, R.W. Collins, J.L. Musfeldt, V. Gopalan, Linear and nonlinear optical properties of BiFeO<sub>3</sub>, *Appl. Phys. Lett.* 92 (2008) 121915, <https://doi.org/10.1063/1.2901168>.
- [22] J. Allibe, K. Bougot-Robin, E. Jacquet, I.C. Infante, S. Fusil, C. Carrétéro, J.-L. Reverchon, B. Marcilhac, D. Creté, J.-C. Mage, A. Barthélémy, M. Bibes, Optical properties of integrated multiferroic BiFeO<sub>3</sub> thin films for microwave applications, *Appl. Phys. Lett.* 96 (2010) 182902, <https://doi.org/10.1063/1.3402763>.
- [23] M. Shariq, D. Kaur, V.S. Chandel, M.A. Siddiqui, Investigation on multiferroic properties of BiFeO<sub>3</sub> ceramics, *Mater. Sci. Poland* 31 (2013) 471, <https://doi.org/10.2478/s13536-013-0128-2>.
- [24] S.J. Clark, J. Robertson, Band gap and Schottky barrier heights of multiferroic BiFeO<sub>3</sub>, *Appl. Phys. Lett.* 90 (2007) 132903, <https://doi.org/10.1063/1.2716868>.
- [25] H. Wang, Y. Zheng, M.-Q. Cai, H. Huang, H.L. Chan, First-principles study on the electronic and optical properties of BiFeO<sub>3</sub>, *Solid State Commun.* 149 (2009) 641, <https://doi.org/10.1016/j.ssc.2009.01.023>.
- [26] S.R. Basu, L.W. Martin, Y.H. Chu, M. Gajek, R. Ramesh, R.C. Rai, X. Xu, J.L. Musfeldt, Photoconductivity in BiFeO<sub>3</sub> thin films, *Appl. Phys. Lett.* 92 (2008) 091905, <https://doi.org/10.1063/1.2887908>.
- [27] A. Mukherjee, M. Banerjee, S. Basu, N.T.K. Thanh, L.A.W. Green, M. Pal, Enhanced magnetic and electrical properties of Y and Mn co-doped BiFeO<sub>3</sub> nanoparticles, *Physica B: Cond. Matt.* 448 (2014) 199–203, <https://doi.org/10.1016/j.physb.2014.03.082>.
- [28] S. Ruby, S.S.R. Inbanathan, Structural properties and electrical conduction mechanisms of Bi<sup>0.9</sup>Sm<sup>0.05</sup>Tb<sup>0.05</sup>FeO<sub>3</sub> thin film, *Appl. Surf. Sci.* 449 (2018) 10–14, <https://doi.org/10.1016/j.apsusc.2017.11.231>.
- [29] H. Fukumura, H. Harima, K. Kisoda, M. Tamada, Y. Noguchi, M. Miyayama, Raman scattering study of multiferroic BiFeO<sub>3</sub> single crystal, *J. Magn. Magn. Mat.* 310 (2007) e367–e369, <https://doi.org/10.1016/j.jmmm.2006.10.282>.
- [30] J. Hlinka, J. Pokorny, S. Karimi, I.M. Reaney, Angular dispersion of oblique phonon modes in BiFeO<sub>3</sub> from micro-Raman scattering, *Phys. Rev. B* 83 (2011) 020101–020104, <https://doi.org/10.1103/PhysRevB.83.020101>.
- [31] J. Bielecki, P. Svedlindh, D.T. Tibebu, S. Cai, S.-G. Eriksson, L. Börjesson, C.S. Knee, Structural and magnetic properties of isovalently substituted multiferroic BiFeO<sub>3</sub>: insights from Raman spectroscopy, *Phys. Rev. B* 86 (2012) 184422–184437, <https://doi.org/10.1103/PhysRevB.86.184422>.
- [32] D.L. Rousseau, R.P. Bauman, S.P.S. Porto, Normal mode determination in crystals, *J. Raman Spectrosc.* 10 (1981) 253–290, <https://doi.org/10.1002/jrs.1250100152>.
- [33] A. Otto, J. Timper, J. Billmann, G. Kovacs, I. Pockrand, Surface roughness induced electronic Raman scattering, *Surf. Sci.* 92 (1980) L55–L57, [https://doi.org/10.1016/0039-6028\(80\)90237-X](https://doi.org/10.1016/0039-6028(80)90237-X).
- [34] R. Monreal, F. Flores, Y. Gao, T. López-Ríos, Raman scattering by electron-hole pairs at metal surfaces, *Europhys. Lett.* 4 (1987) 115–120, <https://doi.org/10.1209/0295-5075/4/1/019>.
- [35] C.Y. Chen, E. Burstein, S. Lundquist, Giant Raman scattering by pyridine and cn adsorbed on silver, *Solid State Commun.* 32 (1979) 63–66, [https://doi.org/10.1016/0038-1098\(79\)90998-0](https://doi.org/10.1016/0038-1098(79)90998-0).
- [36] H.L. Liu, S. Yoon, S.L. Cooper, S.-W. Cheong, P.D. Han, D.A. Payne, Probing anisotropic magnetotransport in manganese perovskites using Raman spectroscopy, *Phys. Rev. B* 58 (1998) R10115–R10118, <https://doi.org/10.1103/PhysRevB.58.R10115>.
- [37] N.F. Mott, E.A. Davis, *Electronic Processes in Non-crystalline Materials*, Oxford University Press, 1979.
- [38] A.L. Efros, B.I. Shklovskii, Coulomb gap and low temperature conductivity of disordered systems, *J. Phys. C Solid State Phys.* 8 (1975) L49–L51, <https://doi.org/10.1088/0022-3719/8/4/003>.
- [39] N.V. Arginskaya, V.I. Kozub, Potential influence of pre-exponential factors on the temperature dependence of variable-range hopping conductivity, *Soviet JETP* 79 (1994) 466–472.
- [40] A. Aharony, Y. Zhang, M.P. Sarachik, Universal crossover in variable range hopping with Coulomb interactions, *Phys. Rev. Lett.* 68 (1992) 3900–3903, <https://doi.org/10.1103/PhysRevLett.68.3900>.

- [41] L. Zuppiroli, L. Forró, Hopping conductivity in polaronic situations, *Phys. Lett. A* 141 (1989) 181–185, [https://doi.org/10.1016/0375-9601\(89\)90785-8](https://doi.org/10.1016/0375-9601(89)90785-8).
- [42] B. Stojadinović, Faculty of Physics, University of Belgrade, 2018 (Ph.D. thesis).
- [43] O. Gunnarsson, M. Calandra, J.E. Han, *Colloquium: saturation of electrical resistivity*, *Rev. Mod. Phys.* 75 (2003) 1085–1099, <https://doi.org/10.1103/RevModPhys.75.1085>.
- [44] N.E. Hussey, K. Takenaka, H. Takagi, Universality of the Mott-Ioffe-Regel limit in metals, *Philos. Mag. A* 84 (2004) 2847–2864, <https://doi.org/10.1080/14786430410001716944>.
- [45] A. Ioffe, A. Regel, Non-crystalline, amorphous and liquid electronic semiconductors, *Prog. Semicond.* 4 (1960) 237–291.
- [46] N.F. Mott, Conduction in non-crystalline systems IX. The minimum metallic conductivity, *Philos. Mag. J. Theor. Exp. Appl. Phys* 26 (4) (1972) 1015–1026, <https://doi.org/10.1080/14786437208226973>.
- [47] F. Gervais, Infrared dispersion in several polar-mode crystals, *Opt. Commun.* 22 (1977) 116–118, [https://doi.org/10.1016/0030-4018\(77\)90260-7](https://doi.org/10.1016/0030-4018(77)90260-7).
- [48] F. Gervais, Optical conductivity of oxides, *Mater. Sci. Eng. R Rep.* 39 (2002) 29–92, [https://doi.org/10.1016/S0927-796X\(02\)00073-6](https://doi.org/10.1016/S0927-796X(02)00073-6).
- [49] R.F. Wallis, M. Balkanski, *Many-body Aspects of Solid State Spectroscopy*, Elsevier Science Ltd, Amsterdam, the Netherlands, 1986.
- [50] A.A. Kukharskii, Plasmon-phonon coupling in GaAs, *Solid State Commun.* 13 (1973) 1761–1765, [https://doi.org/10.1016/0038-1098\(73\)90724-2](https://doi.org/10.1016/0038-1098(73)90724-2).
- [51] D.A.G. Bruggeman, Berechnung verschiedener physikalischer Konstanten von heterogenen substanzen. I. Dielektrizitätskonstanten und Leitfähigkeiten der Mischkörper aus isotropen Substanzen, *Ann. Phys.* 416 (7) (1935) 636–664, <https://doi.org/10.1002/andp.19354160705>.
- [52] Z.V. Popović, M. Grujić-Brojčin, N. Paunović, M.M. Radonjić, V.D. Araújo, M.I.B. Bernardi, M.M. de Lima, A. Cantarero, Far-infrared spectroscopic study of CeO<sub>2</sub> nanocrystals, *J. Nanopart. Res.* 17 (2015) 23–30, <https://doi.org/10.1007/s11051-015-2859-y>.
- [53] A. Younis, D. Chu, S. Li, Cerium oxide nanostructures and their applications, in: *Functionalized Nanomaterials*, 2016, pp. 52–68, <https://doi.org/10.5772/65937>. Ch. 3.
- [54] P. Jasinski, T. Suzuki, H.U. Anderson, Nanocrystalline undoped ceria oxygen sensor, *Sensor. Actuator. B Chem.* 95 (2003) 73–77, [https://doi.org/10.1016/S0925-4005\(03\)00407-6](https://doi.org/10.1016/S0925-4005(03)00407-6).
- [55] X. Han, J. Lee, H.-I. Yoo, Oxygen-vacancy-induced ferromagnetism in CeO<sub>2</sub> from first principles, *Phys. Rev. B* 79 (2009) 100403–100406, <https://doi.org/10.1103/PhysRevB.79.100403>.
- [56] G. Feher, A.F. Kip, Electron spin resonance absorption in metals. I Experimental, *Phys. Rev.* 98 (1955) 337–348, <https://doi.org/10.1103/PhysRev.98.337>.
- [57] F.J. Dyson, Electron spin resonance absorption in metals. II. Theory of electron diffusion and the skin effect, *Phys. Rev.* 98 (1955) 349–359, <https://doi.org/10.1103/PhysRev.98.349>.
- [58] M.I. Azbel, V.I. Gerasimenko, I.M. Lifshitz, Paramagnetic resonance and polarization of nuclei in metals, *Sov. Phys. JETP* 5 (1957) 986–996.
- [59] M.I. Azbel, V.I. Gerasimenko, I.M. Lifshitz, On the theory of paramagnetic resonance in metals, *Sov. Phys. JETP* 8 (1959) 480–487.
- [60] D.M. Djokić, D. Stepanenko, Z. Dohčević-Mitrović, Extreme conduction electron spin resonance:  $A/B \rightarrow (5+3\sqrt{3})/4$ , the universal limit of lineshape asymmetry ratio, *J. Magn. Magn. Mater.* 491 (2019) 165616, <https://doi.org/10.1016/j.jmmm.2019.165616>.
- [61] A.C. Chapman, P. Rhodes, E.F.W. Seymour, The effect of eddy currents on nuclear magnetic resonance in metals, *Proc. Phys. Soc. B* 70 (1957) 345–360, <https://doi.org/10.1088/0370-1301/70/4/301>.
- [62] P.M. Platzman, P.A. Wolff, Spin-wave excitation in nonferromagnetic metals, *Phys. Rev. Lett.* 18 (1967) 280–283, <https://doi.org/10.1103/PhysRevLett.18.280>.
- [63] H.R. Webb, Electron-spin-resonance line shape in spherical metal particles, *Phys. Rev.* 158 (1967) 225–233, <https://doi.org/10.1103/PhysRev.158.225>.
- [64] J.H. Pifer, R. Magno, Conduction-electron spin resonance in a lithium film, *Phys. Rev. B* 3 (1971) 663–673, <https://doi.org/10.1103/PhysRevB.3.663>.



- [65] A.H. Kahn, Theory of microwave eddy currents and paramagnetic resonance in materials of intermediate conductivity, *Phys. Rev. B* 16 (1977) 64–72, <https://doi.org/10.1103/PhysRevB.16.64>.
- [66] J.I. Kaplan, J. Reuben, Electron spin resonance line shapes of paramagnetic species on surfaces, *J. Phys. Chem.* 86 (1982) 4465–4466, <https://doi.org/10.1021/j100220a001>.
- [67] A.G. Marshall, D.C. Roe, Dispersion versus absorption: spectral line shape analysis for radiofrequency and microwave spectrometry, *Analyt. Chem.* 50 (1978) 756–763, <https://doi.org/10.1021/ac50027a023>.
- [68] L. Walmsley, G. Ceotto, J.H. Castilho, C. Rettori, Magnetic field modulation frequency, sample size and electromagnetic configuration effects on the spin resonance spectra of graphite intercalation compounds, *Synth. Met.* 30 (1989) 97–107, [https://doi.org/10.1016/0379-6779\(89\)90645-0](https://doi.org/10.1016/0379-6779(89)90645-0).
- [69] L. Walmsley, Translating conduction-electron spin-resonance lines into lorentzian lines, *J. Magn. Reson. A* 122 (1996) 209–213, <https://doi.org/10.1006/jmra.1996.0196>.
- [70] M. Oshikawa, I. Affleck, Electron spin resonance in  $S=1/2$  antiferromagnetic chains, *Phys. Rev. B* 65 (2002) 134410–134437, <https://doi.org/10.1103/PhysRevB.65.134410>.
- [71] J.P. Joshi, S.V. Bhat, On the analysis of broad Dysonian electron paramagnetic resonance spectra, *J. Magn. Res.* 168 (2004) 284–287, <https://doi.org/10.1016/j.jmr.2004.03.018>.
- [72] K.W. Blazey, K.A. Müller, F. Blatter, E. Schumacher, Conduction electron spin resonance of Caesium metallic clusters in zeolite X, *Europhys. Lett.* 4 (1987) 857–861, <https://doi.org/10.1209/0295-5075/4/7/017>.
- [73] J.J. van der Klink, H.B. Brom, NMR in metals, metal particles and metal cluster compounds, *Prog. Nucl. Magn. Reson. Spectr.* 36 (2) (2000) 89–201, [https://doi.org/10.1016/S0079-6565\(99\)00020-5](https://doi.org/10.1016/S0079-6565(99)00020-5).
- [74] S. Iijima, Helical microtubules of graphitic carbon, *Nature* 354 (1991) 56–58, <https://doi.org/10.1038/354056a0>.
- [75] L. Forró, C. Schönenberger, *Physical Properties of Multi-Wall Nanotubes*, Springer Berlin Heidelberg, Berlin, Heidelberg, 2001, pp. 329–391, [https://doi.org/10.1007/3-540-39947-X\\_13](https://doi.org/10.1007/3-540-39947-X_13).
- [76] D.M. Djokić, A. Goswami, Quantum yield in polymer wrapped single walled carbon nanotubes: a computational model, *Nanotechnology* 28 (2017) 465204, <https://doi.org/10.1088/1361-6528/aa8f38>.
- [77] A. Bachtold, M. Henny, C. Terrier, C. Strunk, C. Schönenberger, J.-P. Salvetat, J.-M. Bonard, L. Forró, Contacting carbon nanotubes selectively with low-ohmic contacts for four-probe electric measurements, *Appl. Phys. Lett.* 73 (1998) 274–276, <https://doi.org/10.1063/1.121778>.
- [78] A. Bachtold, C. Strunk, J.-P. Salvetat, J.-M. Bonard, L. Forró, T. Nussbaumer, C. Schönenberger, Aharonov-Bohm oscillations in carbon nanotubes, *Nature* 397 (1999) 673–675, <https://doi.org/10.1038/17755>.
- [79] L. Langer, V. Bayot, E. Grivei, J.-P. Issi, J.P. Heremans, C.H. Olk, L. Stockman, C. Van Haesendonck, Y. Bruynseraede, Quantum transport in a multiwalled carbon nanotube, *Phys. Rev. Lett.* 76 (1996) 479–482, <https://doi.org/10.1103/PhysRevLett.76.479>.
- [80] W. Yi, L. Lu, Z. Dian-lin, Z.W. Pan, S.S. Xie, Linear specific heat of carbon nanotubes, *Phys. Rev. B* 59 (1999) R9015–R9018, <https://doi.org/10.1103/PhysRevB.59.R9015>.
- [81] M. Bockrath, D.H. Cobden, J. Lu, A.G. Rinzler, R.E. Smalley, L. Balents, P.L. McEuen, Luttinger-liquid behaviour in carbon nanotubes, *Nature* 398 (1999) 598–601, <https://doi.org/10.1038/17569>.

The Serbian Society for Ceramic Materials

Institute for Multidisciplinary Research (IMSI), University of Belgrade

Institute of Physics, University of Belgrade

Center of Excellence for the Synthesis, Processing and Characterization of  
Materials for use in Extreme Conditions "CEXTREME LAB" - Institute of  
Nuclear Sciences "Vinča", University of Belgrade

Faculty of Mechanical Engineering, University of Belgrade

Center for Green Technologies, Institute for Multidisciplinary Research,  
University of Belgrade

Faculty of Technology and Metallurgy, University of Belgrade

Faculty of Technology, University of Novi Sad

# PROGRAMME and the BOOK of ABSTRACTS

## 5CSCS-2019

5<sup>th</sup> Conference of  
the Serbian Society for Ceramic Materials  
June 11-13, 2019, Belgrade Serbia

Edited by:

**Branko Matović**  
**Zorica Branković**  
**Aleksandra Dapčević**  
**Vladimir V. Srdić**

5. F. Cordero, F. Trequattrini, F. Craciun, et al., *Phys. Rev. B*, **99** (2019) 064106
6. F. Cordero, F. Craciun, F. Trequattrini, et al., *J. Phys. Chem. Lett.*, **9** (2018) 4401

I-23

## VARIABLE RANGE HOPPING MECHANISM OF CARRIER TRANSPORT IN BiFeO<sub>3</sub> NANO-PARTICLES REVEALED VIA RAMAN SCATTERING TECHNIQUE

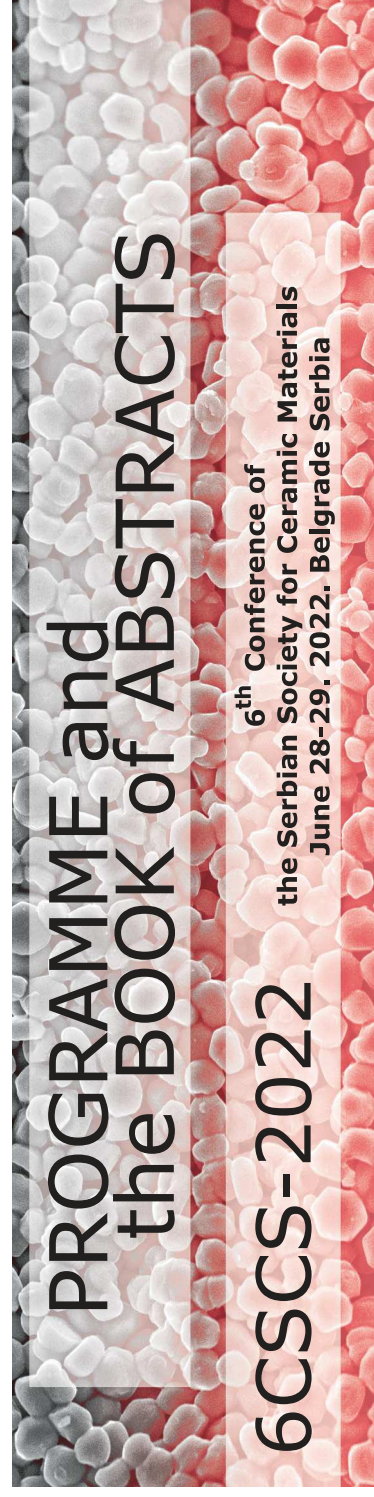
Dejan M. Djokić, Bojan Stojadinović, Dimitrije Stepanenko,  
Sonja Aškrabić, Zorana Dohčević-Mitrović

*Nanostructured Matter Laboratory, Institute of Physics Belgrade, University of Belgrade, Pregrevica 118, 11 080 Belgrade, Serbia*

Single-phase multiferroic BiFeO<sub>3</sub> compound has recently captivated much attention because of its desirably high ferroelectric Curie temperature of ~1100 K and antiferromagnetic Néel temperature  $T_N$  of ~640 K, which both slightly decrease with decreasing crystallite size. As such, BiFeO<sub>3</sub> at nanoscale proves to be promising for prospective applications in memory smart devices, satellite communications, novel sensing technologies, and spintronics. In order to meet these industrial requirements, the electric resistance of BiFeO<sub>3</sub> nanopowders must far exceed low insulation electric transport values, of which mechanism is hard to capture using contact probes. As highly informative experimental tool, Raman spectroscopy demonstrates ability to assess the nature and dynamics of charge carriers in conductive systems in a contactless indirect manner. In the present study we have analyzed broad electronic Raman scattering response of BiFeO<sub>3</sub> nanoparticles as a function of temperature (80–723 K) from which the carrier scattering rate can be estimated [1]. Two different 3D phonon-assisted Variable Range Hopping (VRH) electron transport mechanisms have been detected. VRH model due to Mott [2] is accompanied with the high-temperature paramagnetic phase (above  $T_N$ ), whereas the VRH mechanism based on Efros & Shklovskii model [3] has been revealed in the strongly correlated low-temperature phase (below  $T_N$ ). Our preliminary estimation of the electronic density of states above  $T_N$  exceeds number of  $10^{19}$  electron states per (eV cm<sup>3</sup>), which is in agreement with the finding by Ruby & Inbanathan [4] obtained directly from DC electrical resistivity measurements in doped BiFeO<sub>3</sub> thin films. In both cases the electron localization length has been found to closely match the average nanoparticle size of few tens of nanometers. This finding indicates that the system is disordered enough to localize the charge-carrier states within the nanoparticles.

1. A. Zawadowski, M. Cardona, *Phys. Rev. B*, **42** (1990) 10732
2. N.F. Mott, *Electronic Processes in Non-Crystalline Materials*, Oxford Univ. Press, 1979
3. A.L. Efros, B.I. Shklovskii, *J. Phys. C: Solid State Phys.*, **8** (1975) L49
4. S. Ruby, S.S.R. Inbanathan, *Appl. Surf. Sci.*, **449** (2018) 10

The Serbian Society for Ceramic Materials  
Institute for Multidisciplinary Research (IMSI), University of Belgrade  
Institute of Physics, University of Belgrade  
Center of Excellence for the Synthesis, Processing and Characterization of  
Materials for use in Extreme Conditions "CEXTREME LAB" - Institute of  
Nuclear Sciences "Vinča", University of Belgrade  
Faculty of Mechanical Engineering, University of Belgrade  
Center of Excellence for Green Technologies, Institute for Multidisciplinary  
Research, University of Belgrade  
Faculty of Technology and Metallurgy, University of Belgrade



Edited by:  
**Branko Matović**  
**Aleksandra Dapčević**  
**Vladimir V. Srdić**

Programme and Book of Abstracts of The Sixth Conference of The Serbian Society for Ceramic Materilas **publishes abstracts from the field of ceramics, which are presented at international Conference.**

***Editors-in-Chief***

Dr Branko Matović  
Prof. Aleksandra Dapčević  
Prof. Vladimir V. Srdić

***Publisher***

Institut za multidisciplinarna istraživanja  
Kneza Višeslava 1, 11000 Belgrade, Serbia

***For Publisher***

Dr Dragica Stanković

***Printing layout***

Vladimir V. Srdić

***Press***

Faculty of Technology and Metalurgy, Research and Development Centre of Printing  
Technology, Karnegieva 4, Belgrade, Serbia

*The year off issue:*

2022.

ISBN 987-86-80109-23-7

CIP - Каталогизacija y publikaciji  
Narodna biblioteka Srbije, Beograd

666.3/.7(048)  
66.017/.018(048)

DRUŠTVO za keramičke materijale Srbije. Konferencija (6 ; 2022 ; Beograd)

Programme ; and the Book of Abstracts / 6th Conference of The Serbian Society for Ceramic Materials, 6CSCS-2022, June 28-29, 2022, Belgrade, Serbia ; [organizers] The Serbian Society for Ceramic Materials ... [et al.] ; edited by Branko Matović, Aleksandra Dapčević, Vladimir V. Srdić. - Belgrade : Institut za multidisciplinarna istraživanja, 2022 (Belgrade : Faculty of technology and metalurgy, Research and development centre of printing technology). - 91 str. : ilustr. ; 25 cm

Tiraž 120. - Str. 7: Welcome message / Branko Matovic. - Registar.

ISBN 978-86-80109-23-7

a) Керамика -- Апстракти б) Наука о материјалима -- Апстракти  
в) Наноматеријали -- Апстракти

COBISS.SR-ID 69088009

**The Serbian Society for Ceramic Materials**  
**Institute for Multidisciplinary Research, University of Belgrade**  
**Institute of Physics, University of Belgrade**  
**Center of Excellence for the Synthesis, Processing and Characterization of**  
**Materials for use in Extreme Conditions “CEXTREME LAB” -**  
**Institute of Nuclear Sciences “Vinča”, University of Belgrade**  
**Faculty of Mechanical Engineering, University of Belgrade**  
**Center of Excellence for Green Technologies, Institute for Multidisciplinary**  
**Research,**  
**University of Belgrade**  
**Faculty of Technology and Metallurgy, University of Belgrade**

# **PROGRAMME AND THE BOOK OF ABSTRACTS**

**6<sup>th</sup> Conference of The Serbian Society for  
Ceramic Materials**

**June 28-29, 2022**

**Belgrade, Serbia**

**6CSCS-2022**

Edited by:

**Branko Matović**

**Aleksandra Dapčević**

**Vladimir V. Srdić**

## Committees

### Organizer

- The Serbian Society for Ceramic Materials
- Institute for Multidisciplinary Research (IMSI), University of Belgrade
- Institute of Physics, University of Belgrade
- Center of Excellence for the Synthesis, Processing and Characterization of Materials for use in Extreme Conditions “CEXTREME LAB” – Institute of Nuclear Sciences “Vinča”, University of Belgrade
- Faculty of Mechanical Engineering, University of Belgrade
- Center of Excellence for Green Technologies, Institute for Multidisciplinary Research, University of Belgrade
- Faculty of Technology and Metallurgy, University of Belgrade

### Scientific Committee

1. Dr. Snežana Bošković, Institute of Nuclear Sciences “Vinča”, University of Belgrade, *Serbia*
2. Prof. Biljana Stojanović, Institute for Multidisciplinary Research, University of Belgrade, *Serbia*
3. Dr. Branko Matović, Institute of Nuclear Sciences “Vinča”, University of Belgrade, *Serbia*
4. Prof. Vladimir V. Srdić, Faculty of Technology, University of Novi Sad, *Serbia*
5. Dr. Zorica Branković, Institute for Multidisciplinary Research, University of Belgrade, *Serbia*
6. Dr. Goran Branković, Institute for Multidisciplinary Research, University of Belgrade, *Serbia*
7. Dr. Zorana Dohčević-Mitrović, Institute of Physics, University of Belgrade, *Serbia*
8. Prof. Tatjana Volkov-Husović, Faculty of Technology and Metallurgy, University of Belgrade, *Serbia*
9. Dr. Zvezdana Baščarević, Institute for Multidisciplinary Research, University of Belgrade, *Serbia*
10. Dr. Dejan Zagorac, INN Vinca, University of Belgrade, *Serbia*

## International Advisory Board

### GERMANY:

Emanuel Ionescu, *Fraunhofer Institution for Materials Recycling and Resource Strategies IWKS, Alzenau*

### UNITED STATES OF AMERICA:

Yuri Rostovtsev, *Department of Physics and the Center for Nonlinear Sciences, University of North Texas, Denton*

### CYPRUS:

Claus Rebholz, *Department of Mechanical & Manufacturing Engineering, University of Cyprus, Nicosia*

### SLOVENIA:

Matejka Podlogar, *Jožef Stefan Institute, Ljubljana*  
Slavko Bernik, *Jožef Stefan Institute, Ljubljana*

### CROATIA:

Tomislav Ivek, *Institut of Physics, Zagreb*

### INDIA:

Hari Kumar, *Laboratory for High Performance Ceramics, Department of Metallurgical and Materials Engineering & Ceramic Technologies Group-Centre of Excellence in Materials & Manufacturing for Futuristic Mobility, Indian Institute of Technology-Madras*

Ravi Kumar, *Laboratory for High Performance Ceramics, Department of Metallurgical and Materials Engineering & Ceramic Technologies Group-Centre of Excellence in Materials & Manufacturing for Futuristic Mobility, Indian Institute of Technology-Madras*

### ROMANIA:

Enikö Volceanov, *Metallurgical Research Institute-ICEM SA, Bucharest*  
Adrian Volceanov, *University "Politehnica" of Bucharest*

### SLOVAKIA:

Peter Tatarko, *Institute of Inorganic Chemistry, Slovak Academy of Sciences, Dúbravská cesta 9, 845 36, Bratislava*

## Organizing Committee

1. Dr. Aleksandra Dapčević, Faculty of Technology and Metallurgy, Belgrade, *Serbia*
2. Dr. Jelena Maletaškić, Institute of Nuclear Sciences "Vinča", Belgrade, *Serbia*
3. Dr. Marija Milanović, Faculty of Technology, Novi Sad, *Serbia*
4. Dr. Maria Čebela, Institute of Nuclear Sciences "Vinča", Belgrade, *Serbia*
5. Dr. Jelena Erčić, Institute of Nuclear Sciences "Vinča", Belgrade, *Serbia*



6. Dr. Milica Počuča Nešić, Institute for Multidisciplinary Research, Belgrade, *Serbia*
7. Dr. Nikola Ilić, Institute for Multidisciplinary Research, Belgrade, *Serbia*
8. Jelena Vukašinović, Institute for Multidisciplinary Research, Belgrade, *Serbia*
9. Dr. Bojan Stojadinović, Institute of Physics, Belgrade, *Serbia*
10. Dr. Bojana Simović, Institute for Multidisciplinary Research, Belgrade, *Serbia*
11. Natalija Milojković, Faculty of Technology and Metallurgy, Belgrade, *Serbia*

I-8

## **SPIN-PHONON COUPLING IN NANOSTRUCTURES REVEALED BY RAMAN SPECTROSCOPY**

Bojan Stojadinović, Sonja Aškračić, Novica Paunović, Dejan Djokić,  
Zorana Dohčević-Mitrović

*Institute of Physics Belgrade, University of Belgrade, Pregrevica 118, 11080  
Belgrade, Serbia*

The knowledge of the subtle interplay between the spin and lattice degrees of freedom (spin-phonon coupling) presents an important aspect in manipulating the magnetic, ferroelectric and magneto-electric properties of composite nanostructures.

Spin-phonon interaction in magnetic nanostructures most often manifests as non-typical temperature dependence of optical phonons frequencies, since phonon energies can be influenced by the exchange coupling between magnetic ions at and below the temperatures of magnetic phase transitions. Due to the complexity of magnetic interactions in nanomaterials, the coupling between the lattice vibration and the magnetic order can be different for different phonon modes and the coupling strength may vary even in the case of the same spin-spin interaction. Raman spectroscopy is a very powerful technique to elucidate the spin dynamics and the effects of the interaction of optical phonons with different magnetic ordering. More or less phonon frequency deviation from anharmonic behaviour manifests in the Raman spectra as positive/negative frequency shift below magnetic ordering temperature and is dependent on the relative strength of antiferromagnetic (AFM) or ferromagnetic (FM) exchange interaction. From this shift it is possible to derive estimates for the spin-phonon coupling strength.

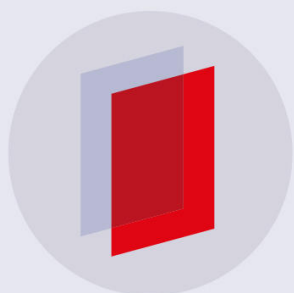
The spin-phonon coupling mechanism will be demonstrated on the example of two different magnetic nanomaterials, antiferromagnetic bismuth ferrite,  $\text{BiFeO}_3$ , and ferrimagnetic iron garnet,  $\text{Dy}_3\text{Fe}_5\text{O}_{12}$ . The spin-phonon interaction in these materials was explained within the mean field approach which enabled to extract the spin-spin correlation function and in addition allowed a quantitative assessment of the spin-phonon coupling strength for different phonon modes.

PAPER

# SnO<sub>2</sub> nanosheets with multifunctional properties for flexible gas-sensors and UVA light detectors

To cite this article: Marko Radovi *et al* 2019 *J. Phys. D: Appl. Phys.* **52** 385305

View the [article online](#) for updates and enhancements.



**IOP | ebooks™**

Bringing you innovative digital publishing with leading voices to create your essential collection of books in STEM research.

Start exploring the collection - download the first chapter of every title for free.

# SnO<sub>2</sub> nanosheets with multifunctional properties for flexible gas-sensors and UVA light detectors

Marko Radović<sup>1</sup> , Georges Dubourg<sup>1</sup>, Zorana Dohčević-Mitrović<sup>2</sup>,  
Bojan Stojadinović<sup>2</sup>, Jelena Vukmirović<sup>3</sup>, Nataša Samardžić<sup>4</sup>  
and Miloš Bokorov<sup>5</sup>

<sup>1</sup> University of Novi Sad, Group for Nano and Microelectronics, Biosense Institute, Novi Sad, Serbia

<sup>2</sup> Laboratory for Nanocomposite Structures and Bio-Vibrational Spectroscopy, Institute of Physics, University of Belgrade, Belgrade, Serbia

<sup>3</sup> University of Novi Sad, Faculty of Technology, Novi Sad, Serbia

<sup>4</sup> University of Novi Sad, Faculty of Technical Sciences, Novi Sad, Serbia

<sup>5</sup> University of Novi Sad, University Center for Electronic Microscopy, Novi Sad, Serbia

E-mail: [marrad@biosense.rs](mailto:marrad@biosense.rs)

Received 10 April 2019, revised 11 June 2019

Accepted for publication 26 June 2019

Published 19 July 2019



## Abstract

The presented research introduces an innovative bottom-up approach, involving synthesis, characterization and application of SnO<sub>2</sub> nanomaterials in advanced technologies. SnO<sub>2</sub> nanosheets are synthesized with a hydrothermal method and screen-printed on a flexible substrate with interdigitated electrodes. The obtained measurements reveal that the synthesized material has a rutile crystal structure with preferable (1 1 0) orientation and oxygen-defects, unique morphology and good electric conductivity. Multifunctional performance is evaluated for gas and ultraviolet A (UVA; 365 nm) light sensing. The designed sensor shows a better response to ethanol in comparison to 2-propanol and acetone, indicating the selectivity feature among the investigated volatile organic compounds. Photocurrent measurements reveal a good photoconversion rate, suitable for UVA monitoring.

Keywords: SnO<sub>2</sub>, oxygen vacancies, electrical properties, gas sensors, light sensors

(Some figures may appear in colour only in the online journal)

## 1. Introduction

Metal oxides stand out as a landmark in materials science due to their unique properties, widely exploited in basic research and technological applications. Among these materials, tin oxide (SnO<sub>2</sub>) is a prime example of multifunctionality, since it possesses low electrical resistance combined with high optical transparency in the visible spectrum. Such a feature is highly demanded for optoelectronic devices (solar cells, light emitting diodes (LEDs) and smart windows) [1–5]. Also, SnO<sub>2</sub> based materials are recognized for their outstanding surface related catalytic properties, leaving high impact on gas-sensing performance and broad applications in sensing technologies [6–8]. Chemical gas sensors based on tin oxide

films, coupled with heater elements, gave rise to the golden era in the evolution of commercial products for monitoring of various types of gases, over the past three decades. However, with the recent advancement of sensor network technologies and increased need for sensor array devices, focus on the application of tin oxide sensors has shifted to cost-efficient platforms, low power consumption (room temperature operating conditions) and to the sub ppm detection range. Significant efforts are being continuously invested in nanomaterials design to improve sensors sensitivity and selectivity.

Chemical routes for the synthesis of SnO<sub>2</sub> nanomaterials have been evolving in parallel with wide adoption and application of these materials in advanced technologies. Among such processes, the hydrothermal method has proven to be

the most versatile, reliable, repeatable, clean and environmentally-friendly technique for obtaining SnO<sub>2</sub> nanomaterials with targeted properties. The portfolio of the hydrothermal method in synthesis of tin oxide-based nanomaterials extends over different types of dimensionality and morphologies, like nanocrystals [9, 10], nanowires [11], nanorods [12, 13], nanoneedles [14, 15], nanosheets [14–20], snowflakes [21] and nanoflowers [22]. An accumulated library of knowledge points to the fact that low dimensional 0D and 1D materials usually have a larger specific surface area than the 3D microstructures, which is highly desired in sensor applications, but they have poor thermal stability. For example, nanoparticles easily tend to form agglomerates, transforming into polycrystalline material and discarding their unique properties related to their nanostructured nature, whereas nanosheet structures are highly effective in mitigating the agglomeration, yielding better structural integrity. Also, synthesis of SnO<sub>2</sub> nanosheets has gained a lot of research interest in recent years since they exhibit exceptional selectivity feature towards ethanol sensing [15–17, 20, 23], compared to the other nanostructures. Two of the biggest problems facing hydrothermal synthesis of tin oxide nanosheets is the precise control of the oxidation state of Sn ions over the exposed surfaces and control of impurities concentration (highly reduced SnO phase) [24]. Optimization of hydrothermal parameters for synthesis of SnO<sub>2</sub> into clean and single phase nanosheet morphology is one of the foundations for their successful application in sensors technologies.

Recent technological developments imposed strong demands for the integration of multifunctional properties of nanomaterials into a single device [25, 26], where metal oxides like SnO<sub>2</sub> hold great potential to meet market demands. Still, many precise and sophisticated technologies used for the fabrication of state-of-art devices involve complex processes which are not compatible with large scale production. Therefore, alternative approaches need to be developed to meet the high demand of such devices, like low-cost and mass producible multifunctional platforms. A major challenge for successful integration of nanomaterials in new technologies lies in the preservation of the material fundamental properties through the functionalization process. This challenge is conditioned with the low production cost of the final device. Lots of research activities are currently dedicated to the development of flexible electronics [27], aiming to take advantage over traditional rigid platforms in cost, mechanical flexibility, biocompatibility and biodegradability.

The main idea behind the conducted research was to uncover versatile surface properties of SnO<sub>2</sub> nanomaterials and to develop a simple and potentially scalable bottom-up approach for implementation of such unique properties into sensing devices, by combining hydrothermal synthesis and screen-printing functionalization. Basic parameters of the hydrothermal method, such as the precursor type, pH value and reaction temperature, were optimized for obtaining SnO<sub>2</sub> nanopowders with the desired structural, morphological, electrical and sensing properties. Functional paste for the screen-printing of synthesized nanomaterial was specially formulated in order to preserve materials fundamental

features without the need for an additional high-temperature curing step. The undertaken approach revealed great potential for the application of SnO<sub>2</sub> nanosheets, with enhanced surface features, in alcohol gas-sensing and UVA photodetection.

## 2. Experimental

The hydrothermal method was used to synthesize SnO<sub>2</sub> powder. The starting precursors were tin(IV) chloride pentahydrate (SnCl<sub>4</sub>·5H<sub>2</sub>O) (Acros Organics, Belgium), sodium hydroxide (NaOH) (Sigma-Aldrich, USA) and hydrochloric acid (HCl) (Centrohem, Serbia). Initially, HCl and distilled water were mixed and stirred on a magnetic stirrer, at 50 °C, for 30 min, to produce the solution with a pH between 0 and 1. Further, SnCl<sub>4</sub> × 5H<sub>2</sub>O (17.529 g) was added and the mixed solution was homogenized under constant stirring. The NaOH solution was added dropwise until the pH value of the solution reached 9. After this process, a whitish liquid was formed and transferred to the autoclave and heated to 180 °C for 12 h. The obtained powders were filtered and dried.

Fabrication of an interdigitated electrodes (IDE) structure and functionalization of the synthesized powders was achieved by screen-printing, using an EKRA 2H screen printer. Silver IDEs were printed using commercial Novacentrix Metalon paste with 75% of Ag loading. The SnO<sub>2</sub>-based screen-printing paste, used for deposition of the sensitive layer, was prepared by dispersing 2 g of SnO<sub>2</sub> synthesized nanoparticles into 400 μl of terpineol (Sigma-Aldrich). To this dispersion, 600 ml of polyvinyl pyrrolidone (Sigma-Aldrich) ethanol solution (1 g/10 ml) was added. Then, dispersion was treated with an ultrasonic horn for 5 min and the obtained paste was left at room temperature to dry for 24 h. The dried film was treated at 100 °C for 2 h.

X-ray diffraction (XRD) measurements were performed on a Rigaku MiniFlex600 system in the 20° to 80° range, with 0.03° scan step. Scanning electron microscopy (SEM) images were taken with JEOL JSM 6460 LV microscope. Micro-Raman measurements were performed on a Tri Vista 557 Raman system equipped with a nitrogen-cooled charge-coupled device (CCD) detector, using a 532 nm laser line (Coherent Verdi G) as an excitation source. Electrical analysis was performed using the impedance spectroscopy measurements on SP-200 Biologic potentiostat/galvanostat, in the 10 Hz–7 MHz frequency range. DC measurements were collected on a Yokogawa–Hewlett–Packard 4145A semiconductor probe analyzer. Gas-sensing performance was evaluated using a custom-built chamber equipped with nitrogen purging inlet/outlet, evaporator and fan. Photocurrent measurements were collected using a custom-built set-up with high power LED, operating at 365 nm with power of 100 mW.

## 3. Results and discussion

XRD spectra of the synthesized SnO<sub>2</sub> powder is shown in figure 1(a). The diffraction peaks can be indexed to tetragonal rutile phase characteristics for tin oxide, with corresponding Miller indices denoted for each diffraction peak according to

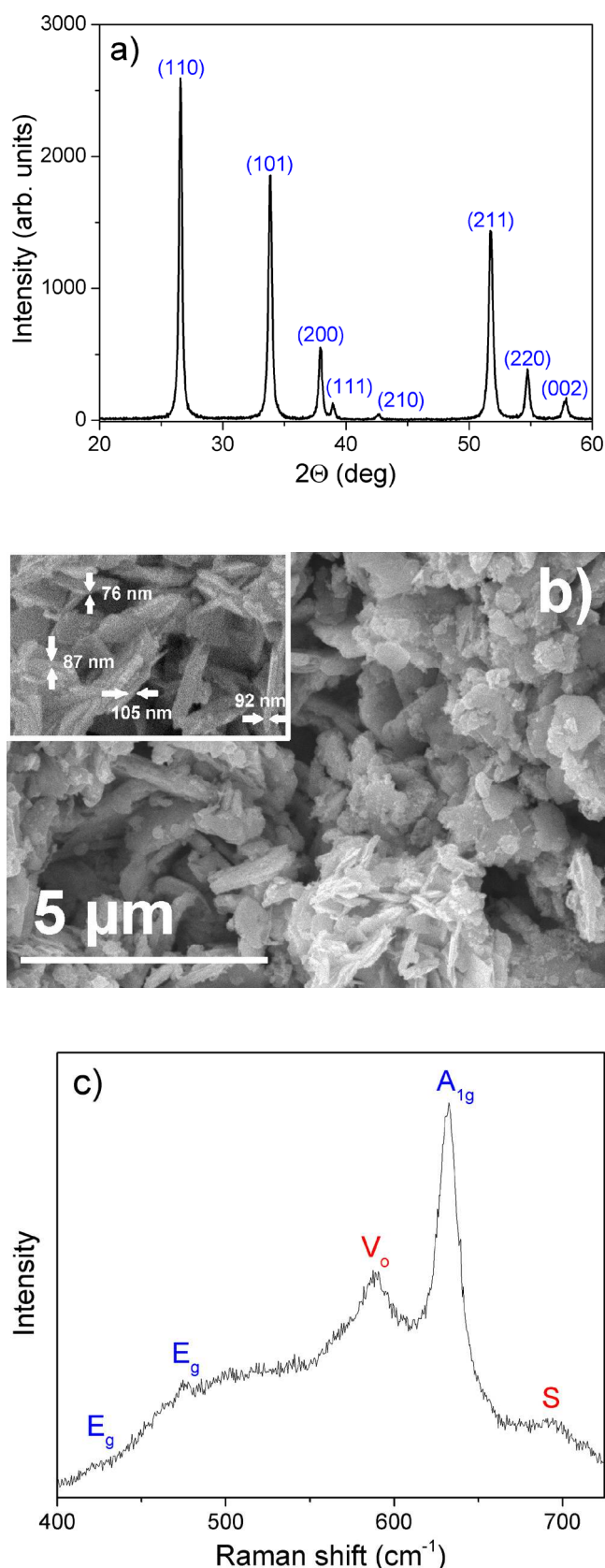


**Figure 1.** Structural and morphological characterization. (a) XRD spectra of the synthesized SnO<sub>2</sub> powder. (b) Large area SEM image of the nanosheets. The inset shows magnified image with denoted sheet thicknesses. (c) Raman spectra of the synthesized SnO<sub>2</sub> nanosheets.

JCPDS card 21-1250. No traces of impurities or other phases were observed. Sharp and narrow diffraction peaks suggest good crystallinity of powders composed of larger crystallites, even though the low hydrothermal temperature was used. The most intense peak in the diffraction spectra comes from the (110) plane, unlike the reported spectra for some sintered and crystalline SnO<sub>2</sub> samples, where (101) peak is dominant [28]. Calculation of the relative ratios between the intensities of the main diffraction peaks in figure 1(a), in comparison with the literature data [28], leads to the assumption that synthesized crystallites have a preferable (110) orientation. Such an assumption is justified with several theoretical and experimental studies [29–31], which demonstrated that (110) is the most stable surface of tin oxide with the lowest formation energy.

The morphology and particle size of the SnO<sub>2</sub> powders were investigated by the SEM technique. An SEM micrograph of the SnO<sub>2</sub> nanosheets is given in figure 1(b). The inset of figure 1(b) shows a magnified SEM image with determined thicknesses of several representative nanosheets. As shown, synthesized SnO<sub>2</sub> powder is composed of nanosheets whose lateral dimensions are in the 1 μm–10 μm range and the thickness of the individual sheets is around 100 nm.

Based on analysis of XRD and SEM results, it can be noted that selected parameters of the synthesis process produce exposed surfaces of the SnO<sub>2</sub> nanosheets with dominant (110) surface termination, which is most suitable for gas-sensing applications [31].

Figure 1(c) presents Raman spectra of the synthesized SnO<sub>2</sub> nanosheets in the 400 cm<sup>-1</sup>–750 cm<sup>-1</sup> range.

The most prominent peak and two weak features are assigned to first order Raman active phonons of SnO<sub>2</sub> rutile structure (triply-degenerate E<sub>g</sub> mode and doubly-degenerate A<sub>2g</sub> mode) [32]. A very interesting feature in the presented spectra is the appearance of the defect-related mode (V<sub>o</sub>) at 580 cm<sup>-1</sup> attributed to the formation of oxygen vacancies and surface mode (S) at 690 cm<sup>-1</sup> which is activated by surface structural disorder [32, 33]. Reported results by Diéguez *et al* [32] and Romyantseva *et al* [33] provide clear evidence that the Raman intensity of these modes is strongly related to surface oxygen species, with a strong influence on the gas-sensing properties of SnO<sub>2</sub> nanomaterials. A pronounced V<sub>o</sub> peak in the measured spectrum is a fingerprint of the high concentration of the oxygen vacancies in the synthesized nanosheets with high potential for applications in sensing technologies.

After successful synthesis and characterization, the SnO<sub>2</sub> nanosheets were functionalized into sensor components using versatile screen-printing technology. A PET substrate was chosen as a flexible platform for integration of a sensor transducer and sensitive layer, because this material is extensively used in modern food and beverage packaging technology. Transducer fabrication was performed by screen-printing of Ag paste in the form of IDEs on the PET substrate. Printed silver paste was cured at 200 C for 1 h and the resulting IDE structure has 200 microns width of individual digits and 100 microns gap between the digits. The effective surface area of

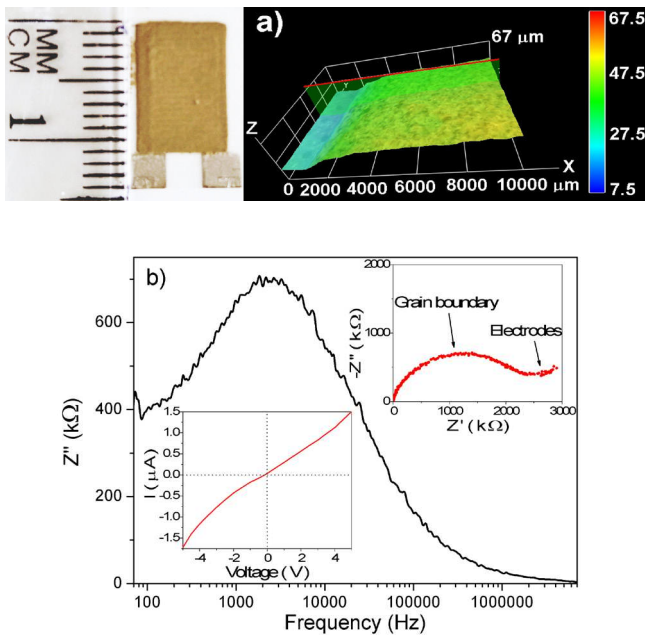


**Figure 2.** (a) (Left) Image of the printed SnO<sub>2</sub> nanosheets on the IDE electrodes and PET substrate. (Right) 3D profile of the screen-printed film, determined with optical profilometry. (b) Imaginary part of complex impedance as a function of frequency. The upper right inset presents the Cole–Cole plot extracted from the impedance measurements. The lower left inset shows DC characterization in the form of  $I(V)$  curves.

the electrodes is 28 mm<sup>2</sup>. Next, the paste with SnO<sub>2</sub> nanoparticles was screen-printed on top of the electrodes. The resulting printed device, exhibited in figure 2(a), is featured by thickness of 32 μm and has a uniform coverage of the IDE structure, with a relatively flat surface as presented in the 3D optical profile image.

AC electrical characterization of the designed sensor device was performed using the impedance spectroscopy measurements in the 10 Hz–7 MHz frequency range and the obtained results are shown in figure 2(b). Electrical response of polycrystalline materials is commonly described using an approximate microstructure model combining grain regions, grain boundaries regions and electrodes [6]. The dependence of the imaginary part of the impedance ( $Z''$ ) with frequency revealed a single broad peak. The appearance of such peaks in the impedance spectrum is a signature of relaxation processes that occur during the current transport and they can be described with the mentioned microstructure model. The main peak in the imaginary part of impedance is centered at a frequency of 2.6 kHz, which could be used for extracting the value of electronic relaxation time in the material  $\tau = 1/f \approx 0.4$  ms. A relatively long relaxation time is favourable for photovoltaic and photocatalytic applications, since it can ensure a longer lifetime of photo or thermally generated electron-hole pairs. In the upper right inset of figure 2(b), the Cole–Cole plot extracted from impedance measurements is shown. The single semicircle arc observed in the Cole–Cole plot can be attributed to grain boundary electrical resistance and the onset of the uncomplete arc can be ascribed to the contribution of the electrode resistance (for the frequencies below 100 Hz)

[34, 35]. The origin of the dominant grain boundary resistance can be explained by taking into account the results of the SEM measurements, where it was established that the synthesized powder consists of nanosheets with a lot of contact surfaces between individual particles. Additional charge is accumulated at the opposite sides of the contact surfaces, disrupting the electron flow between the nanosheets and giving rise to the so-called interfacial polarization in impedance measurements. The intersection of the Cole–Cole plot with the  $Z'$  axis occurs near the origin, which reveals negligible grain resistance ( $R_g \approx 0$ ).

From the diameter of the existing semicircle (figure 2(b), inset), we could estimate grain boundary resistance  $R_{gb} \approx 2.7$  kΩ, as well as microscopic electrical conductivity:

$$\sigma_{gb} = \frac{1}{R_{gb}} \left( \frac{L}{A} \right) \approx 20.25 \text{ S m}^{-1}.$$

Furthermore, the capacitance of grain boundary  $C_{gb} \approx 0.14$  μF is calculated from the value of relaxation time and grain boundary resistance [18].

DC electrical characterization is shown in the lower left inset of figure 2(b), as the  $I(V)$  curve measured in the  $-5$  V to  $+5$  V range. The curve has a linear response in the wide voltage range, indicating ohmic contacts between the printed film and electrode surface. The prepared device exhibits very good current values in comparison to similar resistive oxide-based sensors [6–8, 35], which represents a very good starting point for application of the synthesized SnO<sub>2</sub> nanomaterial in sensing devices. DC conductivity  $\sigma_{DC} = 6.7$  S m<sup>-1</sup> of nanosheets was calculated from  $I(V)$  measurements. From direct comparison of AC/DC measurements, it can be noted that the main contribution to electrical resistance in the DC regime also comes from the detected interfacial polarization, which can be observed as a low frequency tail of the main peak in the  $Z''$  spectrum in figure 2(b).

Afterwards, the gas-sensing performance of the SnO<sub>2</sub> printed device was investigated. In figure 3(a), the dynamic gas response curves are shown, for the SnO<sub>2</sub> nanosheets, towards different concentrations of ethanol (from 10 ppm to 500 ppm), measured at room temperature and low relative humidity (10% RH). Sensor response is defined as the ratio between air (Ra) and target gas (Rg) resistivities ( $S = R_a/R_g$ ). Variations in sensor response are typical for n-type semiconductor materials and the sensor shows a high response for the investigated ppm concentrations of ethanol. The response and recovery times are shown in the inset of figure 3(a). The printed sensor has average response times and relatively good and stable recovery times, even at higher levels of ethanol vapor, which is very important for sensing performance.

For practical applications, the ethanol concentration of 50 ppm is of great interest, since it is the concentration usually measured by breath analyzers and food decay monitors [36, 37]. Therefore, we have conducted selectivity testing to establish the influence of the most common interfering VOC gases and humidity on the performance of the designed sensor. In figure 3(b), time resolved gas responses of the SnO<sub>2</sub> nanosheets towards 30% RH and 50 ppm of ethanol, 2-propanol and acetone vapor are compared. The obtained results

**Table 1.** Comparison of the gas sensing performance of hydrothermally synthesized SnO<sub>2</sub> nanomaterials. In the table, morphology, hydrothermal temperature, transducer design, response and recovery times, sensor response, selectivity and operating temperature are presented from the literature data.

Morphology	ht temp (°C)	transducer	Resp/Rec time	Response	Selectivity feature	Operating temp	Ref
SnO <sub>2</sub> /graphene composite	120	Ceramic + Au IDE	/	15	NH <sub>3</sub>	RT	[40]
SnO <sub>2</sub> @rGO composite	180	Al <sub>2</sub> O <sub>3</sub> + Au IDE	61 s/330 s	47.6%	CH <sub>4</sub>	150 C	[41]
Porous nanotubes	160	Al <sub>2</sub> O <sub>3</sub> tube + Au electrodes	6 s/20 s	7.5	/	/	[42]
Porous nanosheets	120	Al <sub>2</sub> O <sub>3</sub> tube + Au electrodes	<10 s	6	Ethanol	300 C	[17]
Flower-like structures	180	/	20 s/15 s	87	No	250 C	[43]
Nanoneedles and nanosheets	180	Al <sub>2</sub> O <sub>3</sub> tube + Au electrodes	6 s–21 s	33–65	Ethanol	240 C	[15]
Hollow spheres	120	/	5 s	11	No	350 C	[44]
Nanosheets	180	PET + Ag IDE	100 s/40 s	1.3	Ethanol	RT	This work

clearly show that humidity has the strongest influence on the sensor performance at room temperature. A recent study [38] has demonstrated that activation of ethanol sensing on the SnO<sub>2</sub> surface is driven by low levels of humidity, but the intricate detection mechanism is quite different for ethanol and humidity, offering the tool for eliminating the influence of humidity by calibration. In comparison with other VOC gases, the investigated sensor has a higher response towards ethanol with faster response/recovery times, whereas the response is significantly lower for 2-propanol and acetone.

The inset of figure 3(b) shows variation in sensor response for different VOC concentrations. The limit of detection (LOD) for ethanol was obtained from the linear fit of experimental data, shown in the inset of figure 3(b), and the calculated value of 1.5 ppm suggests that SnO<sub>2</sub> nanosheets have very good operating sensitivity in the 1 ppm to 500 ppm range. Reported DFT calculations [30, 31] have established that a SnO<sub>2</sub> (1 1 0) surface has the highest adsorption affinity for gas molecules and therefore offer very good sensing characteristics. Keeping in mind the above mentioned findings, it can be stated that good sensitivity and selectivity originate from unique surface termination, morphology and defect structure of the synthesized SnO<sub>2</sub> nanosheets. In comparison with the previously reported data on hydrothermally synthesized SnO<sub>2</sub> nanomaterials, presented in table 1, the obtained results in the presented research suggest that the undertaken approach offers relatively good sensing characteristics of the synthesized nanosheets. One of the most important advancements in the presented research can be viewed through utilization of low cost technology for sensor fabrication and in the use of low hydrothermal temperature with no subsequent calcination steps for obtaining the high quality SnO<sub>2</sub> nanosheets, with ethanol selectivity feature.

In order to fully exploit the potential offered by the hydrothermally synthesized SnO<sub>2</sub> nanosheets, time-resolved photoconductivity measurements of the same sensor were performed, as shown in figure 4. Analysis of the obtained measurements and comparison with literature data [39] revealed that synthesized SnO<sub>2</sub> nanosheets produce high photocurrent

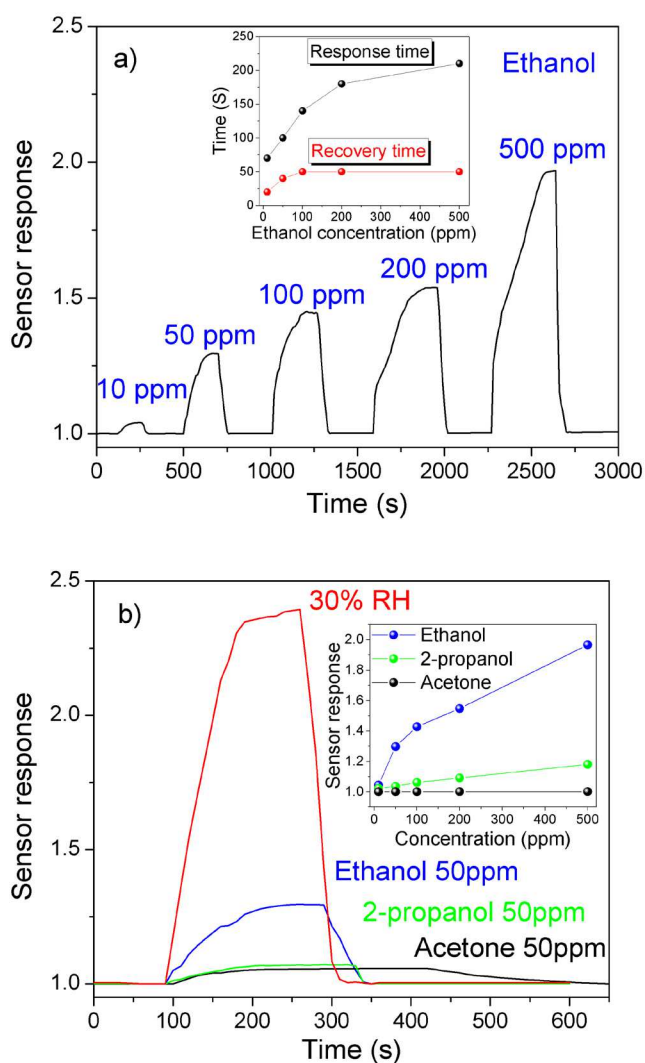


**Figure 3.** Characterization of gas sensing properties. (a) Time resolved gas sensing measurements of the SnO<sub>2</sub>-based sensor for different concentrations of ethanol, at room temperature. (b) Dynamic response of the investigated sensor towards 30% RH and 50 ppm of ethanol, 2-propanol and acetone. The inset shows variation in sensor response for different VOC concentrations.



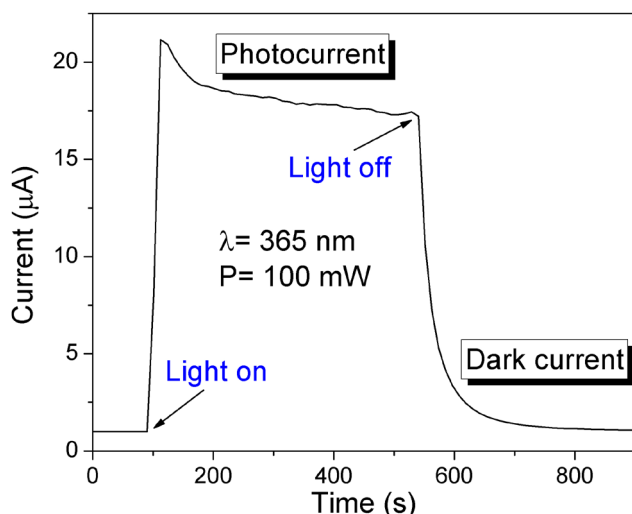


**Figure 4.** Time-resolved photocurrent response of the screen printed SnO<sub>2</sub> nanosheets.

values and that the sensor exhibits good photoconversion rates suitable for UVA (315 nm–400 nm) radiation monitoring, but the rise and decay times (22 s and 67 s) are average and not suitable for fast photodetection.

The major influence on the good photoconversion properties of SnO<sub>2</sub> nanosheets can be ascribed to specific surface morphology and the formation of oxygen vacancies in the crystal lattice, which was detected with SEM measurements and Raman spectroscopy. Previous studies [29, 30] demonstrated that oxygen vacancies introduce additional electronic states above the O 2p valence band, which can have a strong impact on the measured electronic relaxation time (figure 2(b)), the lifetime of the photogenerated electron–hole pair and the observed good photoconversion rate for the UVA radiation.

#### 4. Conclusion

In summary, SnO<sub>2</sub> powder, with a unique structure, shape and surface morphology, was synthesized by the hydrothermal method. Results from XRD, SEM and Raman measurements revealed that the synthesized sample exhibits a rutile crystal structure, with a crystallite size in the micrometer range and that the investigated powder consists of plane-shaped nanosheets with a high concentration of oxygen vacancies. Paste with SnO<sub>2</sub> nanosheets was screen-printed on a flexible PET substrate with IDEs. AC measurements revealed only a single relaxation time characteristic for interfacial polarization, which originates from the contact surfaces between SnO<sub>2</sub> nanosheets. DC measurements showed that the designed device exhibits very good conductivity with linear dependence of the sensor current with applied voltage. Gas-sensing performance was evaluated at room temperature through the detection of humidity and VOC vapors. The designed sensor showed good response to ethanol in

comparison to 2-propanol and acetone indicating selectivity feature of the SnO<sub>2</sub> nanosheets. Moreover, photocurrent measurements showed that the printed flexible sensor has very good photoconversion rate suitable for the UVA radiation detection and monitoring.

#### Acknowledgments

This work was supported by the Serbian Ministry of Education, Science and Technological Development through projects III44006, III45021 and OI171032.

#### ORCID iDs

Marko Radović  <https://orcid.org/0000-0001-7565-4015>

#### References

- [1] Wang D, Liu S, Shao M, Zhao J, Gu Y, Li Q, Zhang X, Zhao J and Fang J 2018 *Materials* **11** 1774
- [2] Bakr Z H, Wali Q, Ismail J, Elumalai N K, Uddin A and Jose R 2018 *Electrochim. Acta* **263** 524
- [3] Ghodsi V and Radovanovic P V 2018 *Chem. Mater.* **30** 3578
- [4] Vasanthi V, Kottaisamy M, Anitha K and Ramakrishnan V 2018 *Mater. Sci. Semicond. Process.* **85** 141
- [5] Huang H, Ng N, Wu Y and Kong L 2015 *Mater. Des.* **88** 38
- [6] Kaur M, Gupta S K, Betty C A, Saxena V, Katti V R, Gadkari S C and Yakhmi J V 2005 *Sensors Actuators B* **107** 360
- [7] Das S and Jayaraman V 2015 *Prog. Mater. Sci.* **67** 161
- [8] Ambardekar V, Bandyopadhyay P P and Majumder S B 2018 *J. Alloys Compd.* **752** 440
- [9] Wu S, Cao H, Yin S, Liu X and Zhang X 2009 *J. Phys. Chem. C* **113** 17893
- [10] Kong Z, Liu D, Liu X, Fu A, Wang Y, Guo P and Li H 2019 *J. Nanosci. Nanotechnol.* **19** 850
- [11] Yann J, Xu M, Zhang F, Ruan X, Yun J, Zhangn Z and Liao F 2016 *Mater. Lett.* **165** 243
- [12] Guo C, Cao M and Hu C 2004 *Inorg. Chem. Commun.* **7** 929
- [13] Zhao B, Fan B, Shao G, Zhao W and Zhang R 2015 *ACS Appl. Mater. Interfaces* **7** 18815
- [14] Li Y, Liu T and Zhang H 2016 *Mater. Lett.* **176** 9
- [15] Xu L, Zeng W and Li Y 2018 *Appl. Surf. Sci.* **457** 1064
- [16] Sun P, Cao Y, Liu J, Sun Y, Ma J and Lu G 2011 *Sensors Actuators B* **156** 779
- [17] Guo J, Zhang J, Ju D, Xu H and Cao B 2013 *Powder Technol.* **250** 40
- [18] Tao T, He L, Li J and Zhang Y 2015 *Mater. Lett.* **138** 45
- [19] Wan W, Li Y, Ren X, Zhao Y, Gao F and Zhao H 2018 *Nanomaterials* **8** 112
- [20] Yan S, Liang X, Song H, Ma S and Lu Y 2018 *Ceram. Int.* **44** 358
- [21] Li Y 2018 *Physica E* **96** 54
- [22] Zhang W, Zeng W, Miao B and Wang Z C 2015 *Appl. Surf. Sci.* **355** 631
- [23] Zhao C, Gong H, Lan W, Ramachandran R, Xu H, Liu S and Wang F 2018 *Sensors Actuators B* **258** 492
- [24] Chen J S and Lou X V 2013 *Small* **9** 1877
- [25] Paulowicz I et al 2015 *Adv. Electron. Mater.* **1** 1500081
- [26] Manikandan K, Dhanuskodi S, Thomas A R, Maheswari N, Muralidharan G and Sastikumar D 2016 *RSC Adv.* **6** 90559

- [27] Han S T, Peng H, Sun Q, Venkatesh S, Chung K S, Lau S C, Zhou Y and Roy V A L 2017 *Adv. Mater.* **29** 1700375
- [28] Floriano E A, de Andrade Scalvi L A, Sambrano J R and Geraldo V 2010 *Mater. Res.* **13** 437
- [29] Cox D F, Fryberger T B and Semancik S 1989 *Surf. Sci.* **224** 121
- [30] Mäki-Jaskari M A and Rantala T T 2002 *Phys. Rev. B* **65** 245428
- [31] Chen Y, Wang X, Shi C, Li L, Qin H and Hu J 2015 *Sensors Actuators B* **220** 279
- [32] Diéguez A, Romano-Rodríguez A, Vila A and Morante J R 2001 *J. Appl. Phys.* **90** 1550
- [33] Romyantseva M N, Gaskov A M, Rosman N, Pagnier T and Morante J R 2005 *Chem. Mater.* **17** 893
- [34] Barsoukov E and Macdonald J R 2005 *Impedance Spectroscopy: Theory, Experiment, and Applications* (New York: Wiley)
- [35] Ponce M A, Bueno P R, Varela J, Castro M S and Aldao C M 2008 *J. Mater. Sci.: Mater. Electron.* **19** 1169
- [36] Righettoni M, Amann A and Pratsinis S E 2015 *Mater. Today* **18** 163
- [37] Matindoust S, Baghaei-Nejad M, Abadi M H S, Zou Z and Zheng L R 2016 *Sens. Rev.* **36** 169
- [38] Zhu H, Li Q, Ren Y, Gao Q, Chen J, Wang N, Deng J and Xing X 2018 *Small* **14** 1703974
- [39] Zhai T, Fang X, Liao M, Xu X, Zeng H, Yoshio B and Golberg D 2009 *Sensors* **9** 6504
- [40] Lin Q, Li Y and Yang M 2012 *Sensors Actuators B* **173** 139
- [41] Navazani S, Shokuhfar A, Hassanisadi M, Askarieh M, Carlo A D and Agresti A 2018 *Talanta* **181** 422
- [42] Zhang J, Guo J, Xu H and Cao B 2013 *ACS Appl. Mater. Interfaces* **5** 7893
- [43] Zhou Q, Chen W, Li J, Tang C and Zhang H 2015 *Mater. Lett.* **161** 499
- [44] Wang B, Sun L and Wang Y 2018 *Mater. Lett.* **218** 290



## Influence of oxygen vacancy defects and cobalt doping on optical, electronic and photocatalytic properties of ultrafine SnO<sub>2-δ</sub> nanocrystals

Zorana D. Dohčević-Mitrović<sup>1,\*</sup>, Vinicius D. Araújo<sup>2</sup>, Marko Radović<sup>3</sup>, Sonja Aškričić<sup>1</sup>, Guilherme R. Costa<sup>4</sup>, Maria Ines B. Bernardi<sup>4</sup>, Dejan M. Djokić<sup>1</sup>, Bojan Stojadinović<sup>1</sup>, Marko G. Nikolić<sup>5</sup>

<sup>1</sup>Nanostructured Matter Laboratory, Institute of Physics Belgrade, University of Belgrade, Pregrevica 118, 11080 Belgrade, Serbia

<sup>2</sup>NanoA-UACSA, Universidade Federal Rural de Pernambuco, UFRPE, Cabo de Santo Agostinho, PE, Brazil

<sup>3</sup>University of Novi Sad, Group for Nano and Microelectronics, Biosense Institute, Novi Sad, Serbia

<sup>4</sup>Instituto de Física de São Carlos, Universidade de São Paulo, USP, 13560-970, São Carlos – SP, Brasil

<sup>5</sup>Institute of Physics Belgrade, University of Belgrade, P.O. Box 68, Pregrevica 118, 11080 Belgrade, Serbia

Received 12 November 2019; Received in revised form 21 February 2020; Accepted 15 March 2020

### Abstract

Ultrafine pure and cobalt doped SnO<sub>2-δ</sub> nanocrystals (Sn<sub>1-x</sub>Co<sub>x</sub>O<sub>2-δ</sub>, 0 ≤ x ≤ 0.05) were synthesized by microwave-assisted hydrothermal method. The as-prepared nanocrystals have single phase tetragonal rutile structure. With increase of Co content (x > 0.01), Co entered into SnO<sub>2</sub> lattice in mixed Co<sup>2+</sup>/Co<sup>3+</sup> state. Pronounced blue shift of the band gap with cobalt doping originated from the combined effect of quantum confinement and Burstein-Moss shift. Raman and photoluminescence study revealed oxygen deficient structure of SnO<sub>2-δ</sub> for which the prevalent defects are in the form of in-plane oxygen vacancies. Co-doping induced decrease of in-plane oxygen vacancy concentration and luminescence quenching. SnO<sub>2-δ</sub> exhibited significantly better photocatalytic activity under UV light irradiation, than Co-doped samples due to better UV light absorption and increased concentration of in-plane oxygen vacancies which, as shallow donors, enable better electron-hole separation and faster charge transport.

**Keywords:** SnO<sub>2</sub> nanopowders, wet-chemical synthesis, defects, optical properties, photocatalysis

### I. Introduction

Tin oxide (SnO<sub>2</sub>) is an n-type semiconductor with large band gap (3.6 eV) at room temperature. Because of its unique electronic, optical and electrochemical properties, SnO<sub>2</sub> is widely used in dye-sensitized solar cells, transparent conductive electrodes, solid state sensors, lithium-ion batteries and catalysis [1–7]. During the past decade, SnO<sub>2</sub> nanostructures have become one of the most important oxide nanostructures due to their exceptional properties and potential applications which are strongly influenced by size effects and morphology [8].

In the past decade various efforts were devoted to

the synthesis of SnO<sub>2</sub> nanostructures with controlled size and morphology. SnO<sub>2</sub> nanostructures like thin films, nanobelts, nanotubes or nanowires, nanodisks and nanocrystals have been prepared using different methods, such as carbothermal reduction process, hydrothermal and solvothermal, chemical vapour condensation, laser ablation, sol-gel and molten salt techniques [9–18]. However, for most of these methods relatively high temperatures are required during the synthesis process and the samples are usually subjected to additional thermal treatment in order to achieve good crystallinity. In recent years hydrothermal approaches appeared to be widely applied as SnO<sub>2</sub> nanostructures can be obtained with different morphologies and tunable size at mild temperatures [8,19]. Microwave-assisted hydrothermal

\* Corresponding author: tel: +381 113713024,  
e-mail: zordoh@ipb.ac.rs

synthesis (MAH) became a very promising method for obtaining size and morphology controllable oxide nanostructures due to the unique advantages, such as fast heating rate and uniform heating without superheating of the solvent, which results in small particle size, narrow size distribution and high purity of the obtained nanopowders. Therefore, MAH appeared to be very convenient method for obtaining ultrafine SnO<sub>2</sub> nanopowders [19,20].

SnO<sub>2</sub> nanostructures are generally less studied as potential photocatalysts compared to TiO<sub>2</sub> and ZnO, despite its crystalline structure being similar to TiO<sub>2</sub> and good properties such as high photochemical stability, non-toxic nature, strong oxidizing power, and low-cost [21]. In order to improve the photocatalytic efficiency of SnO<sub>2</sub>, selective doping with metal ions, transition metals (gold, manganese, silver and iron) and rare-earth elements (Ce, Sm, Gd) was performed and well presented in the review paper by Al-Hamdi *et al.* [21]. Among the transition metals, cobalt is rarely applied as dopant. In fact, there are only few papers dedicated to potential applicability of Co-doped SnO<sub>2</sub> nanostructures as photocatalysts [22–24], but none of them investigated the synergic influence of defective nature and Co-doping on photocatalytic properties of very fine SnO<sub>2</sub> nanocrystals. It is well known that photocatalytic efficiency of metal oxide nanostructures can be influenced by the presence of intrinsic defects such as oxygen vacancies [25–28]. The presence of oxygen vacancies strongly influences the charge recombination process and the band gap structure. Namely, oxygen vacancies introduce the defect levels (near conduction or valence band) inside the gap and behave as trapping centres for photogenerated carriers preventing the fast recombination. Besides, oxygen vacancies can facilitate the transferring of charge carriers to adsorbed species (OH<sup>-</sup> or water molecules and dissolved oxygen present on the surface of the catalyst) and enhance the formation of reactive radicals which are responsible for improved photocatalytic activity of oxide nanostructures [26,27]. Moreover, the formation of defect states inside the gap reduces the band gap and extends the absorption to visible light [25,27]. The prominent intrinsic defects in SnO<sub>2</sub> nanostructures are oxygen vacancies as well, which form donor/acceptor states inside the SnO<sub>2</sub> gap, influencing its electronic structure and making it conductive [4]. As oxygen vacancies play a critical role in many new physical phenomena, it is important to investigate associated changes in the optical and electronic properties of pure and Co-doped SnO<sub>2</sub> nanomaterials which can have a strong impact on photocatalytic activity of these materials.

In the work presented here, ultrafine, nonstoichiometric pristine and Co-doped SnO<sub>2-δ</sub> nanopowders were synthesized via simple and cost effective microwave-assisted hydrothermal method. This paper intends to explore how defective structure and Co-doping provoke changes of optical and electronic properties of

SnO<sub>2-δ</sub> nanocrystals influencing the photocatalytic performances.

## II. Experimental procedure

### 2.1. Materials preparation

Sn<sub>1-x</sub>Co<sub>x</sub>O<sub>2-δ</sub> (where  $x = 0, 1, 3$  and  $5$  mol%) nanopowders were synthesized by microwave-assisted hydrothermal method using SnCl<sub>4</sub> · 5 H<sub>2</sub>O (98%, Aldrich), CoCl<sub>2</sub> · 6 H<sub>2</sub>O, NaOH and HCl as starting precursors. Initially, 1 ml of hydrochloric acid was added to 10 ml of distilled water at 50 °C resulting in a solution with pH between 0 and 1. Next, 17.529 g of SnCl<sub>4</sub> · 5 H<sub>2</sub>O was added and the mixed solution was homogenized under stirring with simultaneous increasing of the water amount to approximately 50 ml. In a case of the doped samples, 0.119 g, 0.357 g and 0.595 g of CoCl<sub>2</sub> · 6 H<sub>2</sub>O were added to obtain 1, 3 and 5 mol% Co-doped samples, respectively. NaOH was added dropwise under vigorous stirring until the pH of the solution was adjusted to 8. The mixed solution was placed in a 110 ml sealed Teflon autoclave and subjected to microwave heating, applying 2.45 GHz of microwave radiation at a maximum power of 800 W. The as-prepared solution was heated at 140 °C for 10 min using heating rate of 14 °C/min and then air-cooled to room temperature. The as-prepared undoped and Co-doped SnO<sub>2-δ</sub> nanopowders were submitted to dialysis in order to be separated from the solution and then dried at 80 °C for 12 h.

### 2.2. Materials characterization

The crystalline structure and average crystallite size of the Sn<sub>1-x</sub>Co<sub>x</sub>O<sub>2-δ</sub> samples were evaluated using X-ray diffraction (XRD) measurements. The measurements were carried out using an automatic X-ray diffractometer (Rigaku, Rotaflex RU200B) with CuK $\alpha$  radiation (50 kV, 100 mA,  $\lambda = 1.5405$  Å) in a  $\theta$ - $2\theta$  configuration using a graphite monochromator. The  $2\theta$  scanning range was between 20 and 70°, with a step size of 0.02°. Microstructural analysis was made by transmission electron microscopy (TEM) FEI Titan 60-300 operating at voltages between 60 and 300 kV, using a field emission gun (FEG) with an objective lens (Super Twin) and a corrector that allows resolution of 0.08 nm.

Micro-Raman scattering measurements were performed at room temperature in the backscattering configuration on Tri Vista 557 Raman system equipped with a nitrogen-cooled CCD detector, using 532 nm laser line of optically pumped semiconductor laser (Coherent Verdi G) as an excitation source. UV-visible diffuse reflectance spectra were acquired with a Cary 5G spectrophotometer in the 200–800 nm range. Diffuse reflectance spectra were transformed into the absorbance spectra by the Kubelka-Munk method. The ellipsometric measurements were performed using high resolution variable angle spectroscopic ellipsometer (SOPRA GES5E-IRSE) of the rotating polarizer type. The data

were collected at room temperature in the UV-Vis spectral range with a resolution of 0.02 eV, for the incidence angle of 70°. Photoluminescence emission measurements were performed at room temperature using Spex Fluorolog spectrofluorometer with C31034 cooled photomultiplier under Xenon lamp excitation at 380 nm.

### 2.3. Photocatalytic experiments

The photocatalytic activity of the  $\text{Sn}_{1-x}\text{Co}_x\text{O}_{2-\delta}$  samples, for the degradation of methylene blue (MB) as model pollutant, was tested under UV illumination. The different samples with the same photocatalyst amount (150 mg/l) were immersed in 20 ml of an aqueous solution of methylene blue (5.0 mg/l). The beakers were placed in a photo-reactor at controlled temperature (15 °C), under magnetic stirring, and were illuminated by six 15 W UV lamps (TUV Philips, maximum intensity at 254 nm). The solution was placed in the dark for 60 min to reach the adsorption/desorption equilibrium before UV light exposure. Blank experiment without UV irradiation demonstrated no adsorption of MB dye on the surface of the  $\text{Sn}_{1-x}\text{Co}_x\text{O}_{2-\delta}$  samples. The photocatalytic experiments were conducted at the natural pH = 6 of MB dye. At regular time intervals 2 ml aliquots were taken, centrifuged to remove any catalyst particles and the concentration of the dye was determined by UV-Vis absorption spectrophotometer (Shimadzu-UV-1601 PC) monitoring the variation of absorbance at 663 nm.

The formation of hydroxyl radicals ( $\text{OH}^\bullet$ ) on the surface of the  $\text{SnO}_{2-\delta}$  sample under the UV light illumination was examined by photoluminescence (PL) technique using terephthalic acid (TA) as a probe molecule. The detailed experimental procedure was described in reference [29]. TA is known to react with  $\text{OH}^\bullet$  radicals induced on the photocatalyst's surface where it produces highly fluorescent 2-hydroxyterephthalic acid which shows an intense PL peak at around 425 nm. The intensity of this peak is proportional to the amount of  $\text{OH}^\bullet$  radicals [30,31] produced in the photocatalytic process. The changes of the 425 nm PL peak intensity were measured at room temperature using 315 nm excitation.

## III. Results and discussion

### 3.1. Crystal structure and morphology

Figure 1a shows XRD patterns of the  $\text{Sn}_{1-x}\text{Co}_x\text{O}_{2-\delta}$  ( $0 \leq x \leq 0.05$ ) nanopowders, whereas the Rietveld refined XRD spectra of the  $\text{SnO}_{2-\delta}$  and  $\text{Sn}_{0.95}\text{Co}_{0.05}\text{O}_{2-\delta}$  samples are presented in Figs. 1b and 1c. The XRD pat-

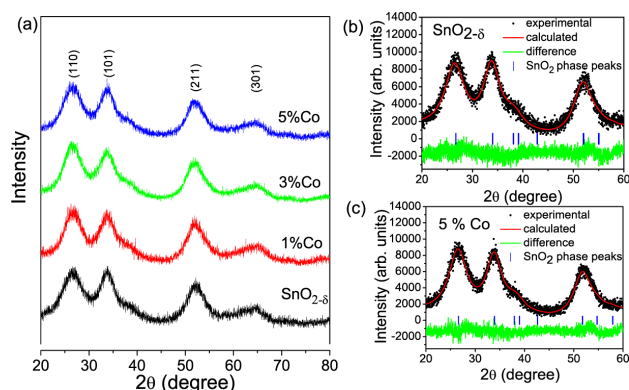


**Figure 1. XRD patterns of  $\text{Sn}_{1-x}\text{Co}_x\text{O}_{2-\delta}$  nanocrystals ( $0 \leq x \leq 0.05$ ) indexed to tetragonal rutile structure of  $\text{SnO}_2$  (a), Rietveld refined XRD spectra of  $\text{SnO}_{2-\delta}$  (b) and  $\text{Sn}_{0.95}\text{Co}_{0.05}\text{O}_{2-\delta}$  (c) nanoparticles**

terns of all the samples revealed single phase tetragonal structure (cassiterite phase). The XRD peaks at 26.6, 33.8, 51.9 and 65.8° can be assigned to (110), (101), (211) and (301) planes, which are in good agreement with literature data (ICDS № 9163). No secondary phases like Co oxides, Co clusters or other tin oxide phases were observed. Moreover, broad diffraction peaks of low intensities compared to those of bulk  $\text{SnO}_2$ , point to low crystallinity and small crystallite size of the  $\text{SnO}_2$  nanoparticles.

The average lattice parameters and unit cell volume obtained from the Rietveld refinement data are given in Table 1. These results showed an expansion of the  $\text{SnO}_2$  unit cell with increasing cobalt content up to 5%. This variation originates from the substitution of smaller  $\text{Sn}^{4+}$  cations (0.83 Å) with larger  $\text{Co}^{2+}$  cations in high spin state (0.89 Å) [32]. The slight shrinkage of the unit cell observed for the 5% Co-doped sample can be related to the presence of increased amount of smaller  $\text{Co}^{3+}$  cations (*ls*: 0.68 Å or *hs*: 0.75 Å). The average crystallite size (*D*) of the  $\text{Sn}_{1-x}\text{Co}_x\text{O}_{2-\delta}$  nanocrystals was calculated with the Scherrer formula using the 110 reflection and their values are reported in Table 1. Obviously, the mean crystallite sizes of the undoped and Co-doped samples are less than Bohr exciton radius (2.7 nm for  $\text{SnO}_2$ ) [33] and with increased Co-doping the crystallite size of the  $\text{Sn}_{1-x}\text{Co}_x\text{O}_{2-\delta}$  nanocrystals decreases. Such a trend implies that Co-doping has an inhibiting effect on the crystal growth. This inhibiting effect of Co on the crystal grains growth was already confirmed in the work of Babu *et al.* [34].

TEM images of the undoped and Co-doped  $\text{SnO}_{2-\delta}$  samples are presented in Fig. 2. TEM images revealed

**Table 1. Lattice parameters (*a*, *c*), unit cell volume (*V*) and average crystallite size (*D*) of the  $\text{Sn}_{1-x}\text{Co}_x\text{O}_{2-\delta}$  nanocrystals**

Sample	<i>a</i> = <i>b</i> [Å]	<i>c</i> [Å]	<i>V</i> [Å <sup>3</sup> ]	<i>D</i> [nm]
$\text{SnO}_{2-\delta}$	4.722 ± 0.002	3.180 ± 0.003	70.905	2.5
$\text{Sn}_{0.99}\text{Co}_{0.01}\text{O}_{2-\delta}$	4.747 ± 0.002	3.201 ± 0.003	72.131	2.4
$\text{Sn}_{0.97}\text{Co}_{0.03}\text{O}_{2-\delta}$	4.759 ± 0.002	3.206 ± 0.002	72.609	2.3
$\text{Sn}_{0.95}\text{Co}_{0.05}\text{O}_{2-\delta}$	4.744 ± 0.002	3.186 ± 0.002	71.703	2.2

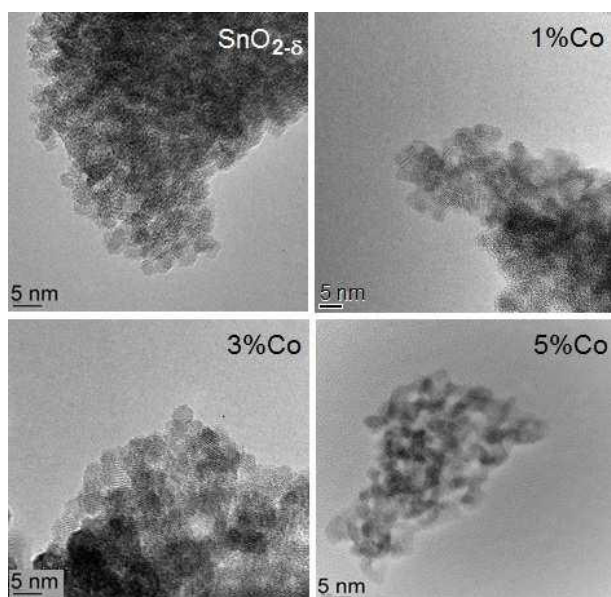


Figure 2. TEM images of  $\text{Sn}_{1-x}\text{Co}_x\text{O}_{2-\delta}$  ( $0 \leq x \leq 0.05$ ) nanoparticles

that the undoped  $\text{SnO}_{2-\delta}$  sample is composed of single crystalline nanoparticles of very small size and quasi-spherical shape. The morphology of the  $\text{Sn}_{1-x}\text{Co}_x\text{O}_{2-\delta}$  nanoparticles remained the same with Co-doping. The particles are of spherical shape with the size less than 3 nm, which is in good agreement with the results obtained from XRD data. The observed agglomeration of the  $\text{Sn}_{1-x}\text{Co}_x\text{O}_{2-\delta}$  nanoparticles can be ascribed to small crystallite sizes.

### 3.2. Raman analysis

$\text{SnO}_2$  tetragonal rutile crystalline structure (space group  $P4_2/mnm$ ) has four active Raman modes (non-degenerate  $A_{1g}$ ,  $B_{1g}$ ,  $B_{2g}$  modes, and a doubly degenerated  $E_g$  mode), two active infrared modes ( $A_{2u}$  and  $E_u$ ) and two silent modes ( $A_{2g}$ ,  $B_{1u}$ ) [35]. The positions of  $A_{1g}$ ,  $B_{1g}$ ,  $B_{2g}$  and  $E_g$  Raman modes in  $\text{SnO}_2$  single crystal under ambient conditions are 634, 123, 776 and 475  $\text{cm}^{-1}$ , respectively, and the  $A_{1g}$  and  $E_g$  modes are of much higher intensity compared to  $B_{1g}$  and  $B_{2g}$  modes [35].

The Raman spectra of nanocrystalline, non-stoichiometric  $\text{SnO}_{2-\delta}$  are modified in comparison with single-crystal or polycrystalline  $\text{SnO}_2$ , because Raman spectroscopy is more sensitive to intrinsic defects and confinement effect than conventional XRD technique. Namely, the position, bandwidth and intensity of Raman modes are size dependent, i.e. Raman modes are broadened, of lower intensity and shifted towards lower or higher energies depending on phonon dispersion curves. Besides, new modes of defect origin can appear [36,37]. The room temperature Raman spectra of the  $\text{Sn}_{1-x}\text{Co}_x\text{O}_{2-\delta}$  nanocrystals are presented in Fig. 3 and they are deconvoluted using Lorentzian profiles (full lines in Fig. 3).

In the Raman spectrum of the pure  $\text{SnO}_{2-\delta}$ , the most prominent mode is located at  $\sim 574 \text{ cm}^{-1}$ . This mode

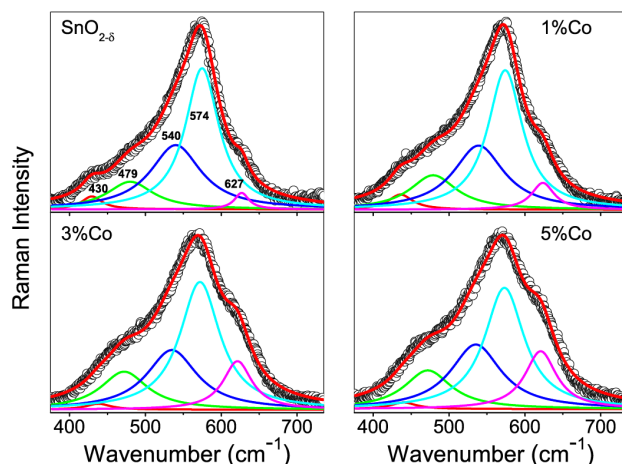


Figure 3. Deconvoluted room-temperature Raman spectra of  $\text{Sn}_{1-x}\text{Co}_x\text{O}_{2-\delta}$  nanoparticles

is characteristic for non-stoichiometric  $\text{SnO}_{2-\delta}$  and it is not present in the Raman spectra of  $\text{SnO}_2$  single-crystal [35]. Density functional calculations performed by Liu *et al.* [38] have shown that this mode arises from in-plane oxygen vacancies ( $V_{Oin}$ ) in the surface region of  $\text{SnO}_{2-\delta}$  nanoparticles, intensity of which is proportional to their concentration. In very fine nanoparticles this mode has the highest intensity due to the increased concentration of oxygen vacancies. Raman mode at  $\sim 627 \text{ cm}^{-1}$  can be ascribed to the  $A_{1g}$  mode of rutile  $\text{SnO}_2$  structure. This mode is of lower intensity, broadened and shifted to lower wave numbers compared to the bulk counterpart, due to the phonon confinement effect [37]. As the crystallite size of the undoped  $\text{SnO}_{2-\delta}$  is smaller than the Bohr exciton radius, the size effect can be very pronounced in this sample. Another broad Raman mode at  $\sim 479 \text{ cm}^{-1}$  is assigned to  $E_g$  mode and it is shifted to higher wavenumbers with size decrease of  $\text{SnO}_{2-\delta}$  nanocrystals [37]. Besides these modes, additional modes at around 430 and 540  $\text{cm}^{-1}$  appear. These new modes are usually seen in very fine  $\text{SnO}_2$  nanoparticles [37–39], nanotubes [40] or nanoribbons [41] because of the increased degree of local disorder, i.e. loss in long-range order due to the large number of lattice vacant positions, especially at the surface of nanoparticles. These modes are of high intensity in small nanoparticles and disappear with particle size increase. According to some literature data, due to the relaxation of the selection rules in nanostructured  $\text{SnO}_2$ , the mode at 540  $\text{cm}^{-1}$  is assigned to the Raman forbidden mode ( $B_{1u}$ ) [40,41], whereas the new mode at around 430  $\text{cm}^{-1}$  can be assigned to the oxygen vacancy clusters ( $V_C$ ) [39]. The  $A_{1g}$  and  $E_g$  modes exhibited redshift and broadening with Co-doping. The redshift and broadening of these modes are expected with substitution of  $\text{Sn}^{4+}$  ions with larger  $\text{Co}^{2+}$  ions and decreased crystallite size due to the phonon confinement effect. The positions and intensities of the  $A_{1g}$ ,  $E_g$  and oxygen vacancy related modes ( $V_{Oin}$  and  $V_C$ ) are presented in Fig. 4. As it can be seen from Fig. 4, the intensity of  $A_{1g}$  mode increases with increased Co concentration, whereas the intensity of  $E_g$

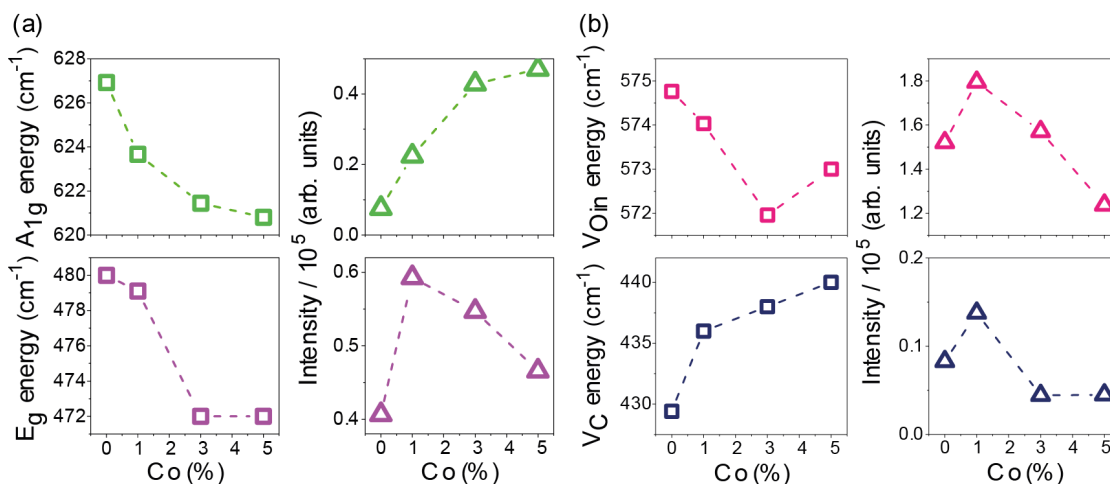


Figure 4. Positions and intensities of  $A_{1g}$  and  $E_g$  (a) and vacancy ( $V_{Oin}$  and  $V_C$ ) (b) Raman modes

mode is higher in the Co-doped samples compared to the undoped  $\text{SnO}_{2-\delta}$ . The  $E_g$  mode intensity slightly decreased in samples doped with higher Co content, as a consequence of lattice distortion and reduction in lattice space symmetry. The position of the Raman mode ascribed to in-plane oxygen vacancies ( $574\text{ cm}^{-1}$ ) did not change significantly, whereas the Raman mode related to vacancy clusters ( $430\text{ cm}^{-1}$ ) shifts to higher energies with Co-doping. The intensity of both modes decreased in the  $\text{Sn}_{0.97}\text{Co}_{0.03}\text{O}_{2-\delta}$  sample and this trend is more evident for the  $\text{Sn}_{0.95}\text{Co}_{0.05}\text{O}_{2-\delta}$  sample. The intensity reduction of oxygen vacancy related modes in these samples implies that the concentration of oxygen vacancies decreased. The decrease of the oxygen vacancy concentration is expected if the part of Co cations were in  $\text{Co}^{3+}$  state or if some Co cations were interstitially incorporated in  $\text{SnO}_{2-\delta}$  lattice [33,42].

In order to see if Co cations substituted  $\text{Sn}^{4+}$  in  $\text{Co}^{2+}$  state or the part of them was in  $\text{Co}^{3+}$  state, UV-Vis absorption measurements were performed and the absorption spectra of the  $\text{Sn}_{1-x}\text{Co}_x\text{O}_{2-\delta}$  samples are presented in Fig. 5. In the UV range, the absorption spectrum of  $\text{SnO}_{2-\delta}$  displays a strong absorption due to

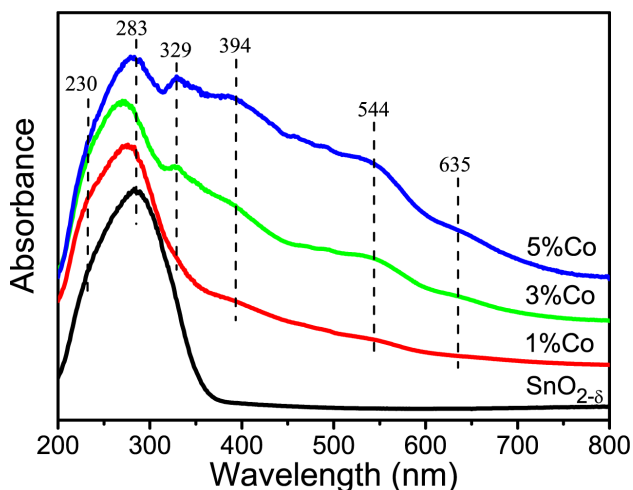


Figure 5. UV-Vis spectra of  $\text{Sn}_{1-x}\text{Co}_x\text{O}_{2-\delta}$  nanoparticles

the  $\text{SnO}_2$  interband transition. Two peaks at 230 and 283 nm are superimposed giving the broad band which might correspond to the surface  $\text{Sn}^{4+}$  species and to the  $\text{Sn}^{4+} \rightarrow \text{Sn}^{2+}$  intervalence charge transfer, respectively [43]. In Co-doped samples the broad band is shifted to lower wavelength implying the band gap increase with Co-doping. In the absorption spectra of the  $\text{Sn}_{0.97}\text{Co}_{0.03}\text{O}_{2-\delta}$  and  $\text{Sn}_{0.95}\text{Co}_{0.05}\text{O}_{2-\delta}$  samples, new bands appear. The band around 329 nm can be assigned to the partial change of oxidation state of  $\text{Co}^{2+}$  to  $\text{Co}^{3+}$  [44], whereas the broad band around 400 nm can be ascribed to  ${}^1A_{1g} \xrightarrow{\nu_2} {}^1T_{2g}$  transition of low spin  $\text{Co}^{3+}$  ions in octahedral environment [45]. The intensity of these bands increased in the  $\text{Sn}_{0.95}\text{Co}_{0.05}\text{O}_{2-\delta}$  sample pointing to the increased concentration of  $\text{Co}^{3+}$  ions. The bands around 544 and 635 nm can be related to  ${}^4A_2(F) \xrightarrow{\nu_2} {}^4T_1(P)$  transition of tetrahedral  $\text{Co}^{2+}$  species [45]. Therefore, from the absorption spectra of the  $\text{Sn}_{0.97}\text{Co}_{0.03}\text{O}_{2-\delta}$  and  $\text{Sn}_{0.95}\text{Co}_{0.05}\text{O}_{2-\delta}$  samples it can be deduced that part of Co cations entered into  $\text{SnO}_2$  lattice in  $\text{Co}^{3+}$  state, concentration of which increased with the increased dopant content. This result supports the finding obtained from the refined XRD spectrum of the  $\text{Sn}_{0.95}\text{Co}_{0.05}\text{O}_{2-\delta}$  sample, since the shrinkage of the unit cell was ascribed to the increased amount of  $\text{Co}^{3+}$  cations.

Our conclusions derived from absorption measurements are well-supported by recently published work of Roy *et al.* [46] concerning Co-doped  $\text{SnO}_2$  nanocrystals. From the XPS study, Roy *et al.* [46] confirmed the mixed valence nature of Co ions in the host lattice and they have found that the relative concentration of  $\text{Co}^{3+}$  exceeds that of  $\text{Co}^{2+}$  with the increase of dopant content. This study also showed that Co incorporation into  $\text{SnO}_2$  leads to the reduction of oxygen vacancies which is consistent with our Raman study.

### 3.3. Optical and electronic properties

The investigation of complex dielectric function by spectroscopic ellipsometry offers an insight into the

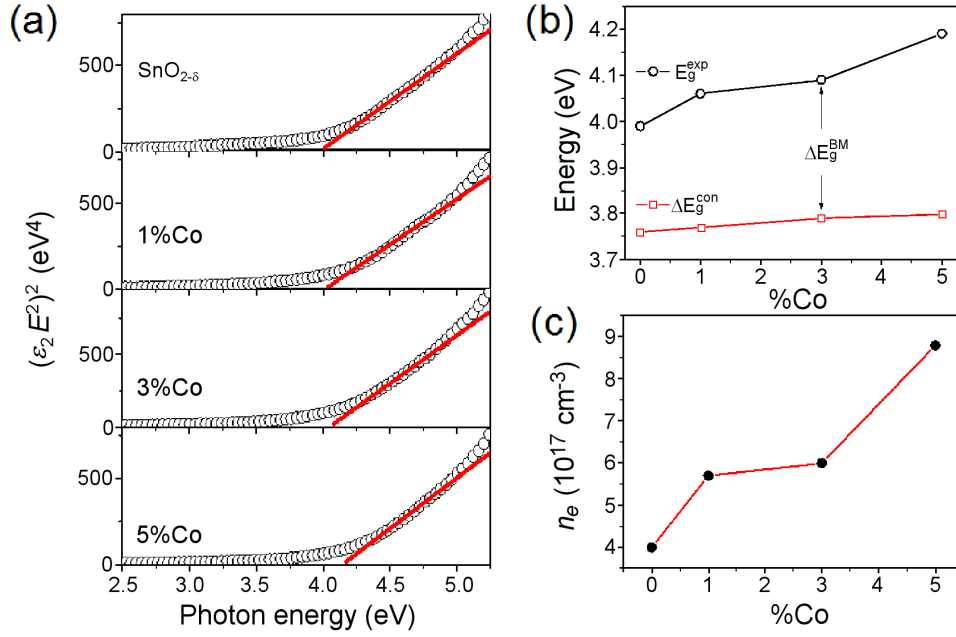


**Figure 6.** Determination of the direct band gap for  $\text{Sn}_{1-x}\text{Co}_x\text{O}_{2-\delta}$  nanoparticles using Tauc law(a); variation of the band gap energy obtained from ellipsometric measurements ( $E_g^{exp}$ ) and from quantum confinement model ( $\Delta E_g^{con}$ ) (b) and concentration of charge carriers  $n_e$  for  $\text{Sn}_{1-x}\text{Co}_x\text{O}_{2-\delta}$  samples (c)

most important optical properties of the nanomaterials, such as, optical band gap, interband and intraband transitions, defect electronic states. The imaginary part of dielectric function is directly related to the electronic density of states and in a case of nanopowders it can be deduced from the ellipsometric measurements by applying two-phase model approximation (in our case:  $\text{SnO}_{2-\delta}$  nanocrystals/air). In order to investigate the optical band gap behaviour and the influence of Co dopant on the absorption edge in  $\text{SnO}_{2-\delta}$  nanocrystals we applied the Tauc model for direct band gap transition [47], knowing that  $\text{SnO}_2$  is a direct band gap material [48]. In this case general expression for  $\epsilon_2(E)$  is:

$$(\epsilon_2 \cdot E^2)^2 = a(E - E_g) \quad (1)$$

where  $E$  is the photon energy,  $E_g$  is the band gap and  $a$  is the constant related to the density of states for the conduction band. The Tauc plots of the  $\text{Sn}_{1-x}\text{Co}_x\text{O}_{2-\delta}$  samples obtained from ellipsometric measurements are presented in Fig. 6a. Linear extrapolation to zero absorption (straight lines in Fig. 6a) gives the band gap energy values of the  $\text{Sn}_{1-x}\text{Co}_x\text{O}_{2-\delta}$  samples.

In Fig. 6b, the dependence of the band gap energy (from Fig. 6a) on dopant content for the  $\text{Sn}_{1-x}\text{Co}_x\text{O}_{2-\delta}$  samples is represented with open circles. It is obvious that Co-doping induces an increase of the  $E_g$ . Also, it is important to notice that all investigated samples have the band gap values higher than that for bulk  $\text{SnO}_2$ . Such changes in electronic properties of  $\text{SnO}_2$  nanomaterials can be a consequence of the quantum confinement effect. This effect causes an increase of the band gap value due to the stronger localization of electronic states inside the volume of nanocrystals. The band gap energy

shift, caused by this effect, can be calculated according to the following relation [49]:

$$\Delta E_g^{con} = E_g + \frac{\hbar^2 \pi^2}{2\mu \cdot D^2} \quad (2)$$

where  $E_g$  is the band gap value for the bulk  $\text{SnO}_2$  (3.6 eV),  $D$  is the crystallite radius and  $\mu$  is the reduced effective mass of the electron-hole pair. From the XRD results it was obtained that the average crystallite size of the undoped  $\text{SnO}_{2-\delta}$  nanocrystals is lower than Bohr exciton radius, and that it has a tendency of further decrease with Co-doping. Therefore, it is reasonable to take into account the quantum confinement effect in order to properly analyse the band gap behaviour of the  $\text{Sn}_{1-x}\text{Co}_x\text{O}_{2-\delta}$  samples. Taking the  $D$  values from Table 1 and knowing that  $\mu = 0.38m_0$  [48], the band gap values ( $\Delta E_g^{con}$ ) that arise from the quantum confinement effect were calculated using Eq. 2. The  $\Delta E_g^{con}$  values are presented in Fig. 6b with open squares. Comparing the  $\Delta E_g^{con}$  values with  $E_g^{exp}$  ones it is obvious that observed band gap increase of the  $\text{Sn}_{1-x}\text{Co}_x\text{O}_{2-\delta}$  samples cannot be ascribed only to the quantum confinement effect.

Another effect that can cause a shift of optical absorption edge to higher energies is the Burstein-Moss effect, which becomes more relevant in doped semiconductors (like transparent conducting oxides) with high charge carrier concentration. The Burstein-Moss effect is already registered in doped  $\text{SnO}_2$  thin films [50,51]. According to this effect, the widening of the optical gap is caused by metallic doping and increase of carrier density which leads to the filling of empty semiconductor electronic states in the vicinity of Fermi level and its shift to higher energies. Assuming parabolic bands and



spherical Fermi surface the band gap shift due to the Burstein-Moss effect can be calculated by simple relation [4]:

$$\Delta E_g^{BM} = \frac{h^2}{2\mu} (3\pi^2 \cdot n_e)^{2/3} \quad (3)$$

where  $h$  is Planck constant,  $\mu$  is the reduced effective mass and  $n_e$  is the carrier concentration.

Additional charge, i.e. increased charge carrier density in pure and doped  $\text{SnO}_{2-\delta}$  nanocrystals, can originate from the donor type defects like oxygen vacancies and Co-dopants. Raman spectra have already evidenced defective structure of  $\text{SnO}_{2-\delta}$ , whereas  $\text{Co}^{2+}$  dopants bring additional charge when substituting  $\text{Sn}^{4+}$  ions. Hence, the observed increase of the  $E_g$  from Fig. 6b can be ascribed to the Burstein-Moss shift ( $\Delta E_g^{BM}$ ). Combining Eqs. 2 and 3 it is possible to estimate the concentration of charge carriers ( $n_e$ ) in the  $\text{Sn}_{1-x}\text{Co}_x\text{O}_{2-\delta}$  samples and the obtained values are presented in Fig. 6c. These calculated values are in good agreement with literature data for  $\text{SnO}_2$  thin films [52]. As can be seen from Fig. 6c, doping of  $\text{SnO}_{2-\delta}$  nanocrystals with Co ions causes an increase of the charge carriers concentration and shift of the optical absorption edge toward UV region, making the investigated material more conductive and at the same time more transparent.

It is well known that large number of defects, such as oxygen vacancies or vacancy clusters, can be formed at the  $\text{SnO}_2$  nanoparticles surface and subsurface [21]. Intrinsic oxygen vacancies can be of three types: in-plane ( $V_{Oin}$ ), bridging ( $V_{OB}$ ) and subbridging ( $V_{OSB}$ ) vacancies [36,38]. These vacancies can be in different charge states, i.e. vacancies which trap one, two or none electrons, so called  $F^+$ ,  $F^0$  and  $F^{++}$  centres, and they can form defect levels inside the  $\text{SnO}_{2-\delta}$  gap [53]. Among the optical spectroscopy methods, photoluminescence (PL) spectroscopy is convenient method to investigate the defect structure of the pure and Co-doped  $\text{SnO}_{2-\delta}$  samples.

Room temperature PL spectra of the  $\text{SnO}_{2-\delta}$ ,  $\text{Sn}_{0.99}\text{Co}_{0.01}\text{O}_{2-\delta}$  and  $\text{Sn}_{0.95}\text{Co}_{0.05}\text{O}_{2-\delta}$  samples using a wavelength of 380 nm for excitation are presented in Fig. 7a. The PL spectrum of  $\text{SnO}_{2-\delta}$  is deconvoluted

into four Gaussian peaks centred at 510, 575, 470 and 446 nm (inset of Fig. 7a). In the deconvoluted PL spectrum of the undoped  $\text{SnO}_{2-\delta}$  two bands dominate: broad intense band centred at around 510 nm and another band of lower intensity at around 575 nm. Since the excitation and emissions are both lower than the band gap of  $\text{SnO}_{2-\delta}$ , neither of these PL bands can be ascribed to the recombination of the Sn 4p conduction electrons with a holes from a O 2p band. The broad green luminescence around 510 nm is already seen in  $\text{SnO}_2$  thin films [10] and nanoparticles [36] and it was attributed to the in-plane oxygen vacancy defects [36]. Therefore, the strong PL peak at 510 nm (2.45 eV) is ascribed to  $V_{Oin}$  defects. This finding is in accordance with corresponding Raman spectrum in which the most prominent Raman mode originates from in-plane oxygen vacancies. Another PL band at 575 nm (2.15 eV) can be ascribed to the isolated bridging oxygen vacancy defects, i.e. singly ionized  $F^+$  defects [53]. The PL bands around 470 and 440 nm were seen in  $\text{SnO}_2$  nanopowders [54]. These PL bands obtained with similar excitation line as in our case were ascribed to have excitonic origin [54]. It is well known that excitonic bands are formed near the band edge and they are usually of much narrower bandwidth than PL bands which originate from defect structures. As the band gap of the  $\text{SnO}_{2-\delta}$  sample is around 4 eV, it can be concluded that PL bands at 446 and 470 nm lie deeper in the gap. Hence, it is unlikely that these two bands originate from some excitonic states. Performing density functional calculation for defective  $\text{SnO}_{2-\delta}$  nanocrystals, Liu *et al.* [38] have shown that PL peaks at 446 and 470 nm originate from the subbridging oxygen vacancies,  $V_{OSB}$ . Schematic model for different relaxation processes in the  $\text{SnO}_{2-\delta}$  nanocrystals is presented in Fig. 7b.

Co-doping induced complete reduction of PL intensity. Even the smallest percent of Co-doping (see Fig. 7a) almost completely quenched the luminescence. By integrating the spectra of the  $\text{Sn}_{1-x}\text{Co}_x\text{O}_{2-\delta}$  samples from Fig. 7a, the areas within the boundary of emission were calculated for both undoped and doped samples in order to compare the quantum efficiencies. As the spectra were recorded under the identical excitation/absorption

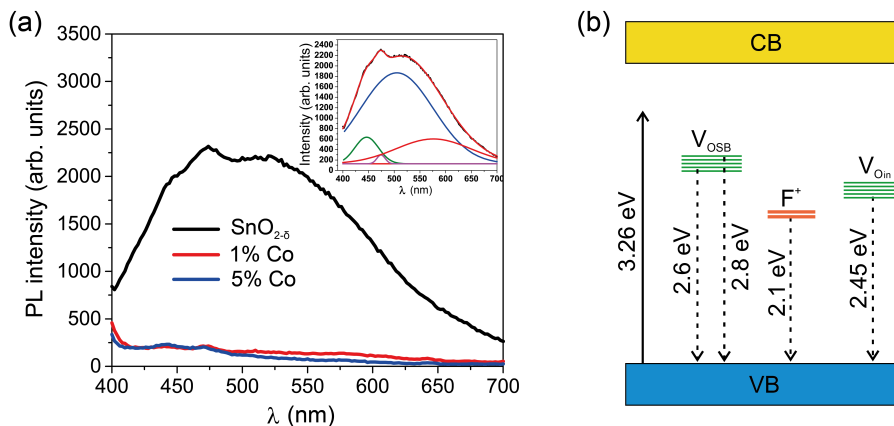
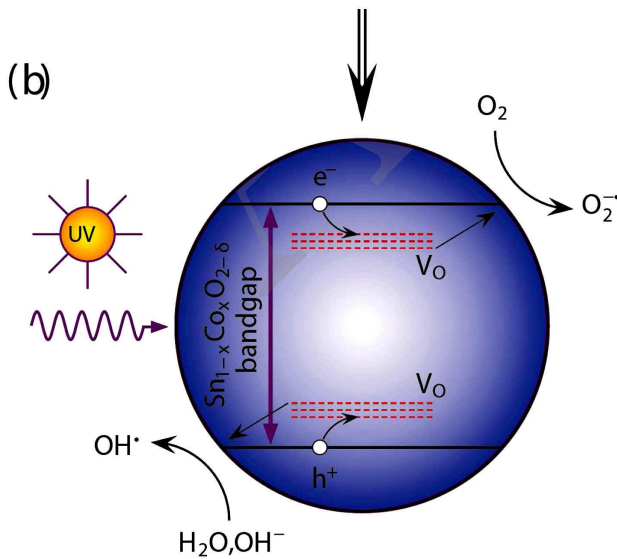
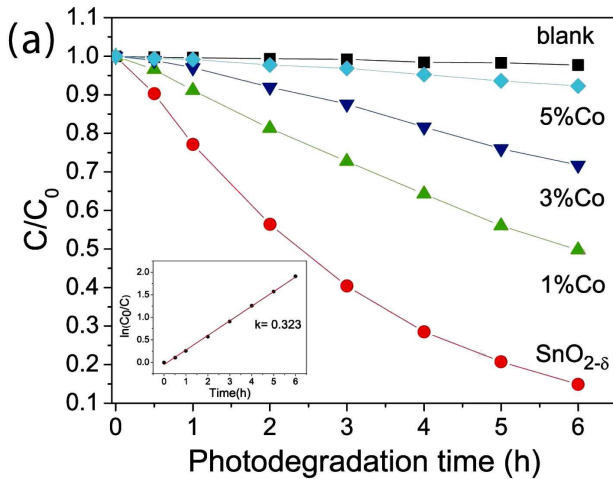


Figure 7. Room-temperature PL spectra of  $\text{Sn}_{1-x}\text{Co}_x\text{O}_{2-\delta}$  nanoparticles (a) and the schematic of relaxation mechanism (b)

conditions, the drop in quantum yield value was estimated to be nearly 93%, which evidently implies that cobalt doping drastically quenches the photoluminescence of SnO<sub>2-δ</sub>. It has been already demonstrated that Co ions act as luminescence quenchers for metal oxides like TiO<sub>2</sub> or ZnO, decreasing the intensity of PL emission by forming the large number of nonradiative centres [55,56]. Therefore, it can be inferred that Co-doping of the SnO<sub>2-δ</sub> nanocrystals increases the nonradiative recombination processes.

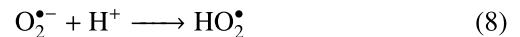
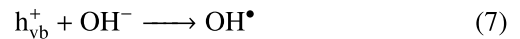
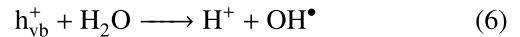
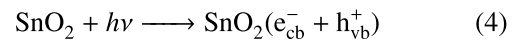
### 3.4. Photocatalytic performances

The degradation of MB under the UV light in the presence of the Sn<sub>1-x</sub>Co<sub>x</sub>O<sub>2-δ</sub> samples is shown in Fig. 8a. The blank experiment in the absence of the catalyst (black curve) displayed almost no photocatalytic degradation of MB under UV irradiation. The SnO<sub>2-δ</sub> nanoparticles exhibited high photocatalytic activity as the degradation of MB was completed after 6 h. The



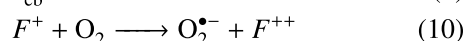
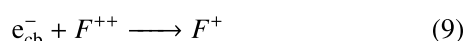
**Figure 8. Photocatalytic degradation of MB in the presence of Sn<sub>1-x</sub>Co<sub>x</sub>O<sub>2-δ</sub> samples (inset: pseudo first-order reaction kinetics of SnO<sub>2-δ</sub> sample) (a) and illustration of proposed photodegradation mechanism under UV light illumination (b)**

photocatalytic efficiency of the SnO<sub>2-δ</sub> nanoparticles is much better than the ones of bulk SnO<sub>2</sub> [53] and is comparable to other reported works on SnO<sub>2</sub> nanoparticles [24,57]. Photoinduced degradation of MB was significantly slower in the presence of Co-doped samples. After 6 h, the MB degradation of 50% was obtained in the presence of the Sn<sub>0.99</sub>Co<sub>0.01</sub>O<sub>2-δ</sub> catalyst, whereas significant decrease of photocatalytic activity was registered for the Sn<sub>0.97</sub>Co<sub>0.03</sub>O<sub>2-δ</sub> and Sn<sub>0.95</sub>Co<sub>0.05</sub>O<sub>2-δ</sub> samples. The obtained results are in accordance with the solitary work of Entradas *et al.* [22] who showed that increased Co-doping resulted in the decreased photocatalytic activity of SnO<sub>2</sub>. The experimental kinetic data for SnO<sub>2-δ</sub> catalyst were fitted to the rate equation of a pseudo first-order reaction  $\ln(C/C_0) = kt$ , where  $k$  is the rate constant and  $C_0$  and  $C$  are the initial dye concentration and that at time  $t$ . The reaction kinetics for the SnO<sub>2-δ</sub> catalyst (inset of Fig. 8a) follows the first order and the reaction rate constant estimated from the slope of the linear fit is 0.323 h<sup>-1</sup>. The degradation process of MB is initiated when the electron-hole pairs are formed on the SnO<sub>2-δ</sub> surface under the UV irradiation. Photo-generated electrons and holes, if not recombined, can migrate to the catalyst surface and react with adsorbed oxygen, water molecules or hydroxyl anions generating hydroxyl (OH•), superoxide (O<sub>2</sub><sup>•-</sup>) or (HO<sub>2</sub><sup>•</sup>) radicals. These reactions can be presented by Eq. 4–8:



The photocatalytic efficiency of semiconductors like SnO<sub>2</sub> can be enhanced by introducing lattice defects such as oxygen vacancies because these defects can be active sites on the photocatalyst surface and delay the recombination of photogenerated electrons and holes [21,58]. The as-prepared SnO<sub>2-δ</sub> nanopowders are very much oxygen deficient as confirmed by Raman results. The oxygen vacancies can form defect states inside the gap influencing the electronic structure of SnO<sub>2-δ</sub> nanoparticles, as already seen from PL spectrum. By applying complementary techniques such as ultraviolet photoelectron spectroscopy and ion-scattering spectroscopy, Cox *et al.* [59] analysed oxygen vacancy electronic states on the SnO<sub>2</sub> surface and they showed that in-plane oxygen vacancies  $V_{\text{Oin}}$  form defect electronic states inside the SnO<sub>2</sub> gap near the conduction band behaving like  $F^+$  centre donor states. Bridging/subbridging oxygen vacancies form states near the valence band [59] playing the role of hole acceptors. These donor/acceptor states can serve as carrier traps for electrons and holes ensuring better charge separation efficiency and suppression of  $e-h$  recombination process. Besides, doubly ionized ( $F^{++}$ ) or singly ionized ( $F^+$ )

in-plane or subbridging vacancies formed at the surface of the catalyst facilitate charge transfer to adsorption species like  $\text{H}_2\text{O}$  or  $\text{O}_2$ , forming reactive radicals responsible for dye degradation. The holes,  $h_{\text{vb}}^+$ , trapped by oxygen vacancies at the nanoparticle surface react with adsorbed  $\text{H}_2\text{O}$  or  $\text{OH}^-$  groups to form  $\text{OH}^\bullet$  radicals (Eqs. 6 and 7). Besides, electrons,  $e_{\text{cb}}^-$ , can be trapped by surface  $F^{++}$  vacancies which convert to  $F^+$ . Molecular oxygen adsorbed on the  $\text{SnO}_{2-\delta}$  surface can capture electrons located on  $F^+$  states [58] to form  $\text{O}_2^{\bullet-}$  radicals:



Therefore, it is reasonable to assume that in-plane and subbridging/bridging oxygen vacancies in different charge states play significant role in enhancing the photocatalytic efficiency of  $\text{SnO}_{2-\delta}$ . The proposed mechanism of photodegradation process is presented in Fig. 8b.

Among the reactive radicals,  $\text{OH}^\bullet$  radicals are considered to be the most important oxidative agent in photocatalytic reactions on metal-oxide nanostructures. They have one of the highest oxidation potentials among the oxidizing species (2.8 V) and can rapidly attack pollutants on the semiconductor surface. These radicals are considered as non-selective oxidizing species, since they can oxidize almost all electron rich organic molecules because of its electrophilic nature.  $\text{OH}^\bullet$  radicals are usually formed by the reaction between the holes and  $\text{OH}^-$  or water molecules present on the surface of the catalyst (Eqs. 6 and 7). The formation of  $\text{OH}^\bullet$  radicals on the surface of UV-illuminated  $\text{SnO}_{2-\delta}$  was tested by performing the experiment with terephthalic acid, described in detail in section 2.3. The concentration of  $\text{OH}^\bullet$  radicals was estimated from the intensity change of the PL peak attributed to 2-hydroxyterephthalic acid which is known to be proportional to the amount of  $\text{OH}^\bullet$  radicals formed [30,31]. Figure 9 showed that intensity of PL peak at around

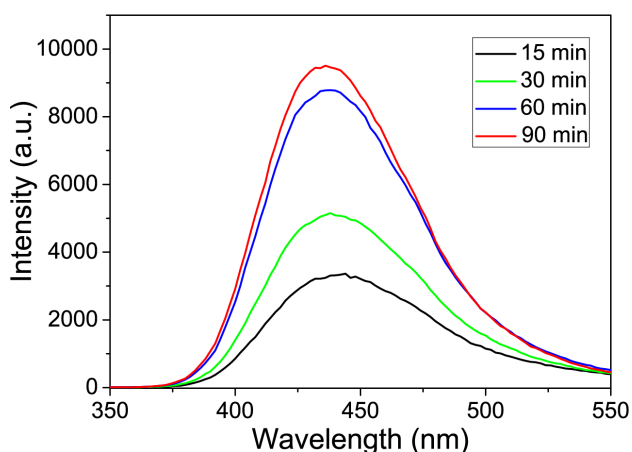


**Figure 9.** PL intensity change of 430 nm peak observed during UV illumination of  $\text{SnO}_{2-\delta}$  sample in the solution of terephthalic acid and recorded at different time

430 nm gradually increased with the prolonged irradiation time pointing to the higher formation rate of hydroxyl radicals. This result indicates that increased formation of  $\text{OH}^\bullet$  radicals has a great effect on the photocatalytic activity of  $\text{SnO}_{2-\delta}$ . Further investigations will be directed to the estimation of the optimal  $\text{SnO}_2$  concentration and the influence of solution pH on the  $\text{SnO}_2$  photocatalytic properties. In that sense, more detailed mechanism study needs to be performed.

With Co-doping the photocatalytic performances of  $\text{SnO}_{2-\delta}$  were deteriorated. The reasons can be found in increased number of nonradiative centres with increasing cobalt concentration which act as trapping centres, immobilizing the fast transfer of photo-generated electrons to the nanoparticle surface. However, one of the main reasons can be found in the decreased concentration of oxygen vacancies which promotes the charge separation enhancing at the same time the photocatalytic activity. Also, the increased band gap of the Co-doped samples decreases the number of photons with sufficient energy to initiate photocatalytic processes, i.e. less UV energy is absorbed.

#### IV. Conclusions

Single phase ultrafine  $\text{Sn}_{1-x}\text{Co}_x\text{O}_{2-\delta}$  nanocrystals, of a tetragonal (cassiterite-type) crystal structure, were prepared using a simple microwave-assisted hydrothermal synthesis at low temperature without the addition of any surfactant. Rietveld refinement of the XRD data showed that Co cations entered substitutionally into  $\text{SnO}_{2-\delta}$  lattice and the unit cell volume increased up to  $x = 0.05$ . The slight shrinkage of the unit cell of the  $\text{Sn}_{0.95}\text{Co}_{0.05}\text{O}_{2-\delta}$  sample was ascribed to the increased amount of  $\text{Co}^{3+}$  cations. The average crystallite size of the  $\text{SnO}_{2-\delta}$  nanocrystals was less than Bohr exciton radius and it was found to decrease with increasing Co-doping level. UV-Vis absorption measurements confirmed that Co cations entered into the  $\text{SnO}_{2-\delta}$  lattice in mixed valence state for higher dopant content ( $x > 0.01$ ) and the concentration of  $\text{Co}^{3+}$  cations increased in the  $\text{Sn}_{0.95}\text{Co}_{0.05}\text{O}_{2-\delta}$  sample. Raman spectra revealed oxygen deficient structure of the  $\text{SnO}_{2-\delta}$  nanocrystals, whereas the oxygen vacancy concentration decreased with increased Co-doping. Further, Co-doping brought significant changes in the optical and electronic properties of tin oxide.  $\text{SnO}_{2-\delta}$  nanocrystals exhibited blue shift of the band gap energy, compared to the bulk counterpart, due to the combined phonon confinement and the Burstein-Moss effects. The optical band gap energy increased with increasing Co concentration. The luminescence process in  $\text{SnO}_{2-\delta}$  nanocrystals mainly originated from oxygen vacancy related defects and it was completely quenched in the Co-doped nanocrystals due to the increased nonradiative recombination processes. The oxygen-deficient  $\text{SnO}_{2-\delta}$  was efficient for the light-induced degradation of methylene blue. Enhanced photocatalytic activity of  $\text{SnO}_{2-\delta}$  can be ascribed to the

oxygen vacancies-assisted better charge separation and faster charge transport to adsorbed species. On the other hand, deteriorated photocatalytic performances of Co-doped SnO<sub>2-δ</sub> nanopowders can be ascribed to the decreased oxygen vacancy concentration and less amount of absorbed UV light because of the band gap widening.

**Acknowledgement:** The authors acknowledge funding by the Institute of Physics Belgrade, through the grant by the Serbian Ministry of Education, Science and Technological Development. V.D. Araújo and M.I.B. Bernardi wish to thank Brazilian agencies FAPESP, FACEPE and CNPq for financial support.

## References

- H. Park, S. Alhammadi, K. Bouras, G. Schmerber, F. Gérald, D. Aziz, S. Abdelilah, J. Chan-Wook, P. Chinho, K. Woo Kyoung, “Nd-doped SnO<sub>2</sub> and ZnO for application in Cu(InGa)Se<sub>2</sub> solar cells”, *Sci. Adv. Mater.*, **9** (2017) 2114–2120.
- J. Lee, N.H. Kim, Y.S. Park, “Characteristics of SnO<sub>2</sub>:Sb films as transparent conductive electrodes of flexible inverted organic solar cells”, *J. Nanosci. Nanotechnol.*, **16** (2016) 4973–4977.
- Y. Chen, J. Lu, S. Wen, L. Lu, J. Xue, “Synthesis of SnO<sub>2</sub>/MoS<sub>2</sub> composites with different component ratios and their applications as lithium ion battery anodes”, *J. Mater. Chem. A*, **2** (2014) 17857–17866.
- M. Batzill, U. Diebold, “The surface and materials science of tin oxide”, *Prog. Surf. Sci.*, **79** (2005) 47–154.
- K. Singh, R. Malakar, R. Narzary, K. Priyanka, M. Biplob, “Hydrogen sensing properties of pure and composites of ZnO and SnO<sub>2</sub> particles: Understanding sensing mechanism”, *Sens. Lett.*, **15** (2017) 771–778.
- Z. Zhao, B. Wang, J. Ma, W. Zhan, L. Wang, Y. Guo, Y. Guo, G. Lu, “Catalytic combustion of methane over Pd/SnO<sub>2</sub> catalysts”, *Chinese J. Catal.*, **38** (2017) 1322–1329.
- J.T. Wiswall, M.S. Wooldridge, H.G. Im, “An experimental investigation of catalytic oxidation of propane using temperature controlled Pt, Pd, SnO<sub>2</sub>, and 90% SnO<sub>2</sub>–10% Pt catalysts”, *Catal. Sci. Technol.*, **3** (2013) 618–625.
- J.S. Chen, X.W.D. Lou, “SnO<sub>2</sub>-based nanomaterials: synthesis and application in lithium-Ion batteries”, *Small*, **9** (2013) 1877–1893.
- M.O. Orlandi, A.J. Ramirez, E.R. Leite, E. Longo, “Morphological evolution of tin oxide nanobelts after phase transition”, *Cryst. Growth Des.*, **8** (2008) 1067–1072.
- J. Jeong, S.-P. Choi, C.I. Chang, D.C. Shin, J.S. Park, B.-T. Lee, Y.-J. Park, H.-J. Song, “Photoluminescence properties of SnO<sub>2</sub> thin films grown by thermal CVD”, *Solid State Commun.*, **127** (2003) 595–597.
- Y. Wang, M.H. Wu, Z. Jiao, J.Y. Lee, “One-dimensional SnO<sub>2</sub> nanostructures: facile morphology tuning and lithium storage properties”, *Nanotechnology*, **20** (2009) 345704.
- Z.R. Dai, Z.W. Pan, Z.L. Wang, “Growth and structure evolution of novel tin oxide diskettes”, *J. Am. Chem. Soc.*, **124** (2002) 8673–8680.
- X. Li, Q. Yu, C. Yu, Y. Huang, R. Li, J. Wang, F. Guo, Y. Zhang, S. Gao, L. Zhao, “Zinc-doped SnO<sub>2</sub> nanocrystals as photoanode materials for highly efficient dye-sensitized solar cells”, *J. Mater. Chem. A*, **3** (2015) 8076–8082.
- Y. Liu, F. Yang, X. Yang, “Size-controlled synthesis and characterization of quantum-size SnO<sub>2</sub> nanocrystallites by a solvothermal route”, *Colloid Surf. A*, **312** (2008) 219–225.
- Y.K. Liu, C.L. Zheng, W.Z. Wang, Y.J. Zhan, G.H. Wang, “Production of SnO<sub>2</sub> nanorods by redox reaction”, *J. Cryst. Growth*, **233** (2001) 8–12.
- J.Q. Hu, Y. Bando, Q.L. Liu, D. Golberg, “Laser-ablation growth and optical properties of wide and long single-crystal SnO<sub>2</sub> ribbons”, *Adv. Funct. Mater.*, **13** (2003) 493–496.
- H.Q. Cao, X.Q. Qiu, Y. Liang, L. Zhang, M.J. Zhao, Q.M. Zhu, “Sol-gel template synthesis and photoluminescence of n- and p-type semiconductor oxide nanowires”, *Chem. Phys. Chem.*, **7** (2006) 497–501.
- Y.K. Liu, C.L. Zheng, W.Z. Wang, C.R. Yin, G.H. Wang, “Synthesis and characterization of rutile SnO<sub>2</sub> nanorods”, *Adv. Mater.*, **13** (2001) 1883–1887.
- D. Chen, S. Huang, R. Huang, Q. Zhang, T.-T. Lee, E. Cheng, Z. Hu, Z. Chen, “Highlights on advances in SnO<sub>2</sub> quantum dots: insights into synthesis strategies, modifications and applications”, *Mater. Res. Lett.*, **6** (2018) 462–488.
- P.G. Mendes, M.L. Moreira, S.M. Tebcherani, M.O. Orlandi, J. Andrés, M.S. Li, N. Diaz-Mora, J.A. Varela, E. Longo, “SnO<sub>2</sub> nanocrystals synthesized by microwave-assisted hydrothermal method: towards a relationship between structural and optical properties”, *J. Nanopart. Res.*, **14** (2012) 750–13.
- A.M. Al-Hamdi, U. Rinner, M. Sillanpää, “Tin dioxide as a photocatalyst for water treatment: A review”, *Process Saf. Environ.*, **107** (2017) 190–205.
- T. Entradas, J.F. Cabrita, S. Dalui, M.R. Nunes, O.C. Monteiro, A.J. Silvestre, “Synthesis of sub-5 nm Co-doped SnO<sub>2</sub> nanoparticles and their structural, microstructural, optical and photocatalytic properties”, *Mater. Chem. Phys.*, **147** (2014) 563–571.
- R. Mani, K. Vivekanandan, K. Vallalperuman, “Synthesis of pure and cobalt (Co) doped SnO<sub>2</sub> nanoparticles and its structural, optical and photocatalytic properties”, *J. Mater. Sci. Mater. Electron.*, **28** (2017) 4396–4402.
- D. Chandran, L.S. Nair, S. Balachandran, K. Rajendra Babu, M. Deepa, “Structural, optical, photocatalytic, and antimicrobial activities of cobalt-doped tin oxide nanoparticles”, *J. Sol-Gel Sci. Technol.*, **76** (2015) 582–591.
- Y. Cao, L. Huang, Y. Bai, K. Jermsittiparsert, R. Hosseinzadeh, H. Rasoulnezhad, G. Hosseinzadeh, “Synergic effect of oxygen vacancy defect and shape on the photocatalytic performance of nanostructured TiO<sub>2</sub> coating”, *Polyhedron*, **175** (2020) 114214.
- X. Xu, X. Ding, X. Yang, P. Wang, S. Li, Z. Lu, H. Chen, “Oxygen vacancy boosted photocatalytic decomposition of ciprofloxacin over Bi<sub>2</sub>MoO<sub>6</sub>: Oxygen vacancy engineering, biotoxicity evaluation and mechanism study”, *J. Hazard. Mater.*, **364** (2019) 691–699.
- Q. Zhang, X. Zhao, L. Duan, H. Shen, R. Liu, “Controlling oxygen vacancies and enhanced visible light photocatalysis of CeO<sub>2</sub>/ZnO nanocomposites”, *J. Photoch. Photobio. A*, **392** (2020) 112156.
- B. Matovic, J. Lukovic, B. Stojadinović, S. Aškračić, A. Zarubica, B. Babic, Z. Dohčević-Mitrović, “Influence of Mg doping on structural, optical and photocatalytic performances of ceria nanopowders”, *Process. Appl. Ceram.*,

- 11 (2017) 304–310.
29. Z. Dohčević-Mitrović, S. Stojadinović, L. Lozzi, S. Aškra-  
bić, M. Rosić, N. Tomić, N. Paunović, S. Lazović, M.G.  
Nikolić, S. Santucci, “WO<sub>3</sub>/TiO<sub>2</sub> composite coatings:  
Structural, optical and photocatalytic properties”, *Mater.  
Res. Bull.*, **83** (2016) 217–224.
  30. T.M. Su, Z.L. Liu, Y. Liang, Z.Z. Qin, J. Liu, Y.Q. Huang,  
“Preparation of PbYO composite photocatalysts for degra-  
dation of methyl orange under visible-light irradiation”,  
*Catal. Comm.*, **18** (2012) 93–97.
  31. K. Ishibashi, A. Fujishima, T. Watanabe, K. Hashimoto,  
“Detection of active oxidative species in TiO<sub>2</sub> photocatal-  
ysis using the fluorescence technique”, *Electrochem. Com-  
mun.*, **2** (2000) 207–210.
  32. D. Menzel, A. Awada, H. Dierke, J. Schoenes, F. Lud-  
wig, M. Schilling, “Free-carrier compensation in ferro-  
magnetic ion-implanted SnO<sub>2</sub>:Co”, *J. Appl. Phys.*, **103**  
(2008) 07D106.
  33. E.J.H. Lee, C. Ribeiro, T.R. Giraldi, E. Longo, E.R. Leite,  
J.A. Varela, “Photoluminescence in quantum-confined  
SnO<sub>2</sub> nanocrystals: Evidence of free exciton decay”, *Appl.  
Phys. Lett.*, **84** (2004) 1745–1747.
  34. B. Babu, Ch.V. Reddy, J. Shim, R.V.S.S.N. Ravikumar,  
J. Park, “Effect of cobalt concentration on morphology  
of Co-doped SnO<sub>2</sub> nanostructures synthesized by solution  
combustion method”, *J. Mater. Sci. Mater. Electron.*, **27**  
(2016) 5197–5203.
  35. P.S. Peercy, B. Morosin, “Pressure and temperature depen-  
dences of the Raman-active phonons in SnO<sub>2</sub>”, *Phys. Rev.  
B*, **7** (1973) 2779–2786.
  36. V. Bonu, A. Das, S. Amirthapandian, S. Dhara, A.K.  
Tyagi, “Photoluminescence of oxygen vacancies and hydro-  
xyl group surface functionalized SnO<sub>2</sub> nanoparticles”,  
*Phys. Chem. Chem. Phys.*, **17** (2015) 9794–9801.
  37. A. Diéguez, A. Romano-Rodríguez, A. Vilà, J.R. Morante,  
“The complete Raman spectrum of nanometric SnO<sub>2</sub> par-  
ticles”, *J. Appl. Phys.*, **90** (2001) 1550–1557.
  38. L.Z. Liu, J.K. Xu, X.L. Wu, T.H. Li, J.C. Shen, P.K. Chu,  
“Optical identification of oxygen vacancy types in SnO<sub>2</sub>  
nanocrystals”, *Appl. Phys. Lett.*, **102** (2013) 031916.
  39. K.N. Yu, Y. Xiong, Y. Liu, C. Xiong, “Microstructural  
change of nano-SnO<sub>2</sub> grain assemblages with the anneal-  
ing temperature”, *Phys. Rev. B*, **55** (1997) 2666–2671.
  40. Y. Liu, M. Liu, “Growth of aligned square-shaped SnO<sub>2</sub>  
tube arrays”, *Adv. Funct. Mater.*, **15** (2005) 57–62.
  41. F. Wang, X. Zhou, J. Zhou, T.-K. Sham, Z. Ding, “Observ-  
ation of single tin dioxide nanoribbons by confocal Ra-  
man microspectroscopy”, *J. Phys. Chem. C*, **111** (2007)  
18839–18843.
  42. C. Van Komen, A. Thurber, K.M. Reddy, J. Hays, A. Pun-  
noose, “Structure-magnetic property relationship in tran-  
sition metal (M = V, Cr, Mn, Fe, Co, Ni) doped SnO<sub>2</sub>  
nanoparticles”, *J. Appl. Phys.*, **103** (2008) 07D141.
  43. D.A. Popescu, J.-M. Herrmann, A. Ensuque, F. Bozon-  
Verduraz, “Nanosized tin dioxide: Spectroscopic (UV-  
VIS, NIR, EPR) and electrical conductivity studies”, *Phys.  
Chem. Chem. Phys.*, **3** (2001) 2522–2530.
  44. I. Rossetti, B. Bonelli, G. Ramis, E. Bahadori, R. Nasi,  
A. Aronne, S. Esposito, “New insights into the role of the  
synthesis procedure on the performance of Co-based cata-  
lysts for ethanol steam reforming”, *Top. Catal.*, **61** (2018)  
734–745.
  45. Y. Brik, M. Kacimi, M. Ziyad, F. Bozon-Verduraz,  
“Titania-supported cobalt and cobalt-phosphorus cata-  
lysts: Characterization and performances in ethane oxida-  
tive dehydrogenation”, *J. Catal.*, **202** (2001) 118–128.
  46. S. Roy, A.G. Joshi, S. Chatterjee, A.K. Ghosh, “Local  
symmetry breaking in SnO<sub>2</sub> nanocrystals with cobalt dop-  
ing and its effect on optical properties”, *Nanoscale*, **10**  
(2018) 10664–10682.
  47. A.S. Ferlauto, G.M. Ferreira, J.M. Pearce, C.R. Wronski,  
R.W. Collins, X. Deng, G. Ganguly, “Analytical model for  
the optical functions of amorphous semiconductors from  
the near-infrared to ultraviolet: Applications in thin film  
photovoltaics”, *J. Appl. Phys.*, **92** (2002) 2424–2436.
  48. P.D. Borges, L.M.R. Scolfaro, H.W. Leite Alves, E.F. da  
Silva Jr., “DFT study of the electronic, vibrational, and op-  
tical properties of SnO<sub>2</sub>”, *Theor. Chem. Acc.*, **126** (2010)  
39–44.
  49. L. Brus, “Electronic wave functions in semiconductor  
clusters: experiment and theory”, *J. Phys. Chem.*, **90**  
(1986) 2555–2560.
  50. S. Dalui, S. Rout, A.J. Silvestre, G. Lavareda, L.C.J.  
Pereira, P. Brogueira, O. Conde, “Structural, electrical and  
magnetic studies of Co:SnO<sub>2</sub> and (Co,Mo):SnO<sub>2</sub> films pre-  
pared by pulsed laser deposition”, *Appl. Surf. Sci.*, **278**  
(2013) 127–131.
  51. H.S. So, J.-W. Park, D.H. Jung, K.H. Ko, H. Lee, “Optical  
properties of amorphous and crystalline Sb-doped SnO<sub>2</sub>  
thin films studied with spectroscopic ellipsometry: Optical  
gap energy and effective mass”, *J. Appl. Phys.*, **118** (2015)  
085303.
  52. A. Oprea, E. Moretton, N. Bârsan, W.J. Becker, J. Wöll-  
enstein, U. Weimar, “Conduction model of SnO<sub>2</sub> thin films  
based on conductance and Hall effect measurements”, *J.  
Appl. Phys.*, **100** (2006) 033716.
  53. A. Kar, M.A. Stroschio, M. Dutta, J. Kumari, M. Meyyap-  
pan, “Growth and properties of tin oxide nanowires and  
the effect of annealing conditions”, *Semicond. Sci. Tech-  
nol.*, **25** (2010) 024012.
  54. I.I. Gontia, M. Baibarac, I. Baltog, “Photolumines-  
cence and Raman studies on tin dioxide powder and tin  
dioxide/single-walled carbon-nanotube composites”,  
*Phys. Status Solidi B*, **248** (2011) 1494–1498.
  55. B. Choudhury, A. Choudhury, “Luminescence character-  
istics of cobalt doped TiO<sub>2</sub> nanoparticles”, *J. Lumin.*, **132**  
(2012) 178–184.
  56. S. Yamamoto, “Photoluminescence quenching in cobalt  
doped ZnO nanocrystals”, *J. Appl. Phys.*, **111** (2012)  
094310.
  57. S.P. Kim, M.Y. Choi, H.C. Choi, “Photocatalytic activ-  
ity of SnO<sub>2</sub> nanoparticles in methylene blue degradation”,  
*Mater. Res. Bull.*, **74** (2016) 85–89.
  58. X. Pan, M.-Q. Yang, X. Fu, N. Zhang, Y.-J. Xu, “Defec-  
tive TiO<sub>2</sub> with oxygen vacancies: synthesis, properties and  
photocatalytic applications”, *Nanoscale*, **5** (2013) 3601–  
3614.
  59. D.F. Cox, T.B. Fryberger, S. Semancik, “Oxygen vacan-  
cies and defect electronic states on the SnO<sub>2</sub>(110)-1 × 1”,  
*Phys. Rev. B*, **38** (1988) 2072–2083.



## Probing charge carrier transport regimes in BiFeO<sub>3</sub> nanoparticles by Raman spectroscopy

Dejan M. Djokić\*, Bojan Stojadinović, Dimitrije Stepanenko, Zorana Dohčević-Mitrović

Nanostructured Matter Laboratory, Institute of Physics Belgrade, University of Belgrade, Pregrevica 118, Belgrade 11 080, Republic of Serbia



### ARTICLE INFO

#### Article history:

Received 18 October 2019

Revised 29 January 2020

Accepted 4 February 2020

#### Keywords:

Raman spectroscopy  
Electronic background  
BiFeO<sub>3</sub> nanoparticles  
Variable range hopping

### ABSTRACT

We report a finding of two transport regimes in multiferroic BiFeO<sub>3</sub> nanoparticles, which correspond to variable range hopping (VRH) mechanisms. Switch between the two regimes coincides with the transition between antiferromagnetic (AF) and paramagnetic (PM) phase. At low temperatures, it was found that temperature dependence of indirectly extracted resistivity is consistent with Efros-Shklovskii mechanism. As with high temperatures, data fit favourably to Mott VRH theory. Estimated resistivity value of  $\sim 350\text{m}\Omega\text{cm}$  violates the Mott-Ioffe-Regel criterion, corroborating that the transport does not proceed through conduction bands. Conductivity was probed noninvasively via Raman contactless setup and studied as a function of temperature.

© 2020 Acta Materialia Inc. Published by Elsevier Ltd. All rights reserved.

**Introduction.** Multiferroic BiFeO<sub>3</sub> has recently attracted much attention due to its desirably high ferroelectric Curie temperature of ca 1100K and AF Néel temperature  $T_N$  of around 640K, both decreasing only slightly with decreasing crystallite size [1,2]. At nanoscales, BiFeO<sub>3</sub> turns out to be rather prospective for industrial applications in photovoltaics, satellite communications, electrically accessed magnetic memory, and novel sensing technologies [3]. Electric resistance of BiFeO<sub>3</sub> is one of the crucial parameters that must meet the relevant industrial requirements. In order to avoid leakage of electric charge, achieving high resistivity is one of the main concerns, and using nano-powders is seen as a promising development route.

As a highly informative experimental tool, Raman scattering spectroscopy stands for a local probe also being able to assess the nature and dynamics of charge carriers in conductive systems in a contactless way. On the other hand, it is exceedingly hard to identify the transport mechanism responsible for charge conduction using exclusively the contact probes [4,5]. Raman spectral response of the scattered light in metals with disorder and doped semiconductors is typically composed of several peaks due to the Raman active phonon excitations and a smooth frequency continuum which reflects direct electronic response [6]. This letter focuses on the temperature evolution of this continuous spectral background which is formed by low-energy electronic excitations, and referred to in the literature as the Raman electronic background [7–11]. The charge carrier scattering rate is intimately linked to the electronic

background in Raman spectra. This enables us to follow the character of charge transport in BiFeO<sub>3</sub> nanoparticles undergoing the AF/PM phase transition at the temperature around 640K.

As the particle size decreases into nanoscale domain, two crucial changes affect the charge transport in semiconductors. Band structures become distorted with decreasing particle size and, eventually, the states change their nature to get localized. Beyond certain scale, there is no conduction band and the commonly adopted picture of the intrinsic semiconductor transport due to the thermal activation via conduction band states breaks down. As the structure becomes more and more disordered, localization centers that can trap carriers appear more prominent with the decreasing particle size. Therefore, hopping varied with distance between the localization centers can be safely hypothesized to be the dominant transport mechanism even at high temperatures due to the evanescence of the conduction band.

Our measurements of temperature dependent electronic Raman background on the multiferroic BiFeO<sub>3</sub> nanoparticles of high purity, synthesized via sol-gel method [12], have been interpreted in terms of the VRH transport mechanism, which appears leading even at quite high temperatures. The role of localization centers is played by the surface states localized within particles, and with energies in the vicinity of Fermi level. An exceptionally high value of resistivity has been evidenced which rules out a metallic type of conductivity to make VRH a viable transport mechanism in the BiFeO<sub>3</sub> nanoparticles. We communicate a detection of the two different 3D VRH charge carrier transport mechanisms in the nanoscaled BiFeO<sub>3</sub>, as probed by Raman spectroscopy. They correspond to different impact of electron correlations upon the

\* Corresponding author.

E-mail address: [djokic@ipb.ac.rs](mailto:djokic@ipb.ac.rs) (D.M. Djokić).

transport on the opposite sides of the AF/PM phase transition. In the AF phase, the transport can well be described by the Efros-Shklovskii VRH theory [13], while in the PM phase, the transport follows the original Mott VRH theory [14].

**Raman Scattering Spectra.**  $\mu$ -Raman scattering measurements were performed using a Linkam THMSG600 microscope heating-cooling stage in the temperature range from 80K up to 723K. Raman spectra were collected in backscattering configuration on TriVista 557 Raman system equipped with a nitrogen cooled CCD detector. The  $\lambda = 532\text{nm}$  line of solid state Nd:YAG laser was used as an excitation source with sub-mW laser powers on the sample in order to eliminate heating effects. In the  $\mu$ -Raman spectra of BiFeO<sub>3</sub> nanoparticles measured over 80 – 723K, more than thirteen optical phonon modes of A<sub>1</sub> and E symmetry have been observed. These spectra, deconvoluted using Lorentzian absorption profiles, are shown in Fig. 1 for four representative temperatures.

The total number and frequencies of the observed Raman active phonon modes of BiFeO<sub>3</sub> nanoparticles are identical to those detected in temperature dependent Raman scattering spectra carried out on bulk BiFeO<sub>3</sub> single crystals [15], apart from the splittings of some of the polar LO+TO phonon modes in the BiFeO<sub>3</sub> nanoparticles [16,17]. In bulk, factor group analysis predicts exactly thirteen ( $4A_1 + 9E$ ) Raman active phonon modes [18]. Unlike the bulk BiFeO<sub>3</sub>, the Raman active optical modes of the BiFeO<sub>3</sub> nanoparticles are seated on a distinctively broad spectroscopic feature (Fig. 1 shaded in light gray), which markedly varies with temperature. A similar spectroscopic background consisting of a non-resonant continuous profile was encountered in metal-oxide thin films [19], but with nearly structureless and of a rather enhanced intensity. This background is associated with a purely electronic Raman response, i.e. electronic scattering contribution independent of phonon bands, as a result of the atomic scale surface roughness. Furthermore, inelastic Raman scattering by particle-hole pair excitations was evidenced to lead to the emergence of electronic background in both metal-island films with adsorbants [20] and in very small metallic particles [21], which was interpreted in terms of the momentum conservation breakdown in the presence of the surface states. In hole-doped manganese perovskites, Liu et al. [22] found out that the broad electronic Raman response, accompanied with the scattering by conduction electrons, exhibits a distinctive change through the phase transition which could be followed quantitatively by the evolution of electron correlation effects.

A theory that describes and quantifies the profiles of Raman electronic background in "dirty" conductors was first developed by Falkovsky [7]. The author observed the effects of electronic excitations at low energies via scattering by impurities or phonons to include a finite momentum transfer ( $q \neq 0$ ) caused by the finite penetration depth. Soon afterwards, Zawadowski and Cardona [8] employed a Feynman diagrammatic approach to evaluate the Kubo response function in the ladder approximation [23] for  $q = 0$ , establishing a close connection with the charge carrier transport lifetime. Feynman diagrams for nonresonant Raman scattering are given in Fig. 2(a). The wavy lines denote photon propagators with initial and final (momentum, energy):  $(\vec{k}_i, \omega_i)$  and  $(\vec{k}_f, \omega_f)$  up to the reduced Planck's constant. The incoming photon generates an electron-hole pair scattered by a phonon or impurity excitation ( $\vec{q} = \vec{k}_i - \vec{k}_f, \omega = \omega_i - \omega_f$ ). In the ladder approximation, a phonon or impurity (dashed line in Fig. 2(a)), excited by the electron within the pair, is caught by the counterpart hole and vice versa. Finally, due to the dominating ladder-like diagrams, the approximation leads to the electronic Raman differential cross section [9,11], which can be written down as

$$\frac{d^2\sigma}{d\omega d\Omega} = \mathcal{A}_\tau \times \frac{1}{1 - \exp(-\hbar\omega/k_B T)} \times \frac{\omega\tau}{1 + (\omega\tau)^2}. \quad (1)$$

The constant  $\mathcal{A}_\tau$  depends on several factors varying from one experiment to another [10], which we attach no importance to in the present study. Bose-Einstein thermal correction factor and Drude-like expression are given by the second and third term in the product, respectively. The effective scattering rate,  $1/\tau$ , includes two terms,

$$1/\tau = \underbrace{1/\tau_0}_{\text{bulk}} + \underbrace{Dq^2}_{\text{nano}}, \quad (2)$$

where  $1/\tau_0$  denotes the scattering rate of the charge carrier by impurities in the  $q = 0$  limit coming from the bulk channel, and the second term describes the effects of momentum non-conserving processes. The bulk term will be safely disregarded in the present case.

Actually, there is no evidence of the electronic Raman background in bulk semiconductor BiFeO<sub>3</sub> crystals [15], as opposed to the present case of BiFeO<sub>3</sub> nanocrystals (Fig. 1). The second term in Eq. (2), which originates from the nanoscopic nature of the crystalline BiFeO<sub>3</sub> particles is due to the momentum conservation breakdown. Thus,  $q = 2\pi/\langle\ell\rangle$ , where  $\langle\ell\rangle$  represents the characteristic length of the expected nanoparticle size. We can automatically assume that the second term dominantly contributes to the effective scattering rate  $1/\tau$ . Prefactor  $D$  represents the diffusion constant and is intimately related to the electric resistivity  $\rho$  by the Einstein relation:  $D^{-1} = e^2 g(\epsilon_F) \rho$ , where  $e = 1.6 \times 10^{-19}$  C, with  $g(\epsilon_F)$  as the average value of the density of electronic states that give rise to the conduction in the vicinity of Fermi level [9]. The temperature evolution of the effective scattering rate  $1/\tau$  can be followed from Fig. 2(b) delineating a temperature set of the normalized Drude-like  $\hbar\omega$ -dependences extracted from the measured Raman temperature dependent spectra of the BiFeO<sub>3</sub> nanoparticles.

**Charge Carrier Transport.** Temperature variation of the logarithm of conductivity,  $\ln(1/\rho)$ , is oftentimes plotted as a function of  $(1/T)^n$  in disordered materials, such as nano BiFeO<sub>3</sub>, and "badly" conducting ceramics [25]. Exponent  $n$  imparts information on the DC conduction mechanism. When it is close to 1/4,  $n$  bears a signature of 3D Mott VRH transport mechanism [14], whereas an  $n$  value close to 1/2 indicates the presence of strong Coulomb correlations in 3D VRH [13]. Both VRH conduction mechanisms are supposed to prevail at low temperatures owing to the localized states around Fermi level in bulk semiconductors with disorder (blue arrow in Fig. 2(c) left). At rather high temperatures, the conduction runs by thermal activation via conduction band of the intrinsic semiconductor (red arrow in Fig. 2(c) left). However, once the particle size reaches nanoscales, the overlaps among the orbitals decrease. As a result, the bands become too sparse to cause splittings by opening up rather large gaps. The bands high in energy, such as conduction band, therefore tend to disappear as often encountered in disordered nanoscale samples, contrary to the corresponding bulk matter. For that reason, it is reasonable to assume that VRH mechanisms are applicable over temperature ranges that may extend up to higher temperatures in disordered nanostructures like BiFeO<sub>3</sub>, and surely far outweigh the intrinsic thermally activated transport via conduction band which can be ignored, as is given in the right part of Fig. 2(c).

Crystalline BiFeO<sub>3</sub> nanoparticles exhibit the phase transition around 640K. At temperatures below it, the Coulomb correlations become sufficiently strong to form the AF phase, while above it the absence of the correlations is manifested through the weakly metallic-like PM state. We postulate the presence of localized surface states with energies close to the Fermi level that mediate the VRH transport over an extended temperature range. Temperature variations of  $\ln(1/\tau)$ , which is  $\propto \ln(1/\rho)$  by Einstein relation, do differ on two sides of the AF/PM phase transition. The  $n$  values, which straighten out the  $\ln(1/\tau) \propto T^{-n}$  curves are essentially different in the two phases.

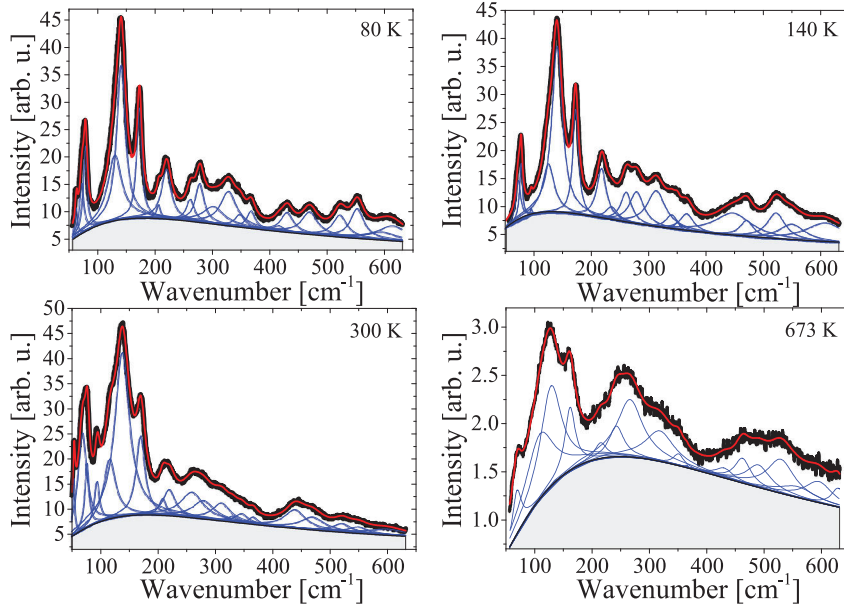


**Fig. 1.** Raman scattering spectra at four representative temperatures comprising of a smooth electronic background (area shaded in light gray) and more than thirteen phonon peaks (blue lines). The total fitting line is drawn in red, whereas the data points are given in black. (For interpretation of the references to colour in this figure legend, the reader is referred to the web version of this article.)

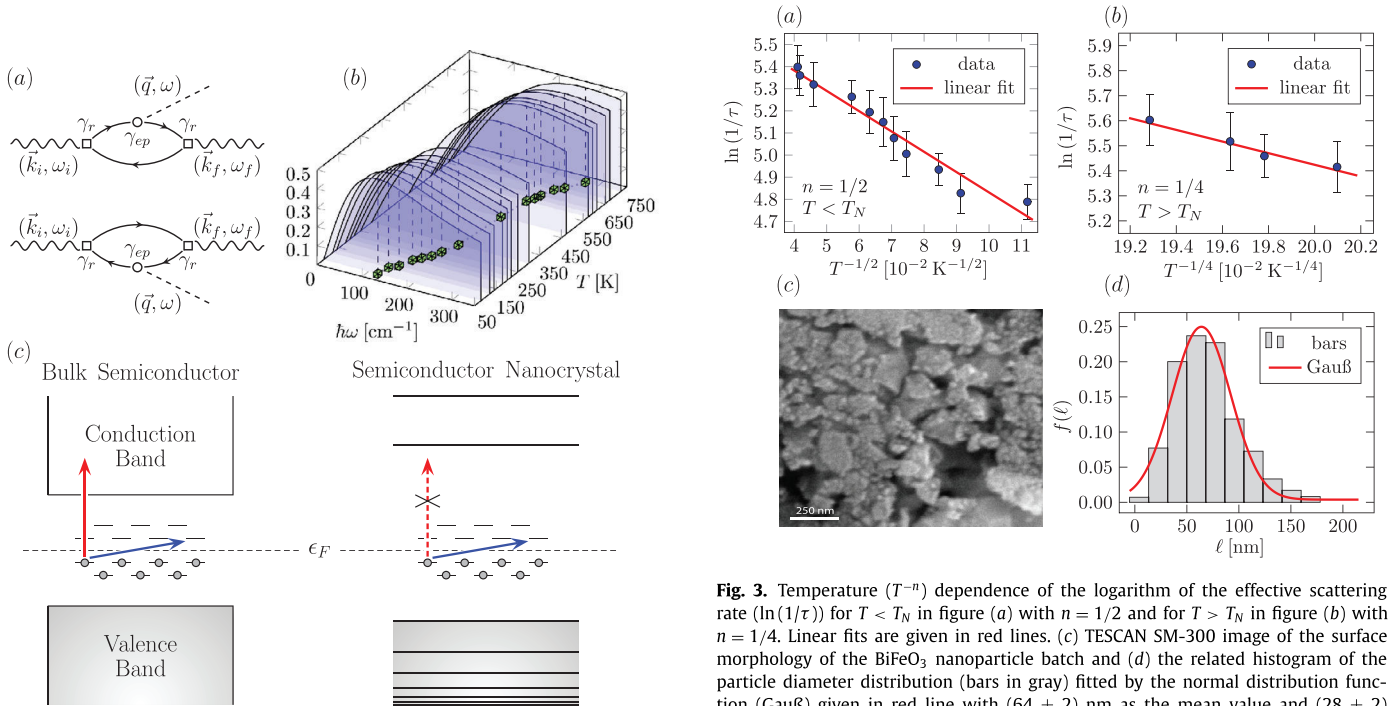


**Fig. 2.** (a) The Feynman diagrams describing the Raman scattering of light (wavy lines) processes by phonons or impurities (dashed lines) with electron-hole formations (solid lines). The processes are of third order in electron or hole scattering by phonons and impurities. Electron and hole contributions are represented by upper and lower diagrams, respectively.  $\gamma_r$  stands for electron-photon interaction ( $\square$  vertex), while  $\gamma_{ep}$  stands for electron-phonon interaction ( $\circ$  vertex) [24]. (b) Temperature dependent Raman electronic Drude-like background of BiFeO<sub>3</sub> nanoparticles (Fig. 1) normalized by both Bose-Einstein thermal correction factor and  $\omega\tau$  (Eq. (1)). Cubes in green follow the temperature evolution of effective scattering rate  $1/\tau$ , in temperature ( $T$ )-Raman shift ( $\hbar\omega$ ) plane. (c) Conduction mechanisms due to the intrinsic activation from valence to conduction band (red arrow) and VRH promoted by localized states around Fermi level (blue arrow) in bulk (left) and nanocrystal (right) semiconductor. (For interpretation of the references to colour in this figure legend, the reader is referred to the web version of this article.)

**Fig. 3.** Temperature ( $T^{-n}$ ) dependence of the logarithm of the effective scattering rate ( $\ln(1/\tau)$ ) for  $T < T_N$  in figure (a) with  $n = 1/2$  and for  $T > T_N$  in figure (b) with  $n = 1/4$ . Linear fits are given in red lines. (c) TESCAN SM-300 image of the surface morphology of the BiFeO<sub>3</sub> nanoparticle batch and (d) the related histogram of the particle diameter distribution (bars in gray) fitted by the normal distribution function (Gauß) given in red line with  $(64 \pm 2)$  nm as the mean value and  $(28 \pm 2)$  nm as the standard deviation.  $f(\ell)$  stands for the frequency of appearance with respect to the nanoparticle size  $\ell$ . (For interpretation of the references to colour in this figure legend, the reader is referred to the web version of this article.)

The temperature dependences of  $\ln(1/\tau)$  are linearized against  $T^{-n}$ , with  $n = 1/2$  (Fig. 3(a)) and  $n = 1/4$  (Fig. 3(b)) in the strongly correlated AF ( $T < T_N$ ) and PM phase ( $T > T_N$ ), respectively, which is in accordance with the predictions for the applicability of the two VRH mechanisms [13,14]. To be precise, the temperature evolution of  $\ln(1/\tau)$  is proportional to  $(T_n/T)^n$ , with  $k_B T_{1/2} \approx e^2/(4\pi\epsilon_0\epsilon_r\xi)$  for  $n = 1/2$  [13] and  $k_B T_{1/4} \approx 18.1/(g(\epsilon_F)\xi^3)$  for  $n = 1/4$  [26], where  $k_B = 1.38 \times 10^{-23}$  J/K and  $\epsilon_0 = 8.85 \times 10^{-12}$  F/m. Parameter  $\xi$  is the localization length of wave function



of the electronic surface states, while  $\epsilon_r$  represents the relative permittivity constant, calculated as  $\epsilon_r \approx 28$  using the impedance dielectric spectroscopy of nanocrystalline BiFeO<sub>3</sub> [27].

Relying on the extracted slopes from the two linear fits in Fig. 3(a) & (b), we have come up with  $\xi \approx 7\text{nm}$ . This finding proves quite meaningful as a localization length of wave function of the electronic surface states since  $\xi < \langle \ell \rangle$ , where the average particle size  $\langle \ell \rangle$  reaches up nearly to 66nm. This value has been computed as the mean value from the Gaussian particle size distribution obtained from Scanning Electron Microscopy (SEM) image of BiFeO<sub>3</sub> nanoparticles at room temperature and using the Scanning Probe Image Processor software (Fig. 3(c) & (d)). Furthermore, the density of localized states,  $g(\epsilon_F)$ , can also be determined by manipulating the fitting parameters extracted from Fig. 3(a) & (b). Namely,  $g(\epsilon_F) \approx 2.1 \times 10^{18}$  localized states per (eV  $\times$  cm<sup>3</sup>) in the high temperature PM phase. This allows us to estimate the resistivity value  $\rho$  from Eq. (1) and the Einstein relation. Thus, following Fig. 2(b), at high temperatures  $h/\tau \approx 250\text{ cm}^{-1}$ , where  $h = 6.626 \times 10^{-34}\text{Js}$ . Accordingly,  $\rho \approx 4\pi^2\tau/(\langle \ell \rangle^2 e^2 g(\epsilon_F)) \approx 350\text{ m}\Omega\text{cm}$  at lowest. Its extraordinarily high value is not possible in conventional metals and exceeds the maximum resistivity value allowed by the Mott-Ioffe-Regel limit of at most  $\sim 1\text{ m}\Omega\text{cm}$  [28,29], which classifies nanocrystalline BiFeO<sub>3</sub> as a bad conductor. This finding strongly suggests that the conduction band energy sector is likely to fade away to ultimately acquire markedly low electronic density of states, leaving no room for the fixed thermally activated transport to take over 3D VRH. Nevertheless, other reliable experimental tools, such as AC/DC transport measurements, infrared and electron spin resonance spectroscopy on somewhat larger particles, might be a good proposal to uphold the validity of the VRH mechanisms we have put forward.

**Conclusions.** In summary, here is reported an indirect finding of the two different VRH transport regimes through the analysis of the temperature dependent electronic Raman background of BiFeO<sub>3</sub> nanoparticles. The switch between the two strikingly different VRH transport regimes coincides with AF/PM phase transition. The VRH exponent of  $n = 1/2$  is associated with the AF strongly correlated phase below  $T_N$  implying the presence of correlations, whereas the exponent  $n = 1/4$  neatly linearizes the temperature dependence of the logarithm of effective scattering rate in the PM state above  $T_N$ . It has been also deduced that the nanoscaled BiFeO<sub>3</sub> falls into the family of bad conductors due to its exceptionally high resistivity value. At last, it is worth mentioning that, to the extent of our knowledge, the existence of different conduction VRH regimes in AF and PM phases has never been previously recognized in BiFeO<sub>3</sub> nanocrystals.

### Declaration of Competing Interest

The authors declare that they have no known competing financial interests or personal relationships that could have appeared to influence the work reported in this paper.

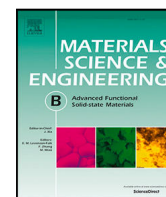
### Acknowledgments

We are grateful to Professor László Forró for valuable discussions on the topics of VRH transport mechanism. This work is

supported by the Serbian Ministry of Education, Science, and Technological Development through project OI 171032.

### References

- [1] J. Wang, J.B. Neaton, H. Zheng, V. Nagarajan, B.S.B. Ogale, Liu, D. Viehland, V. Vaithyanathan, D.G. Schlom, U.V. Waghmare, N.A. Spaldin, K.M. Rabe, M. Wuttig, R. Ramesh, Science 299 (2003) 1719–1722, doi:10.1126/science.1080615.
- [2] T.J. Park, G.C. Papaefthymiou, A.J. Viescas, A.R. Moodenbaugh, S.S. Wong, Nano Lett. 7 (2007) 766–772, doi:10.1021/nl063039w.
- [3] G. Catalan, J.F. Scott, Adv. Mater. 21 (2009) 2463–2485, doi:10.1002/adma.200802849.
- [4] A. Mukherjee, M. Banerjee, S. Basu, N.T.K. Thanh, L.A.W. Green, M. Pal, Physica B: Cond. Matt. 448 (2014) 199–203, doi:10.1016/j.physb.2014.03.082.
- [5] S. Ruby, S.S.R. Inbanathan, Appl. Surf. Sci. 449 (2018) 10–14, doi:10.1016/j.apsusc.2017.11.231.
- [6] L.A. Falkovsky, Phys. Usp. 47 (2004) 249–272, doi:10.1070/pu2004v047n03abeh001735.
- [7] L.A. Falkovsky, Sov. Phys. JETP 68 (1989) 661–663.
- [8] A. Zawadowski, M. Cardona, Phys. Rev. B 42 (1990) 10732–10734, doi:10.1103/PhysRevB.42.10732.
- [9] T.P. Devereaux, Phys. Rev. B 45 (1992) 12965–12975, doi:10.1103/PhysRevB.45.12965.
- [10] E.Y. Sherman, O.V. Misochko, J. Phys. Condens. Matter 15 (2003) 3751–3758, doi:10.1088/0953-8984/15/22/309.
- [11] T.P. Devereaux, R. Hackl, Rev. Mod. Phys. 79 (2007) 175–233, doi:10.1103/RevModPhys.79.175.
- [12] B. Stojadinović, Z. Dohčević-Mitrović, D. Stepanenko, M. Rosić, I. Petronijević, N. Tasić, N. Ilić, B. Matović, B. Stojanović, Ceram Int. 43 (2017) 16531–16538, doi:10.1016/j.ceramint.2017.09.038.
- [13] A.L. Efros, B.I. Shklovskii, J. Phys. C Solid State Phys. 8 (1975) L49–L51, doi:10.1088/0022-3719/8/4/003.
- [14] N.F. Mott, E.A. Davis, Electronic Processes in Non-Crystalline Materials, Oxford University Press, 1979.
- [15] H. Fukumura, H. Harima, K. Kisoda, M. Tamada, Y. Noguchi, M. Miyayama, J. Magn. and Magn. Mat. 310 (2007) e367–e369, doi:10.1016/j.jmmm.2006.10.282.
- [16] J. Hlinka, J. Pokorny, S. Karimi, I.M. Reaney, Phys. Rev. B 83 (2011) 020101–020104, doi:10.1103/PhysRevB.83.020101.
- [17] J. Bielecki, P. Svedlindh, D.T. Tibebe, S. Cai, S.-G. Eriksson, L. Börjesson, C.S. Knež, Phys. Rev. B 86 (2012) 184422–184437, doi:10.1103/PhysRevB.86.184422.
- [18] D.L. Rousseau, R.P. Bauman, S.P.S. Porto, J. Raman Spectrosc. 10 (1981) 253–290, doi:10.1002/jrs.1250100152.
- [19] A. Otto, J. Timper, J. Billmann, G. Kovacs, I. Pockrand, Surf. Sci. 92 (1980) L55–L57, doi:10.1016/0039-6028(80)90237-X.
- [20] C.Y. Chen, E. Burstein, S. Lundquist, Solid State Commun. 32 (1979) 63–66, doi:10.1016/0038-1098(79)90998-0.
- [21] R. Monreal, F. Flores, Y. Gao, T. López-Ríos, Europhys. Lett. 4 (1987) 115–120, doi:10.1209/0295-5075/4/1/019.
- [22] H.L. Liu, S. Yoon, S.L. Cooper, S.-W. Cheong, P.D. Han, D.A. Payne, Phys. Rev. B 58 (1998) R10115–R10118, doi:10.1103/PhysRevB.58.R10115.
- [23] A.A. Abrikosov, L.P. Gorkov, I.E. Dzyaloshinsky, Quantum Field Theoretical Methods in Statistical Physics, Pergamon Press (Oxford), 1965.
- [24] M. Cardona, Light Scattering in Solids I - Introductory Concepts, Springer-Verlag (Berlin), 1983.
- [25] L. Zuppiroli, L. Forró, Phys. Lett. A 141 (1989) 181–185, doi:10.1016/0375-9601(89)90785-8.
- [26] W.D. Rice, R.T. Weber, P. Nikolaev, S. Arepalli, V. Berka, A.L. Tsai, J. Kono, Phys. Rev. B 88 (2013) 041401–041405, doi:10.1103/PhysRevB.88.041401.
- [27] B. Stojadinović, University of Belgrade, 2018 Ph.D. thesis. Faculty of Physics.
- [28] O. Gunnarsson, M. Calandra, J.E. Han, Rev. Mod. Phys. 75 (2003) 1085–1099, doi:10.1103/RevModPhys.75.1085.
- [29] N.E. Hussey, K. Takenaka, H. Takagi, Philos. Mag. 84 (2004) 2847–2864, doi:10.1080/14786430410001716944.



# Unveiling the spin–phonon coupling in nanocrystalline BiFeO<sub>3</sub> by resonant two-phonon Raman active modes

Bojan Stojadinović<sup>a,\*</sup>, Dejan M. Djokić<sup>a</sup>, Novica Paunović<sup>a</sup>, Ivica Živković<sup>b</sup>, Luka Ćirić<sup>c</sup>, Vladan Kusigerski<sup>d</sup>, Zorana Dohčević-Mitrović<sup>a,\*</sup>

<sup>a</sup> Institute of Physics Belgrade, University of Belgrade, Pregrevica 118, 11080 Belgrade, Serbia

<sup>b</sup> Laboratory for Quantum Magnetism, Institute of Physics, Ecole Polytechnique Fédérale de Lausanne, CH-1015 Lausanne, Switzerland

<sup>c</sup> Laboratory of Nanostructures and Novel Electronic Materials, Ecole Polytechnique Fédérale de Lausanne, CH-1015 Lausanne, Switzerland

<sup>d</sup> “Vinča” Institute of Nuclear Sciences, University of Belgrade, P.O. Box 522, Belgrade 11001, Serbia

## ARTICLE INFO

### Keywords:

BiFeO<sub>3</sub> nanomaterials  
Sol–gel processes  
Raman spectroscopy  
Magnetic measurements  
Spin–phonon interactions

## ABSTRACT

We report on temperature dependence of two-phonon Raman spectra in BiFeO<sub>3</sub> nanocrystals, above and below the Néel temperature  $T_N$  using a resonant laser excitation line ( $\lambda = 532$  nm). Two-phonon modes exhibited anomalous frequency hardening and deviation from the anharmonic decay below  $T_N$ . Such behavior strongly supported the existence of spin–two-phonon interaction, because these modes are known to be very sensitive to the antiferromagnetic ordering. Within the mean-field theory for the nearest-neighbor interaction, the linear relationship between spin–spin correlation function and observed two-phonon frequency shift below  $T_N$  was obtained. This approach enabled to quantify the spin–phonon interaction by spin–phonon coupling strength for both two-phonon modes and justified the application of mean-field approach. Magnetic measurements revealed the coexistence of antiferromagnetic and weak ferromagnetic phases below  $T_N$ , which were found non competitive, additionally supporting the mean-field approach from which we deduced that the two-phonon modes in BiFeO<sub>3</sub> are correlated with antiferromagnetic ordering below  $T_N$ .

## 1. Introduction

Multiferroic materials attract a lot of attention because of their multifunctional properties and interesting fundamental physics [1,2]. Among all the single-phase multiferroic materials studied so far, BiFeO<sub>3</sub> takes a prominent place because both ferroelectric (Curie temperature,  $T_C \approx 1150$  K) and magnetic (Néel temperature,  $T_N \approx 640$  K) transition temperatures are well above room temperature (RT). In bulk phase BiFeO<sub>3</sub> has G-type antiferromagnetic ordering (AFM), with a long period cycloidal modulation (62 nm) superimposed below  $T_N$ . Above  $T_N$ , BiFeO<sub>3</sub> becomes paramagnetic (PM) [3]. In nanophased BiFeO<sub>3</sub> spin spiral structure can be suppressed [4] and Dzyaloshinskii–Moriya (DM) interaction becomes important. DM interaction induces non-collinear spin states which compete with the exchange interaction that favors anti-parallel spin alignment providing a coexistence of ferromagnetic (FM) and antiferromagnetic ordering [2,5]. Furthermore, the appearance of strong magnetoelectric effect in epitaxial BiFeO<sub>3</sub> thin films [6] and nanoparticles [4], positions nanophased BiFeO<sub>3</sub> as a leading candidate material for spintronics, magnetic field sensor devices and ferroelectric non-volatile memories [1,5,7–9]. However, the coupling between magnetic and ferroelectric degrees of freedom

in BiFeO<sub>3</sub> nanostructures still remains an open issue. Therefore, it is of great importance to study the interplay between lattice vibrations and magnetic excitations, because lattice distortion influences the ferroelectric polarization and accordingly affects its coupling to magnetic order. Furthermore, spin–phonon interaction is fundamental for driving relaxation in magnetic materials.

Among the optical spectroscopy methods, Raman spectroscopy proves to be a powerful experimental tool to elucidate spin–phonon (s-ph) interactions, since Raman mode can be sensitive to the spin correlations. In magnetic nanomaterials, such as BiFeO<sub>3</sub>, optical phonon modes can be influenced by the exchange coupling between magnetic ions at and below the temperatures of magnetic phase transitions. The spin–phonon interaction usually manifests as atypical temperature dependence of Raman phonon frequency, linewidth or integrated intensity. From the deviation of the Raman mode frequency from the anharmonicity at and below the magnetic phase transition, it is possible to estimate the spin–phonon coupling strength in the antiferromagnets or ferromagnets. Being rather phenomenological, the approach developed by Lockwood and Cottam [10] treats the strength of the spin–phonon coupling through the emergence of the AFM order

\* Corresponding authors.

E-mail addresses: [bojans@ipb.ac.rs](mailto:bojans@ipb.ac.rs) (B. Stojadinović), [zordoh@ipb.ac.rs](mailto:zordoh@ipb.ac.rs) (Z. Dohčević-Mitrović).

<https://doi.org/10.1016/j.mseb.2021.115444>

Received 29 March 2021; Received in revised form 24 August 2021; Accepted 4 September 2021

Available online 25 September 2021

0921-5107/© 2021 Elsevier B.V. All rights reserved.

parameter, that is the sublattice magnetization, but not the net one. Moreover, it turns out that a thorough microscopic treatment due to Djokic et al. [11] further corroborates this fact whereby the majority of the AFM ordering contribution to the phonon spectra is observed through the magnitude of the sublattice magnetization. The influence of any weak FM ordering (canted or so) in the system upon spin-phonon strength is thus greatly overwhelmed by the AFM ordering. Phonon anomalies around and below  $T_N$  were observed in the first-order Raman spectra of BiFeO<sub>3</sub> single crystal [12,13], ceramics [14] and thin films [15,16] and were ascribed to the influence of spin correlations on the phonon energies. The pioneering works of Cazayous [17] and Ramirez [18] pointed at possible strong spin-two-phonon interaction in BiFeO<sub>3</sub> single crystals and thin films, but all above mentioned works were restricted to qualitative description of the effects of spin correlations on the Raman active first and second-order phonons without any deeper analysis of spin-phonon coupling mechanism.

In the light of these facts, to examine more thoroughly the coupling between lattice and spin degrees of freedom in nanocrystalline BiFeO<sub>3</sub>, we investigated temperature-dependent second-order Raman spectra of BiFeO<sub>3</sub> nanocrystals in a wide temperature range below, at and above the Néel temperature using a resonant excitation line. The anomalous phonon hardening and obvious deviation from the anharmonicity of two-phonon Raman modes below Néel temperature was elaborated within a mean-field approach in order to correlate the spin-spin correlation function with observed frequency shift and to estimate the nearest-neighbor spin-phonon coupling constant. Magnetic measurements have shed more light on the nature of spin-phonon coupling mechanism in BiFeO<sub>3</sub> nanocrystals.

## 2. Experimental details

BiFeO<sub>3</sub> nanocrystals were synthesized by a sol-gel method and detailed sample preparation and characterization of the crystal structure and phase composition was given in Ref. [19]. BiFeO<sub>3</sub> nanoparticles were of spherical shape with average particle size of 64 nm deduced from SEM measurements [19,20]. Raman spectra of BiFeO<sub>3</sub> nanocrystals were collected in a backscattering geometry using TriVista 557 triple spectrometer with the spectral resolution of 2 cm<sup>-1</sup>. Second-order Raman spectra of BiFeO<sub>3</sub> nanocrystals pressed into pellets were recorded between 80 and 723 K in the 1000–1500 cm<sup>-1</sup> frequency range using a Linkam THMSG600 microscope heating stage. The resonant 532 nm line of a solid-state Nd:YAG laser was used as an excitation source, with output laser power low enough (less than 2 mW) to avoid the heating effects and/or sample thermal degradation. The Raman spectra were corrected by thermal occupation factor for the second-order scattering  $S(\omega) = S_0(\omega)/(n+1)^2$ , where  $S_0(\omega)$  is measured intensity and  $n = (e^{h\omega/k_B T} - 1)^{-1}$  is the Bose-Einstein thermal occupation factor [21]. Magnetic measurements at and below 300 K were performed on a SQUID-based Quantum Design magnetometers MPMS-5T and MPMS XL-5.

## 3. Results and discussions

The room-temperature Raman spectrum of BiFeO<sub>3</sub> nanocrystalline sample in the range 40–1500 cm<sup>-1</sup> is shown in Fig. 1.

Factor group analysis for the rhombohedral  $R3c$  structure of BiFeO<sub>3</sub> predicts 13 Raman active modes ( $4A_1 + 9E$ ), but the assignment of the Raman modes from the literature is somewhat controversial even in the case of BiFeO<sub>3</sub> single crystal Raman spectra measured or calculated in different polarizations [22–26]. As shown in Fig. 1, among the first order  $\Gamma$ -point phonons, modes around 79, 146, 175, 219, 261, 282, 332, 367, 435, 480 and 550 cm<sup>-1</sup> are clearly seen. According to the polarized Raman spectra of BiFeO<sub>3</sub> single crystals [23,25], ceramics [27] and thin films [28] we assigned modes around 146, 175 and 219 cm<sup>-1</sup> to  $A_1$  modes and modes around 79, 261, 282, 332, 367, 435, 480 and 550 cm<sup>-1</sup> to  $E$  modes. Beside these modes, weaker Raman

modes at around 575 and 656 cm<sup>-1</sup> and a stronger mode at  $\approx 630$  cm<sup>-1</sup> are also observed. The 575 and 656 cm<sup>-1</sup> modes (marked with \* in Fig. 1) can be ascribed to the mullite-type (Bi<sub>2</sub>Fe<sub>4</sub>O<sub>9</sub>) secondary phase [29], the presence of which has been confirmed from the X-ray diffraction analysis of BiFeO<sub>3</sub> nanocrystalline sample [19]. The Raman mode at  $\approx 630$  cm<sup>-1</sup> is not a zone center mode [27,30]. According to Bielecki et al. [30] this mode can be assigned to the Raman inactive  $A_2$  LO phonon mode which appears in BiFeO<sub>3</sub> thin films, ceramics and nanoparticles [18,30–33]. As can be seen in Fig. 1, the intense second-order Raman modes were observed above 1000 cm<sup>-1</sup> and from now on we will focus our attention on the temperature behavior of these Raman modes.

The high-order Raman modes of the ferroelectric materials are usually very weak, but in the spectrum of BiFeO<sub>3</sub> from Fig. 1 an intense multiphonon band around 1000–1500 cm<sup>-1</sup> is observed. This prominent band is already reported in BiFeO<sub>3</sub> thin films and single crystals [17,18,25], as well as in BiFeO<sub>3</sub> nanoparticles [31,32]. The broad band at 300 K from Fig. 1 was deconvoluted with Lorentzian type profile into four modes: mode at 1090 cm<sup>-1</sup>, a strong mode at 1252 cm<sup>-1</sup> and two low-intensity phonon modes at 1150 and 1330 cm<sup>-1</sup>. The second-order modes at 1090 and 1252 cm<sup>-1</sup>, labeled as  $S_1$  and  $S_2$  in Fig. 1, are, within the error limits, at the double frequency of the first-order Raman  $E$  mode at around 550 cm<sup>-1</sup> and inactive  $A_2$  mode at around 630 cm<sup>-1</sup> [22,30]. These modes were ascribed to two-phonon modes in accordance with literature data [13,17,18,30], whereas the remaining two modes can be assigned to  $2A_g$  modes of Bi<sub>2</sub>Fe<sub>4</sub>O<sub>9</sub> secondary phase [29]. Yang et al. [34] have investigated the behavior of two-phonon modes in BiFeO<sub>3</sub> powders using different excitation lines and reported that the intensity of two-phonon  $S_1$  and  $S_2$  modes are significantly enhanced under the 532 nm excitation. The intensity enhancement of  $S_1$  and  $S_2$  modes was attributed to the resonant enhancement when the excitation energy (532 nm  $\approx 2.34$  eV) is close to the absorption edge of BiFeO<sub>3</sub>. The resonant behavior of these modes was explained by exchange mechanism between Fe<sup>3+</sup> ions. Weber et al. [35] also reported resonant enhancement of second-order Raman modes in BiFeO<sub>3</sub> single crystals using 532 nm excitation, but suggested that in-gap electronic states like defect states from oxygen vacancies can be involved in the resonance process. Accordingly, we used 532 nm laser line in order to track the temperature evolution of  $S_1$  and  $S_2$  Raman modes. Two-phonon  $S_1$  and  $S_2$  modes are related to the Fe–O vibrations, i.e. octahedral rotations [17,18,32] which are very sensitive to the change of magnetic ordering. Moreover, it is well known that any perturbation of spiral spin structure in antiferromagnetic BiFeO<sub>3</sub> and distortion of FeO<sub>6</sub> octahedra due to the change of Fe–O–Fe bond angle can lead to the appearance of ferromagnetism [2,4,5]. Therefore, we have analyzed the behavior of  $S_1$  and  $S_2$  modes at temperatures below and above the magnetic phase transition.

In Fig. 2a are presented second-order Raman spectra in the 80–723 K temperature range. With increased temperature  $S_1$  and  $S_2$  modes gradually shift to lower wavenumbers and approaching the 600 K, the wavenumber shift is followed by a pronounced decrease of intensity (Fig. 2a). Similar behavior of  $S_2$  mode was first observed by Ramirez [18] and Cazayous [17] and was ascribed to the coupling of  $S_2$  mode with the magnetic sublattice. The accurate wavenumber change of  $S_1$  and  $S_2$  modes with temperature was obtained by deconvoluting the spectra from Fig. 2a with Lorentzian line shape function and Raman spectra at several representative temperatures together with cumulative fits are presented in Fig. 2b.

In magnetic materials, the change of phonon mode frequency with temperature can be expressed as [36,37]:

$$\omega(T) - \omega_0 \equiv \Delta\omega(T) = \Delta\omega_{\text{lat}}(T) + \Delta\omega_{\text{anh}}(T) + \Delta\omega_{\text{e-ph}}(T) + \Delta\omega_{\text{s-ph}}(T), \quad (1)$$

where  $\omega(T)$  is measured frequency at temperature  $T$  and  $\omega_0$  is the harmonic mode frequency at  $T = 0$  K. The first term on the right-hand side of the Eq. (1) is the frequency-independent pure-volume contribution due to the lattice expansion/contraction. The second term

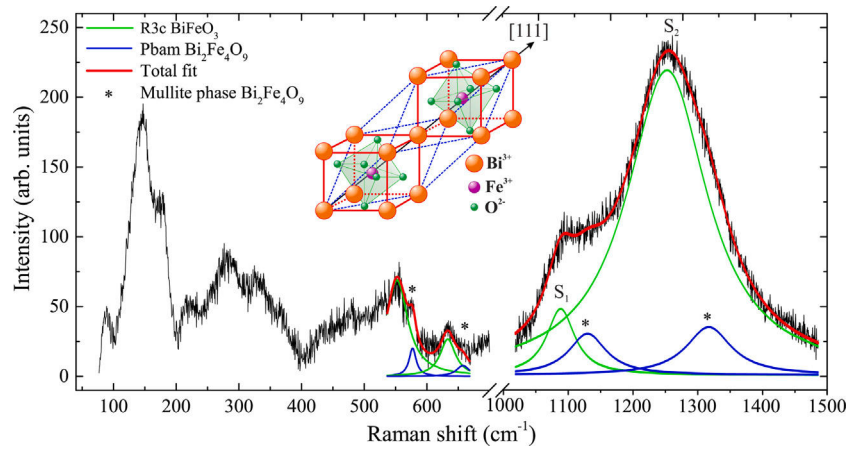


Fig. 1. Room-temperature Raman spectrum of nanocrystalline BiFeO<sub>3</sub> with Lorentzian fit (red line) of the first- and second-order phonon regions. The modes of mullite-type secondary phase Bi<sub>2</sub>Fe<sub>4</sub>O<sub>9</sub> are marked with (\*). Inset represents the schematic of a pseudocubic unit cell including one formula unit with principle axis of polarization [111].

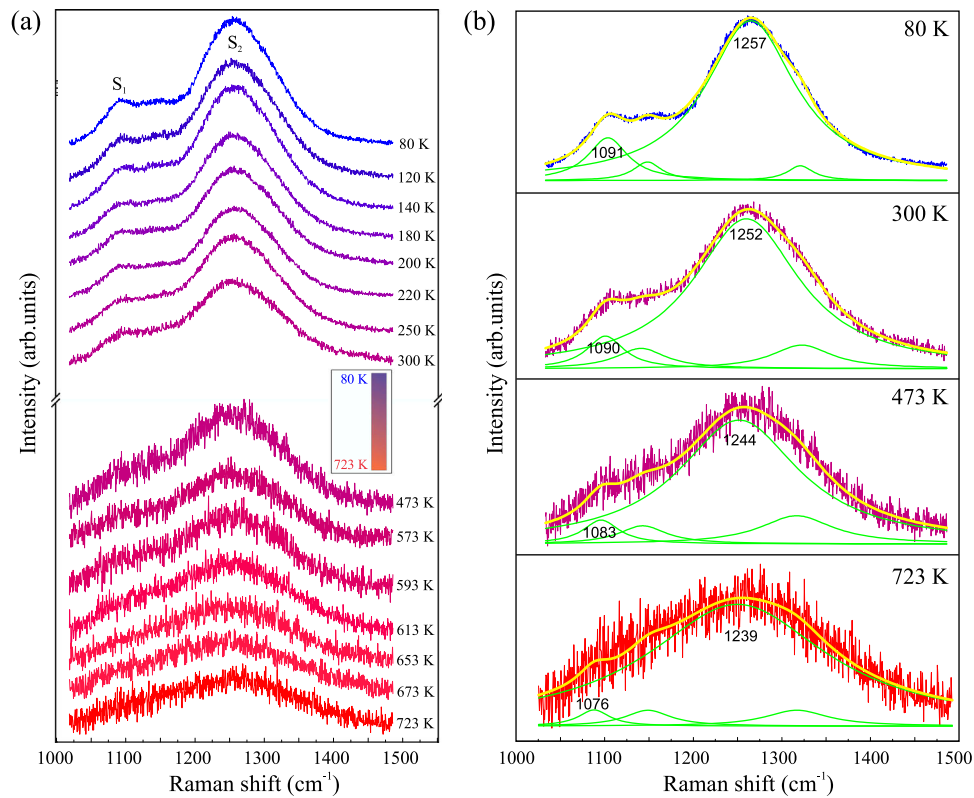


Fig. 2. Second-order Raman spectra of nanocrystalline BiFeO<sub>3</sub> (a) in the 80–723 K temperature range and (b) at selected temperatures. The solid lines represent Lorentzian fits of the experimental spectra.

is the anharmonic contribution due to phonon–phonon interactions. The last two terms account for the effects of renormalization of the phonon frequency due to electron–phonon and spin–phonon coupling.

In general, the change of phonon frequency due to pure-volume contribution is much smaller than the intrinsic anharmonic contribution, especially at low temperatures. BiFeO<sub>3</sub> in the form of powders or thin films is structurally stable up to 500 °C (773 K) [38] and any phonon frequency change due to lattice distortion is expected to be minimal, hence the first term can be neglected. The anharmonic interactions, significant at elevated temperatures, imply the phonon decay into two or three phonons, with a higher probability of the former. The phonon frequency change due to the decay of the phonon into two lower-energy

phonons (three-phonon processes) can be expressed as [39,40]:

$$\Delta\omega_{\text{anh}}(T) = A \left( 1 + \frac{2}{e^{\frac{h\omega(T)}{2k_B T}} - 1} \right), \quad (2)$$

where  $A$  is the anharmonic constant. In semiconductor materials like BiFeO<sub>3</sub>, when the carrier concentration is low the third term can be ignored. Finally, the last term in Eq. (1) is the spin–phonon contribution,  $\Delta\omega_{\text{s-ph}}(T)$ , caused by the modulation of the exchange integral by lattice vibration [36]. In magnetic materials such as BiFeO<sub>3</sub>, the phonon frequencies can be very sensitive to the spin correlations and in a case of Heisenberg model, Baltensberger and Helman [41] derived the relation for the shift of the phonon frequency due to the spin–phonon

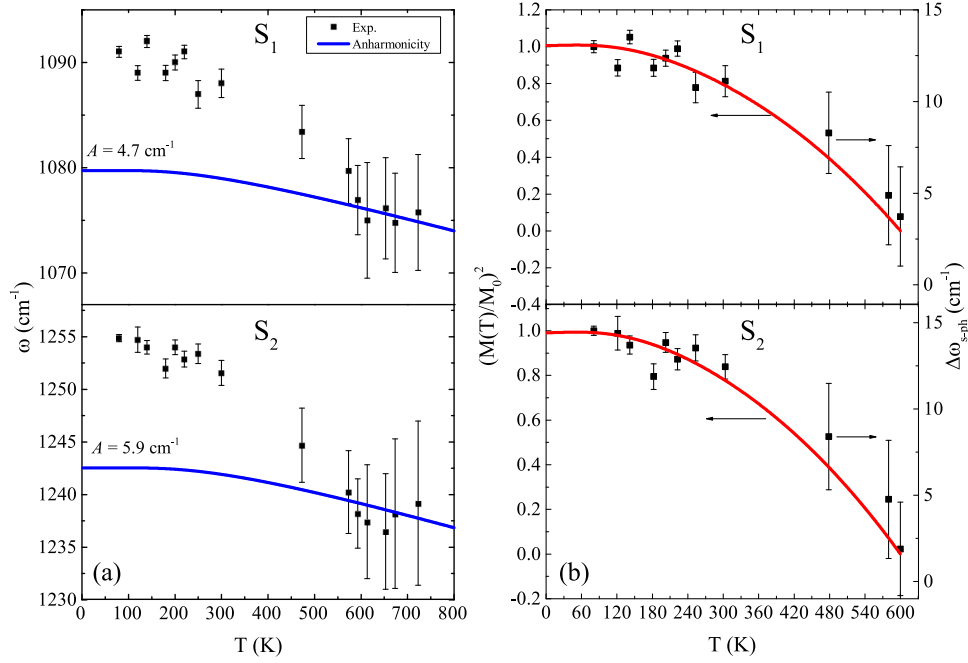


**Fig. 3.** (a) Temperature dependence of frequencies of the  $S_1$  and  $S_2$  two-phonon modes. The theoretically predicted anharmonic trend is presented by blue line together with the best fit anharmonic parameter ( $A$ ). (b) Comparison of  $(M(T)/M_0)^2$  (left) and  $\Delta\omega_{s-ph}(T)$  (right) temperature dependences.

interaction,

$$\Delta\omega_{s-ph}(T) = -\lambda \langle S_i \cdot S_{i+1} \rangle, \quad (3)$$

where  $\lambda$  stands for the spin–phonon coupling constant and  $\langle S_i \cdot S_{i+1} \rangle$  is the spin–spin correlation function between adjacent spins.

The temperature dependence of  $S_1$  and  $S_2$  mode frequencies (squares) is shown in Fig. 3a. As can be seen, at lower temperatures ( $T < 300$  K) frequencies of  $S_1$  and  $S_2$  modes exhibit a slower change and at temperature around 600 K display step like anomaly. This temperature should coincide with Néel temperature, since there is no any known structural transition in  $\text{BiFeO}_3$  at this temperature.

In order to determine the strength of spin–phonon coupling, it is necessary to separate spin–phonon and anharmonic contributions from the change of the phonon frequency with temperature. Knowing that phonon frequencies can be affected by AFM ordering below  $T_N$  and that the anharmonic processes should dominate over the spin–phonon coupling at high temperatures ( $T > T_N$ ) for which the  $\text{BiFeO}_3$  is in the PM state, the data for  $T > 593$  K from Fig. 3a were fitted by Eq. (2) (blue line on Fig. 3a extrapolated to  $T = 0$  K) in order to determine the anharmonic contribution to the phonon frequencies change. It is obvious that frequency change of both  $S_1$  and  $S_2$  modes below  $T_N$  show distinct deviation away from the expected anharmonic behavior. Similar frequency behavior has been observed in the Raman spectra of other antiferromagnetic [10,36,42–45] and ferromagnetic materials [46,47]. Thus, anomalous frequency hardening of  $S_1$  and  $S_2$  modes below  $T_N$  points out at the presence of spin-two-phonon coupling in nanocrystalline  $\text{BiFeO}_3$ . The difference between measured two-phonon frequencies from Fig. 3a and the calculated and extrapolated anharmonic behavior gives us the temperature dependent frequency shift due to spin–phonon interaction,  $\Delta\omega_{s-ph}(T) = \omega(T) - \omega_{anh}(T)$ . The  $\Delta\omega_{s-ph}$  vs  $T$  dependence (squares) for  $S_1$  and  $S_2$  two-phonon modes is presented in Fig. 3b.

Within the mean-field approximation introduced by Weiss [48], spin–spin correlation function  $\langle S_i \cdot S_{i+1} \rangle$  for adjacent spins at the  $i$ th and  $(i+1)$ th sites is proportional to the square of normalized magnetization,  $(M(T)/M_0)^2$ , and can be expressed as [49]

$$\frac{\langle S_i \cdot S_{i+1} \rangle}{S^2} = \left( \frac{M(T)}{M_0} \right)^2, \quad (4)$$

where  $M(T)$  is in our case sublattice magnetization at temperature  $T$  and  $M_0$  is the maximal value of sublattice magnetization. Having a look at Eqs. (3) and (4) it is obvious that  $\Delta\omega_{s-ph}(T)$  should scale with  $(M(T)/M_0)^2$  curve. The  $(M(T)/M_0)^2$  curve was obtained using a numerical solution for Weiss equation in a case of  $\text{Fe}^{3+}$  ions having spin  $S = 5/2$  [50] and then compared with experimentally obtained  $\Delta\omega_{s-ph}(T)$  for both two-phonon modes, as presented in Fig. 3b. Obviously, for temperatures  $T \leq T_N$ ,  $\Delta\omega_{s-ph}(T)$  scales very good with  $(M(T)/M_0)^2$  curve confirming that the significant deviation of  $S_1$  and  $S_2$  phonon frequencies from anharmonic behavior below  $T_N$ , i.e. the anomalous hardening, is actually due to spin–phonon interaction.

According to Eq. (3), from the plot  $\Delta\omega_{s-ph}(T)$  vs  $\langle S_i \cdot S_{i+1} \rangle(T)$  shown in Fig. 4, the spin–phonon coupling constant  $\lambda$  can be determined for both two-phonon modes  $S_1$  and  $S_2$ .

The red solid lines on Fig. 4 present the linear fit of the data from which the spin–phonon coupling constants  $\lambda_{S_1} = (2.54 \pm 0.10) \text{ cm}^{-1}$  and  $\lambda_{S_2} = (2.51 \pm 0.10) \text{ cm}^{-1}$  were determined. The linear behavior of  $\Delta\omega_{s-ph}(T)$  vs  $\langle S_i \cdot S_{i+1} \rangle(T)$  for the  $T \leq T_N$  justifies the application of Eq. (3), implying that in the AFM phase spin–phonon coupling dominates over the anharmonicity and terminates in the paramagnetic phase. Furthermore, the fact that both two-phonon modes exhibit anomalous frequency hardening below magnetic ordering temperature and that the values for  $\lambda$  are very similar, indicates that there is a universal influence of the AFM magnetic ordering upon the two-phonon spectra.

Up to now it is well established that in antiferromagnetic  $\text{BiFeO}_3$  nanoparticles with particle size close to or less than the period of spin cycloid appear ferromagnetic phase at room temperature [4,51–53].  $\text{BiFeO}_3$  nanoparticles can be considered to be composed of AFM core and FM shell giving rise to changes in the magnetic characteristics [53] or to the appearance of exchange bias and training effects [[52], and references within]. Since our  $\text{BiFeO}_3$  nanoparticles are of the average size close to the spin cycloid period, we performed magnetic measurements in order to get better insight into the two-phonon Raman modes coupling with magnetic ordering below  $T_N$ .

Fig. 5a presents room-temperature magnetization ( $M$ ) vs magnetic field ( $H$ ) dependence for  $\text{BiFeO}_3$  nanoparticles. From the M–H loop it can be seen that the magnetization curve (black circles) displays

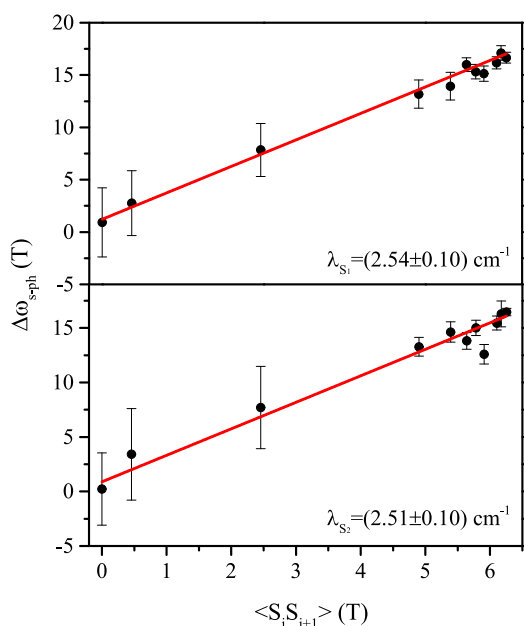


Fig. 4. The plot  $\Delta\omega_{s-ph}(T)$  vs  $\langle S_i \cdot S_{i+1} \rangle(T)$  for both two-phonon modes  $S_1$  and  $S_2$ . The  $\lambda$  values for both modes were determined from the linear fit (red solid line) of the data. (For interpretation of the references to color in this figure legend, the reader is referred to the web version of this article.)

a hysteresis in the low-field region, indicating a presence of weak ferromagnetism. The FM component is superimposed over a linear background from antiferromagnetic BiFeO<sub>3</sub> phase and paramagnetic mullite phase. After subtracting the linear background, the ferromagnetic hysteresis curve (red squares) with the saturation magnetization value  $M_S = 0.094$  emu/g was obtained. The inset in Fig. 5a displays the magnification of the hysteresis loop in the low-field region. The FM ordering can be considered as genuine one and does not originate from mullite or iron oxide impurity phases. Namely, mullite (Bi<sub>2</sub>Fe<sub>4</sub>O<sub>9</sub>) phase is paramagnetic at room temperature and undergoes a transition to an antiferromagnetic state at  $T_N \approx 264$  K [54]. Besides, the presence of iron oxides, leads to significantly enhanced ferromagnetism with large values of saturation magnetization [55]. The origin of FM ordering in otherwise antiferromagnetic BiFeO<sub>3</sub> is usually ascribed to the suppression of the spiral spin structure in particles with diameter less than the period of spin cycloid (62 nm) and higher distortion of FeO<sub>6</sub> octahedra or to the uncompensated spins on the nanoparticle surface. All of these effects lead to enhanced Dzyaloshinskii–Moriya interaction and appearance of ferromagnetism in nanocrystalline BiFeO<sub>3</sub> [2, 4,52,56]. In that case BiFeO<sub>3</sub> nanoparticles can be considered to be constituted of core/shell structure, i.e. antiferromagnetic core and ferromagnetic shell. As our nanocrystalline BiFeO<sub>3</sub> powders are composed of nanoparticles with average particle size of 64 nm [19,20] it can be supposed that the interruption of long-range AFM ordering takes place primarily on the nanoparticle surface. This assumption is supported by a report of Huang et al. [4] who have shown that BiFeO<sub>3</sub> nanoparticles of core-shell structure, with size close to the period of spin cycloid, exhibit increased ferromagnetism. It was further argued that FM ordering originates not only from the surface uncompensated spins, but from enhanced distortion of FeO<sub>6</sub> octahedra around the [111] direction. Such enhanced structural distortion can cause suppression of spiral spin structure and strengthening of DM interaction responsible for the appearance of FM. Accordingly, both effects, the suppression of spin cycloid and uncompensated surface spins, can lead to the occurrence of weak ferromagnetism in our sample.

Fig. 5b displays zero field cooled (ZFC) and field cooled (FC) magnetization curves, measured at 1000 Oe. The ZFC and FC curves started

to split below 250 K and the divergence became more pronounced with decreasing temperature. The ZFC curve showed a peak around the temperature of spin reorientation transition (200 K) [17,57] at which the Fe<sup>3+</sup> magnetic moments are canted out of cycloidal plane. Besides, ZFC curve does not tend to  $M = 0$  with approaching  $T = 0$ , as one would expect in a case of the presence of iron oxide impurity phases [58]. The ZFC/FC magnetization curves of our sample are very different from the ZFC/FC magnetization behavior of BiFeO<sub>3</sub> single crystal which was ascribed to the spin-glass ordering [59]. Recent ZFC/FC measurements on BiFeO<sub>3</sub> nanoparticles with sizes close to or less than the period of spin cycloid [4,7,56] have shown similar pronounced splitting of the ZFC/FC curves when antiferromagnetic and ferromagnetic orderings co-exist. Unlike the BiFeO<sub>3</sub> single crystal with antiferromagnetic ordering, those BiFeO<sub>3</sub> nanostructures can be considered as core-shell structures composed of antiferromagnetic core and ferromagnetic shell [4,52,56] in which more pronounced ZFC/FC splitting than in bulk BiFeO<sub>3</sub> suggests some irreversible effect on magnetic properties like breaking of AFM order and appearance of ferromagnetism [4,7,51,52]. Furthermore, more detailed analysis of ZFC/FC magnetization measurements on nanocrystalline BiFeO<sub>3</sub> [53] has shown that pronounced ZFC/FC splitting more likely originates from the changes in the domain structure at low temperatures and eventual antiferromagnetic domain pinning effect [4] than from spin-glass ordering.

In order to justify the use of mean-field theory approximation which does not include magnetic frustrations nor quantum fluctuations apart from the temperature ones [49], we refer to the study of Rao et al. on polycrystalline BiFeO<sub>3</sub> [60], where one can infer from that the Curie–Weiss temperature ( $\theta_{CW}$ ) tends to a very large value. Knowing that in bulk BiFeO<sub>3</sub>  $T_N = 640$  K [1,2] and in nanostructured BiFeO<sub>3</sub>  $T_N$  slightly decreases with decreasing crystallite size [61], the BiFeO<sub>3</sub> is only seemingly frustrated system, since the frustration factor,  $f = |\theta_{CW}|/T_N$  can exceed low frustration values [62]. However, we find magnetic frustration inconsequential because of the two noncompeting magnetic interactions: antiferromagnetic and ferromagnetic. These interactions are known to be cooperative in forming the stable Néel phase like in MnSe<sub>2</sub> [11]. Therefore, even at low temperatures, the average value of the relevant spin component per site is nearly 5/2, implying the stability of the AFM phase in BiFeO<sub>3</sub>. Otherwise, spin-phonon coupling would be more complex, the  $\Delta\omega_{s-ph}(T)$  would substantially deviate from the mean-field approximation model which we applied [44, 47] and a different treatment of the spin-phonon coupling mechanism would be required. The presented magnetic measurements are in favor of the picture in which nothing else, but the AFM magnetic ordering, without the presence of magnetic frustrations, influences the anomalous hardening of two-phonon Raman modes below  $T_N$  in nanocrystalline BiFeO<sub>3</sub>.

#### 4. Concluding remarks

In conclusion, we have investigated the temperature evolution of the resonant Raman two-phonon modes in BiFeO<sub>3</sub> nanocrystals, which are known to be very sensitive to magnetic ordering. Temperature studies have shown anomalous hardening and significant deviation of two-phonon frequencies from the anharmonicity below Néel temperature. The anomalous phonon hardening was ascribed to spin-two-phonon coupling. Within the mean-field approach, the spin-spin correlation function was correlated to the two-phonon frequency shift and the spin-phonon coupling strength for two-phonon modes was derived. The linear relation between spin-spin correlation function and frequency shift below Néel temperature confirmed no presence of fluctuations or magnetic frustrations and justified the application of mean-field approach. Magnetic measurements revealed the presence of weak FM phase below  $T_N$ . The coexistence of AFM and FM ordering were found not competitive, justifying the conclusion derived from mean-field approach that two-phonon Raman modes below  $T_N$  are strongly coupled to AFM ordering.

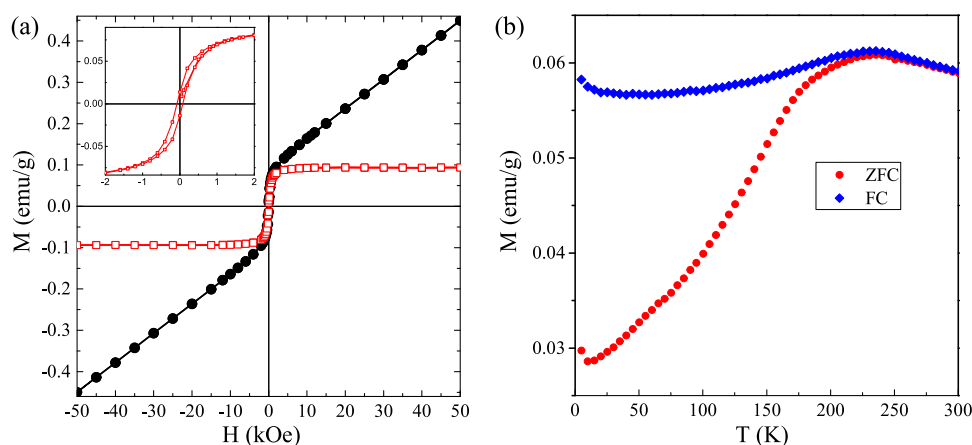


Fig. 5. (a) Room-temperature magnetization ( $M$ ) vs magnetic field ( $H$ ) dependence for  $\text{BiFeO}_3$  nanoparticles, before (circles) and after subtraction (squares) of the linear background component. Inset shows zoom in view of  $M$ - $H$  curve. (b) ZFC and FC magnetization curves measured at  $H = 1000$  Oe.

### Declaration of competing interest

The authors declare that they have no known competing financial interests or personal relationships that could have appeared to influence the work reported in this paper.

### Acknowledgments

The authors greatly acknowledge funding provided by the Institute of Physics Belgrade, through the grant by the Ministry of Education, Science, and Technological Development of the Republic of Serbia.

### References

- [1] N.A. Spaldin, Multiferroics: Past, present, and future, *Phys. Today* 63 (2010) 38–43, <http://dx.doi.org/10.1063/1.3502547>.
- [2] G. Catalan, J.F. Scott, Physics and applications of Bismuth ferrite, *Adv. Mater.* 21 (2009) 2463–2485, <http://dx.doi.org/10.1002/adma.200802849>.
- [3] I. Sosnowska, T.P. Neumaier, E. Steichele, Spiral magnetic ordering in bismuth ferrite, *J. Phys. C: Solid State* 15 (1982) 4835–4846, <http://dx.doi.org/10.1088/0022-3719/15/23/020>.
- [4] F. Huang, Z. Wang, J. Zhang, K. Min, W. Lin, R. Ti, T. Xu, J. He, C. Yue, J. Zhu, Peculiar magnetism of  $\text{BiFeO}_3$  nanoparticles with size approaching the period of the spiral spin structure, *Sci. Rep.* 3 (2013) 2907–2913, <http://dx.doi.org/10.1038/srep02907>.
- [5] C.-H. Yang, D. Kan, I. Takeuchi, V. Nagarajan, J. Seidel, Doping  $\text{BiFeO}_3$ : approaches and enhanced functionality, *Phys. Chem. Chem. Phys.* 14 (2012) 15953–15962, <http://dx.doi.org/10.1039/C2CP43082G>.
- [6] J. Wang, J.B. Neaton, H. Zheng, V. Nagarajan, S.B. Ogale, B. Liu, D. Viehland, V. Vaithyanathan, D.G. Schlom, U.V. Waghmare, N.A. Spaldin, K.M. Rabe, M. Wuttig, R. Ramesh, Epitaxial  $\text{BiFeO}_3$  multiferroic thin film heterostructures, *Science* 299 (2003) 1719–1722, <http://dx.doi.org/10.1126/science.1080615>.
- [7] J. Wu, S. Mao, Z.-G. Ye, Z. Xie, L. Zheng, Room-temperature ferromagnetic/ferroelectric  $\text{BiFeO}_3$  synthesized by a self-catalyzed fast reaction process, *J. Mater. Chem.* 20 (2010) 6512–6516, <http://dx.doi.org/10.1039/c0jm00729c>.
- [8] J. Ma, J. Hu, Z. Li, C.-W. Nan, Recent progress in multiferroic magnetoelectric composites: from bulk to thin films, *Adv. Mater.* 23 (2011) 1062–1087, <http://dx.doi.org/10.1002/adma.201003636>.
- [9] R. Ramesh, N.A. Spaldin, Multiferroics: progress and prospects in thin films, *Nature Mater.* 6 (2007) 21–29, <http://dx.doi.org/10.1038/nmat1805>.
- [10] D.J. Lockwood, M.G. Cottam, The spin-phonon interaction in  $\text{FeF}_2$  and  $\text{MnF}_2$  studied by Raman spectroscopy, *J. Appl. Phys.* 64 (1988) 5876–5878, <http://dx.doi.org/10.1063/1.342186>.
- [11] D.M. Djokić, Z.V. Popović, F.R. Vukajlović, Influence of antiferromagnetic spin ordering on the far-infrared active optical phonon modes of  $\alpha\text{MnSe}$ , *Phys. Rev. B* 77 (2008) 014305, <http://dx.doi.org/10.1103/PhysRevB.77.014305>.
- [12] C.-S. Chen, C.-S. Tu, P.-Y. Chen, V.H. Schmidt, Z.-R. Xu, Y. Ting, Spin-lattice coupling phase transition and phonon anomalies in bismuth ferrite  $\text{BiFeO}_3$ , *J. Alloy. Compd.* 687 (2016) 442–450, <http://dx.doi.org/10.1016/j.jallcom.2016.06.193>.
- [13] T.M.H. Nguyen, X.N. Nguyen, X.-B. Chen, X.T. To, S. Lee, T.H. Nguyen, I.-S. Yang, Study of spin-phonon coupling in multiferroic  $\text{BiFeO}_3$  through Raman spectroscopy, *J. Mol. Struct.* 1222 (2020) 128884, <http://dx.doi.org/10.1016/j.molstruc.2020.128884>.
- [14] J. Wei, C. Wu, Y. Liu, Y. Guo, T. Yang, D. Wang, Z. Xu, R. Haumont, Structural distortion, spin-phonon coupling, interband electronic transition, and enhanced magnetization in rare-earth-substituted bismuth ferrite, *Inorg. Chem.* 56 (2017) 8964–8974, <http://dx.doi.org/10.1021/acs.inorgchem.7b00914>.
- [15] M.K. Singh, W. Prellier, H.M. Jang, R.S. Katiyar, Anomalous magnetic ordering induced spin-phonon coupling in  $\text{BiFeO}_3$  thin films, *Solid State Commun.* 149 (2009) 1971–1973, <http://dx.doi.org/10.1016/j.ssc.2009.07.036>.
- [16] A. Ahlawat, S. Satapathy, S. Maan, V.G. Sathe, P.K. Gupta, Correlation of structure and spin-phonon coupling in (La, Nd) doped  $\text{BiFeO}_3$  films, *J. Raman Spectrosc.* 45 (2014) 958–962, <http://dx.doi.org/10.1002/jrs.4573>.
- [17] M. Cazayous, A. Sacuto, D. Lebeugle, D. Colson, Possible interplay between a two phonon mode and high energy magnetic excitations in  $\text{BiFeO}_3$ , *Eur. Phys. J. B* 67 (2009) 209–212, <http://dx.doi.org/10.1140/epjb/e2009-00033-7>.
- [18] M.O. Ramirez, M. Krishnamurthi, S. Denev, A. Kumar, S.-Y. Yang, Y.-H. Chu, E. Saiz, J. Seidel, A.P. Pyatakov, A. Bush, D. Viehland, J. Orenstein, R. Ramesh, V. Gopalan, Two-phonon coupling to the antiferromagnetic phase transition in multiferroic  $\text{BiFeO}_3$ , *Appl. Phys. Lett.* 92 (2008) 022511, <http://dx.doi.org/10.1063/1.2829681>.
- [19] B. Stojadinović, Z. Dohčević-Mitrović, D. Stepanenko, M. Rosić, I. Petronijević, N. Tasić, N. Ilić, B. Matović, B. Stojanović, Dielectric and ferroelectric properties of Ho-doped  $\text{BiFeO}_3$  nanopowders across the structural phase transition, *Ceram. Int.* 43 (2017) 16531–16538, <http://dx.doi.org/10.1016/j.ceramint.2017.09.038>.
- [20] D.M. Djokić, B. Stojadinović, D. Stepanenko, Z. Dohčević-Mitrović, Probing charge carrier transport regimes in  $\text{BiFeO}_3$  nanoparticles by Raman spectroscopy, *Scr. Mater.* 181 (2020) 6–9, <http://dx.doi.org/10.1016/j.scriptamat.2020.02.008>.
- [21] S.S. Mitra, *Infrared and Raman spectra due to lattice vibrations*, Springer US, Boston, MA, 1969, pp. 398–400, <http://dx.doi.org/10.1007/978-1-4757-1123-3-14>.
- [22] R. Palai, R.S. Katiyar, H. Schmid, P. Tissot, S.J. Clark, J. Robertson, S.A.T. Redfern, G. Catalan, J.F. Scott,  $\beta$  Phase and  $\gamma$ - $\beta$  metal-insulator transition in multiferroic  $\text{BiFeO}_3$ , *Phys. Rev. B* 77 (2008) 014110, <http://dx.doi.org/10.1103/PhysRevB.77.014110>.
- [23] M. Cazayous, D. Malka, D. Lebeugle, D. Colson, Electric field effect on  $\text{BiFeO}_3$  single crystal investigated by Raman spectroscopy, *Appl. Phys. Lett.* 91 (2007) 071910, <http://dx.doi.org/10.1063/1.2771380>.
- [24] C. Beekman, A.A. Reijnders, Y.S. Oh, S.W. Cheong, K.S. Burch, Raman study of the phonon symmetries in  $\text{BiFeO}_3$  single crystals, *Phys. Rev. B* 86 (2012) 020403, <http://dx.doi.org/10.1103/PhysRevB.86.020403>.
- [25] H. Fukumura, S. Matsui, H. Harima, T. Takahashi, T. Itoh, K. Kisoda, M. Tamada, Y. Noguchi, M. Miyayama, Observation of phonons in multiferroic  $\text{BiFeO}_3$  single crystals by Raman scattering, *J. Phys. Condens. Mat.* 19 (2007) 365224, <http://dx.doi.org/10.1088/0953-8984/19/36/365224>.
- [26] P. Hermet, M. Goffinet, J. Kreisel, F. Ghosez, Raman and infrared spectra of multiferroic bismuth ferrite from first principles, *Phys. Rev. B* 75 (2007) 220102, <http://dx.doi.org/10.1103/PhysRevB.75.220102>.
- [27] J. Hlinka, J. Pokorný, S. Karimi, I.M. Reaney, Angular dispersion of oblique phonon modes in  $\text{BiFeO}_3$  from micro-Raman scattering, *Phys. Rev. B* 83 (2011) 020101, <http://dx.doi.org/10.1103/PhysRevB.83.020101>.
- [28] M.K. Singh, H.M. Jang, S. Ryu, M.-H. Jo, Polarized Raman scattering of multiferroic  $\text{BiFeO}_3$  epitaxial films with rhombohedral  $R3c$  symmetry, *Appl. Phys. Lett.* 88 (2006) 042907, <http://dx.doi.org/10.1063/1.2168038>.
- [29] M.N. Iliev, A.P. Litvinchuk, V.G. Hadjiev, M.M. Gospodinov, V. Skumryev, E. Ressouche, Phonon and magnon scattering of antiferromagnetic  $\text{Bi}_2\text{Fe}_2\text{O}_7$ , *Phys. Rev. B* 81 (2010) 024302, <http://dx.doi.org/10.1103/PhysRevB.81.024302>.

- [30] J. Bielecki, P. Svedlindh, D.T. Tibebe, S. Cai, S.-G. Eriksson, L. Börjesson, C.S. Knee, Structural and magnetic properties of isovalently substituted multiferroic BiFeO<sub>3</sub>: Insights from Raman spectroscopy, *Phys. Rev. B* 86 (2012) 184422, <http://dx.doi.org/10.1103/PhysRevB.86.184422>.
- [31] S. Chauhan, M. Kumar, P. Pal, Substitution driven structural and magnetic properties and evidence of spin phonon coupling in Sr-doped BiFeO<sub>3</sub> nanoparticles, *RSC Adv.* 6 (2016) 68028–68040, <http://dx.doi.org/10.1039/C6RA11021E>.
- [32] M. Kumar, M. Arora, S. Chauhan, S. Joshi, Raman spectroscopy probed spin-phonon coupling and improved magnetic and optical properties in Dy and Zr substituted BiFeO<sub>3</sub> nanoparticles, *J. Alloy. Compd.* 692 (2017) 236–242, <http://dx.doi.org/10.1016/j.jallcom.2016.09.031>.
- [33] B. Stojadinović, Z. Dohčević-Mitrović, N. Paunović, N. Ilić, N. Tasić, I. Petronijević, D. Popović, B. Stojanović, Comparative study of structural and electrical properties of Pr and Ce doped BiFeO<sub>3</sub> ceramics synthesized by auto-combustion method, *J. Alloy. Compd.* 657 (2016) 866–872, <http://dx.doi.org/10.1016/j.jallcom.2015.09.235>.
- [34] Y. Yang, J.Y. Sun, K. Zhu, Y.L. Liu, J. Chen, X.R. Xing, Raman study of BiFeO<sub>3</sub> with different excitation wavelengths, *Physica B* 404 (2009) 171–174, <http://dx.doi.org/10.1016/j.physb.2008.10.029>.
- [35] M.C. Weber, M. Guennou, C. Toulouse, M. Cazayous, Y. Gillet, X. Gonze, J. Kreisel, Temperature evolution of the band gap in BiFeO<sub>3</sub> traced by resonant Raman scattering, *Phys. Rev. B* 93 (2016) 125204, <http://dx.doi.org/10.1103/PhysRevB.93.125204>.
- [36] E. Granado, A. García, J.A. Sanjurjo, C. Rettori, I. Torriani, F. Prado, R.D. Sánchez, A. Caneiro, S.B. Oseroff, Magnetic ordering effects in the Raman spectra of La<sub>1-x</sub>Mn<sub>1-x</sub>O<sub>3</sub>, *Phys. Rev. B* 60 (1999) 11879–11882, <http://dx.doi.org/10.1103/PhysRevB.60.11879>.
- [37] X.-B. Chen, N.T. Minh Hien, K. Han, J. Chul Sur, N.H. Sung, B.K. Cho, I.-S. Yang, Raman studies of spin-phonon coupling in hexagonal BaFe<sub>12</sub>O<sub>19</sub>, *J. Appl. Phys.* 114 (2013) 013912, <http://dx.doi.org/10.1063/1.4812575>.
- [38] J. Ryu, C.-W. Baek, D.-S. Park, D.-Y. Jeong, Multiferroic BiFeO<sub>3</sub> thick film fabrication by aerosol deposition, *Met. Mater. Int.* 16 (2010) 639–642, <http://dx.doi.org/10.1007/s12540-010-0818-9>.
- [39] P.G. Klemens, Anharmonic decay of optical phonons, *Phys. Rev.* 148 (1966) 845–848, <http://dx.doi.org/10.1103/PhysRev.148.845>.
- [40] M. Balkanski, R.F. Wallis, E. Haro, Anharmonic effects in light scattering due to optical phonons in silicon, *Phys. Rev. B* 28 (1983) 1928–1934, <http://dx.doi.org/10.1103/PhysRevB.28.1928>.
- [41] W. Baltensperger, J.S. Helman, Influence of magnetic order in insulators on the optical phonon frequency, *Helv. Phys. Acta* 41 (1968) 668–673, <http://dx.doi.org/10.5169/seals-113910>.
- [42] E. Aytan, B. Debnath, F. Kargar, Y. Barlas, M.M. Lacerda, J. Li, R. Lake, J. Shi, A.A. Balandin, Spin-phonon coupling in antiferromagnetic nickel oxide, *Appl. Phys. Lett.* 111 (2017) 252402, <http://dx.doi.org/10.1063/1.5009598>.
- [43] P.-H. Shih, C.-L. Cheng, S.Y. Wu, Short-range spin-phonon coupling in in-plane CuO nanowires: a low-temperature Raman investigation, *Nanoscale Res. Lett.* 8 (2013) 1–6, <http://dx.doi.org/10.1186/1556-276X-8-398>.
- [44] C. Kant, J. Deisenhofer, T. Rudolf, F. Mayr, F. Schrettle, A. Loidl, V. Gnezdilov, D. Wulferding, P. Lemmens, V. Tsurkan, Optical phonons, spin correlations, and spin-phonon coupling in the frustrated pyrochlore magnets CdCr<sub>2</sub>O<sub>4</sub> and ZnCr<sub>2</sub>O<sub>4</sub>, *Phys. Rev. B* 80 (2009) 214417–214426, <http://dx.doi.org/10.1103/PhysRevB.80.214417>.
- [45] J. Zhang, Q. Lian, Z. Pan, W. Bai, J. Yang, Y. Zhang, X. Tang, J. Chu, Spin-phonon coupling and two-magnons scattering behaviors in hexagonal NiAs-type antiferromagnetic MnTe epitaxial films, *J. Raman Spectrosc.* 51 (2020) 1383–1389, <http://dx.doi.org/10.1002/jrs.5928>.
- [46] M.N. Iliev, M.V. Abrashev, A.P. Litvinchuk, V.G. Hadjiev, H. Guo, A. Gupta, Raman spectroscopy of ordered double perovskite La<sub>2</sub>CoMnO<sub>6</sub> thin films, *Phys. Rev. B* 75 (2007) 104118, <http://dx.doi.org/10.1103/PhysRevB.75.104118>.
- [47] R.X. Silva, M.C.C. Júnior, S. Yáñez-Vilar, M.S. Andújar, J. Mira, M.A. Señaris-Rodríguez, C.W.A. Paschoal, Spin-phonon coupling in multiferroic Y<sub>2</sub>CoMnO<sub>6</sub>, *J. Alloy. Compd.* 690 (2017) 909–915, <http://dx.doi.org/10.1016/j.jallcom.2016.07.010>.
- [48] B.D. Cullity, C.D. Graham, Introduction to magnetic materials, Second Edition, Wiley-IEEE Press, New Jersey, 2008, pp. 91–99, <http://dx.doi.org/10.1002/9780470386323>.
- [49] K. Yosida, Theory of magnetism, Springer-Verlag Berlin Heidelberg, 1996, pp. 72–74.
- [50] V. Barsan, V. Kuncser, Exact and approximate analytical solutions of Weiss equation of ferromagnetism and their experimental relevance, *Phil. Mag. Lett.* 97 (2017) 359–371, <http://dx.doi.org/10.1080/09500839.2017.1366081>.
- [51] K.P. Remya, D. Prabhu, R.J. Joseyphus, A.C. Bose, C. Viswanathan, N. Ponpandian, Tailoring the morphology and size of perovskite BiFeO<sub>3</sub> nanostructures for enhanced magnetic and electrical properties, *Mater. Des.* 192 (2020) 108694, <http://dx.doi.org/10.1016/j.matdes.2020.108694>.
- [52] F. Huang, X. Xu, X. Lu, M. Zhou, H. Sang, J. Zhu, The exchange bias behavior of BiFeO<sub>3</sub> nanoparticles with natural core-shell structure, *Sci. Rep.-UK* 8 (2018) 2311, <http://dx.doi.org/10.1038/s41598-018-19676-5>.
- [53] S. Vijayanand, M.B. Mahajan, H.S. Potdar, P.A. Joy, Magnetic characteristics of nanocrystalline multiferroic BiFeO<sub>3</sub> at low temperatures, *Phys. Rev. B* 80 (2009) 064423, <http://dx.doi.org/10.1103/PhysRevB.80.064423>.
- [54] N. Shamir, E. Gurewitz, H. Shaked, The magnetic structure of Bi<sub>2</sub>Fe<sub>2</sub>O<sub>9</sub> analysis of neutron diffraction measurements, *Acta Crystallogr. A* 34 (1978) 662–666, <http://dx.doi.org/10.1107/S0567739478001412>.
- [55] H. Béa, M. Bibes, A. Barthélémy, K. Bouzehouane, E. Jacquet, A. Khodan, J.-P. Contour, S. Fusil, F. Wycisk, A. Forget, D. Lebeugle, D. Colson, M. Viret, Influence of parasitic phases on the properties of BiFeO<sub>3</sub> epitaxial thin films, *Appl. Phys. Lett.* 87 (2005) 072508, <http://dx.doi.org/10.1063/1.2009808>.
- [56] M. Sakar, S. Balakumar, P. Saravanan, S. Bharathkumar, Particulates Vs. fibers: Dimension featured magnetic and visible light driven photocatalytic properties of Sc modified multiferroic bismuth ferrite nanostructures, *Nanoscale* 8 (2016) 1147–1160, <http://dx.doi.org/10.1039/C5NR06655G>.
- [57] J.F. Scott, M.K. Singh, R.S. Katiyar, Critical phenomena at the 140 and 200 K magnetic phase transitions in BiFeO<sub>3</sub>, *J. Phys. Condens. Matter* 20 (2008) 322203, <http://dx.doi.org/10.1088/0953-8984/20/32/322203>.
- [58] D. Parker, V. Dupuis, F. Ladieu, J.-P. Bouchaud, E. Dubois, R. Perzynski, E. Vincent, Spin-glass behavior in an interacting γ-Fe<sub>2</sub>O<sub>3</sub> nanoparticle system, *Phys. Rev. B* 77 (2008) 104428, <http://dx.doi.org/10.1103/PhysRevB.77.104428>.
- [59] M.K. Singh, W. Prellier, M.P. Singh, R.S. Katiyar, J.F. Scott, Spin-glass transition in single-crystal BiFeO<sub>3</sub>, *Phys. Rev. B* 77 (2008) 144403, <http://dx.doi.org/10.1103/PhysRevB.77.144403>.
- [60] T.D. Rao, S. Asthana, Evidence of improved ferroelectric phase stabilization in Nd and Sc co-substituted BiFeO<sub>3</sub>, *J. Appl. Phys.* 116 (2014) 164102–164109, <http://dx.doi.org/10.1063/1.4898805>.
- [61] S.M. Selbach, T. Tybell, M.-A. Einarsrud, T. Grande, Size-dependent properties of multiferroic BiFeO<sub>3</sub> nanoparticles, *Chem. Mater.* 19 (2007) 6478–6484, <http://dx.doi.org/10.1021/cm071827w>.
- [62] A.P. Ramirez, Strongly geometrically frustrated magnets, *Annu. Rev. Mater. Sci.* 24 (1994) 453–480, <http://dx.doi.org/10.1146/annurev.ms.24.080194.002321>.





Cite this: *J. Mater. Chem. C*, 2023, 11, 5524

## On the coexistence of ferroelectric and antiferroelectric polymorphs in $\text{NaNbO}_3$ fibers at room temperature†

Guilhermina Ferreira Teixeira,<sup>a</sup> Heitor Secco Seleghini,<sup>b</sup> Wagner Benício Bastos,<sup>c</sup> Natalia Jacomaci,<sup>d</sup> Bojan Stojadinović,<sup>e</sup> Zorana Dohčević-Mitrović,<sup>e</sup> Flavio Colmati,<sup>a</sup> Miguel Angel San-Miguel,<sup>b</sup> Elson Longo<sup>c</sup> and Maria Aparecida Zaghete<sup>cf</sup>

$\text{Na}_2\text{Nb}_2\text{O}_6 \cdot \text{H}_2\text{O}$  fibers were synthesized in a short time using a microwave-assisted hydrothermal method and later used as a precursor for obtaining  $\text{NaNbO}_3$  fibers with piezoelectric characteristics. The  $\text{NaNbO}_3$  fibers consist of a mix of antiferroelectric (*Pbcm*) and ferroelectric (*P2<sub>1</sub>ma*) orthorhombic phases. The ferroelectric structure comprises about 87% wt of the sample, and a theoretical approach indicated that an electric field could induce an inversion in the relative stability between the most stable antiferroelectric structure and the ferroelectric one. Piezoresponse force microscopy showed that an individual fiber is composed of regions with ferroelectric domains and regions with no ferroelectric characteristics.

Received 23rd September 2022,  
Accepted 22nd March 2023

DOI: 10.1039/d2tc04039e

rsc.li/materials-c

### Introduction

Contemporary society has experienced technological development that has led research to focus on materials that have and combine functional properties. Sodium niobate ( $\text{NaNbO}_3$ ) is a multifunctional perovskite-structured material with interesting properties<sup>1–6</sup> and shows a complex structural phase transition as a function of pressure, temperature, and particle size.<sup>7–9</sup>

$\text{NaNbO}_3$  shows polymorphism that is yet to be fully understood, and several studies have focused on elucidating its crystalline structures. Depending on the processing route,  $\text{NaNbO}_3$  can grow in paraelectric, antiferroelectric, or ferroelectric phases.<sup>10–13</sup> Although  $\text{NaNbO}_3$  exhibits an orthorhombic antiferroelectric phase at room temperature, some studies have reported the ferroelectric phase of the orthorhombic structure under this condition.<sup>14–16</sup>

Piezoelectricity is one of the most interesting properties of  $\text{NaNbO}_3$ , making this compound an environmentally friendly substitute for lead titanate zirconate ( $\text{PZT}$  ( $\text{Pb}(\text{Zr}_{1-x}\text{Ti}_x)\text{O}_3$ ))<sup>12</sup> ceramics in piezoelectric devices. The piezoelectric effect may be classified as direct or converse. The direct effect consists of creating an electric charge by submitting a material to mechanical stress. In turn, the converse piezoelectric effect occurs by converting electric energy into mechanical stress.<sup>17</sup>

Non-centrosymmetric crystals show spontaneous polarization that is an important condition for piezoelectricity to occur; however, nonpolar materials such as zinc oxide ( $\text{ZnO}$ ) with a hexagonal wurtzite crystal structure might also present the piezoelectric effect. This occurs because piezoelectricity is a property with tensorial character, and the piezoelectric tensor may vary according to the crystallographic group.<sup>18</sup>

Energy harvesting devices<sup>19,20</sup> operate based on the piezoelectric effect and the piezoelectric constant of nanomaterials is lower than that of bulk piezoelectric materials. Thus, synthesizing compounds whose characteristics allow increasing the charges generated under certain stress is an important step to improve the piezoelectric behavior of nanostructures. In this sense, the growth of particles with one-dimensional morphology has been a great alternative to enhance the piezoelectric response of a nanomaterial.<sup>21</sup> This occurs because the elastic coefficient of the piezoelectric particles with one-dimensional morphology decreases, thus increasing the elastic limit and piezoelectric constant along with the lower particle diameter. Thus, the material becomes very sensitive to low-frequency and irregular mechanical

<sup>a</sup> Universidade Federal de Goiás, Instituto de Química, Goiânia, GO, Brazil.  
E-mail: mina.guilher@gmail.com

<sup>b</sup> Unicamp Material Simulation Lab, Institute of Chemistry,  
State University of Campinas, Campinas, SP, Brazil

<sup>c</sup> CDMF-Universidade Federal de São Carlos, PO Box, 676, 13565-905 São Carlos,  
SP, Brazil

<sup>d</sup> Renato Archer Information Technology Center, Campinas, SP, Brazil

<sup>e</sup> Nanostructured Matter Laboratory, Institute of Physics Belgrade,  
University of Belgrade, Pregrevice 118, 11080 Belgrade, Serbia

<sup>f</sup> Universidade Estadual Paulista Júlio de Mesquita Filho, Instituto de Química,  
Araraquara, SP, Brazil

† Electronic supplementary information (ESI) available. See DOI: <https://doi.org/10.1039/d2tc04039e>

vibration.<sup>21</sup> Therefore, for energy harvesting applications, it is essential to choose the best route to prepare particles with these characteristics.

Studies that explore one-dimensional perovskite nanostructures for applications in energy harvesting devices have grown.<sup>22</sup> Many of them have addressed the one-dimensional  $\text{NaNbO}_3$  obtained from the thermal treatment of the  $\text{Na}_2\text{Nb}_2\text{O}_6 \cdot \text{H}_2\text{O}$  metastable phase synthesized using a hydrothermal method.

Hydrothermal synthesis methods have the advantage of obtaining crystalline particles with different morphologies at low temperatures and relatively short synthesis periods. However, by using microwave radiation as a heating source, the time and temperature to obtaining crystalline particles decrease considerably.<sup>23</sup> Such a variation in hydrothermal synthesis is known as the Microwave-Assisted Hydrothermal Method (MAHM). In a conventional hydrothermal method, orthorhombic  $\text{NaNbO}_3$  with the  $P2_1ma$  space group is obtained from  $\text{Na}_2\text{Nb}_2\text{O}_6 \cdot \text{H}_2\text{O}$  synthesized at 200 °C in 4 hours of synthesis, while  $\text{NaNbO}_3$  with the  $Pbma$  space group is obtained after 24 hours of hydrothermal treatment.<sup>16</sup> Furthermore, using the MAHM,  $\text{NaNbO}_3$  ( $Pbma$ ) is obtained at 180 °C in 30 minutes.<sup>24</sup>

The spontaneous polarization in the non-centrosymmetric orthorhombic  $P2_1ma$  phase of  $\text{NaNbO}_3$  is a fundamental condition for the particles to present piezoelectric and ferroelectric behaviors.<sup>14,16,25</sup> Therefore, ensuring the growth of  $\text{NaNbO}_3$  in an orthorhombic structure with the  $P2_1ma$  space group rather than antiferroelectric symmetries (e.g.,  $Pbcm$  or  $Pbma$ ) is a significant aspect to consider when aiming to synthesize  $\text{NaNbO}_3$  with a piezoelectric response. In this sense, the conventional heating of  $\text{Na}_2\text{Nb}_2\text{O}_6 \cdot \text{H}_2\text{O}$  synthesized using the hydrothermal method has been a suitable route for obtaining one-dimensional orthorhombic  $\text{NaNbO}_3$  with the  $P2_1ma$  space group.<sup>16,25</sup>

Piezoresponse force microscopy (PFM) is a powerful tool for investigating the ferroelectricity of bulk materials, as well as materials at the nanoscale level (nanostructures and thin films).<sup>26–31</sup> In the last few decades, PFM has allowed comprehensive studies on the processes of electrical polarization and wall dynamics of the ferroelectric domains,<sup>32,33</sup> switching of polarization and nucleation domains,<sup>34,35</sup> and the behavior of ferroelectric properties with different parameters in the preparation of materials.<sup>36–38</sup>

Thus, in this context, this work is a thorough study of the structure of one-dimensional  $\text{NaNbO}_3$  based on a set of experimental characterization techniques and an atomistic computational approach. In addition, the piezoresponse force microscopy tool was fundamental to measure the piezoelectric response of individual fibers, unveiling the relationship between the crystalline structure of the fibers and their piezoelectric behavior. The results indicate that the fibers can be applied as piezoelectric materials.

## Experimental procedure

### $\text{NaNbO}_3$ fiber synthesis

The  $\text{NaNbO}_3$  fibers were produced through conventional thermal treatment of  $\text{Na}_2\text{Nb}_2\text{O}_6 \cdot \text{H}_2\text{O}$  fibers synthesized using the MAHM.

The synthesis of  $\text{Na}_2\text{Nb}_2\text{O}_6 \cdot \text{H}_2\text{O}$  fibers started with NaOH (p.a. Quemis), which acts as a mineralizer agent and sodium source,  $\text{Nb}_2\text{O}_5$  (Alfa Aesar, 99%), and PVA (NEON). The reaction was carried out in a Teflon vessel model XP-1500 (CEM-Corp) in a MARS-5 (CEM-Corp.) microwave oven. The precursor suspension was prepared by adding 0.70 g of  $\text{Nb}_2\text{O}_5$  to 30 mL of a solution containing 0.36 g L<sup>-1</sup> of PVA. After 10 minutes of stirring, 10.0 g of NaOH was introduced to the suspension and kept under stirring for 30 minutes. Then, the suspension was transferred to a Teflon vessel and placed inside the microwave oven. The synthesis was carried out at 160 °C for 40 minutes. The product was washed with distilled water through centrifugation until neutralizing pH and then dried at room temperature. After drying, the  $\text{Na}_2\text{Nb}_2\text{O}_6 \cdot \text{H}_2\text{O}$  product was calcinated at 550 °C for 4 hours in a muffle furnace to produce  $\text{NaNbO}_3$  with an anisotropic morphology.

### Characterization techniques

The product obtained was characterized through X-ray powder diffraction (XRD) using a Rigaku-DMAX/2500PC diffractometer (Japan) with Cu-K $\alpha$  radiation ( $\lambda = 1.5406 \text{ \AA}$ ) in the  $2\theta$  range from 20° to 80° with 0.20° min<sup>-1</sup>. The Rietveld refinement was performed on the TOPAS Academic (v.5) software. The morphology of the as-prepared samples was observed using a high-resolution field-emission gun scanning electron microscopy FE-SEM system (JEOL, JSM-7500F). The micro-Raman spectra were collected in a backscattering geometry using a TriVista 557 triple spectrometer equipped with a nitrogen-cooled CCD detector. Micro-Raman scattering measurements were performed using a Linkam THMSG600 microscope heating stage in a temperature range between room temperature and 180 K. The 532 nm line of a solid-state Nd:YAG laser was used as an excitation source, with an incident laser power of less than 40 mW to minimize the heating effects and/or sample degradation. The topography, piezo response images, and local piezohysteresis loops in the nanoscale were obtained using a commercial AFM (MultiMode Nanoscope V, Bruker). The AFM system was modified to work as a piezoresponse force microscopy (PFM)<sup>39</sup> system using a function generator (33220A, Agilent), a power source (2410C Source Meter, Keithley), and a lock-in amplifier (SR850, Stanford). The sample was prepared by depositing the fibers on a Pt-coated substrate (bottom electrode). For deposition, the fibers were suspended in isopropyl alcohol and dropped onto the substrate. The tip was used as a mobile electrode top. During the piezo response measurements, an external AC electric signal of 1V (RMS) was applied between a conductive probe (PPP-NCHR, Nanosensors, 42 N m<sup>-1</sup>) and a bottom Pt electrode. Frequencies of 50 kHz and 5 kHz were used to obtain out-of-plane (OP-PFM) and in-plane (IP-PFM) piezo response measurements, respectively. The piezo response image scans were performed with a relative angle of 17° between the cantilever and the  $\text{NaNbO}_3$  fiber.

### Computational details

We carried out the computational RAMAN and relative stability study based on Density Functional Theory (DFT) calculations<sup>40,41</sup> using the CRYSTAL17 package version 1.0.2,<sup>42</sup> which employs Gaussian-type orbitals as basic functions. The basic sets for Na,

Nb, and O were 8-511G, 986-31(631d) G, and 8-411,<sup>43–45</sup> respectively. The exchange–correlation term was treated with the following three different functionals: PBE,<sup>46</sup> B3LYP,<sup>47,48</sup> and HSE06<sup>49–51</sup> to compare the relative stability between the polymorphs and using only the B3LYP functional for obtaining the vibrational modes. All calculations treated the van der Waals interactions using the D3 semi-empirical dispersion scheme with BJ-damping.<sup>52–54</sup> The  $k$ -points were sampled through the Monkhorst–Pack method with a  $5 \times 5 \times 5$  mesh.<sup>55</sup> Since it is necessary to use standard space groups for input in the CRYSTAL17 package, the  $P2_1ma$  space group was treated as the standard  $Pmc2_1$  space group. The vibrational modes at the  $G$ -point were obtained according to the FREQCAL routine implemented in CRYSTAL17, and the analytical RAMAN intensities were obtained using the coupled perturbed Hartree–Fock method<sup>56,57</sup> with a simulated laser irradiation frequency of 532 nm and a simulated temperature of 295 K. We performed the simulated application of an external electric field to the polymorphs using the finite-field approach (FIELD-tag)<sup>58</sup> with 60 Fourier terms for the triangular-form potential expansion. Due to the computational cost, the Monkhorst–Pack  $k$ -points mesh was reduced to  $4 \times 4 \times 4$ .

## Results and discussion

As the metastable  $\text{Na}_2\text{Nb}_2\text{O}_6 \cdot \text{H}_2\text{O}$  is normally used as a precursor of  $\text{NaNbO}_3$  anisotropic particles, we employed microwaves as a heating source to accelerate the process of obtaining  $\text{Na}_2\text{Nb}_2\text{O}_6 \cdot \text{H}_2\text{O}$ . The precursor obtained by the MAHM after a 40 minute synthesis was identified using powder XRD (Fig. S1, ESI†) as monoclinic  $\text{Na}_2\text{Nb}_2\text{O}_6 \cdot \text{H}_2\text{O}$  with space group  $C12/c1$ .<sup>59</sup> According to the diffractogram shown in Fig. 1, the conventional thermal treatment of  $\text{Na}_2\text{Nb}_2\text{O}_6 \cdot \text{H}_2\text{O}$  promotes the formation of orthorhombic  $\text{NaNbO}_3$ . The inset of the most intense peaks (I, II, and III) shows the peak overlap between the  $\text{NaNbO}_3$  obtained and theoretical patterns, indicating that the sample might be composed of two possible orthorhombic  $\text{NaNbO}_3$  phases: the ferroelectric phase with the  $P2_1ma$  space group and the antiferroelectric phase with the  $Pbcm$  space group.

To clarify the polymorphism in the sample, we performed the Rietveld refinement by combining the  $P2_1ma$  and  $Pbcm$  phases, and each phase individually (Fig. 2). The best statistical values and optimal curve fitting were achieved by including both  $P2_1ma$  and  $Pbcm$  phases in the refinement calculations, as shown in Table 1.

According to the Rietveld refinement quantitative analysis, the sample consists of 87.10 wt% of the  $P2_1ma$  ferroelectric phase and 12.90 wt% of the  $Pbcm$  antiferroelectric phase.

In the  $\text{NaNbO}_3$  perovskite structure, sodium is located at the interstitial sites in the vertex of the unit cell with twelve-coordinated sodium sites, with niobium occupying the octahedral site.

Octahedral tilting is an intrinsic characteristic of perovskite structures ( $\text{ABO}_3$ ) caused by the difference in the size of the A- and B-sites; in addition to the  $\text{NaNbO}_3$  structure, A =  $\text{Na}^+$ , and B =  $\text{Nb}^{5+}$  cations. The  $[\text{BO}_6]$  tilting of the orthorhombic

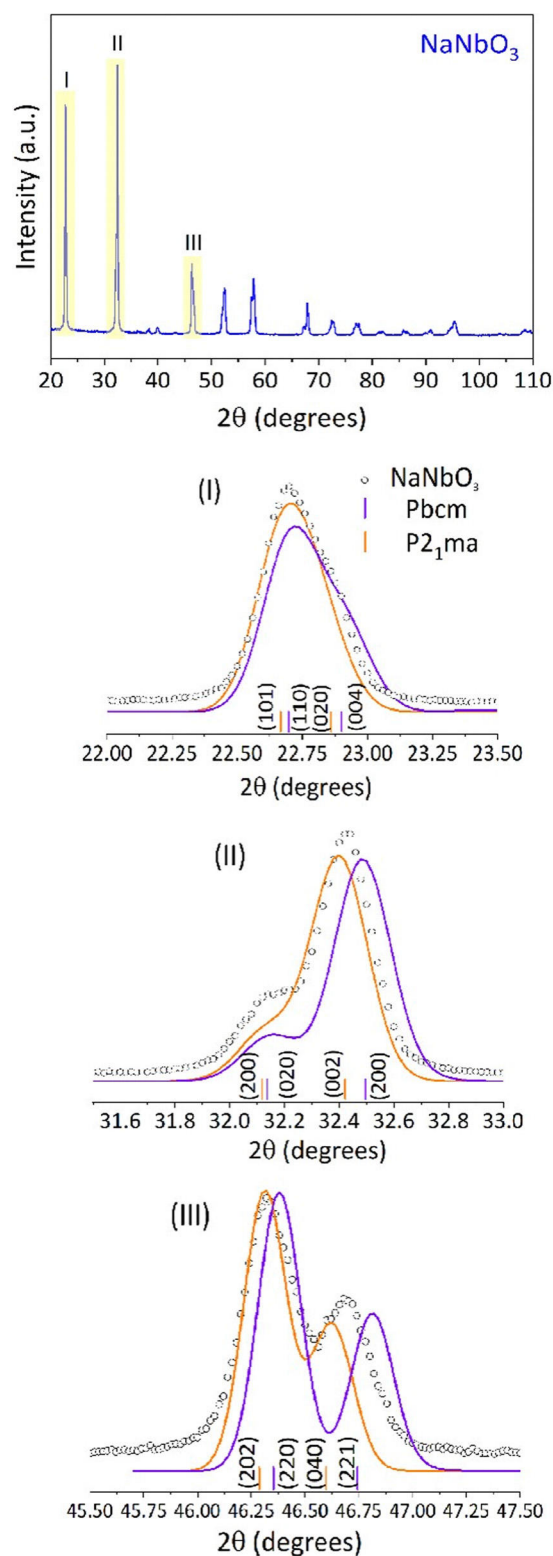


Fig. 1 X-ray diffraction of  $\text{NaNbO}_3$  obtained after thermal treatment at 550 °C of  $\text{Na}_2\text{Nb}_2\text{O}_6 \cdot \text{H}_2\text{O}$ . The insets highlight the peaks at around 22 °C (I), 32 °C (II), and 46 °C (III).

perovskite structure occurs around the  $b$  and  $c$  axes.<sup>24</sup> The phase transition in  $\text{NaNbO}_3$  has been linked to the tilting and distortion on  $[\text{NbO}_6]$  octahedra and the off-centered displacement

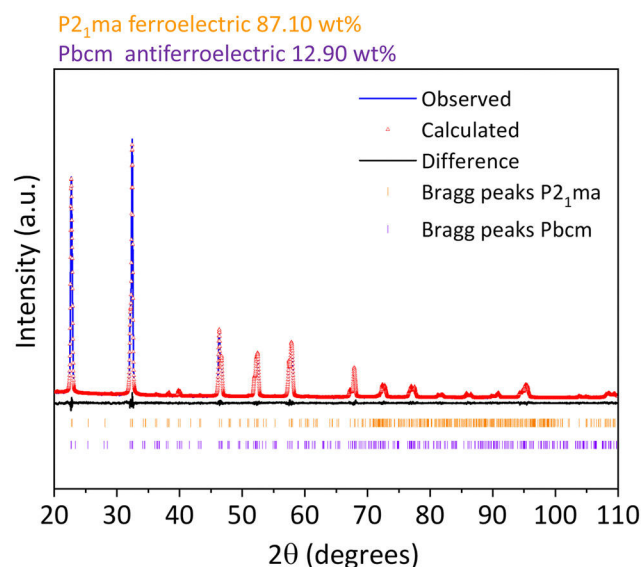
Fig. 2 Rietveld refinement of NaNbO<sub>3</sub> fibers.

Table 1 Statistical values obtained by Rietveld refinement

Refinement parameters	Ferroelectric phase ( <i>P2<sub>1</sub>ma</i> : CIF n° 39624)	Antiferroelectric phase ( <i>Pbcm</i> : CIF n° 23239)	Ferroelectric and antiferroelectric phase
$\chi^2$	1.40	1.43	1.11
$R_{wp}$	7.16	7.29	5.85
$R_{exp}$	5.11	5.11	5.24
$R_{wp\_dash}$	12.10	12.31	9.09
$R_{exp\_dash}$	8.64	8.64	8.15
$d$ -DW	0.82	0.79	1.33
$R_{Bragg}$	0.71	0.90	0.39 to <i>P2<sub>1</sub>ma</i> 0.60 to <i>Pbcm</i>

of niobium atoms.<sup>60</sup> Atom positions for most phases were refined, providing considerable variations in the positions of Na1, Nb1, O1, and O2 atoms (see Tables S1 and S2, ESI†).

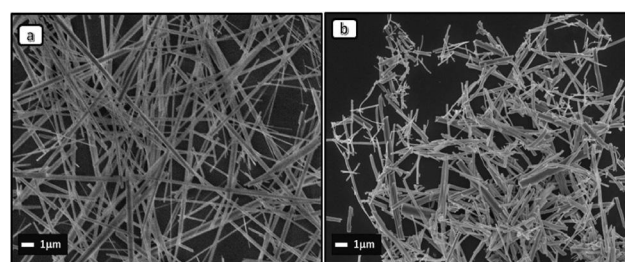
These variations are caused by the displacement of atoms resulting in more distortions in the *P2<sub>1</sub>ma* phase than in *Pbcm*.

Additionally, the Nb–O bonding distortions are more pronounced in the *P2<sub>1</sub>ma* structure,<sup>60</sup> and displacements of oxygen positions within the planes formed by Nb and O atoms increase the NbO<sub>6</sub> octahedra tilts more in the antiferroelectric phase than in the ferroelectric one.<sup>61</sup> Table 2 shows the comparative results obtained from Rietveld refinement and DFT calculations. The values obtained indicate an agreement between the theoretical and experimental parameters.

The FEG-SEM micrographs of the powders synthesized (Fig. 3) show that the product obtained by the MAHM consists of fibers (Fig. 3a), and the fiber-like shape has remained after the conventional thermal treatment at 550 °C (Fig. 3b); in addition, it is evident that conventional heating reduces the length of the fibers. Since microwave radiation quickly heats the reaction medium, we produced Na<sub>2</sub>Nb<sub>2</sub>O<sub>6</sub>·H<sub>2</sub>O fibers in a shorter synthesis time than the conventional hydrothermal method,<sup>16</sup> employing PVA to ensure the growth of

Table 2 Summary of the structural parameters from Rietveld refinement and DFT calculations

	<i>P2<sub>1</sub>ma</i>				
	Experimental		Theoretical		
	Rietveld	Literature <sup>61</sup>	PBE	B3LYP	HSE06
Wt% phase	87.10	—	—	—	—
<i>a</i> [Å]	5.5651(1)	5.569	5.610	5.557	5.539
<i>b</i> [Å]	7.7731(2)	7.790	7.829	7.755	7.739
<i>c</i> [Å]	5.5098(2)	5.518	5.540	5.471	5.466
<i>V</i> [Å <sup>3</sup> ]	238.347 (17)	239.38	243.32	235.77	234.37
$R_{Bragg}$	0.39	—	—	—	—
	<i>Pbcm</i>				
	Experimental		Theoretical		
	Rietveld	Literature <sup>62</sup>	PBE	B3LYP	HSE06
Wt% phase	12.90	—	—	—	—
<i>a</i> [Å]	5.5147(25)	5.506	5.540	5.479	5.473
<i>b</i> [Å]	5.5809(19)	5.566	5.617	5.569	5.548
<i>c</i> [Å]	15.6511(84)	15.52	15.628	15.469	15.447
<i>V</i> [Å <sup>3</sup> ]	481.703(382)	475.632	486.31	472.00	469.13
$R_{Bragg}$	0.60	—	—	—	—

Fig. 3 FE-SEM images of (a) Na<sub>2</sub>Nb<sub>2</sub>O<sub>6</sub>·H<sub>2</sub>O before thermal treatment at 550 °C for 4 hours; and (b) NaNbO<sub>3</sub> obtained after thermal treatment of Na<sub>2</sub>Nb<sub>2</sub>O<sub>6</sub>·H<sub>2</sub>O at 550 °C.

one-dimensional morphology and avoid the formation of the isotropic NaNbO<sub>3</sub>.

Herein, we can consider that two types of templates influence the growth of NaNbO<sub>3</sub>: the polymeric template that acts to obtaining Na<sub>2</sub>Nb<sub>2</sub>O<sub>6</sub>·H<sub>2</sub>O, and the as-prepared Na<sub>2</sub>Nb<sub>2</sub>O<sub>6</sub>·H<sub>2</sub>O, working as a self-sacrificing template for the NaNbO<sub>3</sub> fibers to grow through conventional heating.<sup>63</sup>

Higher temperatures have been reported to promote a phase transition between two centrosymmetric structures (*Pmma* to *Pbcm*) passing to a non-centrosymmetric *Pmc2<sub>1</sub>* structure (alternative setting *P2<sub>1</sub>ma*); in addition, the presence of each phase is also related to the particle size.<sup>8,9</sup> According to Johnston *et al.*,<sup>14</sup> the pure phase and the coexistence of the *Pbcm* and *P2<sub>1</sub>ma* polymorphs are associated with the synthesis methods and their varying parameters. A mix of *Pbcm* and *P2<sub>1</sub>ma* structures is obtained through the solid-state reaction and molten salt synthesis; however, regardless of the synthesis parameters, the *Pbcm* phase was consistently present as the major phase, suggesting it to be the more thermodynamically stable of the two polymorphs. In addition, molten salt approaches allow obtaining a pure *Pbcm* phase after a long

Table 3 Energy difference between the NaNbO<sub>3</sub> polymorphs

Functional	$E_{P2_1ma} - E_{Pbcm}$ (meV/f.u.)
PBE(D3-BJ)	5.8337
B3LYP(D3-BJ)	6.8644
HSE06(D3-BJ)	3.8225

heating period at 1000 °C.<sup>14</sup> A mix of *Pbma* and *P2<sub>1</sub>ma* structures is also obtained through hydrothermal synthesis at 200 °C for 24 hours; in addition, as in the aforementioned methods, the *Pbma* phase predominates. In this case, the *Pbma* phase is isolated by heating the as-prepared NaNbO<sub>3</sub> at 950 °C for 24 hours, while the pure *P2<sub>1</sub>ma* structure is produced through thermal treatment at 600 °C for 6 hours.<sup>60</sup>

Despite the similar thermodynamic stability of the two phases,<sup>14</sup> the *Pbcm* structure is formed more easily. DFT simulations allow estimating the energy difference between the polymorphs (Table 3), showing that the antiferroelectric *Pbcm* phase is slightly more stable than the ferroelectric *P2<sub>1</sub>ma* phase.

Unlike our work, in the cases reported above, NaNbO<sub>3</sub> was crystallized directly from the chosen synthesis method. Although the evidence showing that the *Pbcm* phase is more stable, in our work, the 4 hour thermal annealing of the metastable Na<sub>2</sub>Nb<sub>2</sub>O<sub>6</sub>·H<sub>2</sub>O at 550 °C favors the formation of the *P2<sub>1</sub>ma* structure of NaNbO<sub>3</sub> instead of *Pbcm*. Our results are consistent with several works that report the production of piezoelectric NaNbO<sub>3</sub> (*P2<sub>1</sub>ma* phase) in one-dimensional morphology by heating a metastable phase of NaNbO<sub>3</sub> under similar conditions used herein<sup>2,15,25,64–66</sup> since the heating at temperatures above 600 °C modifies the one-dimensional morphology and produces a monoclinic phase of NaNbO<sub>3</sub>.<sup>66</sup>

In our previous work,<sup>24</sup> Rietveld refinement showed that a pure antiferroelectric phase of NaNbO<sub>3</sub> was obtained from the direct crystallization into solution using the MAHM.<sup>24</sup> However, in the present study, the MAHM was employed to produce Na<sub>2</sub>Nb<sub>2</sub>O<sub>6</sub>·H<sub>2</sub>O, and the conventional treatment of the product obtained from the MAHM promotes obtaining NaNbO<sub>3</sub> with the coexistence of antiferroelectric and ferroelectric structures. Besides, through this processing, the ferroelectric phase is preferably formed than the antiferroelectric, implying that somehow such phase is stabilized during the synthesis, or it is the kinetic product in such a synthesis condition.

In addition to X-ray diffraction and Rietveld refinement, Raman spectroscopy is an excellent tool for structural investigation and unveiling the short-range order since it is sensitive to the vibrations of the atoms in the crystalline structure.

The Raman spectra of the NaNbO<sub>3</sub> structure (Fig. 4) are composed of low-energy external and high-energy internal vibrational modes. External vibrational modes are translation modes resulting from the interaction between the NbO<sub>6</sub> octahedron and Na<sup>+</sup> cation and are responsible for a split band profile due to the presence of the Na<sup>+</sup> site. The interaction between NbO<sub>6</sub>–NbO<sub>6</sub> octahedra contributes to external vibrational modes. Internal vibrational modes arise from bending between O–Nb–O bonding angles and stretching of the Nb–O bonds. The variation in the geometric center of the NbO<sub>6</sub>

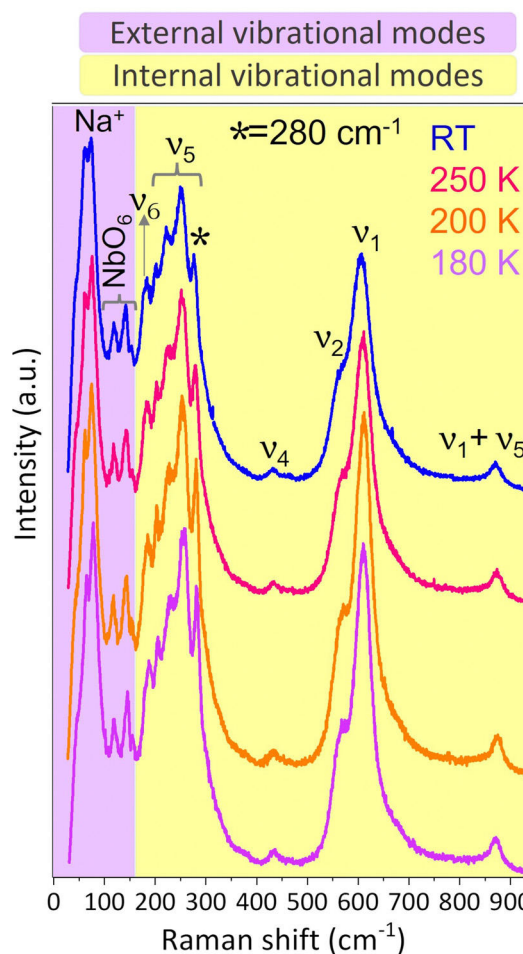


Fig. 4 Raman spectra of NaNbO<sub>3</sub> fibers (obtained after thermal treatment of Na<sub>2</sub>Nb<sub>2</sub>O<sub>6</sub>·H<sub>2</sub>O) recorded at different temperatures.

octahedron and the displacement of Na<sup>+</sup> cations cause tilt and distortion in the octahedron leading to the phase transition.<sup>67</sup>

Several reports draw on Raman spectroscopy under various temperature conditions as a tool to understand the NaNbO<sub>3</sub> phase transition. As NaNbO<sub>3</sub> has an orthorhombic symmetry between –100 °C and 575 °C,<sup>68</sup> we performed Raman spectroscopy measurements at 180 K (~ –93 °C), 200 K (~ –73 °C), 250 K (~ –23 °C) and, at room temperature (RT). According to Jauhari *et al.*, the low temperature leads to a structural disorder resulting in the appearance, disappearance, and displacement of vibrational modes.<sup>69</sup> Therefore, Raman spectra were recorded to further prove the presence of both antiferroelectric and ferroelectric phases in NaNbO<sub>3</sub> with an orthorhombic crystalline structure.

Investigating the phase transition from *Pbcm* to *P2<sub>1</sub>ma* structure, Lin *et al.* verified that the band intensities at 62 and 75 cm<sup>–1</sup> decrease with increased temperature.<sup>70</sup> In work by Shiratori *et al.*, the Raman spectrum obtained for the *Pbcm* structure presents a splitting in the band located between 61 and 74 cm<sup>–1</sup>; however, no splitting is noticed for the ferroelectric phase.<sup>9</sup> Shakhovoy *et al.* also relate the ferroelectric and antiferroelectric polymorphs of NaNbO<sub>3</sub> to the profile of the

bands at lower wavenumbers.<sup>71</sup> Herein, the bands between 44 and 78  $\text{cm}^{-1}$  are split (Fig. 4); moreover, the splitting profile changes as a function of temperature. The DFT calculations (Tables S3 and S4, ESI<sup>†</sup>) allow assigning the 65  $\text{cm}^{-1}$  vibration to a  $B_2$  mode in the  $P2_1ma$  polymorph, with a DFT calculated frequency of 58  $\text{cm}^{-1}$  and schematics shown in Fig. 5b, and the 78  $\text{cm}^{-1}$  vibration to an  $A_g$  mode from the  $Pbcm$  one, with a DFT calculated frequency of 73  $\text{cm}^{-1}$  (shown in Fig. 5a).

According to Ji *et al.*,<sup>2</sup> the ferroelectric and antiferroelectric structures are differentiated by the splitting in the bands located in the region from 150 to 300  $\text{cm}^{-1}$ ; furthermore, the intensity of the peak at 274  $\text{cm}^{-1}$  is lower for the ferroelectric structure.<sup>16</sup> This intense peak has a contribution of an  $A_1$  mode from the  $P2_1ma$  polymorph with a DFT calculated frequency of 277  $\text{cm}^{-1}$ . In addition, the peak at 280  $\text{cm}^{-1}$  appears to have a significant contribution from the  $A_g$  mode with a DFT calculated frequency of 291  $\text{cm}^{-1}$ , and such a peak decreases in intensity as the temperature increases.

To better compare the bands, the intensities of the spectra obtained at room temperature and 180 K were normalized

(Fig. 6). By examining the normalized spectra, we notice that the temperature rise promotes the increase in the intensity of the peak at 65  $\text{cm}^{-1}$  and decreases the intensity of the bands related to the Nb–O vibrations (225, 255, and 280  $\text{cm}^{-1}$ ) and the  $\text{NbO}_6$  octahedra (560 and 609  $\text{cm}^{-1}$ ) vibrations. The spectra shown in Fig. 6 and the relative intensities obtained from the DFT calculations (Tables S3 and S4, ESI<sup>†</sup>) show the  $P2_1ma$  polymorph with the most intense peak around 65  $\text{cm}^{-1}$  without the  $Pbcm$  polymorph presenting intense peaks in the same region. Thus, the  $P2_1ma$  polymorph is responsible for decreasing the intensity of the bands resulting from the internal vibrational modes with the lower temperature, which, in turn, increases the structural disorder of the material and reduces the unit cell polarity.<sup>72,73</sup>

In the spectra collected at 180, 200, and 250 K (Fig. 4), the band pattern located between 55 and 80  $\text{cm}^{-1}$  is the same as those obtained by Shakhovoy *et al.*<sup>71</sup> when analyzing regions with the coexistence of the ferroelectric and antiferroelectric phases. Therefore, based on the intensity of the bands and their respective splitting, we assume that the higher temperature

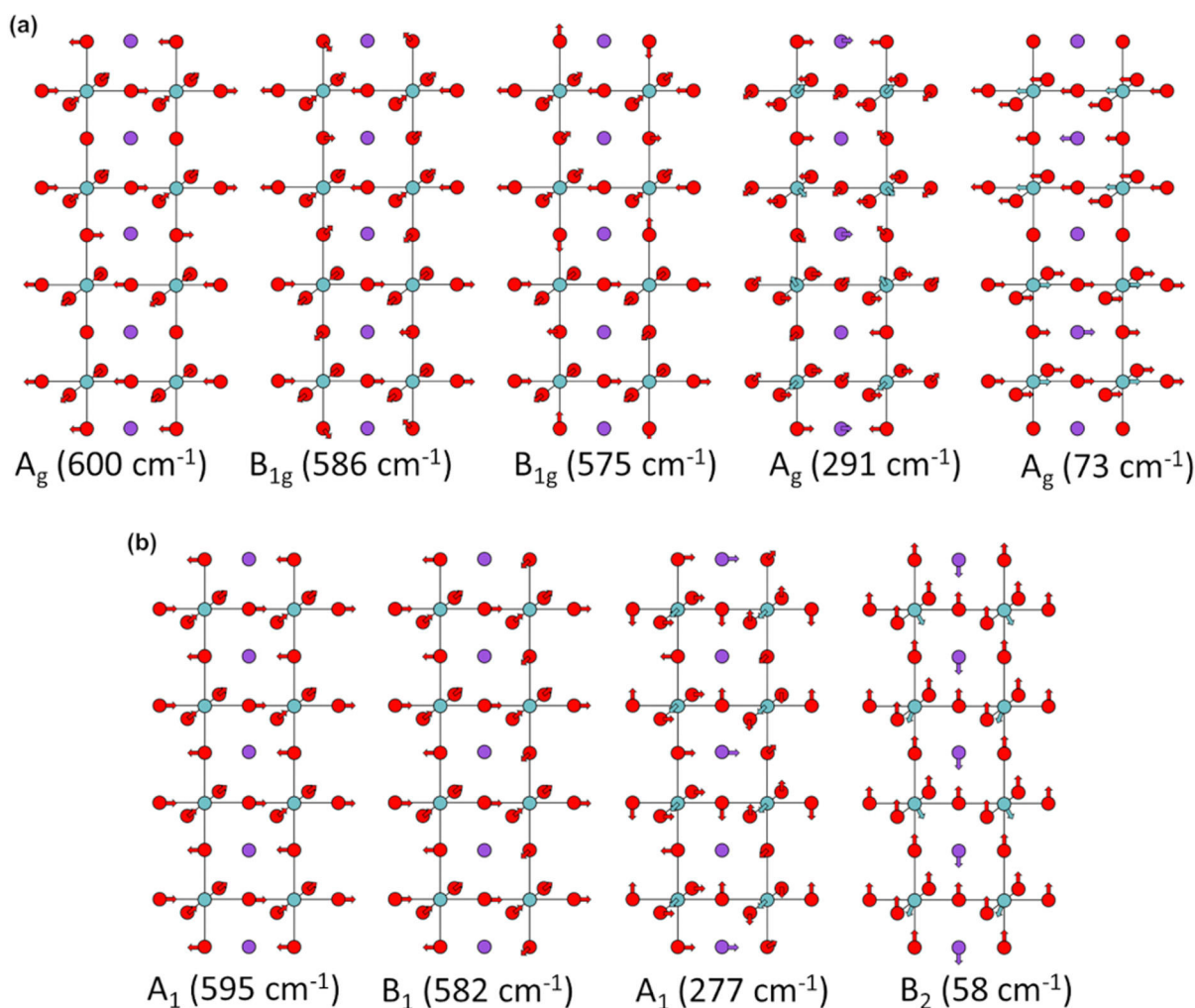


Fig. 5 Schematics of some Raman modes obtained using DFT of the (a)  $Pbcm$  and (b)  $P2_1ma$  space groups. Color scheme: oxygen (red), niobium (green), and sodium (purple). To ease the visualization, all the octahedral distortions were removed.

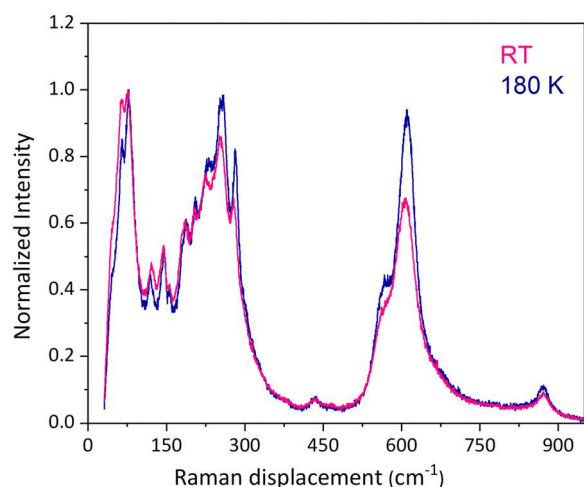


Fig. 6 Raman normalized spectra for NaNbO<sub>3</sub> fibers recorded at RT and 180 K.

favors the presence of a ferroelectric structure, although the ferroelectric and antiferroelectric phases coexist at all temperatures throughout the analysis.

The electric field has been reported to induce the transformation of the antiferroelectric phase into the ferroelectric phase. This phase modification occurs because the atomic displacements caused by the electric field distort the oxygen octahedrally and modify the NaNbO<sub>3</sub> structure.<sup>61</sup>

Based on such a behavior presented by NaNbO<sub>3</sub>, we verified the possibility of a phase transition occurring. DFT simulations allow us to observe the effect of applying an electric field on the relative energy between the NaNbO<sub>3</sub> polymorphs. The Electronic Supplementary Information (ESI†) contains the complete procedure for the rotations of the standard *Pmc*2<sub>1</sub> unit cell, the growth manner to make the atomic sites match the positions between the polymorphs, and the relationship between the applied internal electric field and the correlated macroscopic field. These calculations (Fig. S2–S4, ESI†) showed that only the electric fields in the *x* and *y* directions can invert the relative energy between the polymorphs. In addition, the electric field magnitudes needed for such inversion are approximately 6.2 MV cm<sup>-1</sup> and 14.6 MV cm<sup>-1</sup>, respectively. Thus, a few orders of magnitude are more prominent than those found experimentally for a single-crystal and powder samples.<sup>61,74,75</sup> Therefore, they should be observed more qualitatively than quantitatively since the literature reports a divergence between the absolute experimental and theoretical values of electric fields.<sup>76</sup>

We employed the piezo response microscopy technique to investigate the nanoscale ferroelectric characteristics and the polarization vector of the ferroelectric domain structure of NaNbO<sub>3</sub> fibers. The out-of-plane (OP-PFM) and in-plane (IP-PFM) piezo response images correspond to the perpendicular (vertical) and parallel (horizontal) contributions to the fiber surface of the ferroelectric polarization vector, respectively. Fig. 8 shows the surface topography and piezo response images with a scan size of 1 μm × 1 μm. The NaNbO<sub>3</sub> fiber has a width of 422 nm and a

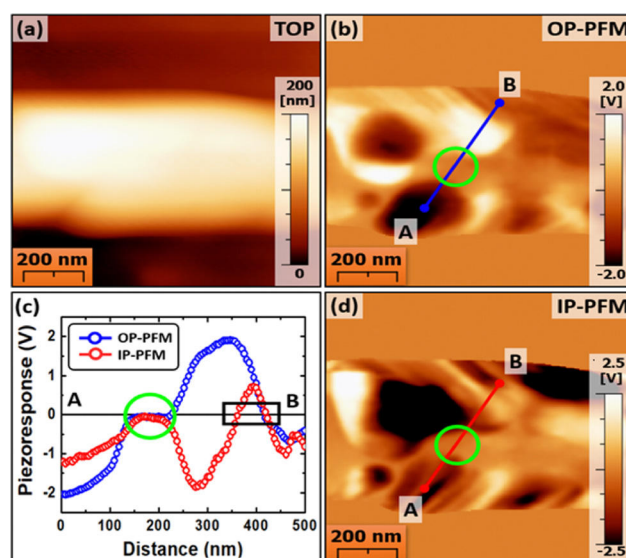


Fig. 7 NaNbO<sub>3</sub> fiber (a) topography, (c) piezo response signal cross-section from blue and red lines in (b) out-of-plane, and (d) in-plane piezo response images with frequencies of 50 kHz and 5 kHz, respectively.

height of 167 nm (Fig. 7a). The out-of-plane (OP-PFM at a frequency of 50 kHz, Fig. 7b) and in-plane (IP-PFM at a frequency of 5 kHz, Fig. 7d) piezo response images correspond to the same ferroelectric domain structure in the fiber surface and reveal high contrasted PFM images. The clear and dark regions of the color scale contrast represent the opposite polarization orientations in the ferroelectric domain structure. The solid lines (A and B, blue and red lines) from the cross-section as shown in Fig. 7c show the piezo response intensity. However, the results indicate that there are regions with a null piezo response signal, thus indicating regions with no ferroelectric characteristics, as highlighted by the green solid line circle.

Fig. 8 shows the following regions measured by PFM in different colors: regions of opposite orientations of the ferroelectric domains (red and blue), regions without piezo response signals (green), and regions corresponding to the substrate (black). The regions without piezo response signals were computed as 17.7% for OP-PFM and 15.8% for IP-PFM. The

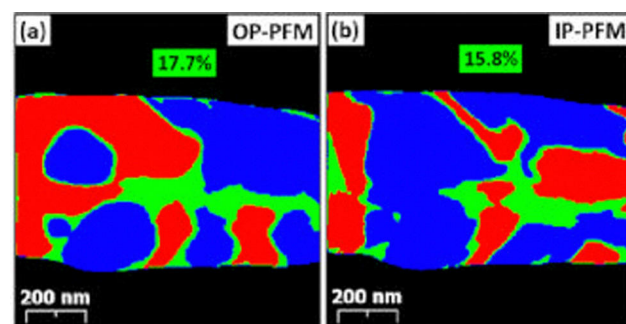


Fig. 8 Ferroelectric domain structure of the NaNbO<sub>3</sub> fiber: (a) and (b) piezo response images in distinct colors (red and blue - opposite polarization orientations, green - non-response, and black - substrate).

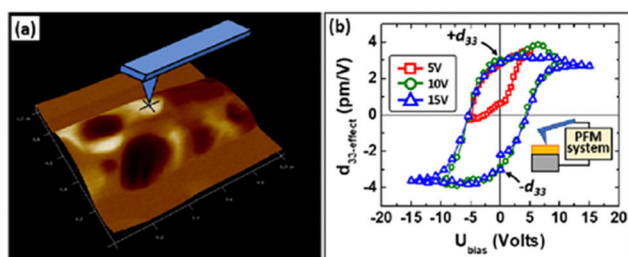


Fig. 9 Local ferroelectric switching: (a) tip position on the  $\text{NaNbO}_3$  fiber and (b) piezo-hysteresis curves with different bias ranges.

different values occur due to the orientation of the polarization vector on the fiber surface and its contributions to the vertical and horizontal orientations.

These percentual values are higher than the value obtained from Rietveld refinement for the antiferroelectric phase (12.9 wt%). PFM generates these higher values because the domain wall regions in PFM measurements with an inverted orientation of ferroelectric domains (see the solid black rectangle in Fig. 8c) were also computed as regions of null values of piezo response signal.<sup>77,78</sup>

To investigate the switching behavior of nanoscale ferroelectric domains, we performed successive measurements of the local piezo loops using electrical voltages of 5 V, 10 V, and 15 V in a region with a high magnitude of piezo response signal. Fig. 9(a) shows the position on top of the  $\text{NaNbO}_3$  fiber where the cycles were performed. Fig. 9(b) shows that the cycle of 5 V bias did not generate an electric field superior to the coercive electric field ( $E_c$ ) of the material capable of switching the ferroelectric domain locally just below the tip. However, the other cycles with a larger bias were able to reorientate the ferroelectric polarization. The peak-to-peak amplitude of the effective  $d_{33}$  coefficient obtained ( $\Delta d_{33} = |d_{33}| + |-d_{33}|$ ) was approximately  $5.89 \text{ pm V}^{-1}$ .

In a previous work, we reported the piezoelectric and ferroelectric effect presented by flexible composites constituted by  $\text{NaNbO}_3$  particles with different morphologies and  $\alpha$ -polyvinylidene difluoride ( $\alpha$ -PVDF).<sup>79</sup> Since  $\alpha$ -PVDF is a non-polar phase of PVDF,<sup>80</sup> we concluded that the piezoelectric and ferroelectric behaviors of the composites originate from  $\text{NaNbO}_3$  particles. Herein, we deepen the study of the structure of  $\text{NaNbO}_3$  fiber-like particles supported by PFM characterization to explain the piezoelectric behavior of  $\text{NaNbO}_3$  fibers.

## Conclusions

In summary,  $\text{Na}_2\text{Nb}_2\text{O}_6 \cdot \text{H}_2\text{O}$  fiber-like particles were obtained at  $160^\circ\text{C}$  over a 40-minute synthesis through a microwave-assisted hydrothermal method in a PVA medium. The  $\text{Na}_2\text{Nb}_2\text{O}_6 \cdot \text{H}_2\text{O}$  fibers were applied as a precursor to obtain anisotropic  $\text{NaNbO}_3$  fiber-like particles. The results of powder XRD, Rietveld refinement, and Raman spectroscopy showed that the antiferroelectric ( $Pbcm$ ) and ferroelectric phases ( $P2_1ma$ ) coexist in the structure of the  $\text{NaNbO}_3$  fibers. The theoretical study demonstrated that the relative stability between

the antiferroelectric and ferroelectric phases could be inverted under the influence of an electric field. Such an inversion depends on the orientation of the field PFM, whose measurements showed that an isolated fiber is composed of ferroelectric and non-ferroelectric phases. This finding, in turn, corroborates the results of the structural analysis.

Furthermore, the analysis of the theoretical results indicates that the non-ferroelectric phase may be an antiferroelectric phase. Since the piezoelectric efficiency of  $\text{NaNbO}_3$ -based devices is linked to the structure of the ceramic structure, the characteristics of the particles reported herein reinforce the potential of  $\text{NaNbO}_3$  for application in technologies based on the piezoelectric effect.

## Author contributions

G. F. Teixeira: conceptualization, methodology, validation, formal analysis, investigation, writing – original draft. H. S. Seleghini: validation, methodology, investigation, formal analysis, writing – original draft. W. B. Bastos: validation, methodology, investigation, formal analysis, writing – original draft. N. Jacomaci: methodology, formal analysis, investigation, writing – original draft. B. Stojadinović: resources, investigation. Z. Dohčević-Mitrović: resources, investigation, supervision. F. Colmati: supervision, conceptualization, writing – original draft. M. A. San-Miguel: resources, supervision, writing – original draft. E. Longo: supervision, resources, funding acquisition. M. A. Zaghete: supervision, resources, funding acquisition, project administration. All authors have read and agreed to the submitted/published version of the manuscript.

## Conflicts of interest

There are no conflicts to declare.

## Acknowledgements

The authors would like to thank the Brazilian research agencies CAPES (Processes number: 88881.068060/2014-01 and 88882.306480/2018-1), FAPESP-(CEPID/CDMF 2013/07296-2, 2016/23891-6, 2017/26105-4, and 2017/10819-8) for the financial support to this research. HSS would like to thank the Brazilian National Council for Scientific and Technological Development (CNPq) for the scholarship 130518/2019-0. Z. D. M. and B. S. would like to thank the Institute of Physics Belgrade for the funding granted by the Ministry of Education, Science, and Technological Development of the Republic of Serbia. This research used the computing resources and assistance of the John David Rogers Computing Center (CCJDR) in the Institute of Physics Gleb Wataghin, University of Campinas.

## Notes and references

- H. You, X. Ma, Z. Wu, L. Fei, X. Chen, J. Yang, Y. Liu, Y. Jia, H. Li, F. Wang and H. Huang, *Nano Energy*, 2018, **52**, 351–359.






- 2 S. Ji, H. Liu, Y. Sang, W. Liu, G. Yu and Y. Leng, *CrystEngComm*, 2014, **16**, 7598–7604.
- 3 S. I. Raevskaya, M. A. Malitskaya, C. C. Chou, A. G. Lutokhin, I. P. Raevski and V. V. Titov, *Phys. Status Solidi A*, 2019, **216**, 1–5.
- 4 D. Fernandes, C. W. Raubach, P. L. G. Jardim, M. L. Moreira and S. S. Cava, *Ceram. Int.*, 2020, **47**, 10185–10188.
- 5 G. F. Teixeira, T. R. Wright, D. C. Manfroi, E. Longo, J. A. Varela and M. A. Zaghete, *Mater. Lett.*, 2015, **139**, 443–446.
- 6 M. H. Prado da Silva, D. N. da Rocha, L. de Andrade Gobbo, L. M. dos Santos Azevedo, L. H. L. Louro, A. Machado Costa and J. Brant de Campos, *J. Biomed. Mater. Res., Part B*, 2016, **104**, 979–985.
- 7 Z. X. Shen, X. B. Wang, S. H. Tang, M. H. Kuok and R. Malekfar, *J. Raman Spectrosc.*, 2000, **31**, 439–443.
- 8 Y. Shiratori, A. Magrez, W. Fischer, C. Pithan and R. Waser, *J. Phys. Chem. C*, 2007, **111**, 18493–18502.
- 9 Y. Shiratori, A. Magrez, J. Dornseiffer, F. H. Haegel, C. Pithan and R. Waser, *J. Phys. Chem. B*, 2005, **109**, 20122–20130.
- 10 M. Tyunina, A. Dejneka, D. Rytz, I. Gregora, F. Borodavka, M. Vondracek and J. Honolka, *J. Phys.: Condens. Matter*, 2014, **26**, 125901.
- 11 X. B. Wang, Z. X. Shen, Z. P. Hu, L. Qin, S. H. Tang and M. H. Kuok, *J. Mol. Struct.*, 1996, **385**, 1–6.
- 12 N. Chaiyo, R. Muanghlua, S. Niemcharoen, B. Boonchom and N. Vittayakorn, *J. Alloys Compd.*, 2011, **509**, 2445–2449.
- 13 H. D. Megaw, *Ferroelectrics*, 1974, **7**, 87–89.
- 14 K. E. Johnston, C. C. Tang, J. E. Parker, K. S. Knight, P. Lightfoot and S. E. Ashbrook, *J. Am. Ceram. Soc.*, 2010, **132**, 8732–8746.
- 15 D. Zhang, F. Shi, J. Cheng, X. Yang, E. Yan and M. Cao, *Ceram. Int.*, 2014, **40**, 14279–14285.
- 16 S. Ji, H. Liu, Y. Sang, W. Liu, G. Yu and Y. Leng, *CrystEngComm*, 2014, **16**, 7598–7604.
- 17 A. Toprak and O. Tigli, *Appl. Phys. Rev.*, 2014, **1**, 031104.
- 18 S. Sharma, R. Kiran, P. Azad and R. Vaish, *Energy Convers Manage*, 2022, **254**, 115272.
- 19 Z. Yang, S. Zhou, J. Zu and D. Inman, *Joule*, 2018, **2**, 642–697.
- 20 M. Safaei, H. A. Sodano and S. R. Anton, *Smart Mater. Struct.*, 2019, **28**, 113001.
- 21 R. Zhu and Z. Whang, Piezoelectric one- to two-dimensional nanomaterials for vibration energy harvesting devices, in *Emerging 2D Materials and Devices for the Internet of Things: Information, Sending and Energy Applications*, ed. E. Tao, D. Akinwande, Elsevier, Amsterdam, 2020. pp. 221–240.
- 22 L.-Q. Cheng and J. F. Li, *J. Materiomics*, 2016, **2**, 25–36.
- 23 G. Yang and S. J. Park, *Materials*, 2019, **12**, 1177.
- 24 G. F. Teixeira, E. Silva Junior, A. Z. Simões, E. Longo and M. A. Zaghete, *CrystEngComm*, 2017, **19**, 4378–4392.
- 25 J. H. Jung, M. Lee, J. il Hong, Y. Ding, C. Y. Chen, L. J. Chou and Z. L. Wang, *ACS Nano*, 2011, **5**, 10041–10046.
- 26 S. Wu, J. Zhang, X. Liu, S. Lv, R. Gao, W. Cai, F. Wang and C. Fu, *Nanomaterials*, 2019, **9**, 190.
- 27 C. Harnagea, M. Azodi, R. Nechache, C.-V. Cojocaru, V. Buscaglia, M. T. Buscaglia, P. Nanni, F. Rosei and A. Pignolet, *Phase Transitions*, 2013, **86**, 635–650.
- 28 C. Harnagea, A. Pignolet, M. Alexe, D. Hesse and U. Gösele, *Appl. Phys. A: Mater. Sci. Process.*, 2000, **70**, 261–267.
- 29 D. S. L. Pontes, W. B. Bastos, A. J. Chiquito, E. Longo and F. M. Pontes, *J. Alloys Compd.*, 2017, **702**, 327–337.
- 30 I. K. Bdikin, J. A. Pérez, I. Coondoo, A. M. R. Senos, P. Q. Mantas and A. L. Kholkin, *J. Appl. Phys.*, 2011, **110**, 52003.
- 31 V. V. Shvartsman, A. L. Kholkin, C. Verdier and D. C. Lupascu, *J. Appl. Phys.*, 2005, **98**, 94109.
- 32 I. K. Bdikin, A. L. Kholkin, A. N. Morozovska, S. V. Svechnikov, S.-H. Kim and S. V. Kalinin, *Appl. Phys. Lett.*, 2008, **92**, 182909.
- 33 W. B. Bastos, E. Longo, A. J. Chiquito, D. S. L. Pontes and F. M. Pontes, *Mater. Chem. Phys.*, 2018, **214**, 180–184.
- 34 L. J. McGilly, L. Feigl and N. Setter, *Thin Solid Films*, 2017, **636**, 214–219.
- 35 N. A. Pertsev, A. Petraru, H. Kohlstedt, R. Waser, I. K. Bdikin, D. Kiselev and A. L. Kholkin, *Nanotechnology*, 2008, **19**, 375703.
- 36 F. M. Pontes, A. J. Chiquito, W. B. Bastos, M. A. Pereira-da-Silva and E. Longo, *J. Mater. Chem. C*, 2016, **4**, 9331–9342.
- 37 R. A. Capeli, F. M. Pontes, A. J. Chiquito, W. B. Bastos, M. A. Pereira-da-Silva and E. Longo, *Ceram. Int.*, 2017, **43**, 5047–5052.
- 38 R. A. Capeli, F. M. Pontes, D. S. L. Pontes, A. J. Chiquito, W. B. Bastos, M. A. Pereira-da-Silva and E. Longo, *Mater. Lett.*, 2017, **196**, 64–68.
- 39 G. M. M. M. Lustosa, G. F. Teixeira, W. B. Bastos, S. M. Zanetti, L. A. Perazolli and M. A. Zaghete, Nanosized ferroelectrics: Preparation, properties, and applications, in *Magnetic, Ferroelectric, and Multiferroic Metal Oxides*, ed. Stojanovic B. D., Elsevier, Amsterdam, 2018. pp. 139–52.
- 40 P. Hohenberg and W. Kohn, *Phys. Rev.*, 1964, **136**, B864.
- 41 W. Kohn and L. J. Sham, *Phys. Rev.*, 1965, **140**, A1133.
- 42 R. Dovesi, A. Erba, R. Orlando, C. M. Zicovich-Wilson, B. Civalleri, L. Maschio, M. Rérat, S. Casassa, J. Baima, S. Salustro and B. Kirtman, *Wiley Interdiscip. Rev.: Comput. Mol. Sci.*, 2018, **8**, e1360.
- 43 R. Dovesi, C. Roetti, C. Freyria-Fava, M. Prencipe and V. R. Saunders, *Chem. Phys.*, 1991, **156**, 11–19.
- 44 B. Civalleri, A. M. Ferrari, M. Llunell, R. Orlando, M. Mérawa and P. Ugliengo, *Chem. Mater.*, 2003, **15**, 3996–4004.
- 45 J. Scaranto and S. Giorgianni, *J. Mol. Struct. THEOCHEM*, 2008, **858**, 72–76.
- 46 J. P. Perdew and Y. Wang, *Phys. Rev. B: Condens. Matter Mater. Phys.*, 1992, **45**, 13244–13249.
- 47 A. D. Becke, *J. Chem. Phys.*, 1993, **98**, 5648–5652.
- 48 C. Lee, W. Yang and R. G. Parr, *Phys. Rev. B: Condens. Matter Mater. Phys.*, 1988, **37**, 785–789.
- 49 J. Heyd, G. E. Scuseria and M. Ernzerhof, *J. Chem. Phys.*, 2003, **118**, 8207–8215.
- 50 A. v Krukau, O. A. Vydrov, A. F. Izmaylov and G. E. Scuseria, *J. Chem. Phys.*, 2006, **125**, 224106.
- 51 J. Heyd, G. E. Scuseria and M. Ernzerhof, *J. Chem. Phys.*, 2006, **124**, 219906.

- 52 S. Grimme, J. Antony, S. Ehrlich and H. Krieg, *J. Chem. Phys.*, 2010, **132**, 154104.
- 53 S. Grimme, S. Ehrlich and L. Goerigk, *J. Comput. Chem.*, 2011, **32**, 1456–1465.
- 54 S. Grimme, *J. Comput. Chem.*, 2006, **27**, 1787–1799.
- 55 H. J. Monkhorst and J. D. Pack, *Phys. Rev. B: Condens. Matter Mater. Phys.*, 1976, **13**, 5188.
- 56 L. Maschio, B. Kirtman, M. Rérat, R. Orlando and R. Dovesi, *J. Chem. Phys.*, 2013, **139**, 164101.
- 57 L. Maschio, B. Kirtman, M. Rérat, R. Orlando and R. Dovesi, *J. Chem. Phys.*, 2013, **139**, 164102.
- 58 C. Darrigan, M. Rérat, G. Mallia and R. Dovesi, *J. Comput. Chem.*, 2003, **24**, 1305–1312.
- 59 T. M. Nenoff, N. W. Ockwig, R. T. Cyan, T. M. Alam, K. Leung, J. D. Pless, H. Xu, M. A. Hartl and L. L. Daemen, *J. Phys. Chem. C*, 2007, **111**, 13212–13221.
- 60 G. Gouget, M. Duttine, E. Durand, A. Villesuzanne, V. Rodriguez, F. Adamietz, T. le Mercier, M.-D. Braidia and A. Demourgues, *ACS Appl. Electron. Mater.*, 2019, **1**, 513–522.
- 61 V. A. Shuvaeva, M. Yu Antipin, R. S. V. Lindeman, O. E. Fesenko, V. G. Smotrakov and Yu. T. Struchkov, *Ferroelectrics*, 1993, **141**, 307–311.
- 62 A. C. Sakowski-Cowley, K. Łukaszewicz and H. D. Megaw, *Acta Crystallogr., Sect. A: Cryst. Phys., Diffr., Theor. Gen. Crystallogr.*, 1969, **25**, 851–865.
- 63 L. Liu, B. Li, D. Yu, Y. Cui, X. Zhou and W. Ding, *Chem. Commun.*, 2010, **46**, 427–429.
- 64 J. H. Jung, C.-H. Chen, W.-W. Wu, J.-I. Hong, B. K. Yun, Y. Zhou, N. Lee, W. Jo, L.-H. Chen, L.-J. Chou and Z. L. Wang, *J. Mater. Chem. C*, 2012, **116**, 22261–22265.
- 65 A. Sharma, U. Bhardwaj, D. Jain and H. S. Kushwaha, *ACS Omega*, 2022, **7**, 7595–7605.
- 66 Q. Gu, K. Zhu, J. Liu, P. Liu, Y. Cao and J. Qiu, *RSC Adv.*, 2014, **4**, 15104–15110.
- 67 S. J. Lin, D. P. Chiang, Y. F. Chen, C. H. Peng, H. T. Liu, J. K. Mei, W. S. Tse, T.-R. Tsai and H.-P. Chiang, *J. Raman Spectrosc.*, 2006, **37**, 1442–1446.
- 68 K. K. Mishra, V. Sivasubramanian and A. K. Arora, *J. Raman Spectrosc.*, 2011, **42**, 517–521.
- 69 M. Jauhari, S. K. Mishra, R. Mittal and S. L. Chaplot, *J. Raman Spectrosc.*, 2019, **50**, 1177–1185.
- 70 S. J. Lin, D. P. Chiang, Y. F. Chen, C. H. Peng, H. T. Liu, J. K. Mei, W. S. Tse, T.-R. Tsai and H.-P. Chiang, *J. Raman Spectrosc.*, 2006, **37**, 1442–1446.
- 71 R. A. Shakhovoy, S. I. Raevskaya, L. A. Shakhovaya, D. V. Suzdalev, I. P. Raevski, Y. I. Yuzyuk, A. F. Semenchov and M. el Marssi, *J. Raman Spectrosc.*, 2012, **43**, 1141–1145.
- 72 H. Qi, A. Xie, J. Fu and R. Zuo, *Acta Mater.*, 2021, **208**, 116710.
- 73 N. Sun, Y. Li, Q. Zhang and X. Hao, *J. Mater. Chem. C*, 2018, **6**, 10693–10703.
- 74 A. V. Ulizheev, A. v Leiderman, V. G. Smotrakov, V. Y. Topolov and O. E. Fesenko, *Phys. Solid State*, 1997, **39**, 972–974.
- 75 M. H. Zhang, L. Fulanović, S. Egert, H. Ding, P. B. Groszewicz, H. J. Kleebe, L. Molina-Luna and J. Koruza, *Acta Mater.*, 2020, **200**, 127–135.
- 76 M. Harb, P. Labéguerie, I. Baraille and M. Rérat, *Phys. Rev. B: Condens. Matter Mater. Phys.*, 2009, **80**, 235131.
- 77 C.-L. Jia, S.-B. Mi, K. Urban, I. Vrejoiu, M. Alexe and D. Hesse, *Nat. Mater.*, 2008, **7**, 57–61.
- 78 L. Tian, A. Vasudevarao, A. N. Morozovska, E. A. Eliseev, S. V. Kalinin and V. Gopalan, *J. Appl. Phys.*, 2008, **104**, 74110.
- 79 G. F. Teixeira, R. A. Ciola, W. K. Sakamoto and M. A. Zaghete, Perovskite-Based Mesostructures and Related Composites—Influence Exerted by Morphology and Interface, in *Ferroelectric Materials-Synthesis and Characterization*, ed. Barranco A. P., IntechOpen, London, 2015, pp. 59–83.
- 80 Z. Cui, N. T. Hassankiadeh, Y. Zhuang, E. Drioli and Y. M. Lee, *Prog. Polym. Sci.*, 2015, **51**, 94–126.

## Article

# Liposomal Bilayer as a Carrier of *Rosa canina* L. Seed Oil: Physicochemical Characterization, Stability, and Biological Potential

Aleksandra A. Jovanović<sup>1,\*</sup>, Danica Čujić<sup>1</sup>, Bojan Stojadinović<sup>2</sup> , Natalija Čutović<sup>3</sup> , Jelena Živković<sup>3</sup>   
and Katarina Šavikin<sup>3</sup>

<sup>1</sup> Institute for the Application of Nuclear Energy INEP, Banatska 31b, Zemun, 11080 Belgrade, Serbia

<sup>2</sup> Institute of Physics, Pregrevica 118, Zemun, 11080 Belgrade, Serbia

<sup>3</sup> Institute for Medicinal Plants Research “Dr Josif Pančić”, Tadeuša Koščuška 1, 11000 Belgrade, Serbia

\* Correspondence: [ajovanovic@inep.co.rs](mailto:ajovanovic@inep.co.rs)

**Abstract:** *Rosa canina* L. seeds are rich in bioactive components that can add value to the various formulations. The focus of the study was the development of liposomes for *R. canina* oil to protect its sensitive compounds and prolong their shelf-life. Oil-loaded liposomes were characterized via the determination of the particle size, polydispersity index (PDI), zeta potential, conductivity, mobility, density, surface tension, viscosity, and stability. Raman and FT-IR spectroscopy were employed to investigate the chemical composition of the non-treated and UV-treated samples, and the presence of different interactions. Antioxidant and antimicrobial activities were examined as well. The liposome size was  $970.4 \pm 37.4$  nm, the PDI  $0.438 \pm 0.038$ , the zeta potential  $-32.9 \pm 0.8$  mV, the conductivity  $0.068 \pm 0.002$  mS/cm, the mobility  $-2.58 \pm 0.06$   $\mu\text{mcm/Vs}$ , the density  $0.974 \pm 0.004$  g/cm<sup>3</sup>, the surface tension  $17.2 \pm 1.4$  mN/m, and the viscosity  $13.5 \pm 0.2$  mPa•s. The Raman and FT-IR spectra showed the presence of lipids, fatty acids, polyphenols, and carotenoids. It was approved that the oil compounds were distributed inside the phospholipid bilayer and were combined with the membrane interface of the bilayer. The UV irradiation did not cause any chemical changes. However, neither the pure oil nor the oil-loaded liposomes showed any antimicrobial potential, while the antioxidant capacity of the oil-loaded liposomes was significantly low. The sizes of the liposomes did not change significantly during 60 days of storage. Due to the proven stability of the oil-loaded liposomes, as well as the liposome’s ability to protect the sensitive oil compounds, their potential application in the pharmaceutical and cosmetic formulations could be investigated with a focus on the skin regeneration effects.

**Keywords:** liposomes; size; Raman spectroscopy; *Rosa canina* seed oil; stability



**Citation:** Jovanović, A.A.; Čujić, D.; Stojadinović, B.; Čutović, N.; Živković, J.; Šavikin, K. Liposomal Bilayer as a Carrier of *Rosa canina* L. Seed Oil: Physicochemical Characterization, Stability, and Biological Potential. *Molecules* **2023**, *28*, 276. <https://doi.org/10.3390/molecules28010276>

Academic Editors: Antoaneta Trendafilova and Miroslav Novaković

Received: 15 November 2022

Revised: 22 December 2022

Accepted: 24 December 2022

Published: 29 December 2022



**Copyright:** © 2022 by the authors. Licensee MDPI, Basel, Switzerland. This article is an open access article distributed under the terms and conditions of the Creative Commons Attribution (CC BY) license (<https://creativecommons.org/licenses/by/4.0/>).

## 1. Introduction

Rosehips are pseudo-fruits from the plants of the *Rosa* genus in the Rosaceae family that possess vitamin C, carotenoids, pectic substances, polyphenols, riboflavin, sugars, lipids, plant acids, and fatty oil [1,2]. They are known to have antioxidant, antimicrobial, anti-inflammatory, anti-diabetic, and anticancer effects [1]. *Rosa canina* is the major commercial source of rosehips. Furthermore, rosehip seeds, as a waste (by-product) from the manufacture of rosehip juice or syrup, contain 4.9–17.8% of fatty oil [3]. *R. canina* seed oil contains polyunsaturated fatty acids, palmitic, stearic, oleic, arachidic, linoleic, and linolenic acids, carotenoids, phenolic acids, tocopherols, squalenes, minerals, and phytosterols, particularly  $\beta$ -sitosterol [4,5]. Plant oil with a high concentration of unsaturated fatty acids possesses the potential health benefits but shows a higher susceptibility to lipid oxidation, as well [6].

*R. canina* seed oil possesses antioxidant, antimicrobial, and anticancerogenic activities, shows a positive influence on dermatoses, ulcers, and other skin diseases, and represents a

valuable source of phytonutrients that can improve the lipid metabolism [3,4,7], thus it is becoming popular in the cosmetic, pharmaceutical, and agro-food industries. According to the exploratory study conducted by Shabykin and Godorayhi [8], *R. canina* seed oil may be a promising topical agent for the treatment of eczema, neurodermatitis, cheilitis, and trophic ulcers of the skin. Grajzer et al. [3] have reported that the oil is a valuable source of linolenic acid, lipophilic antioxidant compounds, particularly  $\gamma$ - and  $\delta$ -tocopherol, as well as carotenoids. The same study has shown its high radical scavenging activity and high content of other unsaturated fatty acids. The microbiological shelf life of the fillets exposed to the *R. canina* seed oil nanoemulsion was prolonged, due to the antimicrobial properties of the oil [9]. According to Butnaru et al. [7], the addition of *R. canina* seed oil in the chitosan-based bionanocomposite films, increased the antibacterial activity against *Escherichia coli*.

Since *R. canina* seed oil contains various flavonoids, phenolic acids, carotenoids, and unsaturated fatty acids that can be sensitive to oxygen, light, UV irradiation, enzymes, and pH value variations, and possess a low bioavailability, the carriers for the oil should be developed to protect the bioactive compounds and provide their higher and controlled release, as well as a more comfortable oral or dermal applications. Namely, Mudrić et al. [6] have shown that after 12 days of storage at 65 °C (corresponding to the one-month storage at 25 °C, according to Chong et al. [10]), in pure *R. canina* seed oil without additional antioxidants, the polyphenol content and radical scavenging activity significantly decreased (~50% and ~1.5%, respectively), while in the oil sample with the polyphenol extract, the polyphenol content, and the antioxidant capacity significantly rose. Additionally, after 12 days of storage at 65 °C, the content of palmitic, stearic, oleic, eicosenoic, and *cis*-11-eicosenoic acid was significantly higher in the oil sample with the polyphenol extract than in the pure oil [6]. Additionally, due to the low solubility in aqueous surroundings, easy oxidization, and poor bioavailability, the application of rosehip fatty oil in hydrophilic food, pharmaceutical, and cosmetic formulations has been limited. Thus, rosehip seed oil requires encapsulation for further application with the aim to protect its sensitive bioactive compounds.

Liposomes have been used as a carrier for delivering enzymes, polyphenols, drugs, proteins, vitamins, aromas, and antioxidant compounds [11–14]. The main advantages of liposomes over other encapsulation procedures are the stability that liposomes provide in products with a typically high water content and the ability of liposomes to encapsulate the hydrophilic, amphiphilic, and lipophilic compounds [15,16]. In addition, liposomes represent non-toxic and biodegradable delivery systems that are usually prepared from naturally occurring compounds, thus new formulations could be easily implemented [11,15]. The liposomal bilayer also provides the enhanced bioavailability of various drugs [17,18], protein/peptide-based therapeutics [17], nutraceuticals [19], and polyphenols [17,20,21]. Proliposome technologies provide the high energy input of agitation and thus smaller and uniform liposomes, compared to the other procedures for the liposomal preparation [11]. Furthermore, the proliposome method may be suitable for producing liposomes on a large scale [22]. Since the textural, rheological, and physical properties, as well as chemical characteristics of the topical and oral drug delivery systems, have a direct influence on the drug bioavailability, as well as on the manufacture of pharmaceutical or cosmetic formulations, the mentioned characteristics of the liposomes should be investigated. The Raman and Fourier transform infrared (FT-IR) spectroscopy are widely used for the investigation of the interaction of the bioactive compounds, drugs, vitamins, or hormones with a phospholipid liposomal bilayer [23–28].

The encapsulation of fatty oils in liposomal particles was the focus of several recent studies [29–31]. Since there is no comprehensive study regarding the encapsulation of *R. canina* seed oil into liposomes, in the present study, the oil-loaded liposomes were developed and characterized with the aim to protect the sensitive biologically active components of the oil, increase their bioavailability, and provide their controlled release, thus be potentially implemented into various pharmaceutical and cosmetic formulations. Specifically,

the particle size, polydispersity index (PDI), zeta potential, conductivity, mobility, density, surface tension, viscosity, the Raman and FT-IR spectra, and the 60-day storage stability of the liposomes (non-treated and UV-irradiated) were examined. Additionally, the determination of their antioxidant and antimicrobial activities was also performed. Therefore, the presented study can provide evidence of the physicochemical properties and the biological activity of the *R. canina* seed oil-loaded liposomes that can add value and improve the quality of the pharmaceutical and cosmetic formulations.

## 2. Results and Discussion

### 2.1. Size, PDI, Zeta Potential, Conductivity, and Mobility of the Non-Treated and UV-Irradiated Liposomes

The particle size, PDI, zeta potential, conductivity, and mobility of the empty and *R. canina* seed oil-loaded liposomes (non-treated and UV-irradiated) were determined using photon correlation spectroscopy (PCS). The results obtained immediately after the liposomal preparation and after the UV irradiation are shown in Table 1.

**Table 1.** Particle size, polydispersity index (PDI), zeta potential ( $\zeta$ ), conductivity ( $G$ ), and mobility ( $\mu$ ) of the empty and *Rosa canina* seed oil-loaded liposomes measured immediately after the preparation and after the UV irradiation.

Sample	Size [nm]	PDI	$\zeta$ [mV]	$G$ [mS/cm]	$\mu$ [ $\mu\text{mcm/Vs}$ ]
L	2145.7 $\pm$ 43.7 <sup>a*</sup>	0.467 $\pm$ 0.012 <sup>a</sup>	−22.7 $\pm$ 0.5 <sup>b</sup>	0.020 $\pm$ 0.002 <sup>c</sup>	−1.79 $\pm$ 0.03 <sup>b</sup>
L <sub>UV</sub>	2127.3 $\pm$ 29.4 <sup>a</sup>	0.472 $\pm$ 0.023 <sup>a</sup>	−17.6 $\pm$ 0.3 <sup>c</sup>	0.021 $\pm$ 0.002 <sup>c</sup>	−1.22 $\pm$ 0.02 <sup>c</sup>
L + oil	970.4 $\pm$ 37.4 <sup>b</sup>	0.460 $\pm$ 0.010 <sup>a</sup>	−32.9 $\pm$ 0.8 <sup>a</sup>	0.068 $\pm$ 0.002 <sup>a</sup>	−2.58 $\pm$ 0.06 <sup>a</sup>
L + oil <sub>UV</sub>	953.4 $\pm$ 12.2 <sup>b</sup>	0.443 $\pm$ 0.017 <sup>a</sup>	−21.9 $\pm$ 0.6 <sup>b</sup>	0.032 $\pm$ 0.001 <sup>b</sup>	−1.72 $\pm$ 0.04 <sup>b</sup>

\* Values with different letters (a–c) in each row showed statistically significant differences ( $p < 0.05$ ;  $n = 3$ ; analysis of variance, Duncan's *post-hoc* test); L, liposomes.

As can be seen in Table 1, the size of the oil-loaded liposomes measured immediately after the liposomal preparation was 970.4  $\pm$  37.4 nm, while the PDI was 0.460  $\pm$  0.010. According to the literature, the procedures that provide a high energy input of the agitation, which was the case of the proliposome technique used in the present study, form lower-sized particles, compared to the other methods, such as the thin film procedure [11,15]. Isailović et al. [11] have reported that the presence of a small amount of ethanol which is used in the proliposome method affects the liposome size, in terms of reducing the parameter. Namely, ethanol causes the modification of the system net charge, causing a steric stabilization. The liposomes with oil had a significantly smaller diameter than their empty parallel (2145.7  $\pm$  43.7 nm, Table 1). Namely, according to Fathi-Azarbayjani et al. [32], the encapsulation of the oil compounds within the liposomal bilayer reduces the number of phospholipids that are incorporated into the membrane and therefore causes the formation of smaller vesicles. The obtained PDI value of the plain and oil-loaded liposomes (~0.460, Table 1), as a measure of the particle size distribution, indicates the existence of a moderately disperse distribution [33]. Zhao et al. [34] have reported that higher concentrations of lipids, particularly sterols, led to the higher PDI values showing an increased heterogeneity. Considering the high concentration of phospholipids in the liposomal samples (0.2 g per mL), as well as the presence of phytosterols from rosehip oil in oil-loaded liposomes, it can be the reason for the higher PDI values, i.e., a moderately disperse size distribution. UV irradiation did not cause statistically significant changes in the vesicle size and uniformity of the system (Table 1).

The zeta potential determined immediately after the preparation of the oil-loaded liposomes was −32.9  $\pm$  0.8 mV (Table 1). The zeta potential can significantly impact the physical stability of the vesicles in suspension by determining the electrostatic repulsion between them [11]. Thus, the negative and high value of the zeta potential (as a measure of liposomes stability) determined in our case, accounts for a good electrostatic stabilization of the system, preventing the aggregation and fusion of the particles [11,15]. Additionally,

the surface charge is a key determinant of the nano-particle and encapsulated content behavior and the elimination in vivo. The anionic nano-particles interact strongly with the reticuloendothelial system cells scavenging the endothelial cells and the blood resident macrophages, whereas the cationic liposomes are rapidly removed from circulation by a combination of non-specific cellular interactions (adsorption to the anionic surface of the blood vessel walls), and clearance by the specialized cells of the reticuloendothelial system [35]. The rosehip oil-loaded liposomes showed a higher zeta potential (absolute value), compared to the plain liposomal bilayer ( $-22.7 \pm 0.5$  mV, Table 1). Namely, several research studies have reported that the sterol incorporation increased the spacing between the phospholipid heads and caused the hydrophobic stabilization of the membrane of the liposomes [36–38]. Therefore, the presence of phytosterols from rosehip oil can change the order of the phospholipids and the thickness of the liposomal membrane regardless of the nature of the functional groups in phospholipids, and these groups can participate in creating hydrogen bonds with phytosterols, as well as in changing the zeta potential of the liposomes [36,39]. In addition to the particle size, the PDI, and the zeta potential, the conductivity of the prepared liposomes was determined as the fourth physical property and amounted to  $0.068 \pm 0.005$  mS/cm for the oil-loaded liposomes (Table 1). The electrical conductivity represents a measure of how easily an electrical current can pass through water or any solution, and it can be used as an indicator of the total dissolved solids [40,41]. In the case of the liposomes, the conductivity is influenced by the exposed charge of the phospholipids and correlates to a volume of the liposome entrapment [41]. The conductivity measurements can also provide evidence of polyions that can induce the liposome aggregation. The additional reasons for the monitoring of the conductivity of the liposomal suspension lay in the fact that the movement of the conductive ions in highly conductive samples can lead to the electro depolarization, degradation, and thus inconsistent zeta potential values, while changes in the conductivity values (the increase in values) may indicate a leakage of the encapsulated contents into the surrounding water medium [40]. Namely, Lidgate et al. [41] have reported that in the case of a higher phospholipid concentration (which was the case of rosehip oil-loaded liposomes, 0.2 g/mL), the ions are inside the liposomal particles, their mobility is reduced, and their contribution to the conductivity is no longer apparent, thus the value of the conductivity is pretty low. However, the conductivity of the plain liposomes was even significantly lower ( $0.020 \pm 0.002$  mS/cm), in comparison to the oil-loaded liposomes. It can be explained by the fact that the small liposomes most notably affected the conductivity, due to a greater surface area which exposes a greater percentage of the phospholipid head groups [41]. Thus, the measured conductivity of the *R. canina* oil-loaded liposomes was greater (smaller particles than of plain liposomes). The mobility of the liposomes, as a function of size, surface charge, and membrane composition, was also examined ( $-2.58 \pm 0.06$   $\mu\text{mcm}/\text{Vs}$ , Table 1). In our previous study [15], the liposomes with sterols showed a higher fluidity, thus a better mobility. Given that the *R. canina* seed oil possessed phytosterols, mainly  $\beta$ -sitosterol—82.1% [4], it can be the explanation for the higher mobility of the oil-loaded liposomes, compared to the plain liposomes ( $-1.79 \pm 0.03$   $\mu\text{mcm}/\text{Vs}$ , Table 1). However, the UV irradiation has caused a significant influence on the zeta potential, conductivity, and mobility of the oil-loaded liposomes. Namely, a drop in the all mentioned values was noticed (Table 1). According to the literature, the UV irradiation of the liposomes resulted in the comprehensive surface charge change or even reversal from the negative to the positive [35]. However, the zeta potential changing or switching do not always induce any large-scale reorganization of the liposomal bilayer, disruption of the liposome integrity, as well as leakage of the encapsulated bioactive compounds. Considering that there was no increase in the conductivity of the oil-loaded liposomes after the UV irradiation, it can be concluded that there was no leakage of the encapsulated compounds from the carrier. Namely, the increase in the conductivity of the liposomes during storage is usually related to the leakage of the encapsulated active compounds. The conductivity of the inner medium of the liposomes can be modified by the encapsulated compounds as well [42].

Since 30-min UV irradiation caused the water evaporation from the liposomal suspension, the decrease in the conductivity of the UV-irradiated samples should be explained by higher lipid concentrations which lead to a higher capture volume, the effective removal of ions from the liposome suspension, and consequently, to the reduction in the conductivity value [32,41]. A drop in the mobility can be explained by the degradation of  $\beta$ -sitosterol from the oil because the UV irradiation can induce the phytosterol peroxidation [43].

2.2. The Storage Stability of the Liposomes

With the aim to investigate the storage stability of the *R. canina* seed oil-loaded liposomes (non-treated and UV-irradiated), the particle size, the PDI, the zeta potential, the conductivity, and the mobility were determined for 60 days and the results are presented as Figure 1a–e. The storage stability of the empty liposomes (non-treated and UV-irradiated) via analyzing the particle size, PDI, zeta potential, conductivity, and mobility were also examined for 60 days and the results are presented in Supplementary Figure S1a,b.

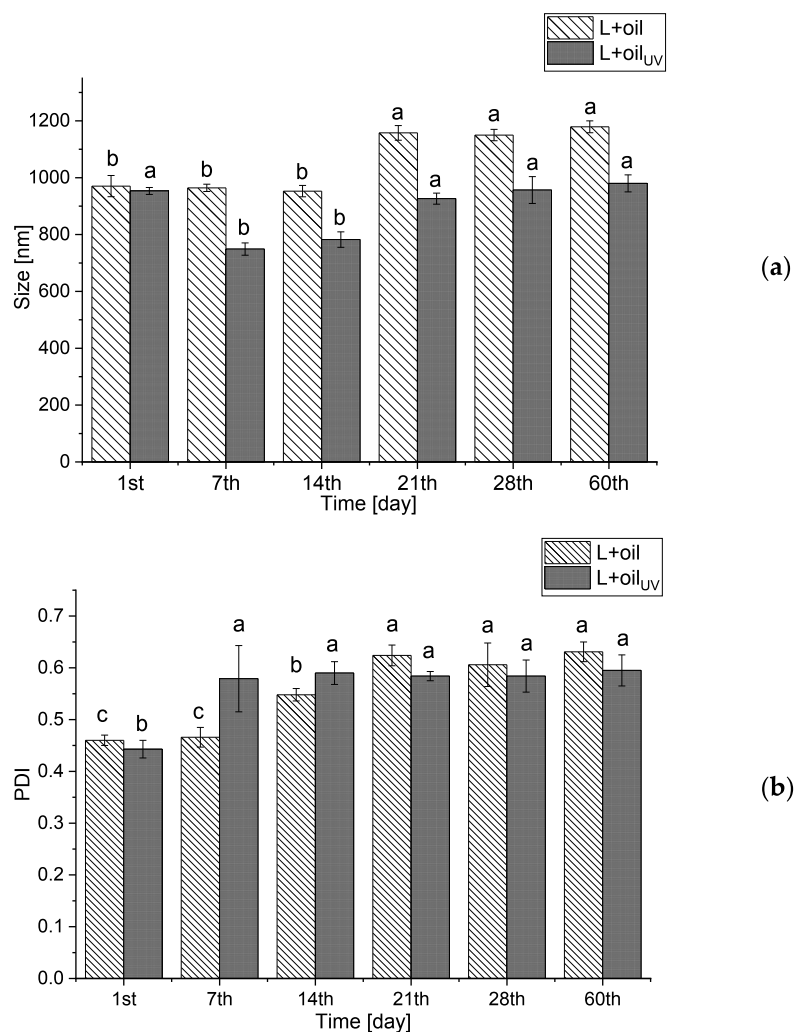
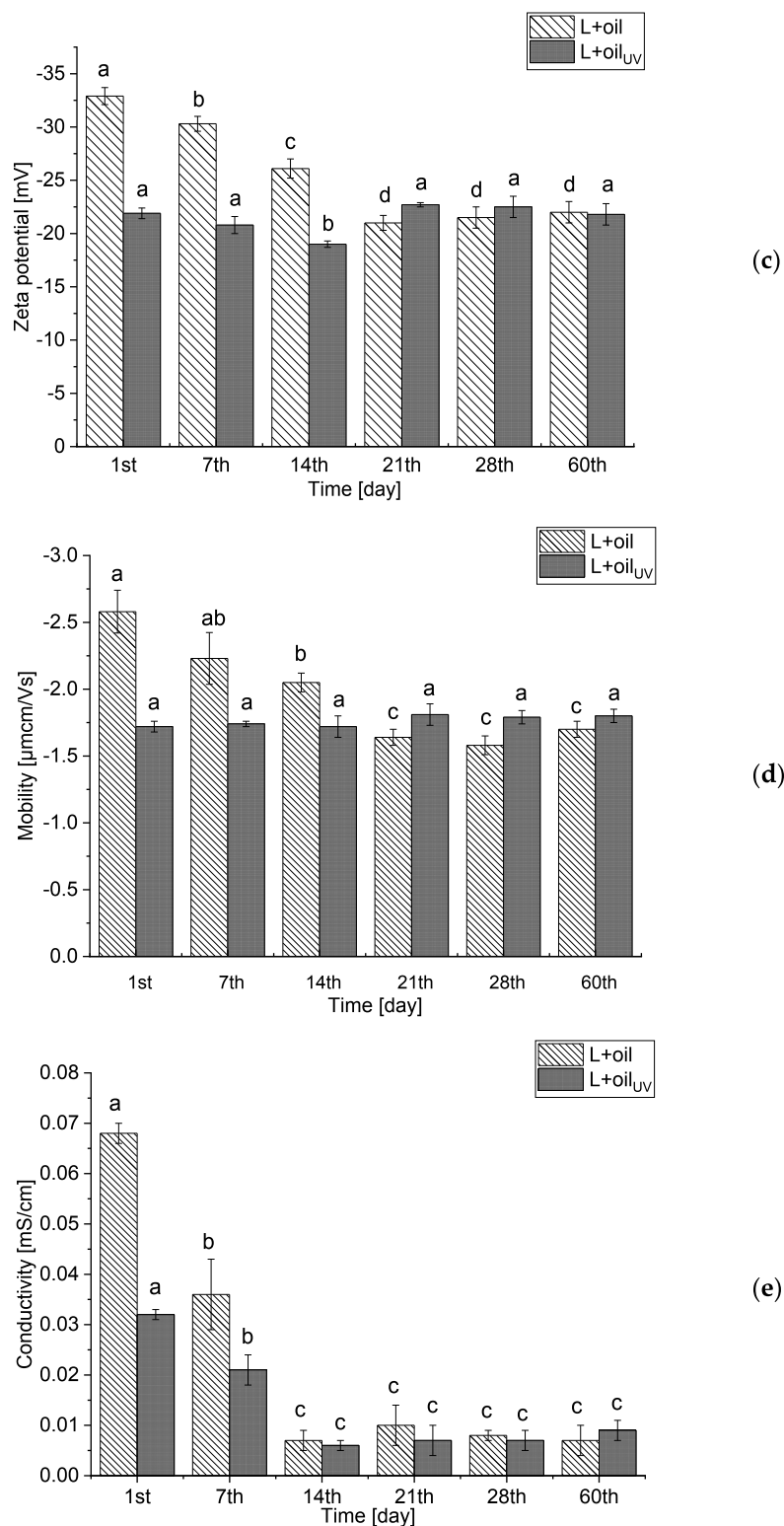


Figure 1. Cont.



**Figure 1.** Liposome size (a), polydispersity index (b), zeta potential (c), mobility (d), and conductivity (e) of the non-treated and UV-irradiated *Rosa canina* seed oil-loaded liposomes during 60 days storage at 4 °C; values with different letters (a–d) in each row showed statistically significant differences ( $p < 0.05$ ;  $n = 3$ ; analysis of variance, Duncan’s *post-hoc* test); L, liposomes.

The size of the liposomal population with the rosehip oil did not change significantly during 14 days of storage at 4 °C, but after the 21st day, the vesicle size rose from  $952.8 \pm 20.1$  nm to  $1157.7 \pm 25.8$  nm and amounted to  $1179.2 \pm 21.4$  nm at the 60th day,



whereas the PDI continuously increased from the 14th day (Figure 1b). As it is mentioned in Section 3.1., a negative zeta potential of the oil-loaded liposomes provides a good electrostatic stabilization of the liposomal suspension, providing the inhibition of the particle aggregation and fusion, which is confirmed by the stability test (the size did not change for more than 11.5% during the 60-day storage at 4 °C). In the UV-irradiated parallel, the same trend is observed.

As can be seen in Supplementary Figure S1a, on the 1st day of the storage stability study, the non-treated vesicles of the plain liposomes had the same diameter as the UV-irradiated vesicles. However, after 60 days of storage at 4 °C incubation, the vesicle diameters changed only for the UV-irradiated sample. Namely, on the 60th day, the diameter for UV-irradiated liposomes was  $2650.5 \pm 27.1$  nm and for the non-treated  $2115.4 \pm 45.5$  nm. The size of the UV-irradiated liposomes changed by 54.6% during the 60-days storage at 4 °C. The obtained results are in agreement with the literature data [44]. In both plain liposomes, the PDI did not change during the storage stability study (Supplementary Figure S1a).

Moreover, the zeta potential varied in both the oil-loaded liposomes, but the trend was different in the non-treated and the UV-irradiated samples (Figure 1c). The zeta potential (absolute value) in the non-treated liposomes decreased from  $-32.9 \pm 0.8$  mV to  $-22.2 \pm 0.9$  mV, while the zeta potential of the UV-irradiated liposomes decreased to  $-18.8 \pm 0.3$  mV on the 14th day, and after that it increased up to  $21.8 \pm 0.9$  mV on the 60th day. The zeta potential of the non-treated plain liposomes did not change significantly during the 60-day storage study, while in the case of the UV-irradiated parallel, the zeta potential increased from  $-17.6 \pm 0.3$  mV to  $-23.8 \pm 0.5$  mV (Supplementary Figure S1b). According to the results of the liposomes' mobility (Figure 1d), it can be concluded that there were no significant changes in the mentioned parameters during the 21 days in the non-treated oil-loaded liposomes, but after that, the mobility decreased up to  $-1.70 \pm 0.06$   $\mu\text{mcm}/\text{Vs}$ . However, the mobility of the UV-irradiated parallel did not change during the 60-day storage. Moreover, in the UV-irradiated plain liposomes, an increase in the mobility of the liposomes after 14 days (from  $-1.22 \pm 0.02$   $\mu\text{mcm}/\text{Vs}$  to  $-1.71 \pm 0.03$   $\mu\text{mcm}/\text{Vs}$ ) is observed, while in the non-treated plain liposomes, there were no changes in the mobility during the 60 days. Therefore, the trend of the zeta potential changes, is the same as the trend of the mobility changes in the case of the unloaded liposomes.

According to Lidgate et al. [41], the measurement of conductivity of the stored liposomal vesicles can provide important information related to their size and integrity, i.e., the potential leaking of the encapsulated substances. Namely, the changes in conductivity can indicate whether the liposomes have fused, i.e., the decrease in conductivity, or leaked, i.e., an increase in conductivity. The conductivity of both non-treated and UV-irradiated oil-loaded liposomes (Figure 1e) significantly decreased during the 60-day stability study (from  $0.068 \pm 0.002$  mS/cm to  $0.007 \pm 0.003$  mS/cm for the non-treated and from  $0.032 \pm 0.001$  mS/cm to  $0.009 \pm 0.001$  mS/cm for the UV-irradiated). The same trend is observed in the case of the plain liposomes (Supplementary Figure S1b). As can be noticed, the conductivity of the oil-loaded liposomes decreased on the 14th day, after that the values did not change. A similar trend was observed in the PDI values of the mentioned liposomes (the increase in the PDI on the 14th day, after that the values were the same). Therefore, the decrease in the conductivity can be related to the fusion of some parts of the liposomal population, which influenced the size distribution, but not particle size represented as the mean value (Figure 1a,b).

### 2.3. Density, Surface Tension, and Viscosity of the Liposomes

The physical properties, including the density, surface tension, and viscosity were determined in the pure *R. canina* seed oil, the empty, and the oil-loaded liposomes (non-treated and UV-irradiated). Since the mentioned parameters have a key role in the manufacture of pharmaceutical and cosmetic products, they should be investigated, in order to improve the product quality.

As can be seen in Table 2, the density of the oil-loaded liposomes was  $0.974 \pm 0.003 \text{ g/cm}^3$  for the non-treated and  $0.959 \pm 0.001 \text{ g/cm}^3$  for the UV-irradiated, whereas the plain liposomes have shown a significantly higher density,  $0.995 \pm 0.003 \text{ g/cm}^3$  and  $0.974 \pm 0.004 \text{ g/cm}^3$  for the non-treated and the UV-irradiated samples. The surface tension of the oil-loaded liposomes was  $20.3 \pm 1.0 \text{ mN/m}$  for the non-treated and  $23.1 \pm 0.2 \text{ mN/m}$  for the UV-irradiated, while the unloaded liposomes had a significantly different surface tension,  $19.7 \pm 0.9 \text{ mN/m}$  for the non-treated and  $21.4 \pm 0.5 \text{ mN/m}$  for the UV-irradiated. The viscosity of the oil-loaded liposomes was  $13.5 \pm 0.2 \text{ mPa}\cdot\text{s}$  for the non-treated and  $20.2 \pm 0.1 \text{ mPa}\cdot\text{s}$  for the UV-irradiated, while the viscosity of the empty liposomes was  $13.9 \pm 0.2 \text{ mPa}\cdot\text{s}$  for the non-treated and  $20.7 \pm 0.4 \text{ mPa}\cdot\text{s}$  for the UV-irradiated. Further, the density and surface tension of the pure oil were  $0.914 \pm 0.001 \text{ g/cm}^3$  and  $30.0 \pm 0.8 \text{ mN/m}$  for the non-treated and  $0.915 \pm 0.002 \text{ g/cm}^3$  and  $28.0 \pm 0.9 \text{ mN/m}$  for the UV-irradiated, while viscosity was  $50.9 \pm 0.3 \text{ mPa}\cdot\text{s}$  for the non-treated and  $45.7 \pm 0.1 \text{ mPa}\cdot\text{s}$  for the UV-irradiated. In the case of the pure oil, the UV irradiation has caused a decrease in the surface tension and viscosity values. Moreover, it was the opposite in the oil-loaded liposomes, where the UV-irradiated samples possessed a higher surface tension and viscosity, probably due to water evaporation during 30 min of UV irradiation. The values of the density and surface tension did not change after the 60th day in the non-treated and UV-irradiated oil-loaded liposomes ( $0.969 \pm 0.003$  and  $0.962 \pm 0.003 \text{ g/cm}^3$  and  $20.1 \pm 1.5$  and  $23.4 \pm 1.5 \text{ mN/m}$ , respectively), while the viscosity significantly decreased ( $6.7 \pm 0.4$  and  $11.4 \pm 0.5 \text{ mPa}\cdot\text{s}$ ), probably due to the hydrolytic reactions characteristic of an aqueous medium.

**Table 2.** Density ( $\rho$ ), surface tension ( $\gamma$ ), and viscosity ( $\eta$ ) of *Rosa canina* seed oil, empty, and oil-loaded liposomes (non-treated and UV-irradiated).

Sample	$\rho \text{ (g/cm}^3\text{)}$	$\gamma \text{ (mN/m)}$	$\eta \text{ (mPa}\cdot\text{s)}$
oil	$0.914 \pm 0.001$ <sup>d*</sup>	$30.0 \pm 0.8$ <sup>a</sup>	$50.9 \pm 0.3$ <sup>a</sup>
oil <sub>UV</sub>	$0.915 \pm 0.002$ <sup>d</sup>	$28.0 \pm 0.9$ <sup>b</sup>	$45.7 \pm 0.1$ <sup>b</sup>
L	$0.995 \pm 0.003$ <sup>a</sup>	$19.7 \pm 0.7$ <sup>e</sup>	$13.9 \pm 0.2$ <sup>d</sup>
L <sub>UV</sub>	$0.967 \pm 0.003$ <sup>b</sup>	$21.4 \pm 0.5$ <sup>d</sup>	$20.7 \pm 0.4$ <sup>c</sup>
L + oil	$0.974 \pm 0.004$ <sup>b</sup>	$20.3 \pm 0.8$ <sup>de</sup>	$13.5 \pm 0.2$ <sup>d</sup>
L + oil <sub>UV</sub>	$0.959 \pm 0.001$ <sup>c</sup>	$23.1 \pm 0.2$ <sup>c</sup>	$20.2 \pm 0.2$ <sup>c</sup>

\* Values with different letters (a–e) in each row showing the statistically significant differences ( $p < 0.05$ ;  $n = 3$ ; analysis of variance, Duncan's *post-hoc* test); L, liposomes.

#### 2.4. Raman Spectra

The Raman spectroscopy was applied as the fast and nondestructive analytical technique for the chemical evaluation and the examination of the presence of different interactions between Phospholipon (Ph, a commercial phospholipid mixture) and the *R. canina* seed oil, as well as the changes between the plain and oil-loaded liposomes, and their UV-treated parallels.

The Raman features of the Ph and plain liposomes spectra (Figure 2a and Supplementary Figure S2, respectively) correspond to the C–N symmetric stretching of choline (phospholipid head-group) at  $\sim 710 \text{ cm}^{-1}$ , C–C=O stretching at  $959 \text{ cm}^{-1}$ , the skeletal stretching of the C–C vibrations at  $\sim 1025 \text{ cm}^{-1}$ , the symmetric stretching of  $\text{PO}_2^-$  at  $1080 \text{ cm}^{-1}$ , the asymmetric stretching region of the  $\text{PO}_2^-$  groups between  $1170\text{--}1200 \text{ cm}^{-1}$ , *cis*=C–H stretching vibration in the oleoyl chain at  $1275 \text{ cm}^{-1}$ , the methylene deformation band ( $\delta\text{CH}_2$ ) of the fatty acid chains at  $1450 \text{ cm}^{-1}$ , C=C stretching vibration in the oleoyl chain at  $1665 \text{ cm}^{-1}$ , carbonyl group (C=O) of the ester bond between glycerol and fatty acids at  $1765 \text{ cm}^{-1}$ , the symmetric and asymmetric stretching modes of the C–H bonds in  $\text{CH}_2$  and  $\text{CH}_3$  groups in the alkyl chains at  $2850\text{--}2950 \text{ cm}^{-1}$ , the CH stretching of the N– $\text{CH}_3$  groups at  $3015 \text{ cm}^{-1}$ , and the mode associated with bound water at  $3325 \text{ cm}^{-1}$  [23,24,28,45,46]. Additionally, the Raman mode at  $\sim 1525 \text{ cm}^{-1}$  can be related to the N–O stretching (probably from the impurity) that occurs at  $1500\text{--}1550 \text{ cm}^{-1}$  or the H–O–H bending vibration in

the phospholipids that occurs between 1500 and 1700  $\text{cm}^{-1}$  [45]. The difference between Ph and the UV-irradiated Ph is in a slight moving from 1275  $\text{cm}^{-1}$  to 1260  $\text{cm}^{-1}$  of the band ascribed to the *cis* =C-H stretching vibration in the oleoyl chain, probably due to the sensitivity of a double bond to the oxidation caused by the UV irradiation. The spectra of the plain liposomes (non-treated and UV-irradiated), presented in Supplementary Figure S2, contain all peaks as the spectra of pure Ph, thus it can be concluded that no chemical changes occur in the phospholipids during the liposome formulation, which is in agreement with the literature data [23]. However, there were differences in the intensity of the peaks between the spectrum of pure Ph and the plain liposomes, possibly due to the formation of hydrogen bonds. Arsov and Quaroni [47] and Chen and Tripp [48] have reported that the relative intensity of the C=O bands is the key parameter to monitor the changes in the relative free and hydrogen bonded populations of the carbonyl groups of the lipid.

The fingerprint region of the Raman spectra of the rosehip oil includes essential bands which correlate with the most important parts of the fatty acids' molecular structure and the region well known to characterize the unsaturation level of the fatty acid chain [49,50]. According to the literature, the dominant compounds in the *R. canina* seed oil are unsaturated acids, including linoleic,  $\alpha$ -linolenic, and oleic acids, while linoleic acid possesses the highest percentage [4,51,52]. Moreover, saturated fatty acids, such as palmitic and stearic acids, are presented in a lower percentage [53]. Linoleic,  $\alpha$ -linolenic, and oleic acids mainly differ in the position of the double bond, and consequently, there are two or three broad C=C bands with higher wavenumbers in their Raman spectra that are highly similar [54,55]. As can be seen in Figure 2, a group of overlapping bands in the region between 800 and 1100  $\text{cm}^{-1}$ , peaking at 1010  $\text{cm}^{-1}$ , may be attributed to the C–C stretching of the  $(\text{CH}_2)_n$  group [56]. A strong Raman phonon in the carbonyl region of the spectrum at 1160  $\text{cm}^{-1}$  can be assigned to the C–C stretching of carotenoids [23,56]. The mode at 1275  $\text{cm}^{-1}$  is related to the presence of the esterified unsaturated fatty acids (*cis* isomers) and can be assigned to the bending of =C-H [53]. The band at 1450  $\text{cm}^{-1}$  can be assigned to the C–H scissoring of  $\text{CH}_2$ , while the peak at 1520  $\text{cm}^{-1}$  can be assigned to the C=C stretching of carotenoids [56]. A broad small peak at  $\sim 1600 \text{ cm}^{-1}$  corresponds to the polyphenolic compounds [53], which is in agreement with the study of Grajzer et al. [3] who identified and determined, apart from a relatively high level of carotenoids in rosehip seed oil, phenolic acids, particularly *p*-coumaric acid methyl ester, vanillin, and vanillic acid. Since rosehip oil possesses an appreciable amount of lipophilic antioxidants, such as tocopherol [3], the phonon arising from the aromatic part (chromanol ring) of tocopherol occurred at 1615  $\text{cm}^{-1}$  [57]. The phonon frequency at 1650  $\text{cm}^{-1}$  can be assigned to the *cis* stretching vibration of the C=C unsaturated lipids (*cis* RHC=CHR) [53,56]. The relative intensity of all unsaturation regions of the unsaturated fatty acids (*cis* isomers) is in accordance with the degree of saturation of the fatty acid in the lipid, especially in the case of the mode at 1650  $\text{cm}^{-1}$  [53]. A broad band in the oil spectrum ranging at  $\sim 2700 \text{ cm}^{-1}$ , originates from  $\text{CH}_2$ , and the  $\text{CH}_3$  symmetric stretching vibration [58]. The UV irradiation did not cause changes that can be visible in the Raman spectra of the pure *R. canina* oil. The obtained spectra are in agreement with the literature data and contain the common characteristic vibrational modes of almost all vegetable oils [56].

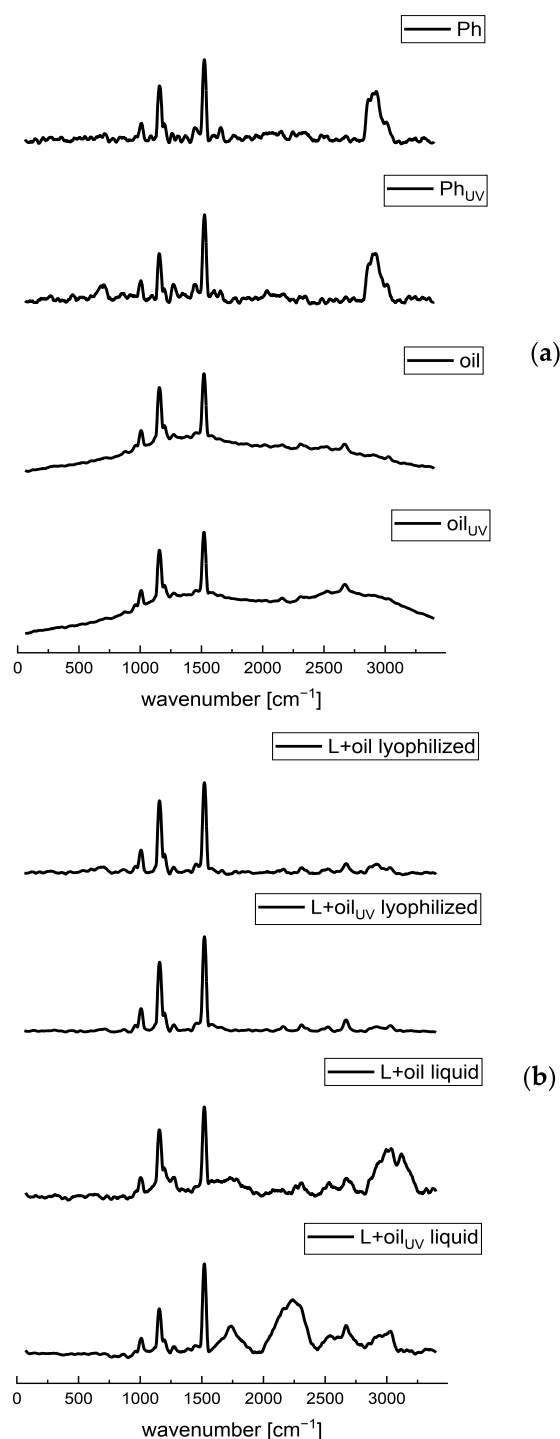


**Figure 2.** Raman spectra of the non-treated and UV-irradiated (a) Ph (a commercial phospholipids mixture) and the *Rosa canina* seed oil, and (b) the oil-loaded liposomes (liquid and lyophilized) in the spectral range from 70 to 3400 cm<sup>-1</sup>; L, liposomes.

The Raman spectrum of the rosehip seed oil-loaded liposomes showed characteristic bands of both phospholipids and oil (Figure 2b). Namely, the mode at 959 cm<sup>-1</sup> corresponds to the phospholipid C–C=O stretching. In a region of 1010–1025 cm<sup>-1</sup>, the C–C stretching of the (CH<sub>2</sub>)<sub>n</sub> group presents in Ph and oil spectra, while the mode 1150 cm<sup>-1</sup> can be assigned to the C–C stretching of carotenoids, which exclusively originates from oil. However, the stretching region of the PO<sub>2</sub><sup>-</sup> groups is from 1170 to 1200 cm<sup>-1</sup>. Namely, in the oil-loaded liposomes spectrum, the stretching region of the PO<sub>2</sub><sup>-</sup> groups of phospholipids was found

at 1135–1195  $\text{cm}^{-1}$  (occurred in the spectrum of raw phospholipids as well, Figure 2a) and it seems to be insensitive to the presence of either bilayer modifiers, such as rosehip oil. Namely, phytosterols from plant oil, such as  $\beta$ -sitosterol and cycloartenol presented in rosehip oil [3], are incorporated within the bilayer membrane, its hydrophilic 3 $\beta$ -hydroxyl head group is placed in the vicinity of the phospholipid ester carbonyl groups, and its hydrophobic steroid ring is oriented parallel to the acyl chains of the phospholipids [24]. The mode at  $\sim 1275 \text{ cm}^{-1}$  relates to the *cis* =C-H stretching vibration in the oleoyl chain and methylene deformation band ( $\delta\text{CH}_2$ ) of the fatty acid chains at  $1450 \text{ cm}^{-1}$  presented in both Ph and oil. The Raman phonon at  $1525 \text{ cm}^{-1}$  can be related to the C=C stretching of carotenoids from oil, whereas the C=C stretching vibration in the oleoyl chain at  $1650 \text{ cm}^{-1}$  is from unsaturated fats presented in Ph and oil. The symmetric and asymmetric stretching modes of the C–H bonds in the  $\text{CH}_2$  and  $\text{CH}_3$  groups in the alkyl chains are in a range of 2700 to  $3000 \text{ cm}^{-1}$  which occurred in the Ph and oil spectra as well. The obtained results are expected since rosehip oil had a very strong signal during the Raman spectra recording. Additionally, in contrast to the aqueous extracts which compounds are water soluble and completely enveloped by the phospholipid layers [23], the liposoluble components of the oil cannot be affected by the effect of “shielding” [59]. Namely, the lipophilic compounds are located within the liposomal bilayer that contains phospholipid tails, whereas the hydrophilic compounds can be located in the water vesicles [15]. According to Pohle et al. [60], the stretching region of the  $\text{PO}_2^-$  groups at  $1080 \text{ cm}^{-1}$  and  $\sim 1200 \text{ cm}^{-1}$  is marked as being quite sensitive to the structural changes of the phosphatidylcholine micelles, particularly in the hydrated state. In the case of the oil-loaded liposomes, a mode at  $1080 \text{ cm}^{-1}$  disappeared, whereas the peak at  $\sim 1200 \text{ cm}^{-1}$  became more pronounced and shifted to the higher wavenumber. In the study by Frías et al. [26], a polyphenol from bearberry, encapsulated into phosphatidylcholine liposomes, influenced both of the  $\text{PO}_2^-$  stretching phonons’ frequency, depending on its location within the liposomal vesicles. Namely, the mode associated with the symmetric  $\text{PO}_2^-$  stretching at  $1080 \text{ cm}^{-1}$  was affected when the polyphenol was outside, whereas the asymmetric stretching phonon at  $\sim 1200 \text{ cm}^{-1}$  was influenced if the polyphenol is both inside and outside. Additionally, the encapsulation of the polyphenols of ground ivy extract in the liposomal bilayer also caused a slight shift of the  $\text{PO}_2^-$  asymmetric stretching band from  $1238 \text{ cm}^{-1}$  (empty liposomes) to  $1243 \text{ cm}^{-1}$  (extract-loaded liposomes) [23]. In the case of rosehip seed oil-loaded liposomes, changes have occurred in both the  $\text{PO}_2^-$  stretching regions indicating that the oil compounds are located both in the phospholipid bilayer and on the surface of the membrane. An additional fact that some of the rosehip oil components can be distributed at the liposomal surface is the diminishing of the intensity of the phonon related to the bound water at  $3325 \text{ cm}^{-1}$ . Namely, the components that interact via the hydrogen bonds can replace molecules of water adsorbed on the membrane surface. The facts that come from the Raman analysis suggest that the oil components are not only entrapped within the liposomal bilayer but also on the membrane surface, having a significant influence on the physicochemical properties of the liposomes. As in the case of the plain liposomes and pure oil, the UV irradiation did not cause changes that can be visible in the Raman spectra of the oil-loaded liposomes.

### 2.5. FT-IR Spectra

The FT-IR spectroscopy was also applied in order to analyze and investigate the presence of different interactions between the phospholipids from liposomes and *R. canina* seed oil, as well as the potential influence of the UV irradiation on the liposomes and oil compounds. The FT-IR spectra of the phospholipid mixture, rosehip oil, plain and oil-loaded liposomes, and their UV-irradiated parallels are presented in Figure 3.

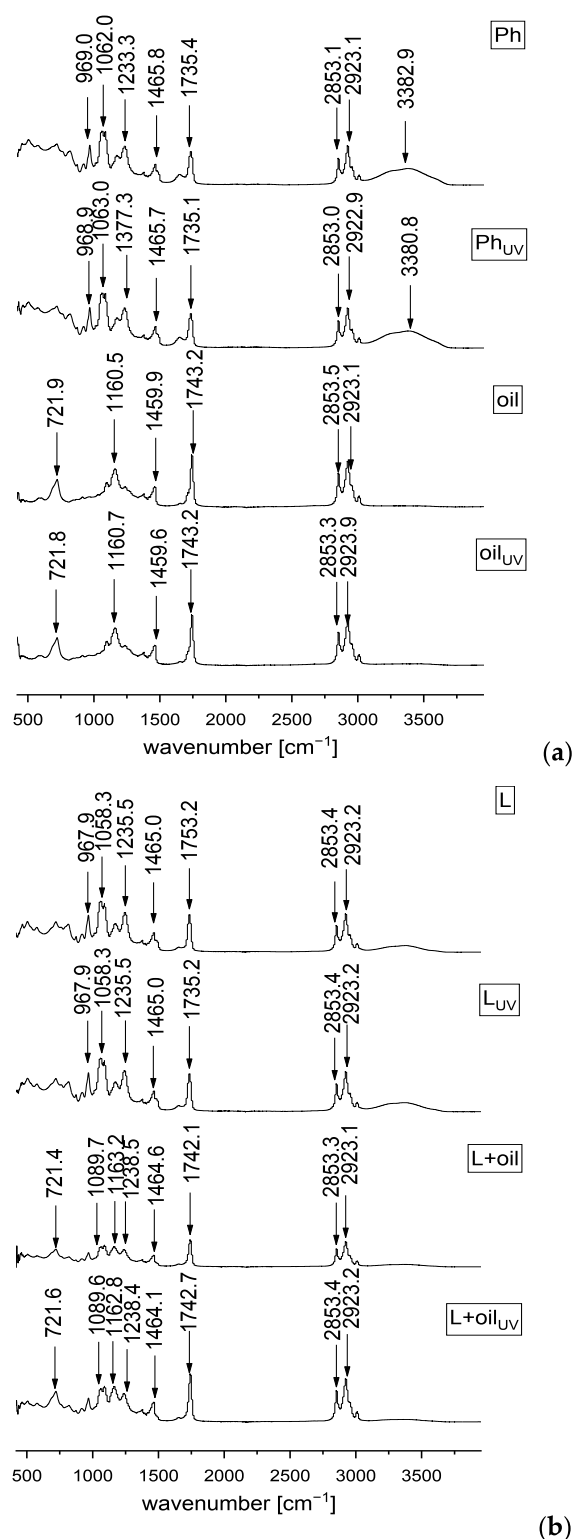


**Figure 3.** FT-IR spectra of the non-treated and UV-irradiated (a) Ph (a commercial phospholipids mixture) and *Rosa canina* seed oil, and (b) the plain and oil-loaded liposomes in the spectral range from 450 to 4000  $\text{cm}^{-1}$ ; L, liposomes.

Regarding the FT-IR spectra of the pure Ph (Figure 3a), a group peak at 623  $\text{cm}^{-1}$  assigned to O-CO-C of phospholipids, C-N symmetric stretching of choline at  $\sim 719.6 \text{ cm}^{-1}$  is observed, and the quaternary ammonium group of choline moiety gives rise to two phonons, at 923.1 and 969  $\text{cm}^{-1}$ , which is related to the symmetric and asymmetric stretch-

ing of the C–N bond, respectively [23,24]. There is a band at  $1086.4\text{ cm}^{-1}$  that corresponds to the symmetric  $\text{PO}_2^-$  stretching that is partially overlapped with the band at  $1062.9\text{ cm}^{-1}$  that represents the C–O–P–O–C stretching, the mode at  $1174.1$  and  $1233.4\text{ cm}^{-1}$  are specific for the symmetric and asymmetric stretching of the  $\text{PO}_2^-$  groups, the mode at  $1377.4\text{ cm}^{-1}$  is accompanied with the methylene group from the lipids, the mode centered at  $1465.8\text{ cm}^{-1}$  assigns to the scissoring vibrations of the  $\text{CH}_2$  groups ascribed to the fatty acid chains, the mode at  $1651.6\text{ cm}^{-1}$  is associated with bound water, the mode at  $1735.4\text{ cm}^{-1}$  represents the stretching vibrations of the ester carbonyl groups (C=O), the mode at  $2923.1\text{ cm}^{-1}$  is specific for the asymmetric stretching vibration in the  $\text{CH}_3$  groups, the mode at  $2853.1$  and  $3009.8\text{ cm}^{-1}$  represent the symmetric and asymmetric C–H stretching, and a broad mode at  $3382.9\text{ cm}^{-1}$  corresponds to the O–H stretching [24,61,62]. Since the FT-IR spectra of the empty liposomes (Figure 3b) showed all characteristic bands of phospholipids, it can be concluded that no chemical reaction occurred during the liposomal preparation that was also approved in the Raman analysis.

The FT-IR spectra of the *R. canina* oil (Figure 3a) show the mode at  $721.8\text{ cm}^{-1}$  that can be assigned to the carbon skeleton vibration, and the mode at  $1098.3\text{ cm}^{-1}$  that is characteristic for the (C–C) stretching of the  $(\text{CH}_2)_n$  group [56,63]. According to Qiu et al. [56], a strong peak at  $1160.5\text{ cm}^{-1}$  is related to the C–C stretching of carotenoids. The band at  $1242.8\text{ cm}^{-1}$  is assigned to the in-plane deformation vibration of the =CH groups from the unconjugated cis double bonds, the phonon observed at  $1377.5\text{ cm}^{-1}$  was associated with the deformation vibration in the phase of a methylene group from the lipids, the band at  $1459.9\text{ cm}^{-1}$  is related to the  $\delta(\text{C–H})$  deformation, the phonon at  $1743.2\text{ cm}^{-1}$  is characteristic for the  $\nu(\text{C–H})$  ester carbonyl, which is a chemical group specific to vegetable oils with a high content in saturated fatty acids and short hydrocarbonated chains, the mode at  $2853.5$  and  $2923.1\text{ cm}^{-1}$  are assigned to the symmetric and asymmetric vibrations  $\nu(\text{C–H})$  of the  $\text{CH}_2$  and  $\text{CH}_3$  aliphatic groups from the alkyl rest of the triglycerides, and the mode at  $3009.3\text{ cm}^{-1}$  is related to the =CH vibration from the lipids (methyl-oleate group) [7,63].

In the FT-IR spectra of the oil-loaded liposomes (Figure 3b), there is one mode specific only for the *R. canina* oil, at  $1163.2\text{ cm}^{-1}$  (related to carotenoids). The presence of a low-intensity band corresponds to carotenoids, clearly originating from oil, indicating that they can be “entrapped” on the liposomal surface. Moreover, an absence of the mode that exists in the FT-IR spectra of pure oil is observed, such as the bands at  $1098.3\text{ cm}^{-1}$  related to the (C–C) stretching of the  $(\text{CH}_2)_n$  group and  $1242.8\text{ cm}^{-1}$  assigned to the in-plane deformation vibration of the =CH groups from the unconjugated cis double bonds. Probably, the components with these functional groups are located within the liposomal particles, thus they cannot be visible in the spectra. Namely, according to the literature, when the peaks that belong to the active compounds are invisible, it means they are completely covered by the carrier, i.e., the indication of the efficient wrapping of the oil compounds during the liposome entrapment, in our case [64,65]. In the FT-IR spectra of the oil-loaded liposomes, there are also observed modes that belong to the liposome phospholipids, including the modes at  $924.7$ ,  $968.6$ ,  $1089.7$ , and  $1058.8\text{ cm}^{-1}$ . However, the mode at  $623\text{ cm}^{-1}$ , assigned to O–CO–C of the phospholipids,  $1174.1$  and  $1233.4\text{ cm}^{-1}$ , related to the symmetric and asymmetric stretching of the  $\text{PO}_2^-$  groups, and  $3382.9\text{ cm}^{-1}$ , corresponding to the O–H stretching, existed in the FT-IR spectra of the plain liposomes, but were not observed in the spectra of the oil-loaded liposomes. According to the literature, when the encapsulated compounds are distributed inside and outside of the liposomes, it affects the asymmetric stretching phonon at  $1233\text{ cm}^{-1}$  [23]. In the case of the *R. canina* oil-loaded liposomes, the mentioned band is moved from  $1233.4$  to  $1238.5\text{ cm}^{-1}$ , indicating that the oil components are located within the liposoluble phospholipid tails and on the liposome surface. Additionally, when the encapsulated components are only on the liposomal surface, it has an influence on the band associated with the symmetric  $\text{PO}_2^-$  stretching ( $1087\text{ cm}^{-1}$ ) [26]. Thus, further evidence that the *R. canina* oil compounds are both inside and outside of the liposomes is in the fact that the mentioned band is the same in the plain and oil-loaded

liposomes. Some of the oil components that are incorporated at the membrane surface, caused a significant diminishing in the intensity of the mode assigned with bound water (at  $\sim 1650$  and  $\sim 3380$   $\text{cm}^{-1}$ ), due to their interactions through the hydrogen bonds which replace the molecules of water adsorbed on the surface of the liposomal bilayer [23]. The obtained results and conclusions are in agreement with the literature data, where the FT-IR analysis showed that the flaxseed oil was encapsulated in the interior of the liposomes and combined with the membrane interface of the bilayer as well [30]. In addition, the same study reported that flaxseed oil loaded-liposomes were spherical with a smooth surface (transmission electron microscopy) due to the flaxseed oil which can fill the gaps created by the imperfect phospholipid arrangement and thus improve the intactness of the liposomal bilayer. Namely, since the mentioned oil compounds were combined with the membrane interface, it can explain the phenomenon that the image of the liposomes with oil had a smooth surface, while the plain liposomes had a rough surface [30]. The phonon at  $1735.4$   $\text{cm}^{-1}$  (in the plain liposomes) associated with  $\nu(\text{C-H})$  ester carbonyl was moved to  $1742.1$   $\text{cm}^{-1}$  (in the oil-loaded liposomes). The changes in the mentioned peak occurred due to the formation of a hydrogen bond between the  $-\text{OH}$  groups present in the oil components and the carbonyl groups of the phospholipids [24]. The mode that is common for both the oil and phospholipids are at  $\sim 720$   $\text{cm}^{-1}$ , related to the C-N symmetric stretching and the carbon skeleton vibration,  $\sim 1377.5$   $\text{cm}^{-1}$  corresponds to the methylene group from the lipids,  $\sim 1465$   $\text{cm}^{-1}$  assigns to the scissoring vibrations of the  $\text{CH}_2$  groups, i.e., the  $\delta(\text{C-H})$  deformation ascribed to the fatty acid chains,  $2853.3$  and  $3009.2$   $\text{cm}^{-1}$ , specific for the symmetric and asymmetric C-H stretching in the lipids, and  $2923$   $\text{cm}^{-1}$ , related to the asymmetric stretching vibration in the  $\text{CH}_3$  groups.

Additionally, in all examined samples, the UV irradiation did not cause chemical changes that can be visible in the FT-IR spectra (Figure 3).

#### 2.6. Antioxidant Potential of the Liposomes

The antioxidant potential of the *R. canina* seed oil, the empty and oil-loaded liposomes (non-treated and UV-irradiated), was determined using two antioxidant assays, the ABTS and DPPH methods.

As can be seen from Figure 4, the ABTS radical scavenging capacity was  $0.200 \pm 0.001$   $\mu\text{mol}/\text{mL}$  and  $0.215 \pm 0.008$   $\mu\text{mol}/\text{mL}$ , while the  $\text{IC}_{50}$  value was  $0.269 \pm 0.004$   $\text{mg}/\text{mL}$  and  $0.215 \pm 0.006$   $\text{mg}/\text{mL}$  for the non-treated and the UV-irradiated oil-loaded liposomes, respectively. The ABTS and DPPH antioxidant activities of pure oil under the same conditions amounted to  $0.215 \pm 0.010$   $\mu\text{mol}/\text{mL}$  and  $0.150 \pm 0.003$   $\text{mg}/\text{mL}$ , respectively. Thus, it can be concluded that the liposome surroundings did not influence the antioxidant activity of the *R. canina* oil components.

Statistically the significantly higher ABTS radical scavenging potential and the lower  $\text{IC}_{50}$  (higher DPPH radical scavenging activity) for the UV-irradiated sample with rosehip oil can be explained by the fact that the UV irradiation can induce the polymerization of the polyphenol compounds (also present in *R. canina* oil) that can have a higher antioxidant potential, in comparison to the single polyphenols [66].

As was expected, the oil-loaded liposomes have shown a statistically significant antioxidant capacity, compared to the empty liposomes, due to the presence of  $\gamma$ -tocopherol,  $\delta$ -tocopherol, carotenoids, catechins, and phenolic acids at a relatively high level, as well as their synergistic effects that induce a significant antioxidant potential [1,3].



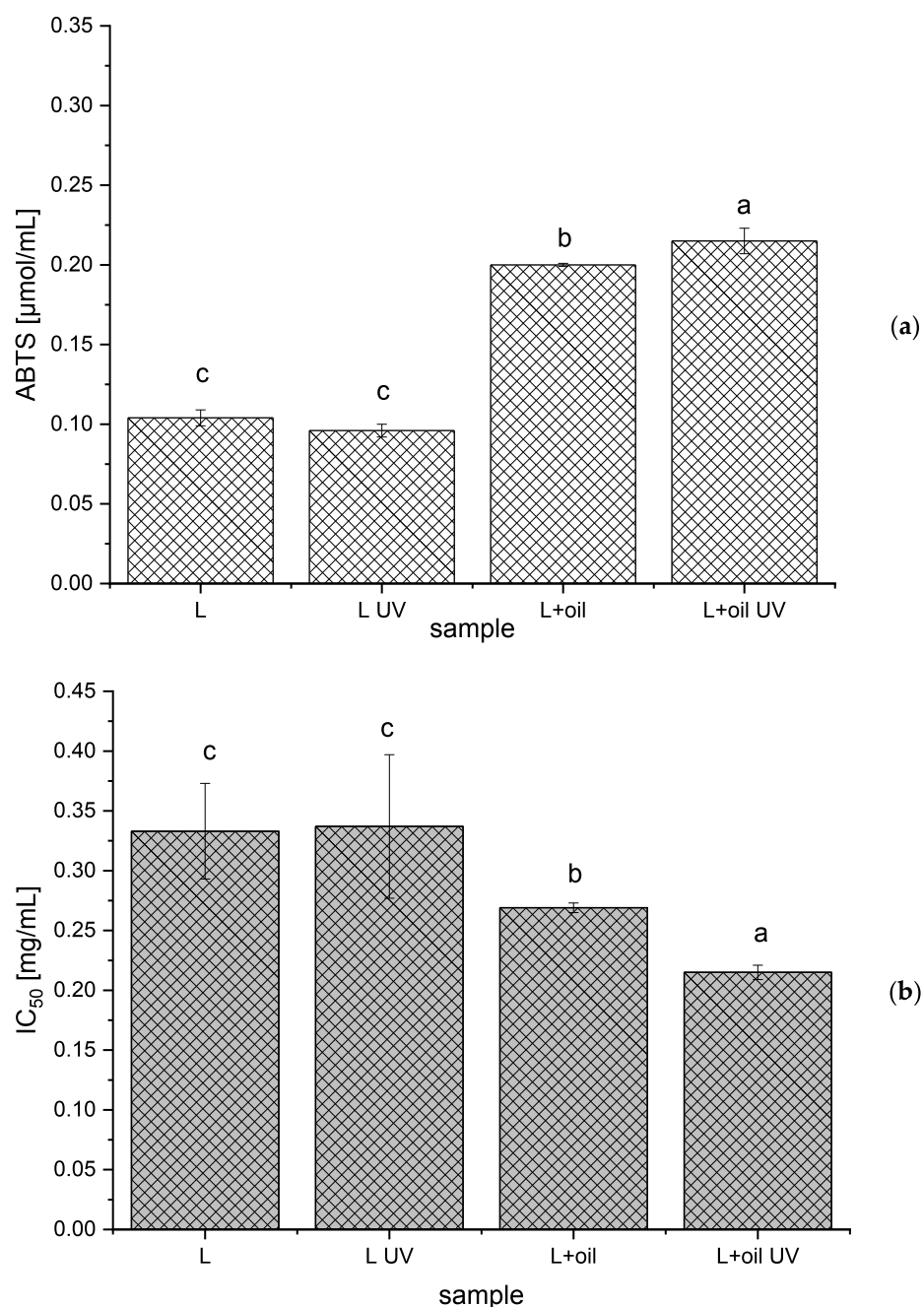


**Figure 4.** Antioxidant capacity of the empty and *Rosa canina* seed oil-loaded liposomes (non-treated and UV-irradiated) obtained in the ABTS (a) and DPPH (b) assays;  $\text{IC}_{50}$ , the concentration of the liposomes required to scavenge 50% of the DPPH radicals; values with different letters (a–c) showed statistically significant differences ( $p < 0.05$ ;  $n = 3$ ; analysis of variance, Duncan's *post-hoc* test).

### 2.7. Antimicrobial Potential of the Liposomes

The antimicrobial effect of rosehip oil and oil-loaded liposomes against *Pseudomonas aeruginosa*, *Klebsiella* spp., *Proteus* spp., *Staphylococcus aureus*, and *Candida albicans*, isolated from wound swabs was investigated. However, neither the *R. canina* seed oil nor the oil-loaded liposomes showed any antimicrobial activity against all investigated microorganisms. The obtained results are in agreement with the literature data where the antibacterial effect of the *R. canina* seed oil prepared using Soxhlet extraction and *n*-hexane was not demonstrated against *P. aeruginosa*, *Staphylococcus* spp., *Lactobacillus plantarum*, *Proteus mirabilis*, *Bacillus cereus*, and *Escherichia coli*, while the methanol sample showed activity

against *E. coli* [67]. According to the literature, the amount of the extracted biologically active substances of rosehip seeds strongly depends on the extraction procedures (Soxhlet, ultrasound-, microwave, sub-, and supercritical fluid extractions) and used conditions (temperature, extraction medium, pressure, time, etc.) [1,52,68]. Namely, Szentmihályi et al. [68] have reported that a higher amount of bioactive compounds was obtained using the supercritical fluid extraction and carbon dioxide/propane, in comparison to Soxhlet, ultrasound-, or microwave-extractions and *n*-hexane. Additionally, a large content of active antimicrobial compounds in the *Rosa* species is probably mainly distributed in pulp, not in seeds. Apart from that, the variation in the oil's chemical composition was also influenced by other environmental factors, including genetic, climatic, ecologic, and the soil conditions for plant growth [1,52].

### 3. Materials and Methods

#### 3.1. Plant Material, Reagents, and Standards

*R. canina* seeds were purchased from the Institute for Medicinal Plants Research “Dr Josif Pančić”, Serbia. The following reagents were used: ethanol (Fisher Scientific, Leicestershire, UK) and Phospholipon 90 G (unsaturated diacyl-phosphatidylcholine) (Lipoid GmbH, Ludwigshafen, Germany), 2,2'-azino-bis(3-ethylbenzothiazoline-6-sulphonic acid)—ABTS, *n*-hexane, Trolox—6-hydroxy-2,5,7,8-tetramethylchroman-2-carboxylic acid, 2,2-diphenyl-1-picrylhydrazyl—DPPH (Sigma Aldrich, St. Louis, MO, USA), and potassium persulfate (Centrohem, Belgrade, Serbia).

#### 3.2. Preparation of the *Rosa Canina* Seed Oil

The oil was extracted from grounded seeds using Soxhlet extraction with *n*-hexane for 6 h at 60 °C. Following the evaporation of the solvent using a IKA RV 05 rotary vacuum evaporator (Staufen, Germany), the oil was stored in the dark at −25 °C.

The chemical characterization of the obtained rosehip seed oil was previously published and the content of the total polyphenols amounted to 0.13 mg of gallic acid equivalents/g, whereas the content of the unsaturated fatty acids was ~90%. The main fatty acid was linoleic (55%), followed by oleic (17.1%),  $\alpha$ -linolenic (18.2%), palmitic (4.2%), stearic, (3.0%), eicosanoic (1.28%), *cis*-11-eicosanoic (0.36%), behenic (0.26%), and *cis*-11,14-eicosadienoic acids (0.14%) [6].

#### 3.3. Preparation of the Liposomal Particles and Lyophilization

The *R. canina* seed oil-loaded liposomes were prepared using the proliposome method [11]. The liposomes were prepared using a mixture of phospholipids (Phospholipon). The phospholipids (2 g), ethanol (2.8 mL), and *R. canina* seed oil (1.2 mL) were stirred at 50 °C. Once cooled to room temperature, the aqueous phase (10 mL) was added in small portions; the emulsion was stirred at 800 rpm for 1 h. The plain liposomes (as a control) were also prepared. In the preliminary screening, the amount of oil in the liposomal preparation was varied (0.5–1.5 mL) and after centrifugation at 17,500 rpm and 4 °C for 45 min in a Thermo Scientific Sorval WX Ultra series ultracentrifuge (Thermo Scientific, Waltham, MA, USA), in the case of the samples prepared using 0.5–1.2 mL of oil, there were no oil drops on the surface of the supernatant. Therefore, 1.2 mL of the oil was selected for the preparation of the future liposomes that were further examined. For the Raman and FT-IR analyses, the lyophilized samples (empty and oil-loaded liposomes before and after the UV irradiation) were prepared as well. Following the centrifugation, the liposomes were frozen in the freezer, LAB11/EL19LT (Elcold, Hobro, Denmark), at −80 °C for 1 h and lyophilized in Beta 2–8 LD plus lyophilizator (Christ, Memmingen, Germany) at −75 °C and 0.011 mbar for 24 h.

#### 3.4. Size, PDI, Zeta Potential, Conductivity, and Mobility Analyses

The particle size, PDI, zeta potential, conductivity, and mobility of the *R. canina* seed oil-loaded liposomes (immediately after the liposome preparation, after the UV irradiation,

and during the 60-day study) were determined using PCS in Zetasizer Nano Series, Nano ZS (Malvern Instruments Ltd., Malvern, UK). Each sample was diluted 200 times and measured three times at 25 °C.

### 3.5. Storage Stability Study

The measurements of the particle size, PDI, zeta potential, conductivity, and mobility of the obtained liposomes were repeated on the 1st, 7th, 14th, 21st, 28th, and 60th day after the preparation of the liposomes. During the 60-day stability study, the liposomal system was stored in the refrigerator at 4 °C.

### 3.6. UV Stability Study

Since the UV irradiation is widely applied commercially for sterilization in food, pharmaceutical, and cosmetic industries, the plain and oil-loaded liposomes (3 mL in a thin layer) were exposed to UV-C irradiation (253.7 nm) in a Petri dish for 30 min [69]; subsequently, the size, PDI, zeta potential, conductivity, mobility, density, surface tension, viscosity, Raman and FT-IR analyses were performed. Additionally, the UV-irradiated samples were analyzed in terms of their biological activities (antioxidant and antimicrobial effects).

### 3.7. Density, Surface Tension, and Viscosity Analyses

The density and surface tension of pure the *R. canina* seed oil, empty and oil-loaded liposomes (non-treated and UV-irradiated) were determined using silicon crystal as the immersion body and a Wilhelmy plate, respectively, in Force Tensiometer K20 (Kruss, Hamburg, Germany). Each sample (20 mL) was examined three times at 25 °C.

The viscosity of the pure *R. canina* seed oil, the empty, and the oil-loaded liposomes (non-treated and UV-irradiated) were examined using a Rotavisc lo-vi device equipment with a VOL-C-RTD chamber, VOLS-1 adapter, and spindle (IKA, Staufen, Germany). Each sample (6.7 mL) was examined three times at 25 °C.

The measurements of the density, surface tension, and viscosity were performed on the 1st and 60th days.

### 3.8. Raman and FT-IR Analyses

The micro-Raman spectra of the pure Phospholipon, the *R. canina* seed oil, the liquid and lyophilized plain and oil-loaded liposomes (non-treated and UV-irradiated samples) were collected in a backscattering configuration using a Jobin-Yvon T64000 triple spectrometer equipped with a nitrogen-cooled charge-coupled device detector (HORIBA Scientific, Kyoto, Japan). The spectral resolution was 2 cm<sup>-1</sup> and the accuracy for all measured wavenumbers was ±3 cm<sup>-1</sup>. The spectra have been excited by a 514.5 nm line of Ar<sup>+</sup>/Kr<sup>+</sup> ion laser with an output power of less than 2 mW to avoid the heating effects and/or sample thermal degradation.

The FT-IR spectra of the pure Phospholipon, *R. canina* seed oil, and lyophilized empty and oil-loaded liposomes (non-treated and UV-irradiated samples) were recorded in the transmission mode between 400 and 4000 cm<sup>-1</sup>, using a Nicolet iS10 spectrometer (Thermo Scientific, Gothenburg, Sweden).

### 3.9. Antioxidant Assays

#### 3.9.1. ABTS Assay

The ABTS method is based on the reduction of the ABTS●<sup>+</sup> radical in an ethanol solution by antioxidants [70]. A mixture of the ABTS solution and 88 μL of a potassium persulfate solution was left to react for 24 h at 4 °C. Subsequently, 2 mL of the ABTS●<sup>+</sup> solution was added to 20 μL of the liposomal samples (non-treated and UV-irradiated empty and oil-loaded liposomes). The free radical scavenging activity of the liposomes was evaluated by measuring the absorbance at 734 nm, after 6 min of incubation in the dark, compared to the blank and calculated as  $\Delta A = A_c - A_x$  ( $A_c$ —the absorbance of ABTS●<sup>+</sup> solution and water;  $A_x$ —the absorbance of ABTS●<sup>+</sup> solution and liposomes). All analyses

were carried out in triplicate and the radical scavenging capacity was expressed as mmol Trolox equivalents per milliliter of the liposomal sample ( $\mu\text{mol}/\text{mL}$ ), using the calibration curve of Trolox (0.2–1 mM).

### 3.9.2. DPPH Assay

The antioxidant activity of the non-treated and UV-irradiated empty and *R. canina* oil-loaded liposomes, in terms of hydrogen donating or radical scavenging ability using the stable DPPH radical, was examined as well [70]. All measurements were performed as follows: the amount of 200  $\mu\text{L}$  of five different concentrations of liposomes was added to 2.8 mL of the DPPH radical solution and the absorbance readings were taken after 20 min against the blank at 517 nm. The antioxidant capacity was calculated using the following equation: radical scavenging capacity (%) =  $(A_c - A_x) \cdot 100 / A_c$  ( $A_c$ —the absorbance of the DPPH solution and water;  $A_x$ —the absorbance of the DPPH solution and different liposomal concentrations). The results, obtained from triplicate analyses, were expressed as the concentration of the liposomes required to scavenge 50% of the free radicals,  $\text{IC}_{50}$  (mg/mL).

All absorbance readings were performed on a UV spectrophotometer, UV-1800 (Shimadzu, Kyoto, Japan).

### 3.10. Antimicrobial Analysis

The antimicrobial potential of the *R. canina* seed oil and the oil-loaded liposomes was investigated using three Gram-negative bacteria (*P. aeruginosa*, *Klebsiella* spp., and *Proteus* spp.), one Gram-positive bacteria (*S. aureus*), and one fungus (*C. albicans*), all isolated from wound swabs in the microbiology laboratory of the Institute for the Application of Nuclear Energy, INEP, Belgrade, Serbia. The antimicrobial activity was examined using the disk diffusion method [71]. The cultivation of the microorganisms was performed aerobically for 24 h on blood agar (for bacteria) and 48 h on Sabouraud agar (for fungus). The microorganism was incubated at 37 °C. The inoculum was prepared to an optical density of 0.5 McFarland ( $1.5 \times 10^8$  CFU/mL) and the inoculum was spread on Petri dishes with Mueller Hinton agar (for bacteria) or Sabouraud agar (for fungus). Subsequently, 75  $\mu\text{L}$  of the samples were transferred to the wells made in agar and incubated aerobically for 24 h at 37 °C. The criterion for detecting the inhibitory activity was the inhibition zone diameter.

### 3.11. Statistical Analysis

In the present study, the statistical analysis was performed using the analysis of variance (one-way ANOVA) followed by Duncan's *post hoc* test, using the statistical software, STATISTICA 7.0. The differences were considered statistically significant at  $p < 0.05$ ,  $n = 3$ .

## 4. Conclusions

Rosehip seed oil, as a valuable source of natural bioactive compounds, was encapsulated in phospholipid liposomes prepared using the proliposome technique. The vesicle sizes of the oil-loaded liposomes did not change significantly during the 60 days of storage, while a slight increase in the PDI values was noticed. The zeta potential and mobility varied in all liposomal populations, but the trend depended on the absence or the presence of rosehip oil and the UV irradiation. The conductivity of all liposomes significantly decreased during the 60-day stability study. The values of the density and surface tension of the oil-loaded liposomes did not change after 60 days, while the viscosity significantly decreased. Due to the possible synergistic beneficial effects of phospholipids and *R. canina* seed oil on human skin, the liposomal particles developed in the present study can find application in different cosmetic or pharmaceutical products. Since rosehip oil has shown a beneficial effect on the skin regeneration in traditional medicine, while the antimicrobial and significant antioxidant potential of the oil-loaded liposomes did not show in the present research, future studies should focus on the *in vitro* effects of the *R. canina* oil preparations on the migration and proliferation of skin cells in a wound scratch healing model.

**Supplementary Materials:** The following supporting information can be downloaded at: <https://www.mdpi.com/article/10.3390/molecules28010276/s1>, Figure S1. Liposome size—bars and polydispersity index—numbers above the bars (a) and zeta potential—bars, mobility ( $\mu\text{mcm/Vs}$ )—numbers above the bars, and conductivity—table (b) of the non-treated and UV-irradiated plain liposomes during the 60 days of storage at 4 °C; values with different letters (a–d) in each row showed statistically significant differences ( $p < 0.05$ ;  $n = 3$ ; analysis of variance, Duncan's *post-hoc* test); L, liposomes; Figure S2. Raman spectra of the non-treated and UV-irradiated plain liposomes (liquid and lyophilized) in the spectral range from 70 to 3400  $\text{cm}^{-1}$ .

**Author Contributions:** Conceptualization, A.A.J.; Formal analysis, A.A.J.; Funding acquisition, K.Š.; Investigation, A.A.J.; Methodology, A.A.J., D.Č., B.S., N.Č. and J.Ž.; Software, A.A.J.; Supervision, K.Š.; Writing—original draft, A.A.J.; Writing—review & editing, J.Ž. and K.Š. All authors have read and agreed to the published version of the manuscript.

**Funding:** This research was supported by the project EthnoHERBS-H2020-MSCA-RISE-2018 under grant agreement No. 823973. The authors also acknowledge their gratitude to the Ministry of Education, Science and Technological Development of Serbia, contract numbers 451-03-68/2022-14/200003, 451-03-68/2022-14/200007, and 451-03-68/2022-14/200019.

**Institutional Review Board Statement:** Not applicable.

**Informed Consent Statement:** Not applicable.

**Data Availability Statement:** The datasets generated during and/or analyzed during the current study are available from the corresponding author upon reasonable request.

**Acknowledgments:** The authors would like to pay special thanks to Dejan Radoičić and Dragan Stojanić, Institute for the Application of Nuclear Energy INEP, University of Belgrade, for performing the antimicrobial analyses and lyophilization, respectively.

**Conflicts of Interest:** The authors declare that they have no financial and commercial conflicts of interest.

**Sample Availability:** Not available.

## References

1. Mármol, I.; Sánchez-de-Diego, C.; Jiménez-Moreno, N.; Ancín-Azpilicueta, C.; Rodríguez-Yoldi, M.J. Therapeutic applications of rose hips from different *Rosa* species. *Int. J. Mol. Sci.* **2017**, *18*, 1137. [[CrossRef](#)] [[PubMed](#)]
2. Khan, I.A.; Abourashed, E.A. *Leung's Encyclopedia of Common Natural Ingredients Used in Food, Drugs, and Cosmetics*; John Wiley & Sons, Inc.: Hoboken, NJ, USA, 2010.
3. Grajzer, M.; Prescha, A.; Korzonek, K.; Wojakowska, A.; Dziadas, M.; Kulma, A.; Grajeta, H. Characteristics of rose hip (*Rosa canina* L.) cold-pressed oil and its oxidative stability studied by the differential scanning calorimetry method. *Food Chem.* **2015**, *188*, 459–466. [[CrossRef](#)] [[PubMed](#)]
4. Ilyasoğlu, H. Characterization of rosehip (*Rosa canina* L.) seed and seed oil. *Int. J. Food Prop.* **2014**, *17*, 1591–1598. [[CrossRef](#)]
5. Ozcan, M. Nutrient composition of rose (*Rosa canina* L.) seed and oils. *J. Med. Food* **2002**, *5*, 137–140. [[CrossRef](#)] [[PubMed](#)]
6. Mudrić, J.; Drinić, Z.; Zdunić, G.; Todosijević, M.; Bigović, D.; Menković, N.; Šavikin, K. Stabilization of rose hip oil by pomegranate peel extract during accelerated storage. *J. Serb. Chem. Soc.* **2020**, *85*, 1553–1563. [[CrossRef](#)]
7. Butnaru, E.; Stoleru, E.; Brebu, M.A.; Darie-Nita, R.N.; Bargan, A.; Vasile, C. Chitosan-based bionanocomposite films prepared by emulsion technique for food preservation. *Materials* **2019**, *12*, 373. [[CrossRef](#)]
8. Shabykin, G.P.; Godorazhi, A.I. A polyvitamin preparation of fat-soluble vitamins (carotolin) and rose hip oil in the treatment of certain dermatoses. *Vestn. Dermatol. I Venerol.* **1967**, *41*, 71–73.
9. Çorapci, B. The effect of rosehip seed oil nanoemulsion on some physical, chemical, and microbiological properties of sea bass fillets stored at  $4 \pm 1$  °C. *J. Aquat. Food Prod. Technol.* **2022**, *31*, 672–685. [[CrossRef](#)]
10. Chong, Y.M.; Chang, S.K.; Sia, W.C.M.; Yim, H.S. Antioxidant efficacy of mangosteen (*Garcinia mangostana* Linn.) peel extracts in sunflower oil during accelerated storage. *Food Biosci.* **2015**, *12*, 18–25. [[CrossRef](#)]
11. Isailović, B.; Kostić, I.; Zvonar, A.; Đorđević, V.; Gašperlin, M.; Nedović, V.; Bugarski, B. Resveratrol loaded liposomes produced by different techniques. *Innov. Food Sci. Emerg. Technol.* **2013**, *19*, 181–189. [[CrossRef](#)]
12. Jovanović, A.A.; Balanč, B.D.; Djordjević, V.B.; Ota, A.; Skrt, M.; Šavikin, K.P.; Bugarski, B.M.; Nedović, V.A.; Ulrih, N.P. Effect of gentisic acid on the structural-functional properties of liposomes incorporating  $\beta$ -sitosterol. *Colloids Surf. B Biointerfaces* **2019**, *183*, 110422. [[CrossRef](#)] [[PubMed](#)]
13. Mozafari, M.; Johanson, C.; Hatziantoniou, S.; Demetzos, C. Nanoliposomes and their applications in food nanotechnology. *J. Liposome Res.* **2008**, *18*, 309–327. [[CrossRef](#)]

14. Taylor, T.; Davidson, P.; Bruce, D.; Weiss, J. Liposomal nanocapsules in food science and agriculture. *Crit. Rev. Food Sci. Nutr.* **2005**, *45*, 587–605. [[CrossRef](#)] [[PubMed](#)]
15. Jovanović, A.A.; Balanč, B.D.; Ota, A.; Ahlin Grabnar, P.; Djordjević, V.B.; Šavikin, K.P.; Bugarski, B.M.; Nedović, V.A.; Ulrih, N.P. Comparative effects of cholesterol and  $\beta$ -sitosterol on the liposome membrane characteristics. *Eur. J. Lipid Sci. Technol.* **2018**, *120*, 1–11. [[CrossRef](#)]
16. Desai, K.; Park, H. Recent developments in microencapsulation of food ingredients. *Dry. Technol.* **2005**, *23*, 1361–1394. [[CrossRef](#)]
17. Jash, A.; Ubeyitogullari, A.; Rizvi, S.S.H. Liposomes for oral delivery of protein and peptide-based therapeutics: Challenges, formulation strategies, and advances. *J. Mater. Chem. B* **2021**, *9*, 4773–4792. [[CrossRef](#)]
18. Lee, M.-K. Liposomes for enhanced bioavailability of water-insoluble drugs. *In Vivo Evid. Recent Approaches Pharm.* **2020**, *12*, 264. [[CrossRef](#)]
19. Shade, C.W. Liposomes as advanced delivery systems for nutraceuticals. *Integr. Med.* **2016**, *15*, 33–36.
20. Seguin, J.; Brulle, L.; Boyer, R.; Lu, Y.M.; Ramos, R.M.; Touil, Y.S.; Scherman, D.; Bessodes, M.; Mignet, N.; Chabot, G.G. Liposomal encapsulation of the natural flavonoid fisetin improves bioavailability and antitumor efficacy. *Int. J. Pharm.* **2013**, *444*, 146–154. [[CrossRef](#)]
21. Yuan, Z.P.; Chen, L.J.; Fan, L.Y.; Tang, M.H.; Yang, G.L.; Yang, H.S.; Du, X.B.; Wang, G.Q.; Yao, W.X.; Zhao, Q.M. Liposomal quercetin efficiently suppresses growth of solid tumors in murine models. *Clin. Cancer Res.* **2006**, *12*, 3193–3199. [[CrossRef](#)]
22. Wagner, A.; Vorauer-Uhl, K. Liposome technology for industrial purposes. *J. Drug Deliv.* **2011**, *2011*, 591325. [[CrossRef](#)] [[PubMed](#)]
23. Šeremet, D.; Štefančić, M.; Petrović, P.; Kuzmić, S.; Doroci, S.; Mandura Jarić, A.; Vojvodić Cebin, A.; Pjanović, R.; Komes, D. Development, characterization and incorporation of alginate-plant protein covered liposomes containing ground ivy (*Glechoma hederacea* L.) extract into candies. *Foods* **2022**, *11*, 1816. [[CrossRef](#)] [[PubMed](#)]
24. Batinić, P.; Đorđević, V.; Stevanović, S.; Balanč, B.; Marković, S.; Luković, N.; Mijin, D.; Bugarski, B. Formulation and characterization of novel liposomes containing histidine for encapsulation of a poorly soluble vitamin. *J. Drug Deliv. Sci. Technol.* **2020**, *59*, 101920. [[CrossRef](#)]
25. Di Foggia, M.; Bonora, S.; Tinti, A.; Tugnoli, V. DSC and Raman study of DMPC liposomes in presence of Ibuprofen at different pH. *J. Therm. Anal. Calorim.* **2017**, *127*, 1407–1417. [[CrossRef](#)]
26. Frías, M.A.; Díaz, S.B.; Ale, N.M.; Altabef, B.; Disalvo, E.A. FTIR analysis of the interaction of arbutin with dimyristoyl phosphatidylcholine in anhydrous and hydrated states. *BBA-Biomembrane* **2006**, *1758*, 1823–1829. [[CrossRef](#)] [[PubMed](#)]
27. Kočišová, E.; Antalík, A.; Procházka, M. Drop coating deposition Raman spectroscopy of liposomes: Role of cholesterol. *Chem. Phys. Lipids* **2013**, *172–173*, 1–5. [[CrossRef](#)]
28. Šeremet, D.; Vugrinec, K.; Petrović, P.; Butorac, A.; Kuzmić, S.; Vojvodić Cebin, A.; Mandura, A.; Lovrić, M.; Pjanović, R.; Komes, D. Formulation and characterization of liposomal encapsulated systems of bioactive ingredients from traditional plant mountain germander (*Teucrium montanum* L.) for the incorporation into coffee drinks. *Food Chem.* **2022**, *370*, 131257. [[CrossRef](#)]
29. Allaw, M.; Manconi, M.; Caboni, P.; Bacchett, G.; Escribano-Ferrer, E.; Esteban Peris, J.; Nacher, A.; Diez-Sales, O.; Letizia Manca, M. Formulation of liposomes loading lentisk oil to ameliorate topical delivery, attenuate oxidative stress damage and improve cell migration in scratch assay. *Biomed. Pharmacother.* **2021**, *144*, 112351. [[CrossRef](#)]
30. Song, F.; Tian, S.; Yang, G.; Sun, X. Effect of phospholipid/flaxseed oil ratio on characteristics, structure change, and storage stability of liposomes. *LWT* **2022**, *157*, 113040. [[CrossRef](#)]
31. Huang, J.; Wang, Q.; Chu, L.; Xi, Q. Liposome-chitosan hydrogel bead delivery system for the encapsulation of linseed oil and quercetin: Preparation and in vitro characterization studies. *LWT* **2020**, *117*, 108615. [[CrossRef](#)]
32. Fathi-Azarbayjani, A.; Jouyban, A.; Yung Chan, S. Impact of surface tension in pharmaceutical sciences. *J. Pharm. Pharmaceut. Sci.* **2009**, *12*, 218–228. [[CrossRef](#)] [[PubMed](#)]
33. Ardani, H.K.; Imawan, C.; Handayani, W.; Djuhana, D.; Harmoko, A.; Fauzia, V. Enhancement of the stability of silver nanoparticles synthesized using aqueous extract of *Diospyros discolor* Willd. leaves using polyvinyl alcohol. *IOP Conf. Ser. Mater. Sci. Eng.* **2017**, *188*, 012056. [[CrossRef](#)]
34. Zhao, L.; Temelli, F.; Curtis, J.; Chen, L. Preparation of liposomes using supercritical carbon dioxide technology: Effects of phospholipids and sterols. *Food Res. Int.* **2015**, *77*, 63–72. [[CrossRef](#)]
35. Arias-Alpizar, G.; Kong, L.; Vlieg, R.C.; Rabe, A.; Papadopoulou, P.; Meijer, M.S.; Bonnet, S.; Vogel, S.; van Noort, J.; Kros, A.; et al. Light-triggered switching of liposome surface charge directs delivery of membrane impermeable payloads in vivo. *Nat. Commun.* **2020**, *11*, 3638. [[CrossRef](#)] [[PubMed](#)]
36. Bhattacharya, S.; Haldar, S. Interactions between cholesterol and lipids in bilayer membranes. Role of lipid headgroup and hydrocarbon chain-backbone linkage. *Biochim. Et Biophys. Acta-Biomembr.* **2000**, *1467*, 39–53. [[CrossRef](#)]
37. Briuglia, M.-L.; Rotella, C.; McFarlane, A.; Lamprou, D. Influence of cholesterol on liposome stability and on in vitro drug release. *Drug Deliv. Transl. Res.* **2015**, *5*, 231–242. [[CrossRef](#)]
38. Lee, S.-C.; Lee, K.-E.; Kim, J.-J.; Lim, S.-H. The Effect of cholesterol in the liposome bilayer on the stabilization of incorporated retinol. *J. Liposome Res.* **2005**, *15*, 157–166. [[CrossRef](#)]
39. Ricci, M.; Olivia, R.; Del Vecchio, P.; Paolantoni, M.; Moressi, A.; Sassi, P. DMSO-induced perturbation of thermotropic properties of cholesterol-containing DPPC liposomes. *Biochim. Et Biophys. Acta-Biomembr.* **2016**, *1858*, 3024–3031. [[CrossRef](#)]
40. Surianarayanan, R.; Gurumallappa Shivakumar, H.; Vegesna, N.S.K.V.; Srivastava, A. Effect of sample Concentration on the Characterization of Liposomes using Dynamic light Scattering Technique. *Pharm. Methods* **2016**, *7*, 1–5. [[CrossRef](#)]

41. Lidgate, D.; Hegde, S.; Maskiewicz, R. Conductivity measurement as a convenient technique for determination of liposome capture volume. *Int. J. Pharm.* **1993**, *96*, 51–58. [[CrossRef](#)]
42. Froude, V.E.; Zhu, Y. Dielectrophoresis of functionalized lipid unilamellar vesicles (liposomes) with contrasting surface constructs. *J. Phys. Chem. B* **2009**, *113*, 1552–1558. [[CrossRef](#)] [[PubMed](#)]
43. Zhang, X.; Julien-David, D.; Miesch, M.; Raul, F.; Geoffroy, P.; Aoude-Werner, D.; Ennahar, S.; Marchioni, E. Quantitative analysis of beta-sitosterol oxides induced in vegetable oils by natural sunlight, artificially generated light, and irradiation. *J. Agric. Food Chem.* **2006**, *54*, 5410–5415. [[CrossRef](#)] [[PubMed](#)]
44. Temprana, C.F.; Amor, M.S.; Femia, A.L.; Gasparri, J.; Taira, M.C.; del Valle Alonso, S. Ultraviolet irradiation of diacetylenic liposomes as a strategy to improve size stability and to alter protein binding without cytotoxicity enhancement. *J. Liposome Res.* **2011**, *21*, 141–150. [[CrossRef](#)] [[PubMed](#)]
45. Dluhy, R.A.; Wright, N.A.; Griffiths, P.R. In situ measurement of the FT-IR spectra of phospholipid monolayers at the air/water interface. *Appl. Spectrosc.* **1988**, *42*, 138–141. [[CrossRef](#)]
46. Erami, S.R.; Amiri, Z.R.; Jafari, S.M. Nanoliposomal encapsulation of bitter melon (*Momordica charantia*) fruit extract as a rich source of health-promoting bioactive compounds. *LWT-Food Sci. Technol.* **2019**, *116*, 108581. [[CrossRef](#)]
47. Arsov, Z.; Quaroni, L. Direct interaction between cholesterol and phosphatidylcholines in hydrated membranes revealed by ATR-FTIR spectroscopy. *Chem. Phys. Lipids* **2007**, *150*, 35–48. [[CrossRef](#)]
48. Chen, C.; Tripp, C.P. A comparison of the behavior of cholesterol, 7-dexydrocholesterol and ergosterol in phospholipid membranes. *Biochim. Biophys. Acta* **2012**, *1818*, 1673–1681. [[CrossRef](#)]
49. Farid Uddin, S.; Farhad, K.M.; Abedin, M.; Islam, R.; Talukder, A.I.; Haider, A.F.M.Y. Determination of ratio of unsaturated to total fatty acids in edible oils by laser Raman spectroscopy. *J. Appl. Sci.* **2009**, *9*, 1538–1543.
50. Vaskova, H.; Buckova, M. Measuring and identification of oils. In Proceedings of the 18th International Conference on Systems, Santorini Island, Greece, 14–17 October 2014; pp. 211–215.
51. Nowak, R. Fatty acids composition in fruits of wild rose species. *Acta Soc. Bot. Pol.* **2005**, *74*, 229. [[CrossRef](#)]
52. Turan, S.; Solak, R.; Kiralan, M.; Ramadan, M.F. Bioactive lipids, antiradical activity and stability of rosehip seed oil under thermal and photo-induced oxidation. *Grasas Y Aceites* **2018**, *69*, e2482018. [[CrossRef](#)]
53. Vasić, D.; Špirović Trifunović, B.; Pećinar, I.; Paunović, D.; Popović-Djordjević, J. Chemical characterization of *Rosa canina* L. rosehip seed: Application of Raman spectroscopy and gas chromatography. *Biol. Life Sci. Forum* **2021**, *3*, 50. [[CrossRef](#)]
54. De Gelder, J.; De Gussem, K.; Vandenabeele, P.; Moens, L. Reference database of Raman spectra of biological molecules. *J. Raman Spectrosc.* **2007**, *38*, 1133–1147. [[CrossRef](#)]
55. Martini, W.S.; Porto, B.L.S.; de Oliveira, M.A.L.; Sant’Ana, A.C. Comparative study of the lipid profiles of oils from kernels of peanut, babassu, coconut, castor and grape by GC-FID and Raman spectroscopy. *J. Braz. Chem. Soc.* **2018**, *29*, 390–397. [[CrossRef](#)]
56. Qiu, J.; Hou, H.-Y.; Yang, I.-S.; Chen, X.-B. Raman spectroscopy analysis of free fatty acid in olive oil. *Appl. Sci.* **2019**, *9*, 4510. [[CrossRef](#)]
57. Renwick Beattie, J.; Maguire, C.; Gilchrist, S.; Barrett, L.J.; Cross, C.E.; Possmayer, F.; Ennis, M.; Elborn, J.S.; Curry, W.J.; McGarvey, J.J.; et al. The use of Raman microscopy to determine and localize vitamin E in biological samples. *FASEB J.* **2007**, *21*, 766–776. [[CrossRef](#)]
58. Schulz, H.; Baranska, M. Identification and quantification of valuable plant substances by IR and Raman spectroscopy. *Vib. Spectrosc.* **2007**, *43*, 13–25. [[CrossRef](#)]
59. Hosseini, S.M.; Abbasalipourkabir, R.; Jalilian, F.A.; Asl, S.S.; Farmany, A.; Roshanaei, G.; Arabestani, M.R. Doxycycline-encapsulated solid lipid nanoparticles as promising tool against *Brucella melitensis* enclosed in macrophage: A pharmacodynamics study on J774A.1 cell line. *Antimicrob. Resist.* **2019**, *8*, 62. [[CrossRef](#)]
60. Pohle, W.; Gauger, D.R.; Fritzsche, H.; Rattay, B.; Selle, C.; Binder, H.; Böhling, H. FTIR-spectroscopic characterization of phosphocholine-headgroup model compounds. *J. Mol. Struct.* **2001**, *563–564*, 463–467. [[CrossRef](#)]
61. Pawlikowska-Pawłęga, B.; Misiak, L.; Zarzyka, B.; Paduch, R.; Gawron, A.; Gruszecki, W. FTIR, <sup>1</sup>H NMR and EPR spectroscopy studies on the interaction of flavone apigenin with dipalmitoylphosphatidylcholine liposomes. *Biochim. Et Biophys. Acta* **2012**, *1828*, 518–527. [[CrossRef](#)]
62. Veisi, H.; Rashtiani, A.; Barjasteh, V. Biosynthesis of palladium nanoparticles using *Rosa canina* fruit extract and their use as a heterogeneous and recyclable catalyst for Suzuki-Miyaura coupling reactions in water. *Appl. Organometal Chem.* **2016**, *30*, 231–235. [[CrossRef](#)]
63. Shi, L.; Liu, Z.; Li, J.; Qin, Z. Analysis of edible vegetable oils by infrared absorption spectrometry. *Adv. Eng. Res.* **2017**, *86*, 286–289.
64. Jovanović, A.; Lević, S.; Pavlović, V.; Marković, S.; Pjanović, R.; Djordjević, V.; Nedović, V.; Bugarski, B. Freeze versus spray drying for dry wild thyme (*Thymus serpyllum* L.) extract formulations: The impact of gelatin as a coating material. *Molecules* **2021**, *26*, 3933. [[CrossRef](#)] [[PubMed](#)]
65. Medina-Torres, L.; Santiago-Adame, R.; Calderas, F.; Gallegos-Infante, J.A.; González-Laredo, R.F.; Rocha-Guzmán, N.E.; Núñez-Ramírez, D.M.; Bernad-Bernad, M.J.; Meterc, D.; Petermann, M.; et al. Extraction of green tea and drying with a high pressure spray process. *Hem. Ind.* **2007**, *61*, 222–228. [[CrossRef](#)]
66. Behboodi-Sadabad, F.; Zhang, H.; Trouillet, V.; Welle, A.; Plumeré, N.; Levkin, P. UV-triggered polymerization, deposition, and patterning of plant phenolic compounds. *Adv. Funct. Mater.* **2017**, *27*, 1700127. [[CrossRef](#)]

67. Kumarasamy, Y.; Cox, P.; Jaspars, M.; Nahar, L.; Sarker, S.D. Screening seeds of Scottish plants for antibacterial activity. *J. Ethnopharmacol.* **2002**, *83*, 73–77. [[CrossRef](#)]
68. Szentmihályi, K.; Vinkler, P.; Lakatos, B.; Illés, V.; Then, M. Rose hip (*Rosa canina* L.) oil obtained from waste hip seeds by different extraction methods. *Bioresour. Technol.* **2002**, *82*, 195–201. [[CrossRef](#)]
69. Delorme, M.; Guimarães, J.; Coutinho, N.; Balthazar, C.; Roch, R.; Silva, R.; Margalho, L.; Pimentel, T.; Silva, M.; Freitas, M.; et al. Ultraviolet radiation: An interesting technology to preserve quality and safety of milk and dairy foods. *Trends Food Sci. Technol.* **2020**, *102*, 146–154. [[CrossRef](#)]
70. Jovanović, A.; Djordjević, V.; Petrović, P.; Pljevljakušić, D.; Zdunić, G.; Šavikin, K.; Bugarski, B. The influence of different extraction conditions on polyphenol content, antioxidant and antimicrobial activities of wild thyme. *J. Appl. Res. Med. Aromat. Plants* **2021**, *25*, 100328. [[CrossRef](#)]
71. Borotová, P.; Galovičová, L.; Valková, V.; Ďúranová, H.; Vuković, N.; Vukić, M.; Babošová, M.; Kačániová, M. Biological activity of essential oil from *Foeniculum vulgare*. *Acta Hort. Et Regiotect.* **2021**, *24*, 148–152. [[CrossRef](#)]

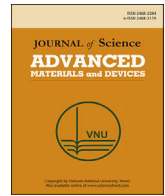
**Disclaimer/Publisher’s Note:** The statements, opinions and data contained in all publications are solely those of the individual author(s) and contributor(s) and not of MDPI and/or the editor(s). MDPI and/or the editor(s) disclaim responsibility for any injury to people or property resulting from any ideas, methods, instructions or products referred to in the content.





Contents lists available at ScienceDirect

Journal of Science: Advanced Materials and Devices

journal homepage: [www.elsevier.com/locate/jsamd](http://www.elsevier.com/locate/jsamd)

Original Article

# Spin-phonon interaction in nanocrystalline Dy<sub>3</sub>Fe<sub>5</sub>O<sub>12</sub> probed by Raman spectroscopy: Effects of magnetic ordering

Bojan Stojadinović<sup>a, \*</sup>, Zorana Dohčević-Mitrović<sup>a, \*\*</sup>, Sonja Aškračić<sup>a</sup>, Novica Paunović<sup>a</sup>, M.T. Rahul<sup>b</sup>, B. Raneesh<sup>b</sup>, Nandakumar Kalarikkal<sup>c, d</sup>

<sup>a</sup> Institute of Physics Belgrade, University of Belgrade, Pregrevica 118, 11080, Belgrade, Serbia

<sup>b</sup> Department of Physics, Catholicate College, Pathanamthitta, Kerala, 689 645, India

<sup>c</sup> School of Pure and Applied Physics, Mahatma Gandhi University, Kottayam, 686 560, India

<sup>d</sup> International & Inter University Centre for Nanoscience and Nanotechnology, Mahatma Gandhi University, Kottayam, Kerala, 686 560, India

## ARTICLE INFO

### Article history:

Received 2 February 2023

Received in revised form

24 May 2023

Accepted 27 June 2023

Available online 7 July 2023

### Keywords:

Rare-earth iron garnets

Dy<sub>3</sub>Fe<sub>5</sub>O<sub>12</sub> nanoparticles

Raman spectroscopy

Spin-phonon interaction

## ABSTRACT

We report the effects of magnetic ordering on the temperature evolution of the Raman modes in nanocrystalline Dy<sub>3</sub>Fe<sub>5</sub>O<sub>12</sub>. The Dy<sub>3</sub>Fe<sub>5</sub>O<sub>12</sub> was synthesized by an aqueous sol–gel method. X-ray diffraction, Raman spectroscopy and transmission electron microscopy studies revealed the phase purity and nanocrystalline nature. We particularly focused on the spin-phonon coupling mechanism in Dy<sub>3</sub>Fe<sub>5</sub>O<sub>12</sub>, as this interaction can greatly affect the magnetoelectric and multiferroic properties of Dy<sub>3</sub>Fe<sub>5</sub>O<sub>12</sub>. Below *T<sub>C</sub>*, four phonon modes from the middle- and high-frequency regions displayed anomalous behavior, which was ascribed to the spin-phonon interaction. The application of the mean-field approach enabled us to quantify the spin-phonon coupling strength for each of these phonon modes. Our study has shown that different phonon modes are coupled to ferromagnetic or antiferromagnetic ordering depending on the type of vibrational motion characteristic for a specific mode. These results significantly enhance the understanding of the complex spin-phonon coupling mechanism and its implications on the multifaceted properties of nanocrystalline Dy<sub>3</sub>Fe<sub>5</sub>O<sub>12</sub>, such as multiferroic, magnetoelectric, and magnetocaloric properties. Moreover, these findings have the potential to drive advancements in the optimization and development of spintronic devices.

© 2023 Vietnam National University, Hanoi. Published by Elsevier B.V. This is an open access article under the CC BY-NC-ND license (<http://creativecommons.org/licenses/by-nc-nd/4.0/>).

## 1. Introduction

Ferrimagnetic rare earth (RE) iron garnets, with general formula RE<sub>3</sub>Fe<sub>5</sub>O<sub>12</sub>, present an important class of magnetic insulators due to their interesting magnetic properties, such as the formation of canted magnetic (double umbrella-like) structure and the huge magnetostriction at low temperatures [1]. Interesting magneto-optical properties [2–4], low magnetic losses in the microwave region, and the appearance of a magnetocaloric effect [5] made them attractive materials for magneto-optic devices, microwave circuits, or magnetic refrigeration applications. The discovery of the magneto-electric and magnetodielectric effects in RE iron garnets

renewed the interest in these materials [6]. In recent years, the possibility of tailoring magnetic properties by changing the material morphology and reducing the grain size to nanometric dimensions focused the research interest towards the nanocrystalline forms of RE iron garnets. These materials, with peculiar magnetic properties, are expected to be particularly useful for the low-temperature refrigeration and spintronic applications [5,7,8].

Among the RE iron garnets, dysprosium iron garnet (Dy<sub>3</sub>Fe<sub>5</sub>O<sub>12</sub>) exhibits numerous attractive physical properties, such as huge magnetostriction [1] and magnetic and magneto-optical properties [9,10]. The observed anisotropic magnetodielectric, magnetocaloric, and magnetoelectric effects [11–14] imply that Dy<sub>3</sub>Fe<sub>5</sub>O<sub>12</sub> may be a promising material for the applications in various novel magnetodielectric, magnetocaloric, and spintronic functional devices in future [15].

In RE iron garnets, due to the complexity of magnetic interactions, the coupling between the spin and lattice vibrations can greatly influence their magnetic, magnetocaloric or

\* Corresponding author.

\*\* Corresponding author.

E-mail addresses: [bojans@ipb.ac.rs](mailto:bojans@ipb.ac.rs) (B. Stojadinović), [zordoh@ipb.ac.rs](mailto:zordoh@ipb.ac.rs) (Z. Dohčević-Mitrović).

Peer review under responsibility of Vietnam National University, Hanoi.

magnetolectric properties. The spin-phonon interaction plays an important role in the spin relaxation processes, or the spin reorientation transition, and can affect the ultrafast magnetic phenomena [16]. Yet, the interplay between spins and phonons in RE iron garnets is almost unstudied. Furthermore, the study of the spin-phonon coupling mechanism in multiferroic nanostructures is of great importance because the spins and phonons can be strongly coupled with the lattice strain, influencing at the same time the ferroelectric ordering and the coupling between electric polarization and the magnetization ordering [17]. It is worth to mention that the microscopic origin of the recently discovered large magnetolectric effect and multiferroic phase in  $\text{Dy}_3\text{Fe}_5\text{O}_{12}$  is still unclear [11]. Therefore, a better understanding of the spin-phonon coupling mechanism in nanocrystalline  $\text{Dy}_3\text{Fe}_5\text{O}_{12}$  is very important both from the fundamental and application point of view. Raman scattering spectroscopy is a highly sensitive and effective method for studying spin dynamics and the effects of exchange coupling between magnetic ions and phonons. This technique also allows to estimate the strength of the spin-phonon coupling in ferromagnetic (FM), ferrimagnetic, or antiferromagnetic (AFM) materials by analyzing the temperature evolution of the Raman mode frequencies at and below the magnetic transition temperature.

To our knowledge, the spin-phonon interaction in RE iron garnets, except for the yttrium iron garnet [18], was not studied before. The lack of such studies and knowing that  $\text{Dy}_3\text{Fe}_5\text{O}_{12}$  has a more complex magnetic structure than yttrium iron garnet motivated us to investigate the effects of magnetic ordering on optical phonon modes in nanocrystalline  $\text{Dy}_3\text{Fe}_5\text{O}_{12}$  analyzing the temperature-dependent Raman spectra. Within the mean-field approach, we were able to quantify the spin-phonon coupling strength of the phonon modes, which were sensitive to magnetic ordering. These results advance the understanding of the spin-phonon interaction in nanocrystalline  $\text{Dy}_3\text{Fe}_5\text{O}_{12}$  and can play an important role in better understanding of multiferroic, magnetolectric or magnetoaloric properties of RE iron garnets.

## 2. Experimental

The nanocrystalline  $\text{Dy}_3\text{Fe}_5\text{O}_{12}$  was prepared by an aqueous sol-gel method. Iron nitrate ( $\text{Fe}(\text{NO}_3)_3 \cdot 9\text{H}_2\text{O}$ ) and dysprosium oxide ( $\text{Dy}_2\text{O}_3$ ) were used as starting materials. Firstly, a stoichiometric amount of dysprosium oxide was dissolved in nitric acid. In the following step, 100 ml of deionized water and a stoichiometric amount of  $\text{Fe}(\text{NO}_3)_3 \cdot 9\text{H}_2\text{O}$  were added to the solution. The chelating agent PVA was added to the solution (the molar ratio of the total metal ions to the PVA = 1:1), and the solution was stirred for several hours at 55–65 °C. The formed gel was dried in an oven (120 °C) for 24 h. Finally, the dry gel was calcined at 800 °C for 3 h in the air.

The crystalline structure of nanocrystalline  $\text{Dy}_3\text{Fe}_5\text{O}_{12}$  was analysed using a Rigaku MiniFlex X-ray diffractometer in the  $2\theta$  range of 15–80°, with the step width of 0.01° and the scanning rate of 5°/min. Transmission electron microscopy (TEM) image of the sample was collected using a JEOL JEM 2100 transmission electron microscope. Energy dispersive X-ray analysis (EDAX) was conducted using an Oxford EDAX system attached to a JEOL JEM 2100 transmission electron microscope. Temperature-dependent micro-Raman spectra of nanocrystalline  $\text{Dy}_3\text{Fe}_5\text{O}_{12}$  (pressed into pellets) were collected in a backscattering configuration using a TriVista 557 triple spectrometer, with the spectral resolution of  $2\text{ cm}^{-1}$ . The temperature measurements from 80 to 700 K were performed in a Linkam THMSG600 cooling/heating stage. The argon/krypton ion laser with an emitting line at  $\lambda = 514.5\text{ nm}$  was used as an excitation source, with the output laser power kept at less than 2 mW to avoid

the heating effects and/or sample degradation. The Raman spectra were corrected by the Bose-Einstein thermal occupation factor. The magnetization vs. temperature was measured in the 6–315 K temperature range in a magnetic field of 10 kOe, using a vibrating sample magnetometer in a high field measuring system (HFMS, Cryogenic Ltd).

## 3. Results and discussion

$\text{Dy}_3\text{Fe}_5\text{O}_{12}$  crystallizes in a cubic crystal structure with space group  $O_h^{10}$  (*Ia3d*). The conventional unit cell consists of eight formula units  $\text{Dy}_3\text{Fe}_2(\text{FeO}_4)_3$ .  $\text{Fe}^{3+}$  ions occupy 16a octahedral ( $\text{Fe}^{\text{O}}$ ) and 24d tetrahedral ( $\text{Fe}^{\text{T}}$ ) sites, and  $\text{Dy}^{3+}$  ions occupy 24c dodecahedral sites. These three cation sites are surrounded by  $\text{O}^{2-}$  oxygen ions (see inset of Fig. 1(a)). The X-ray diffraction (XRD) pattern of nanocrystalline  $\text{Dy}_3\text{Fe}_5\text{O}_{12}$  sample is illustrated in Fig. 1(a).

The XRD peaks are indexed to the body-centered cubic  $\text{Dy}_3\text{Fe}_5\text{O}_{12}$  crystalline structure with the  $O_h^{10}$  (*Ia3d*) space group (JCPDS 23–0237). No impurity phases were detected. The average crystallite size, calculated by Scherrer formula, was 60 nm. Fig. 1(b) shows the TEM image of nanocrystalline  $\text{Dy}_3\text{Fe}_5\text{O}_{12}$  sample. The particles of different sizes (approximately 30–80 nm) and irregular shapes can be observed in the TEM image. The captured HRTEM image of the sample (Fig. 1(c)) exhibits clear lattice planes, and the distance between the adjacent planes is ~0.28 nm. The measured plane distance matches with the (420) reflection of the  $\text{Dy}_3\text{Fe}_5\text{O}_{12}$  crystal. The Selected Area Electron Diffraction (SAED) pattern, presented in the inset of Fig. 1(c), shows a large number of bright spots confirming the polycrystalline structure of the prepared  $\text{Dy}_3\text{Fe}_5\text{O}_{12}$  sample. The EDAX spectrum of  $\text{Dy}_3\text{Fe}_5\text{O}_{12}$ , given in Fig. 1(d), shows the signature peaks of Dy, Fe and O elements. Moreover, the peaks from Cu were also noticed, which originate from the Cu grid used for dispersing the  $\text{Dy}_3\text{Fe}_5\text{O}_{12}$  particles for the imaging and EDAX studies. The weight and atomic percentage of constituent elements (with and without Cu content) are listed in Table 1. From EDAX analysis it can be concluded that the stoichiometry of  $\text{Dy}_3\text{Fe}_5\text{O}_{12}$  sample is very close to the anticipated values.

Factor group analysis for the body-centered cubic garnet crystalline structure with  $O_h^{10}$  (*Ia3d*) space group predicts 25 Raman active modes (3  $A_{1g}$ , 8  $E_g$  and 14  $T_{2g}$ ) [19,20]. In Fig. 2(a) are presented Raman spectra of nanocrystalline  $\text{Dy}_3\text{Fe}_5\text{O}_{12}$  in the 80–700 K temperature range. In order to follow the evolution of the Raman modes with temperature and to determine more precisely the mode frequency, the spectra from Fig. 2(a) were deconvoluted using Lorentzian-type profiles. The deconvoluted Raman spectra, for some selected temperatures, are presented in Fig. 2(b). The insets display the enlarged view of the high-frequency modes together with the best Lorentzian fits.

In Table 1 are presented the frequencies of the Raman modes, obtained from the deconvoluted Raman spectrum at 80 K (Fig. 2(b)). The modes are classified according to the symmetry assignments taken from the literature for iron garnets [21–23] and are compared with the data of Song et al. for  $\text{Dy}_3\text{Fe}_5\text{O}_{12}$  crystal [21]. As can be seen, in the spectrum of nanocrystalline  $\text{Dy}_3\text{Fe}_5\text{O}_{12}$  the number of the Raman modes is smaller than in the spectrum of  $\text{Dy}_3\text{Fe}_5\text{O}_{12}$  crystal [21]. The appearance of fewer modes than predicted is a consequence of lower crystallinity of nanomaterials compared to the bulk counterparts.

The assignation of the Raman modes in iron garnets is very complex due to the presence of three different lattices in the garnet structure. Based on the lattice dynamical calculations of the Raman spectra in RE aluminum garnets [19, 20, 24], the high-frequency modes ( $> 500\text{ cm}^{-1}$ ) can be assigned to the internal vibrations of the tetrahedral ( $\text{FeO}_4$ ) units. In the middle-frequency region

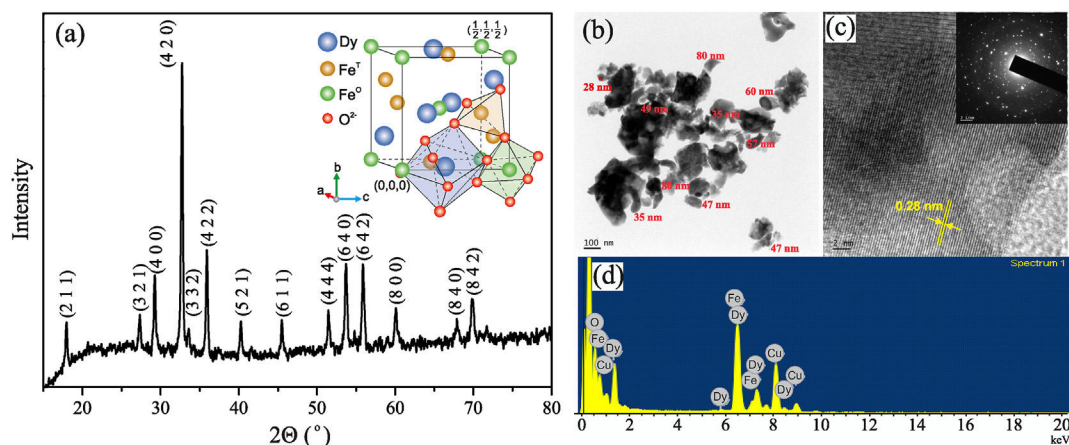


**Fig. 1.** (a) XRD pattern of the nanocrystalline  $\text{Dy}_3\text{Fe}_5\text{O}_{12}$ . The inset presents a garnet-type structure of space group  $O_h^{10}$  ( $1a3d$ ) with three distinct cation crystallographic sublattices surrounded by oxygen. (b) TEM image, (c) HRTEM image (SAED pattern is presented in the inset), and (d) EDAX spectrum of the nanocrystalline  $\text{Dy}_3\text{Fe}_5\text{O}_{12}$ .

**Table 1**

Estimated stoichiometry for  $\text{Dy}_3\text{Fe}_5\text{O}_{12}$  sample from EDAX analysis. The left half of the table is with, and the right one is without Cu content.

Element	Weight % ±3%	Atomic % ±3%	Element	Weight % ±3%	Atomic % ±3%
O K	17.64	53.77	O K	21.38	62.84
Fe K	21.64	18.90	Fe K	26.08	21.96
Cu K	19.50	14.97	Dy L	52.54	15.20
Dy L	41.21	12.37			
Total	100	100	Total	100	100

( $300\text{--}500\text{ cm}^{-1}$ ), the  $E_g$  Raman modes correspond to the internal vibrations of the RE ions, tetrahedral  $\text{Fe}^{\text{T}}$  ions, and oxygen, where the RE and  $\text{Fe}^{\text{T}}$  ions can move in phase or in antiphase.  $T_{2g}$  modes from the middle-frequency region present a combination of internal and rotational modes of tetrahedral units. It can be concluded that the Raman modes from the middle-frequency region are more complex and of mixed character. The low-frequency modes ( $< 300\text{ cm}^{-1}$ ) were attributed to  $\text{RE}^{3+}$ ,  $\text{FeO}_4$  and/or  $\text{FeO}_6$  translational modes [24,25]. At this point, it is worth mentioning the conclusions of Hurrell et al. [19], who pointed out that there is no apparent grouping of modes reflecting strong tetrahedral or octa-

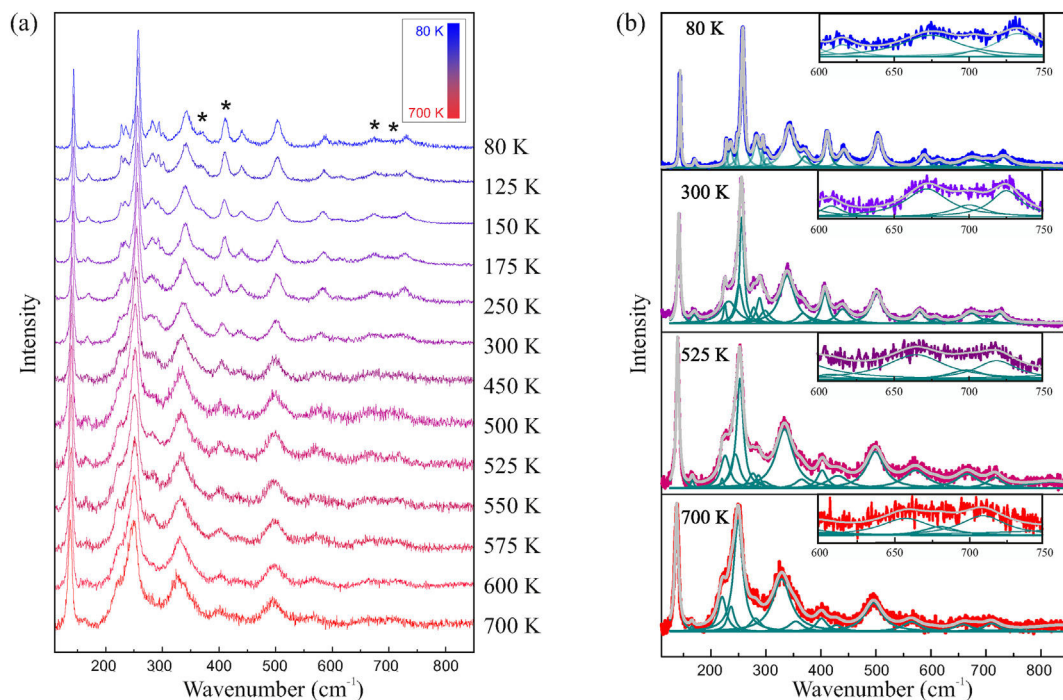


**Fig. 2.** Raman spectra of nanocrystalline  $\text{Dy}_3\text{Fe}_5\text{O}_{12}$  (a) in the  $80\text{--}700\text{ K}$  temperature range, and (b) at selected temperatures. The dark cyan lines represent Lorentzian fits of the experimental data and the grey lines are the cumulative fits. The anomalous phonon modes are marked with asterisk. The insets display the enlarged view of the high-frequency modes, together with individual and cumulative Lorentzian fits.

hedral bonding of the oxygen anions, as each oxygen atom belongs to one tetrahedron, one octahedron and two dodecahedra. Hurrell et al. also concluded that the Raman modes which do not involve the motion of cations (like  $A_{1g}$  modes), reflect more the octahedral vibrations of oxygen anions.

In magnetic materials, the exchange coupling between magnetic ions can affect phonon frequencies at and below the magnetic ordering temperature ( $T_C$  or  $T_N$ ). In FM materials, for  $T < T_C$ , the temperature dependence of the phonon mode frequency ( $\omega(T)$ ) can substantially deviate from the  $\omega(T)$  behavior predicted by the phonon–phonon anharmonic model [26]:

$$\omega_{\text{anh}}(T) = \omega_{\text{anh}}(0) - A \left( 1 + \frac{2}{e^{\frac{\hbar\omega(T)}{2k_B T}} - 1} \right), \quad (1)$$

where  $\omega_{\text{anh}}(0)$  is the phonon frequency at 0 K,  $A$  is the anharmonic constant related to the three-phonon scattering strength,  $\hbar$  is Planck's constant and  $k_B$  is Boltzmann's constant.

In the paramagnetic phase, at temperatures above  $T_C$ , spin-phonon coupling effects diminish and become negligible compared to the anharmonic effects [27]. Therefore, purely anharmonic contribution to the phonon frequency can be extracted from the  $\omega(T)$  dependence in the paramagnetic phase. In magnetically ordered state below  $T_C$ , an anomalous behavior of the phonon frequency is ascribed to the spin-lattice interaction [27–39]. As a result, the change of phonon frequency below  $T_C$  can be expressed as the sum of anharmonic ( $\omega_{\text{anh}}(T)$ ) and spin-phonon ( $\omega_{\text{s-ph}}(T)$ ) contributions:  $\omega(T) = \omega_{\text{anh}}(T) + \Delta\omega_{\text{s-ph}}(T)$ .

Based on the Heisenberg model for the nearest-neighbor spin interaction, the phonon frequency shift, due to the spin-phonon interaction [40], can be expressed as

$$\Delta\omega_{\text{s-ph}}(T) = \lambda \langle \mathbf{S}_i \cdot \mathbf{S}_j \rangle, \quad (2)$$

where  $\lambda$  is the spin-phonon coupling constant and  $\langle \mathbf{S}_i \cdot \mathbf{S}_j \rangle$  is the spin–spin correlation function between the nearest-neighbor spins localized at the  $i$ th and  $j$ th site.

In magnetic materials with coexisting FM and AFM ordering, the  $\Delta\omega_{\text{s-ph}}$  term, according to the theoretical model [41], can be expressed in the form:

$$\Delta\omega_{\text{s-ph}}(T) \propto -J \langle \mathbf{S}_i \cdot \mathbf{S}_j \rangle + K \langle \mathbf{S}_i \cdot \mathbf{S}_k \rangle, \quad (3)$$

where  $\mathbf{S}_i$ ,  $\mathbf{S}_j$  and  $\mathbf{S}_k$  indicate the spin of the  $i$ th,  $j$ th and  $k$ th magnetic ion, and  $\langle \mathbf{S}_i \cdot \mathbf{S}_j \rangle$  and  $\langle \mathbf{S}_i \cdot \mathbf{S}_k \rangle$  are the spin correlation functions for the nearest-neighbor or the next nearest-neighbor interactions, respectively. The constants  $J$  and  $K$  are the spin dependent force constants of the lattice vibrations, and present the summation of second derivatives of the exchange integrals with respect to the phonon displacement. The constants  $J$  and  $K$  are associated with the FM and AFM nearest-neighbor or next nearest–neighbor exchange.

Assuming that the spin correlation functions  $\langle \mathbf{S}_i \cdot \mathbf{S}_j \rangle$  and  $\langle \mathbf{S}_i \cdot \mathbf{S}_k \rangle$  have the same temperature dependence, and that  $J$  and  $K$  have constant values for the same Raman mode [33,41], the above expression can be written in a simplified form:

$$\Delta\omega_{\text{s-ph}}(T) \propto (K - J) \langle \mathbf{S}_i \cdot \mathbf{S}_j \rangle. \quad (4)$$

Depending on the relative strength between the FM and AFM exchange interactions, from Eq. (4) follows that the frequency shift of the Raman mode will be positive or negative depending on the sign of the  $(K - J)$  difference. Comparing Eq. (2) and Eq. (4) it is obvious that  $\lambda$  can take negative or positive values depending on whether the FM or AFM interaction is more dominant for the particular mode.

Knowing that in ferrimagnetic materials like iron garnets, the phonon frequencies can be influenced by magnetic ordering below  $T_C$ , and that anharmonic processes should dominate in paramagnetic phase at  $T > T_C$ , the  $\omega(T)$  dependence for each Raman mode from Fig. 2(a) was fitted using three-phonon anharmonic model (Eq. (1)) for  $T > T_C$ . This analysis showed that four Raman modes from the middle- and high-frequency regions exhibited anomalous frequency behavior below  $T_C$ . The positions of these modes at 80 K are 370, 411, 674 and 703  $\text{cm}^{-1}$ , respectively (see Table 2). The rest of the Raman modes have similar  $\omega(T)$  dependence in the whole temperature range, which can be well fitted using Eq. (1). The  $\omega(T)$  dependences for 370, 411, 674 and 703  $\text{cm}^{-1}$  modes, together with the anharmonic fits, are presented in Fig. 3, where the regions of paramagnetic and ferrimagnetic phases are clearly marked. The anomalous frequency softening of 370, 674 and 703  $\text{cm}^{-1}$  modes (Fig. 3(a), (c) and (d)), and hardening of the 411  $\text{cm}^{-1}$  mode (Fig. 3(b)), below  $T_C$ , imply that these modes are strongly affected by magnetic ordering.

$\text{Dy}_3\text{Fe}_5\text{O}_{12}$  is a ferrimagnetic material with three magnetic sublattices (see inset of Fig. 4, where  $M_d$ ,  $M_a$  and  $M_c$  are the sublattice magnetizations).  $\text{Fe}^{3+}$  ions, located in tetrahedral  $d$  sites and octahedral  $a$  sites, are strongly coupled via AFM superexchange interaction ( $\text{Fe}^{\text{T}(3+)} - \text{O}^{2-} - \text{Fe}^{\text{O}(3+)}$ ). Because of the unequal number of Fe ions in two magnetic sublattices, the magnetizations  $M_d$  and  $M_a$  are of different magnitudes, resulting in a ferrimagnetic ordering below  $T_C$ . The noncompensated resultant magnetization ( $M_d - M_a$ ) is coupled antiparallely to the magnetization of Dy ions ( $M_c$ ) at dodecahedral  $c$  sites. The magnetization of  $\text{Dy}_3\text{Fe}_5\text{O}_{12}$  is very dependent on temperature [13,42–45]. At very low temperatures, the magnetization of the Dy sublattice surpasses the resultant magnetization of Fe sublattices. With increasing temperature, the magnetization of the Dy sublattice falls off more quickly than that of the Fe sublattices, and at the compensation temperature,  $T_{\text{comp}}$ , the magnetizations of Dy and Fe sublattices are mutually compensated [1,13,43–45]. Above the  $T_{\text{comp}}$ , and up to the magnetic transition temperature  $T_C = 525$  K, the resultant magnetization of the Fe sublattices predominates. In Fig. 4 is shown the measured magnetization vs. temperature for nanocrystalline  $\text{Dy}_3\text{Fe}_5\text{O}_{12}$ . The compensation temperature ( $T_{\text{comp}}$ ) is around 225 K, in accordance with literature data [13,43–45].

**Table 2**

The frequencies (in  $\text{cm}^{-1}$ ) and symmetry assignments of Raman active phonons in nanocrystalline  $\text{Dy}_3\text{Fe}_5\text{O}_{12}$  at 80 K, compared with the data from Ref. [21].

Mode	Present work $\pm 3 \text{ cm}^{-1}$	Song et al. [21] $\pm 3 \text{ cm}^{-1}$
$T_{2g}$		101
$T_{2g}$	143	144
$T_{2g}$	170	173
$T_{2g}$	235	236
$E_g$	257	259
$T_{2g}$		276
$E_g$	283	285
$T_{2g}$		325
$E_g + A_{1g}$	342	347
$T_{2g}$	370	371
$E_g$	411	410
$E_g$		435
$T_{2g}$	442	448
$T_{2g}$	504	501
$A_{1g}$		507
$T_{2g}$	587	589
$E_g$		624
$E_g + T_{2g}$	674	676
$A_{1g} + T_{2g}$	703	695
$A_{1g} + T_{2g}$	732	734

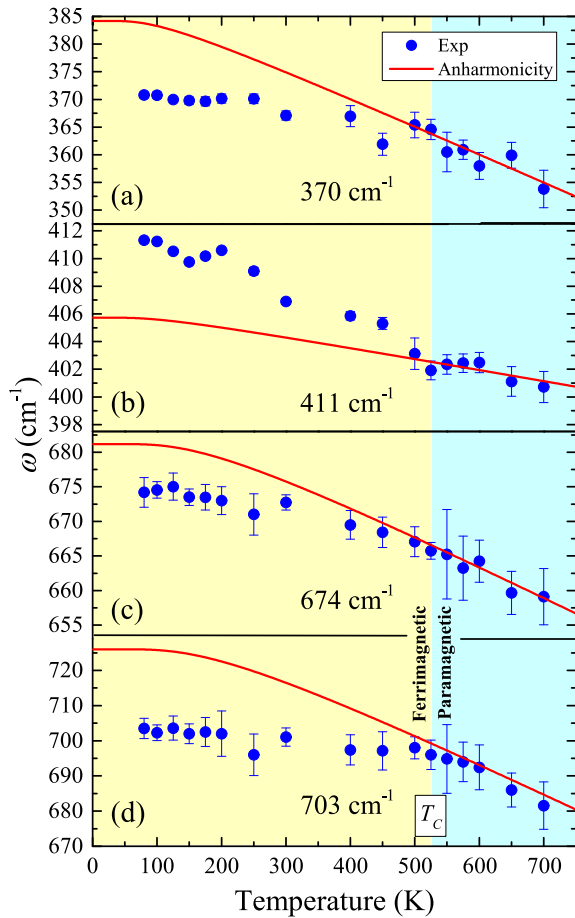


**Fig. 3.** Temperature dependence of the phonon frequencies (blue circles) at (a) 370, (b) 411, (c) 674, and (d) 703  $\text{cm}^{-1}$ . The theoretically predicted anharmonic trend is presented by solid lines.

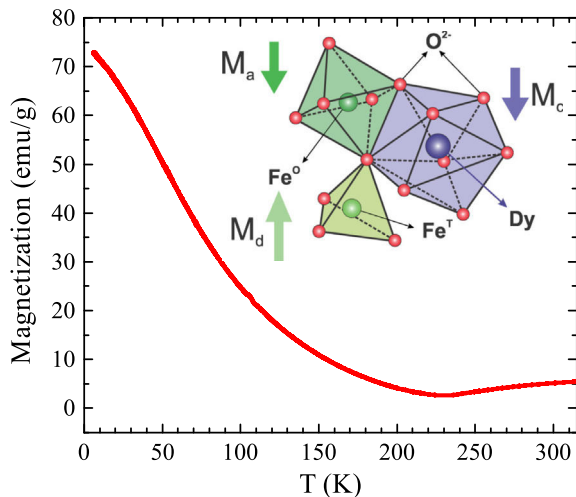


**Fig. 4.** Magnetization vs. temperature for nanocrystalline  $\text{Dy}_3\text{Fe}_5\text{O}_{12}$ . In the inset is given a schematic representation of three different magnetic sublattices of  $\text{Dy}_3\text{Fe}_5\text{O}_{12}$  with polyhedra of oxygens.

In dysprosium iron garnet, among six different FM or AFM exchange interactions between the Fe and the Dy spins (three Fe–Fe interactions, two Fe–Dy interactions and one Dy–Dy interaction), the dominant superexchange interaction is between Fe spins in tetrahedral and octahedral sites ( $\text{Fe}^{\text{T}}\text{--Fe}^{\text{O}}$  interaction). The second

strongest interaction is AFM interaction between Dy and  $\text{Fe}^{\text{T}}$  spins (the first-nearest-neighbor Dy– $\text{Fe}^{\text{T}}$  interaction) [44,46,47].

In materials with competitive FM and AFM interactions, like  $\text{Dy}_3\text{Fe}_5\text{O}_{12}$ , the exchange interactions between magnetic ions depend on their positions and on the positions of some nearby non-magnetic neighbors. On the other hand, each Raman mode involves vibrations of different magnetic and/or non-magnetic ions. Therefore, the contribution of FM or AFM exchange integrals to the spin dependent force constants ( $J$  and  $K$  in Eq. (3)) can be different for different modes [33,40,41]. As a result, the frequency shift due to the spin-phonon coupling (see Eq. (4)) will be negative or positive, depending on whether the FM or AFM exchange interaction is more dominant for a particular mode.

In magnetically ordered phase, the opposite frequency shifts of 370, 674 and 703  $\text{cm}^{-1}$  modes on one side, and the 411  $\text{cm}^{-1}$  mode on the other side, can be explained in the following way. The Raman modes at 674 and 703  $\text{cm}^{-1}$  are assigned to the internal vibrational modes of the tetrahedral ( $\text{FeO}_4$ ) units, whereas the mode at 370  $\text{cm}^{-1}$  corresponds to a combination of rotational modes of the same units [20,23,24]. The ferromagnetic  $\text{Fe}^{\text{T}}\text{--O--Fe}^{\text{T}}$  exchange interactions between nearest-neighbor tetrahedral ( $\text{Fe}^{\text{T}}\text{--O}$ ) vibrations. As a consequence, detectable changes in the phonon frequencies on entering the magnetic phase should be seen. According to the Eq. (4), the anomalous frequency softening of 370, 674 and 703  $\text{cm}^{-1}$  modes (Fig. 3(a), (c) and (d)) below  $T_c$  imply that these modes are effectively modulated by FM exchange interactions between  $\text{Fe}^{\text{T}}$  ions in the magnetically ordered phase. On the other hand, in RE iron garnets, some phonon modes from the middle-frequency region can be sensitive to the AFM ordering between the RE and  $\text{Fe}^{\text{T}}$  ions. The Raman mode at 411  $\text{cm}^{-1}$  involves the motion of dodecahedral Dy ions, tetrahedral  $\text{Fe}^{3+}$  ions and oxygen ions [24]. Hence, it is reasonable to assume that the antiferromagnetic Dy–O– $\text{Fe}^{\text{T}}$  exchange interaction strongly affects the frequency of 411  $\text{cm}^{-1}$  mode below magnetic ordering temperature and is responsible for the noticed anomalous positive frequency shift of this mode.

In order to determine the strength of the spin-phonon coupling of these modes, the influence of the spin-phonon coupling effect on the phonon frequency  $\Delta\omega_{\text{s-ph}}(T)$  should be separated from the anharmonic contribution  $\omega_{\text{anh}}(T)$ . This is usually done by taking the difference between the measured frequency and the expected anharmonic contribution (see Eq. (1)),  $\Delta\omega_{\text{s-ph}}(T) = \omega(T) - \omega_{\text{anh}}(T)$ . The temperature dependence of  $|\Delta\omega_{\text{s-ph}}|$  for the four phonons modes from Fig. 3 is presented in Fig. 5.

According to the mean-field approximation, and considering an interaction between the nearest-neighbor spins localized at the  $i$ th and  $j$ th site, the spin–spin correlation function  $\langle \mathbf{S}_i \cdot \mathbf{S}_j \rangle$  is proportional to the square of normalized magnetization:

$$\frac{\langle \mathbf{S}_i \cdot \mathbf{S}_j \rangle}{S^2} = \left( \frac{M(T)}{M_0} \right)^2, \quad (5)$$

where  $M(T)$  is spontaneous magnetization at temperature  $T$  and  $M_0$  is the maximal value of spontaneous magnetization [48]. Comparing Eqs. (2) and (5), the frequency shift due to the spin-phonon coupling  $\Delta\omega_{\text{s-ph}}(T)$  should scale with the  $(M(T)/M_0)^2$  curve. The  $(M(T)/M_0)^2$  curve was obtained using a numerical solution of the Brillouin function [49] for the case of  $S = 5/2$  (for Fe and Dy ions). From Fig. 5 it can be seen that the  $|\Delta\omega_{\text{s-ph}}|(T)$  for each mode scales very well with  $(M(T)/M_0)^2$  curve (solid lines), confirming that the observed significant frequency deviation of these modes from the anharmonic behavior below  $T_c$ , originates from the spin-phonon coupling effects.

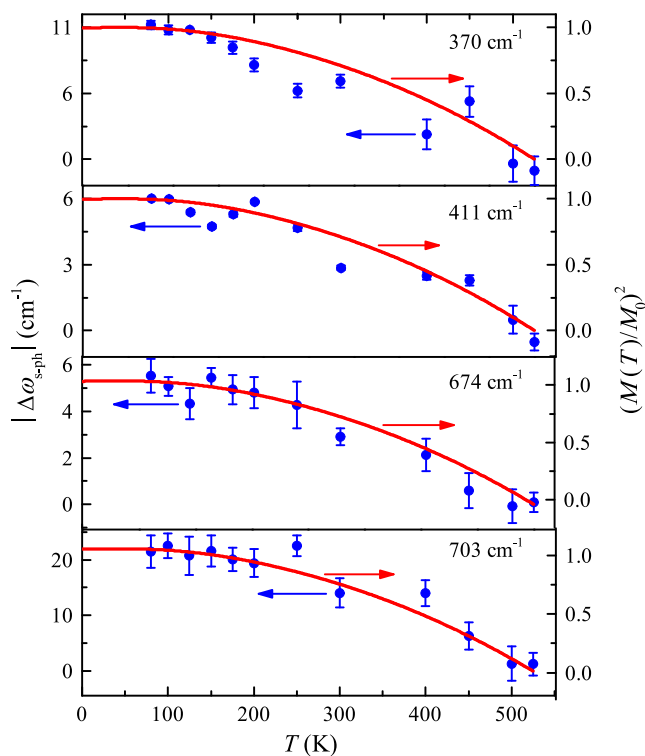


**Fig. 5.** Temperature dependences of  $|\Delta\omega_{s-ph}|$  (left axis, blue circles) compared with the theoretically obtained curve  $(M(T)/M_0)^2$  (right axis, solid lines) for the 370, 411, 674, and 703  $\text{cm}^{-1}$  phonon modes.

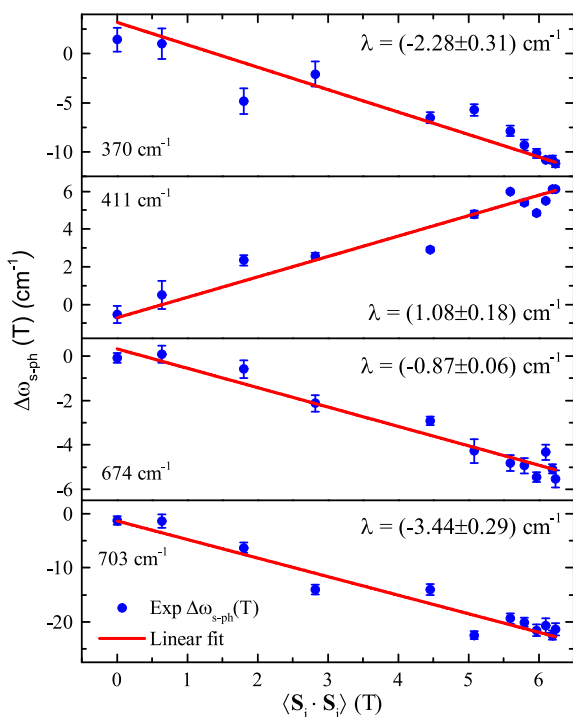


**Fig. 6.** The plot of  $\Delta\omega_{s-ph}(T)$  vs.  $\langle\mathbf{S}_i \cdot \mathbf{S}_j\rangle(T)$  for anomalous phonon modes from Fig. 5 (blue circles). The solid lines are linear fits to the data. The obtained values for spin-phonon coupling constant,  $\lambda$ , are presented for each mode.

According to the Eqs. (2) and (5), the spin-phonon coupling constant  $\lambda$ , as a measure of the strength of the spin-phonon interaction, can be deduced from the plot  $\Delta\omega_{s-ph}(T)$  vs. spin-spin correlation function  $\langle\mathbf{S}_i \cdot \mathbf{S}_j\rangle(T)$ . The plot of  $\Delta\omega_{s-ph}(T)$  vs.  $\langle\mathbf{S}_i \cdot \mathbf{S}_j\rangle(T)$  for four anomalous phonon modes is presented in Fig. 6, where the solid lines represent a linear fit of the data.

The spin-phonon coupling constants  $\lambda$  were determined from the slopes of the linear fits, and  $\lambda$  values are given for each mode in Fig. 6. From this study it can be deduced that  $\lambda$  values obtained by this approach are comparable for all four modes, but have different signs. This result implies that competitive FM and AFM exchange interactions affect the Raman modes differently. The negative values of  $\lambda$ , which are larger for the 703 and 370  $\text{cm}^{-1}$  modes than for the 674  $\text{cm}^{-1}$  mode, imply that these two modes are more affected by FM ordering. The positive sign for the 411  $\text{cm}^{-1}$  mode implies that this mode is dominantly influenced by AFM ordering. Since these modes originate from different vibrations between magnetic ions, it can be concluded that the relative strength of FM or AFM interactions and their contributions to the particular Raman mode are closely related to the vibrational pattern of the mode.

#### 4. Conclusion

We presented the influence of spin-phonon coupling interaction on the phonon modes in nanocrystalline  $\text{Dy}_3\text{Fe}_5\text{O}_{12}$  using Raman spectroscopy. The nanocrystalline  $\text{Dy}_3\text{Fe}_5\text{O}_{12}$  was prepared by an aqueous sol-gel method synthesis method and the crystal structure, morphology and composition were investigated by XRD, TEM and Raman measurements. From the temperature evolution of the Raman modes, it is shown that four phonon modes from middle- and high-frequency regions displayed significant frequency deviation from the expected anharmonic behavior below  $T_C$ . It is concluded that the spin-phonon interaction lies behind the observed anomalous frequency behavior. Different Raman modes exhibited negative or positive shifts with respect to the anharmonicity. Raman modes at 370, 674 and 703  $\text{cm}^{-1}$ , which were assigned to the internal tetrahedral ( $\text{FeO}_4$ ) vibrations, experienced negative frequency shift with respect to the anharmonicity due to resultant FM interaction among tetrahedral  $\text{Fe}^{3+}$  ions. The Raman mode at 411  $\text{cm}^{-1}$ , which involves the motion of dodecahedral  $\text{Dy}^{3+}$  and tetrahedral  $\text{Fe}^{3+}$  ions, was found to be more sensitive to the AFM exchange interaction between these ions. Within the mean-field approach, the spin-spin correlation function was related to the phonon frequency shift and the spin-phonon coupling strength was estimated for each mode. It was concluded that the coupling of Raman modes with FM or AFM ordering as well as, the strength of this coupling are largely dependent on the vibrational pattern of the particular mode. This study provides a foundation for a better understanding of the fundamental physical properties of  $\text{Dy}_3\text{Fe}_5\text{O}_{12}$  based on complex magnetic behavior, thus providing valuable information for the optimization and development of spintronic devices in the near future.

#### Acknowledgments

The authors acknowledge funding provided by the Institute of Physics Belgrade and the Serbia-India bilateral project through the Grants No: 451-03-47/2023-01/200024 and No: 451-02-697/2022-09/02 of the Ministry of Science, Technological Development and Innovation of the Republic of Serbia. The authors B.R. and N.K. acknowledge the support from the Department of Science and Technology, Govt. of India through India Serbia Joint S and T project (DST/INT/IND-SERBIA/2022/2).

## Declaration of competing interests

The authors declare that they have no known competing financial interests or personal relationships that could have appeared to influence the work reported in this paper.

## References

- [1] F. Sayetat, Huge magnetostriction in  $Tb_3Fe_5O_{12}$ ,  $Dy_3Fe_5O_{12}$ ,  $Ho_3Fe_5O_{12}$ ,  $Er_3Fe_5O_{12}$  garnets, *J. Magn. Magn. Mater.* 58 (1986) 334–346.
- [2] W.R. Eppler, M.H. Kryder, Garnets for short wavelength magneto-optic recording, *J. Phys. Chem. Solid.* 56 (1995) 1479–1490.
- [3] T. Yoshimoto, T. Goto, R. Isogai, Y. Nakamura, H. Takagi, C.A. Ross, M. Inoue, Magnetophotonic crystal with cerium substituted yttrium iron garnet and enhanced Faraday rotation angle, *Opt Express* 24 (2016) 8746–8753.
- [4] R. Booth, E. White, Magneto-optic properties of rare earth iron garnet crystals in the wavelength range 1.1–1.7  $\mu\text{m}$  and their use in device fabrication, *J. Phys. D Appl. Phys.* 17 (2000) 579–587.
- [5] M.H. Phan, M.B. Morales, C.N. Chinnsamy, B. Latha, V.G. Harris, H. Srikanth, Magnetocaloric effect in bulk and nanostructured  $Gd_3Fe_5O_{12}$  materials, *J. Phys. D Appl. Phys.* 42 (2009) 115007.
- [6] N. Hur, S. Park, S. Guha, A. Borissov, V. Kiryukhin, S.-W. Cheong, Low-field magnetodielectric effect in terbium iron garnets, *Appl. Phys. Lett.* 87 (4) (2005) 042901.
- [7] S.M. Zanjani, M.C. Onbasli, Thin film rare earth iron garnets with perpendicular magnetic anisotropy for spintronic applications, *AIP Adv.* 9 (2019) 035024.
- [8] C. Suchomski, C. Reitz, D. Pajić, Z. Jagličić, I. Djerdj, T. Brezesinski, Large-pore mesoporous  $Ho_3Fe_5O_{12}$  thin films with strong room temperature perpendicular magnetic anisotropy by sol-gel processing, *Chem. Mater.* 26 (2014) 2337–2343.
- [9] W. Wang, R. Chen, X. Qi, Analysis on three-sublattice model of magnetic properties in rare-earth iron garnets under high magnetic fields, *J. Alloys Compd.* 512 (2012) 128–131.
- [10] A. Boutaba, M. Lahoubi, V. Varazashvili, S. Pu, Magnetic, magneto-optical and specific heat studies of the low temperature anomalies in the magnetodielectric DyIG ferrite garnet, *J. Magn. Magn. Mater.* 476 (2019) 551–558.
- [11] Y. Tokunaga, S. Iguchi, T. Arima, Y. Tokura, Magnetic-field-induced ferroelectric state in  $DyFeO_3$ , *Phys. Rev. Lett.* 101 (2008) 097205.
- [12] K.M. Song, Y.A. Park, K.D. Lee, B.K. Yun, M.H. Jung, J. Cho, J.H. Jung, N. Hur, Magnetodielectric effect via a noncollinear-to-collinear spin reorientation in rare-earth iron garnets, *Phys. Rev. B* 83 (2011) 012404.
- [13] P.J. von Ranke, B.P. Alho, E.J.R. Plaza, A.M.G. Carvalho, V.S.R. de Sousa, N.A. de Oliveira, Theoretical investigation on the magnetocaloric effect in garnets  $R_3Fe_5O_{12}$  where (R=Y and Dy), *J. Appl. Phys.* 106 (2009) 053914.
- [14] C. Li, G.O. Barasa, Y. Qiu, S. Yuan, Magnetocaloric effect and sign reversal of magnetic entropy change across the spin reorientation temperature in  $R_3Fe_5O_{12}$  (R = Gd, Dy), *J. Alloys Compd.* 820 (2020) 153138.
- [15] J.J. Bauer, E.R. Rosenberg, S. Kundu, K.A. Mkhoyan, P. Quarterman, A.J. Grutter, B.J. Kirby, J.A. Borchers, C.A. Ross, Dysprosium iron garnet thin films with perpendicular magnetic anisotropy on silicon, *Adv. Electron. Mater.* 6 (2020) 1900820.
- [16] M. Deb, P. Molho, B. Barbara, J.-Y. Bigot, Controlling laser-induced magnetization reversal dynamics in a rare-earth iron garnet across the magnetization compensation point, *Phys. Rev. B* 97 (2018) 134419.
- [17] C.Y. Tsai, H.M. Cheng, H.R. Chen, K.F. Huang, L.N. Tsai, Y.H. Chu, C.H. Lai, W.F. Hsieh, Spin and phonon anomalies in epitaxial self-assembled  $CoFe_2O_4$ - $BaTiO_3$  multiferroic nanostructures, *Appl. Phys. Lett.* 104 (2014) 252905.
- [18] K.S. Olsson, J. Choe, M. Rodriguez-Vega, G. Khalsa, N.A. Benedek, J. He, B. Fang, J. Zhou, G.A. Fiete, X. Li, Spin-phonon interaction in yttrium iron garnet, *Phys. Rev. B* 104 (2021) L020401.
- [19] J.P. Hurrell, S.P.S. Porto, I.F. Chang, S.S. Mitra, R.P. Bauman, Optical phonons of yttrium aluminum garnet, *Phys. Rev.* 173 (1968) 851–856.
- [20] G. Mace, G. Schaack, T. Ng, J.A. Koningstein, Optical phonons of terbium-, dysprosium-, and ytterbium-garnet, *Phys. B Condens. Matter* 230 (1970) 391–402.
- [21] J.-J. Song, P.B. Klein, R.L. Wadsack, M. Selders, S. Mroczkowski, R.K. Chang, Raman-active phonons in aluminum, gallium, and iron garnets, *J. Opt. Soc. Am.* 63 (1973) 1135–1140.
- [22] J.-M. Costantini, S. Miro, F. Beuneu, M. Toulemonde, Swift heavy ion-beam induced amorphization and recrystallization of yttrium iron garnet, *J. Phys. Condens. Matter* 27 (2015) 496001.
- [23] P. Grunberg, J.A. Koningstein, L.G.V. Uitert, Optical phonons in iron garnets, *J. Opt. Soc. Am.* 61 (1971) 1613–1617.
- [24] K. Papagelis, G. Kanellis, S. Ves, G. Kourouklis, Lattice dynamical properties of the rare earth aluminum garnets ( $RE_3Al_5O_{12}$ ), *Phys. Status Solidi B* 233 (2002) 134–150.
- [25] P. Fechine, E. Silva, A. de Menezes, J. Derov, J. Stewart, A. Drehman, I. Vasconcelos, A. Ayala, L. Cardoso, A. Sombra, Synthesis, structure and vibrational properties of  $GdIG_xYIG_{1-x}$  ferrimagnetic ceramic composite, *J. Phys. Chem. Solid.* 70 (2009) 202–209.
- [26] P.G. Klemens, Anharmonic decay of optical phonons, *Phys. Rev.* 148 (1966) 845–848.
- [27] E. Aytan, B. Debnath, F. Kargar, Y. Barlas, M.M. Lacerda, J.X. Li, R.K. Lake, J. Shi, A.A. Balandin, Spin-phonon coupling in antiferromagnetic nickel oxide, *Appl. Phys. Lett.* 111 (2017) 252402.
- [28] D.J. Lockwood, M.G. Cottam, The spin-phonon interaction in  $FeF_2$  and  $MnF_2$  studied by Raman spectroscopy, *J. Appl. Phys.* 64 (1988) 5876–5878.
- [29] E. Granado, A. García, J.A. Sanjurjo, C. Rettori, I. Torriani, F. Prado, R.D. Sánchez, A. Caneiro, S.B. Oseroff, Magnetic ordering effects in the Raman spectra of  $La_{1-x}Mn_{1-x}O_3$ , *Phys. Rev. B* 60 (1999) 11879–11882.
- [30] D.J. Lockwood, Spin-phonon interaction and mode softening in  $NiF_2$ , *Low Temp. Phys.* 28 (2002) 505–509.
- [31] J. Laverdière, S. Jandl, A.A. Mukhin, V.Y. Ivanov, V.G. Ivanov, M.N. Iliev, Spin-phonon coupling in orthorhombic  $RMnO_3$  (R=Pr,Nd,Sm, Eu,Gd,Tb,Dy,Ho,Y): A Raman study, *Phys. Rev. B* 73 (2006) 214301.
- [32] C. Kant, J. Deisenhofer, T. Rudolf, F. Mayr, F. Schrettle, A. Loidl, V. Gnezdilov, D. Wulferding, P. Lemmens, V. Tsurkan, Optical phonons, spin correlations, and spin-phonon coupling in the frustrated pyrochlore magnets  $CdCr_2O_4$  and  $ZnCr_2O_4$ , *Phys. Rev. B* 80 (2009) 214417–214426.
- [33] J.A. Moreira, A. Almeida, W.S. Ferreira, J.E. Araújo, A.M. Pereira, M.R. Chaves, J. Kreisel, S.M.F. Vilela, P.B. Tavares, Coupling between phonons and magnetic excitations in orthorhombic  $Eu_{1-x}Y_xMnO_3$ , *Phys. Rev. B* 81 (2010) 054447.
- [34] X.-B. Chen, N.T. Minh Hien, K. Han, J. Chul Sur, N.H. Sung, B.K. Cho, I.-S. Yang, Raman studies of spin-phonon coupling in hexagonal  $BaFe_{12}O_{19}$ , *J. Appl. Phys.* 114 (2013) 013912.
- [35] P.-H. Shih, C.-L. Cheng, S.Y. Wu, Short-range spin-phonon coupling in in-plane  $CuO$  nanowires: a low-temperature Raman investigation, *Nanoscale Res. Lett.* 8 (398) (2013).
- [36] A. Ahlawat, S. Satapathy, S. Maan, V.G. Sathe, P.K. Gupta, Correlation of structure and spin-phonon coupling in (La, Nd) doped  $BiFeO_3$  films, *J. Raman Spectrosc.* 45 (2014) 958–962.
- [37] Y. Sharma, S. Sahoo, W. Perez, S. Mukherjee, R. Gupta, A. Garg, R. Chatterjee, R.S. Katiyar, Phonons and magnetic excitation correlations in weak ferromagnetic  $YCrO_3$ , *J. Appl. Phys.* 115 (2014) 183907.
- [38] C.-S. Chen, C.-S. Tu, P.-Y. Chen, V.H. Schmidt, Z.-R. Xu, Y. Ting, Spin-lattice coupling phase transition and phonon anomalies in bismuth ferrite  $BiFeO_3$ , *J. Alloys Compd.* 687 (2016) 442–450.
- [39] R.X. Silva, M.C.C. Júnior, S. Yáñez-Vilar, M.S. Andújar, J. Mira, M.A. Señarís-Rodríguez, C.W.A. Paschoal, Spin-phonon coupling in multiferroic  $Y_2CoMnO_6$ , *J. Alloys Compd.* 690 (2017) 909–915.
- [40] W. Baltensperger, J.S. Helman, Influence of magnetic order in insulators on the optical phonon frequency, *Helv. Phys. Acta* 41 (1968) 668–673.
- [41] K. Wakamura, T. Arai, Effect of magnetic ordering on phonon parameters for infrared active modes in ferromagnetic spinel  $CdCr_2S_4$ , *J. Appl. Phys.* 63 (1988) 5824–5829.
- [42] R. Pauthenet, Spontaneous magnetization of some garnet ferrites and the aluminum substituted garnet ferrites, *J. Appl. Phys.* 29 (1958) 253–255.
- [43] M. Uemura, T. Yamagishi, S. Ebisu, S. Chikazawa, S. Nagata, A double peak of the coercive force near the compensation temperature in the rare earth iron garnets, *Philos. Mag. A* 88 (2008) 209–228.
- [44] T.D. Kang, E.C. Standard, P.D. Rogers, K.H. Ahn, A.A. Sirenko, A. Dubroka, C. Bernhard, S. Park, Y.J. Choi, S.-W. Cheong, Far-infrared spectra of the magnetic exchange resonances and optical phonons and their connection to magnetic and dielectric properties of  $Dy_3Fe_5O_{12}$  garnet, *Phys. Rev. B* 86 (2012) 144112.
- [45] D.T.T. Nguyen, N.P. Duong, T. Satoh, L.N. Anh, T.T. Loan, T.D. Hien, Crystallization and magnetic characterizations of dyig and hoig nanopowders fabricated using citrate sol-gel, *J. Sci.: Adv. Mater. Devices* 1 (2016) 193–199.
- [46] R. Nakamoto, B. Xu, C. Xu, H. Xu, L. Bellaiche, Properties of rare-earth iron garnets from first principles, *Phys. Rev. B* 95 (2017) 024434.
- [47] T. Bayarara, C. Xu, D. Campbell, L. Bellaiche, Tuning magnetization compensation and Curie temperatures in epitaxial rare earth iron garnet films, *Phys. Rev. B* 100 (2019) 214412.
- [48] K. Yosida, Theory of Magnetism, Springer-Verlag Berlin Heidelberg, 1996.
- [49] V. Barsan, V. Kuncser, Exact and approximate analytical solutions of Weiss equation of ferromagnetism and their experimental relevance, *Phil. Mag. Lett.* 97 (2017) 359–371.